

The University Of Sheffield.

Investigation of c-BN tipped blade performance in gas turbine ceramic abradable seal systems

Alvaro Parody Martin

A thesis submitted in partial fulfilment of the requirements for the degree of

Doctor of Philosophy

The University of Sheffield

Faculty of Engineering

Department of Mechanical Engineering

Submission Date

Spring 2024

This thesis is dedicated to
my father Francisco Javier, in loving memory. I fondly remember his playful jokes about my good school grades with a 'con un cinco también se aprueba' and my mother Maria Paz, who has consistently encouraged and supported me in pursuing my dreams.

Acknowledgements

I would like to express my sincere gratitude to my supervisor Prof. Matthew Marshall who has supported me during this long journey. I truly value your technical advice and mentorship, but what I cherish even more is your patience, your positive attitude, your willingness to help and your personal support, especially during my moments of demotivation. Your counsel on my professional career development has been invaluable, and I am profoundly grateful for the privilege of having you as my supervisor.

I am indebted to Rolls-Royce, particularly Matthew Hancock, Glen Pattinson, and Lloyd Pallet, for entrusting me with the opportunity to work with a company I have always been passionate about. Special thanks to Matthew Hancock for his unwavering industrial support and prompt responsiveness in facilitating additional assistance from Rolls-Royce when needed.

Gratitude extends to the technicians at the Department of Mechanical Engineering who made this experimental PhD possible. I want to express my individual thanks to Oliver Cooper, with whom I have spent countless hours in the test cell, learning immensely; Christopher Todd, for his guidance in handling electrical and electronic tasks; Matt Kirkland, for managing my urgent manufacturing job requisitions; and in loving memory of Richard Kay, whose willingness to help and cheerful spirit are deeply missed.

I would also like to acknowledge my lab, and outside-the-lab, buddies: Eldar, Allan, Julian, Aaron, Aleena and Boxiu, for the camaraderie, support and the good memories together. They have alleviated the challenges of this lengthy and demanding journey, making it not only more bearable but also more enjoyable. To my friends back in Sevilla, with whom our relationships remain unaffected by the passage of time. Special mention to my friends from "Los Chavales", "Los Gitans" and "Tocar Huevos",

and an individually thanks to Cristina who has always been there when I needed.

Finally, I would express my deepest and most sincere gratitude to my mother Maria Paz, my brother Javier, my sister Maria Paz and my father, Francisco Javier, who remains in my heart in loving memory, and his inspiration continues to guide and inspire me.

In closing, I extend my gratitude to everyone who has played a role, no matter how small, in the completion of this journey. Your collective contributions have made this personal, and academical, achievement possible.

Abstract

Abradable seal systems play a crucial role in ensuring the efficient functioning of the compressor and turbine stages in gas turbines. These systems involve a sacrificial abradable lining which is cut by a blade, either bare or abrasive tipped. The interaction between these components during engine break-in defines the blade tip clearance, a critical factor for engine efficiency. Tight tip clearances are essential to prevent increased fuel consumption and reduce component lifespan. In the challenging conditions of the high-pressure turbine, where extreme temperatures prevail, the material selection for abradable seal systems becomes crucial.

Magnesia Alumina Spinel (MAS) ceramic material, known for its stability at high temperatures, is employed as a sacrificial lining in the High Pressure Turbine (HPT) and due to the hardness of ceramics, abrasive tipped blades are required for their cut. The current abrasive solutions, electroplated c-BN tipped blades, have reported durability limitations in service due to the matrix (NiCoCrAlY) weakening at high temperatures and alternative Directed Energy Deposition (DED) c-BN tipped blade variants with higher thermally stable matrices (Inconel 792 and NiAlTa) have been proposed to overcome these limitations.

The absence of a standardized testing method for evaluating blade performance at elevated temperatures has prompted the development of a High-Temperature Incursion Rig (HTR). This rig aims to assess novel Directed Energy Deposition (DED) solutions in comparison to the current electroplated baseline, simulating representative gas turbine conditions. Alongside rig development, new methodologies have been implemented to evaluate the performance and wear of both blade architectures.

Incursion tests conducted at both room and high temperatures have unveiled specific wear mechanisms observed in electroplated and DED c-BN tipped blades during the incursion process. Although these wear mechanisms vary between the two blade architectures, they are united by a

common triggering factor: heat accumulation. The primary cause of this heat accumulation is the frictional heat generated from the contact, with blade morphology and incursion rate playing critical roles. Additionally, external heat sources can contribute to the rise in blade temperature, thereby exerting additional influence on the resulting wear mechanisms.

In a direct comparison between TBT429 and DELTA abrasive coatings on MAS abradable linings at high temperature, the electroplated abrasive coating (TBT429) demonstrated superior performance. Although DELTA features a more thermally stable matrix material (Inconel 792), the abrasive coating design where both grits and matrix are in constant contact with the abradable surface results in less effective interaction than the electroplated coating, in which only the grits lead the cutting process. This interaction disadvantage in DELTA coatings diminishes the matrix strength gains achieved by using the high-yield-strength Inconel 792 superalloy, which, despite its benefits, does not fully compensate for the inherent limitations observed above 650 °C.

Contents

1 Introduction **1**

1.1 Gas turbines 1
1.2 Abradable seal linings 4
1.3 Aims and objectives 9
1.4 Thesis layout 10

2 Literature Review **12**

2.1 Blade tips in abradable seal systems 12
2.1.1 Shrouded blade tip design 13
2.1.2 Shroudless blade tip design 14
2.2 Environment and materials 16
2.3 Abradable ceramic linings 18
2.3.1 Structure, composition and coating process 18
2.3.2 Properties and performance 23
2.4 Abrasive blade tip coating 33
2.4.1 Abrasive Particles 33
2.4.1.1 Geometry characterization 34
2.4.1.2 Wear mechanisms 36
2.4.1.3 c-BN 40
2.4.2 Bonding system 41
2.4.2.1 NiCoCrAlY 41
2.4.2.2 Inconel 792 43
2.4.2.3 IP75 45
2.5 Previous testing of ceramic abradable seal systems 47
2.6 Summary 59

3 Materials and methodology **62**
3.1 Planned work . . . 62
3.2 Test Samples . . . 63
3.2.1 Blades . . . 63
3.2.2 Abradable coatings . . . 65
3.3 Test rigs . . . 66
3.3.1 Low Speed Rig . . . 68
3.3.1.1 Rotor . . . 68
3.3.1.2 Stage . . . 69
3.3.1.3 Containment . . . 69
3.3.1.4 Instrumentation . . . 69
3.3.2 High Temperature Rig . . . 80
3.3.2.1 Rotor . . . 81
3.3.2.2 Stage . . . 82
3.3.2.3 Induction Coil . . . 83
3.3.2.4 Containment . . . 85
3.3.2.5 Instrumentation . . . 86
3.4 Material Characterization . . . 90
3.4.1 Optical 3D measuring system . . . 90
3.4.2 SEM-EDS measurements . . . 91

4 Analytical tool for quantifying the damage on electroplated tipped blades **92**
4.1 Introduction . . . 92
4.2 Data capture . . . 95
4.2.1 Data extraction . . . 95
4.2.1.1 3D Data . . . 95
4.2.1.2 Image . . . 97
4.2.2 Normalisation of blade orientation . . . 97
4.2.2.1 Rotation . . . 98
4.2.2.2 Centering . . . 98
4.2.2.3 Tilt . . . 99
4.3 Analytical approach to blade tip classification . . . 100
4.3.1 Establishment of the matrix plane . . . 101
4.3.2 Volume evaluation . . . 102
4.3.3 Feature detection . . . 105

4.3.4 Material pick-up 108
4.4 Results 109
4.5 Discussion 115
4.6 Conclusion 117

5 Cutting performance and wear mechanisms of electroplated tipped blades 119
5.1 Introduction 119
5.2 Grit density 121
5.2.1 Materials and methodology 122
5.2.2 Results 122
5.3 Incursion rate 128
5.3.1 Material and methodology 129
5.3.2 Results 130
5.4 Incursion depth 136
5.4.1 Material and methodology 136
5.4.2 Results 136
5.5 Discussion 145
5.6 Conclusion 148

6 Cutting performance and wear mechanisms of DED tipped blades 150
6.1 Introduction 150
6.2 Standard incursion test 152
6.2.1 Materials and methodology 152
6.2.2 Results 153
6.2.2.1 DELTA 153
6.2.2.2 IP75 162
6.3 Deep incursion test 165
6.3.1 Materials and methodology 166
6.3.2 Results 166
6.4 Discussion 173
6.5 Conclusion 176

7 TBT429 vs DELTA blade performance at high temperature 177
7.1 Introduction 177
7.2 Materials and methodology 178
7.3 Results 179

7.3.1 TBT429 179
7.3.2 DELTA 187
7.4 Discussion 194
7.5 Conclusion 204

8 Conclusions **205**
8.1 Test Method development 206
8.2 Performance of abrasive tipped blades 207
8.3 Impact on industry 209

9 Gap in knowledge and future work **211**

A Convergence and sensitivity studies of the analytical tool **215**
A.1 Grid refinement 215
A.2 Number of picked areas for establishing the matrix plane 216
A.3 Material pick-up 218

Bibliography **215**

List of Figures

1.1 Schematic of a jet engine. 1
1.2 Shrouded turbine stage 3
1.3 Shroudless vs shrouded blade design 3
1.4 Tip clearance control of an HPT during the different stages of a jet engine operation 4
1.5 Schematic of a single blade rubbing against the casing with and without the use of an abradable lining on it 5
1.6 Global and local oversizing as a result of whether an abradable seal system is used 6

2.1 Fins and fences on the tip of a shrouded blade. 14
2.2 Flat cylindrical blade. 15
2.3 Squealer blade. 15
2.4 Winglet blade concept. 16
2.5 Maximum service temperature of the most common abradable sealing materials. 18
2.6 Cross section of a TBC turbine blade with internal cooling where the different layers are indicate and the temperature gradient is represented along the section. 19
2.7 Cross section of a specimen where YSZ was sprayed onto a NiCoCrAlY bond-coat and oxidized at 1100 ℃ for 50 hours. 21
2.8 Schematic of an Atmospheric Plasma Spraying process. 23
2.9 Crack nucleation in the interface between the TGO and the topcoat due to residual stresses. 25
2.10 Presence of internal oxide and chronium sulfide in the bond coat after corrosion for 100 hours in Na_2SO_4 + NaCl at 900 ℃. 26
2.11 Phase diagram of Yttria-Stabilised Zirconia. 29
2.12 Schematic diagram of the phase evolution that YSZ undergoes upon the annealing process. 30

2.13 MAS coated samples after thermal cycling with identical conditions: (a) MAS sprayed with an intermediate YSZ layer over a CoNiCrAlY bond-coat after 500 cycles and (b) MAS directly sprayed over a WHIPOX substrate after 1515 cycles. 32
2.14 MAS curved specimens after thermal cycling with identical conditions: (a) without 3D interface after less than 2000 and (b) with 3D interface after 3000 cycles. 33
2.15 Schematic of the projected area of a particle and the area of the idealized elastic membrane across it. 34
2.16 (a) Schematic representation of two different set of Ω and Λ and (b) relationship between Ω and Λ for a single particle in a fixed orientation. 35
2.17 Example of the main wear mechanisms in abrasive grains. 37
2.18 Wheel wear trend over time. 38
2.19 Tensile and compressive stresses of an undamaged abrasive grain at contacting the workpiece. 39
2.20 BSE image of c-BN grits on a NiCoCrAlY matrix deposited on the substrate by electroplating. 43
2.21 Schematic diagram of the DED process. 45
2.22 Abradability rig developed by Pratt & Whitney Aircraft: (a) rotor and (b) burner. 48
2.23 Schematic of the constant coating-to-blade interaction rig developed by Sulzer Metco. 50
2.24 Schematic of the commercial abradability rig developed by Oerlikon Metco. 51
2.25 Wear maps of the ceramic abradable linings with different level of porosity when rubbed by a Inconel 718 bare blade at different testing conditions. 52
2.26 Test results of YSZ ceramic samples rubbed by bare and c-BN tipped blades at blade speeds of 250, 350 and 410 m/s and a fixed incursion speed of 50 μm/s: (a) bare blade test specimens, (b) c-BN tipped blade test specimens and (c) blade wear as a total incursion percentage. . . 53
2.27 Images of electroplating c-BN coated pins from pin-on-disc tests: (a) before test at 900 °C, (b) after test at 900 °C, (c) before test at 1100 °C and (d) after test at 1100 °C. 54

2.28 Curved MAS specimens (a) with a plain and (b) with a 3D bond-coat interfaces tested against electroplating c-BN blades at the same conditions in the Sulzer Metco rig. 55
2.29 Abradable low temperature testing rigs in the University of Sheffield: (a) Low-Speed Rig and (b) High-Speed Rig. 57

3.1 Blade geometries: (a) standard design (16 mm) and (b) short design (14 mm). 64
3.2 TBT429 abrasive blade coating. 64
3.3 Delta abrasive blade coating. 64
3.4 IP75 abrasive blade coating. 65
3.5 MAS abradable samples: (a) standard and (b) stepped designs. . . . 66
3.6 Rotor, Stage and Front Camera of the Low Speed Rig. 68
3.7 Containment of the Low Speed Rig. 69
3.8 Force data diagram. 70
3.9 Data captured by the dynamometer and plotted in Matlab: (a) raw data, (b) detailed view of peaks and (c) peaks envelope. 71
3.10 Example of a frame captured by the thermal camera from the MAS coating sample during a test. 72
3.11 Experiment conducted for characterizing the emissivity of MAS samples at 90°:(a) thermal camera set up at 90°and 0.4 from the sample, (b) half painted MAS samples with the blade groove in the middle and (c) radiance measured by the thermal camera for each half. 74
3.12 Schematic of the thermal camera viewing angle. 76
3.13 Radiance measured from a MAS coating sample at 500 °C by the thermal camera. 77
3.14 Example of the data post-processed from the front camera imaging: (a) maximum abradable temperature and (b) abradable temperature across the blade length throughout the test. 78
3.15 Example of a frame captured by the front camera. 78
3.16 Example of the data post-processed from the front camera imaging: (a) blade length variation across the blade length and (b) projected area variation during the test. 79
3.17 Examples of frames captured by the video camera: (a) side view of the Low Speed Rig, (b) a contact with a low amount of sparks and (c) a contact with a high amount of sparks. 80

3.18 Spindle, Rotor, Stage and Induction Coil of the High Temperature Rig (without electrical or piping connections). 81
3.19 Components of the High Temperature Rig Stage 83
3.20 Induction Coil systems: (a) control system (left) and heating station (right), and (b) C-shape coil. 84
3.21 Water cooling of the High Temperature Rig 84
3.22 Temperature reached by the blade during the static pre-heating at an optimum angular position 85
3.23 Containment of the High Temperature Rig Stage 86
3.24 Dynamometer used on the High Temperature Rig for measuring contact forces 87
3.25 High frequency pyrometer used on the High Temperature Rig for measuring the blade temperature 88
3.26 Temperature data capture by the high frequency pyrometer from the blade in the HTR and plotted in Matlab: (a) raw data and (b) detailed view of peaks. 89
3.27 Example of the temperature measured on the blade from (a) a good and (b) a poor cutting performance where the blade experience overheating. 89
3.28 Bruker Alicona InfiniteFocusSL system. 90

4.1 Blade set up in the Bruker Alicona InfiniteFocus SL machine. 96
4.2 Point cloud of the blade surface exported from Alicona software (IF-MeasureSuite) into Matlab. 97
4.3 2D image exported from Alicona software (MeasureSuiteSL). 97
4.4 Blade edges detection and trendlines employed for finding out the offset rotation. 98
4.5 Results of the sensitivity analysis of the length of the areas for the blade tilting. 99
4.6 Areas employed to calculate the gradient of the offset tilting in both x (magenta boxes) and y (blue boxes) axes. 100
4.7 Blade after applying tilting corrections and sampled area to be analysed. 100
4.8 Sampled area and selected points to calculate the surface roughness parameters of the matrix 101
4.9 Blade surface after being zeroed at the matrix level. 102
4.10 Normal distribution of the points height for a high and a low grit density untested blade. 103

4.11 Normal distribution of the points height for an untested and a tested blade. 103
4.12 Portion of a blade showing the non-uniformity between grits in terms of colour and shapes. 105
4.13 Example of the grit detection process for a 1.8×1.8 mm area at (a) 5%, (b) 35%, (c) 65%, and (d) 100% of the process. 106
4.14 Example of grits active detected by the tool: (a) image of the grits on a TBT429 blade and (b) Matlab matrix of what is detected as active grits. 107
4.15 Example of the features detected by the tool: (a) image of region of a TBT429 blade and (b) Matlab matrix of the detected features. 107
4.16 Example of material pick-up detected by the tool: (a) image of a TBT429 blade with MAS material adhered to it and (b) Matlab matrix of the detected material. 109
4.17 Comparison between the analytical parameters for a set of six blades with different initial grit density: (a) grit density, (b) volume above the matrix level, (c) void density and (d) volume below the matrix level. 111
4.18 Relationship between the volume above the matrix level per area and grit density for untested blades. 112
4.19 Differences in the relationship between the volume above the matrix level per area and grit density for untested and tested blades. 113
4.20 Relationship between the volume below the matrix level per area and void density for tested blades. 114
4.21 Comparison of the apparent material pick-up for a set of eight blades before and after being tested. 115

5.1 Post-test images of the abradable samples the TBT429 blades (top view) tested at 200 m/s and 0.3 μm/pass up to 500 μm with different grit density blades: (a,b) low, (c,d) medium and (e,f) high grit density. 123
5.2 Force and temperature data for the tests performed with TBT429 blades at 200 m/s and 0.3 μm/pass up to 500 μm with different grit density blades: (a,b) low, (c,d) medium and (e,f) high grit density. . . 124
5.3 Comparison of the maximum normal force and maximum temperature recorded on the abradable surface between the tests performed with TBT429 blades at 200 m/s and 0.3 μm/pass up to 500 μm with different grit density blades. 125

5.4 Scratches produced on the matrix due to the lack of grits for the EWM1T1 test: (a) EWM1T1 blade with profile cut (b) blade height profile, (c) scratches and (d) thermal map during the test. 126
5.5 Comparison of the initial volume above the matrix level and its reduction during the tests performed with TBT429 blades at 200 m/s and 0.3 μm/pass up to 500 μm with different grit density blades. 128
5.6 Details of material pick-up observed on one of the TBT429 blade tested (EPIDT9 (i)) at 2 μm/pass up to 500 μm. 130
5.7 Post-test images of the abradable samples and the TBT429 blades (top view) tested up to 500 μm at 200 m/s and different incursion rates: (a,b) 0.001 μm/pass, (c,d) 0.005 μm/pass, (e,f) 0.3 μm/pass, (g,h) 0.7 μm/pass, (i,j) 1.5 μm/pass and (k,l) 2.0 μm/pass. 131
5.8 Force and temperature data for the tests performed with TBT429 blades up to 500 μm at 200 m/s and different incursion rates: (a,b) 0.001 μm/pass, (c,d) 0.005 μm/pass, (e,f) 0.3 μm/pass, (g,h) 0.7 μm/pass,(i,j) 1.5 μm/pass and (k,l) 2.0 μm/pass. 132
5.9 Comparison of the maximum normal force, G ratio and the maximum temperature recorded on the abradable surface between the tests performed with TBT429 blades up to 500 μm at 200 m/s and different incursion rates. 133
5.10 Volume above and below the matrix level measured after the tests performed up to 500 μm at 200 m/s and different incursion rates. . . 134
5.11 Post-test images of the abradable samples and the TBT429 blades (top view) for the stepped tests (1250, 750 and 250 μm) performed at 200 m/s and different incursion rates: (a,b,c) 0.005 μm/pass, (d,e,f) 0.3 μm/pass, (g,h,i) 0.7 μm/pass and (l) 2 μm/pass. 138
5.12 Details of one of the TBT429 blade tested (EPIDT02 (b)) at 0.005 μm/pass up to 1250, 750 and 250 μm. 139
5.13 Details of one of the TBT429 blade tested (EPIDT06 (f)) at 0.3 μm/pass up to 1250, 750 and 250 μm. 139
5.14 Details of one of the TBT429 blade tested (EPIDT03) at 0.7 μm/pass up to 1250, 750 and 250 μm. 140
5.15 Details of one of the TBT429 blade tested (EPIDT10 (j)) at 2 μm/pass up to 1250, 750 and 250 μm. 140

5.16 Force and temperature data for the stepped tests (1250, 750 and 250 μm) performed with TBT429 blades at 200 m/s and different incursion rates: (a,b,c) 0.005 μm/pass, (d,e,f) 0.3 μm/pass, (g,h,i) 0.7 μm/pass and (l) 2 μm/pass. 141
5.17 Comparison of the maximum normal force and the maximum temperature recorded on the abradable surface between the stepped tests performed with TBT429 blades up to 500 μm at 200 m/s and different incursion rates. 142
5.18 2D thermal maps and blade images of the stepped tests performed at (a,c) 0.7 and (b,d) 2 μm/pass. 143
5.19 Difference of the volume above the matrix level per area for the stepped tests performed at 200 m/s and at different incursion rates, and divided by the three stepped incursion depths. 144

6.1 Schematic of abrasive grains stack-up in cold-pressed grinding wheels. 151
6.2 Post-test images of the abradable samples and DELTA blades (top view) for the tests performed up to 500 μm at 200 m/s and different incursion rates: (a,b) 0.02 μm/pass, (c,d) 0.3 μm/pass, (e,f) 0.7 μm/pass and (g,h) 1.5 μm/pass. 154
6.3 Wear features on the post-test DELTA blades for both ends of the studied incursion rate range: (a) 0.02 μm/pass and (b) 1.5 μm/pass. . 155
6.4 Example of the fresh grit exposure on DELTA blades as a result of the dressing mechanism: (a) pre and (b) post test images from the DEDIRT01 test blade. 156
6.5 Force and temperature data for the tests performed with DELTA blades up to 500 μm at 200 m/s and different incursion rates: (a,b) 0.02 μm/pass, (c,d) 0.3 μm/pass, (e,f) 0.7 μm/pass and (g,h) 1.5 μm/pass. 157
6.6 Abradable thermal maps from the tests performed with DELTA blades up to 500 μm at 200 m/s and different incursion rates: (a) DEDIRT01 - 0.02 μm/pass, (b) DEDIRT03 - 0.3 μm/pass, (c) DEDIRT05 - 0.7 μm/pass and (d) DEDIRT07 - 1.5 μm/pass. 158
6.7 Comparison of the G ratio, the maximum normal force and the maximum temperature recorded on the abradable surface between the tests performed with DELTA blades up to 500 μm at 200 m/s and different incursion rates. 159

6.8 Measurements of the (a) projected area variation and (b) projected profile root-mean-square roughness (Rq) of the DELTA blades tested up to 500 μm at 200 m/s and different incursion rates. 160
6.9 Relative profile height maps of the DELTA blades tested up to 500 μm at 200 m/s and different incursion rates: (a) DEDIRT01 - 0.02 μm/pass and (b) DEDIRT07 - 1.5 μm/pass. 161
6.10 Post-test images of the abradable samples and IP75 blades (top view) for the tests performed up to 500 μm at 200 m/s and different incursion rates: (i,j) 0.02 μm/pass and (k,l) 0.3. 162
6.11 Force and temperature data for the tests performed with IP75 blades up to 500 μm at 200 m/s and different incursion rates: (a,b) 0.02 μm/pass and (c,d) 0.3 μm/pass. 163
6.12 Abradable thermal maps from the tests performed with IP75 blades up to 500 μm at 200 m/s and different incursion rates: (a) DEDIRT09 - 0.02 μm/pass and (b) DEDIRT11 - 0.3 μm/pass 163
6.13 Comparison of the maximum normal force and the maximum temperature recorded on the abradable surface between the tests performed with IP75 blades up to 500 μm at 200 m/s and different incursion rates.164
6.14 Comparison between the variation of the blade projected area suffered by the DELTA and IP75 blades, both tested up to 500 μm at 200 m/s, and 0.02 and 0.3 μm/pass. 165
6.15 Post-test images of the abradable samples and DELTA blades (top view) for the tests performed up to 1250 μm at 200 m/s and different incursion rates: (a,b) 0.02 μm/pass, (c,d) 0.3 μm/pass, (e,f) 0.7 μm/pass and (g,h) 1.5 μm/pass. 167
6.16 Details of the matrix abrasion produced on the blade and the material adhesion left on the abradable sample in DEDIDT04 test. 168
6.17 Post test images of the blades from the tests performed with DELTA blades up to 1250 μm at 200 m/s and different incursion rates: (a) DEDIDT02 - 0.02 μm/pass, (b) DEDIDT04 - 0.3 μm/pass, (c) DEDIDT06 - 0.7 μm/pass and (d) DEDIDT08 - 1.5 μm/pass. 168
6.18 Force and temperature data for the tests performed with DELTA blades up to 1250 μm at 200 m/s and different incursion rates: (a,b) 0.02 μm/pass, (c,d) 0.3 μm/pass, (e,f) 0.7 μm/pass and (g,h) 1.5 μm/pass. 169

6.19 Abradable thermal maps from the tests performed with DELTA blades up to 1250 μm at 200 m/s and different incursion rates: (a) DEDIDT04 - 0.3 μm/pass and (b) DEDIDT06 - 0.7 μm/pass. 170
6.20 Comparison of the maximum normal force and the maximum temperature recorded on the abradable surface between the tests performed with DELTA blades up to 1250 μm at 200 m/s and different incursion rates. 171
6.21 Measurements of the (a) projected area variation and (b) projected profile root-mean-square roughness (Rq) of the blades tested up to 1250 μm at 200 m/s and different incursion rates. 172

7.1 Post-test images of the abradable samples and TBT429 blades (top view) for the cold and hot tests performed on the HTR up to 1250 μm at 100 m/s and different incursion rates: (a,b,c,d) 0.3 μm/s, (e,f,g,h) 0.7 μm/s, (i,j,k) 1.0 μm/s and (l,m) 1.5 μm/s. 181
7.2 Detailed view of one of the TBT429 blades tested at each incursion rate and at both cold and hot condition: (a) 0.3 μm/pass - HTEPT01 and HTEPT03, (b) 0.7 μm/pass - HTEPT05 and HTEPT07, (c) 1.0 μm/pass - HTEPT09 and HTEPT10, and (d) 1.5 μm/pass - HTEPT12 and HTEPT13. 182
7.3 Wear features of a section from the HTEPT10 blade that failed when tested at 1.0 μm/pass and hot conditions. Wear features: (a) matrix abrasion, (b) fractured/embedded grits and (c) abradable material entrapped in the matrix. 183
7.4 Comparison of (a) the material pick-up ratio and (b) the remaining blade cutting capability between the tests performed with TBT429 blades up to 1250 μm at 100 m/s and different incursion rates for both cold and hot test conditions. 184
7.5 Force and temperature data for the tests performed with DELTA blades up to 1250 μm at 100 m/s and different incursion rates: (a,b) 0.02 μm/s, (c,d) 0.3 μm/s, (e,f) 0.7 μm/s and (g,h) 1.5 μm/s. 185
7.6 Comparison of the maximum normal force and the maximum blade between the tests performed with TBT429 blades up to 1250 μm at 100 m/s and different incursion rates for both (a) cold and (b) hot test conditions. 186

7.7 Comparison between the Root-Mean-Square roughness of the abradable sample profile at the lowest point for one test per condition of the TBT429 test batch conducted at the HTR. 187
7.8 Post-test images of the abradable samples and DELTA blades (top view) for the cold and hot tests performed on the HTR up to 1250 μm at 100 m/s and different incursion rates: (a,b,c,d) 0.3 μm/s, (e,f,g) 0.7 μm/s and (h,i,j,k) 1.0 μm/s. 189
7.9 Detailed view of one of the DELTA blades tested at each incursion rate and at both cold and hot condition: (a) 0.3 μm/pass - HTDEDT01 and HTDEDT03, (b) 0.7 μm/pass - HTDEDT05 and HTDEDT06, and (c) 1.0 μm/pass - HTDEDT8 and HTDEDT10. 190
7.10 Force and temperature data for the cold and hot tests performed on the HTR with DELTA blades up to 1250 μm at 100 m/s and different incursion rates: (a,b,c,d) 0.3 μm/s, (e,f,g) 0.7 μm/s and (h,i,j,k) 1.0 μm/s. 192
7.11 Comparison of the maximum normal force and the maximum blade between the tests performed with DELTA blades up to 1250 μm at 100 m/s and different incursion rates for both (a) cold and (b) hot test conditions. 194
7.12 Maximum mean normal force and maximum blade temperature comparison between blades and temperature condition for a given incursion rates: (a,b) 0.3 and (c,d) 0.7 μm/pass. 196
7.13 Damage produced on the TBT429 blades and recorded temperatures for the two repetitions at 0.7 μm/pass and hot condition: (a,b) HTEPT09 and (c,d) HTEPT10. 197
7.14 SEM Image of a portion of the HTEPT10 blade tested at 100 m/s, 1.0 μm/pass and 1250 μm. 200
7.15 2D SEM-EDS elemental mapping of (a) B, (b) N, (c) Ni and (d) Co on the surface of the HTEPT10 blade post test. 201
7.16 2D SEM-EDS elemental mapping of (a) Mg, (b) Al and (c) O on the surface of the HTEPT10 blade post test. 202
7.17 SEM images of the HTEP10 TBT429 blade depicting the abrasive coating structure at regions where the blade (a) did not fail and (b) did fail after test. 202

9.1 Schematics of the magnetic field (a) anti-nodes in the circumferential direction as well as of the resulting heating at (a) an anti-node and (c) a node captured by the thermal camera. 212

A.1 Convergence study of the grid refinement parameter set on the Alicona IF-MeasureSuite software regarding the analysis output number of grits. 215
A.2 Convergence study of the grid refinement parameter set on the Alicona IF-MeasureSuite software regarding the analysis output number of voids. 216
A.3 Convergence study of the Ra surface roughness parameter regarding the selected areas for establishing the matrix plane. 217
A.4 Convergence study of the Rv surface roughness parameter regarding the selected areas for establishing the matrix plane. 217
A.5 Convergence study of the Rp surface roughness parameter regarding the selected areas for establishing the matrix plane. 218
A.6 Sensitivity study of the material pick-up ratio regarding the greyscale threshold. 219
A.7 Example of the material pick-up detected by the analytical tool for an untested blade with a 0.64 greyscale threshold. 219
A.8 Example of the material pick-up detected by the analytical tool for an tested blade with a 0.64 greyscale threshold. 220

Chapter 1

Introduction

1.1 Gas turbines

A gas turbine is a power plant that produces energy through the continuous combustion of an air-fuel mixture. Atmospheric air flows into the gas turbine where its pressure is increased by the compressor. Fuel is atomised and sprayed into the compressed air and the mixture is ignited, generating a high-temperature and high-pressure gas. The turbine is used to expand the gas and extract some energy from it to drive the high-pressure compressor. The remaining energy of the gas is then used for rotating another compressor-turbine set, for rotating an independent turbine or for accelerating the exhausted gases through its expansion in the nozzle, producing thrust (1; 2). The different stages of a jet engine are presented in Figure 1.1.

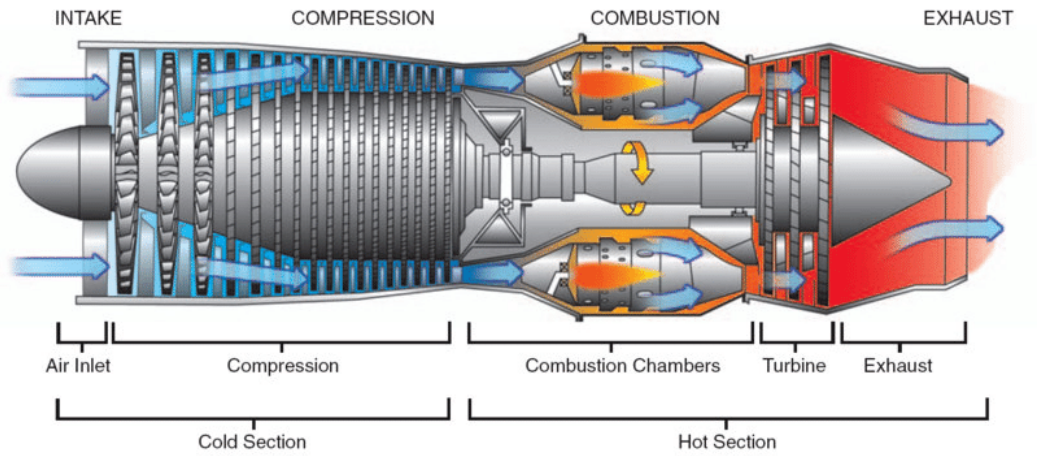

Figure 1.1: Schematic of a jet engine (3).

The Brayton cycle can be used to approximate the different thermodynamic processes the gas flow undertakes through the engine (2). The efficiency of this cycle is

defined by the maximum temperature of the gas after the combustion process, being unity only when this temperature tends to infinity (4). The temperature of the gas between the combustion section and the first turbine stage is generally defined as TIT (Turbine Inlet Temperature). Therefore, an increment on the TIT corresponds to an increase in the thermal efficiency of the gas turbine. However, this increment is limited by the HPT (High Pressure Turbine) components which must withstand such extreme environments. Until the end of the eighties, the increment of the TIT was mainly handled by the development of superalloys and their manufacturing processes (5). Since then, other techniques have appeared with the same purpose such as blade cooling (6) and TBC (Thermal Barrier Coating) (7).

The blades of the first stages are the most critical parts of HPTs (8). It is where the highest temperatures arise and therefore the related failure mechanisms are more aggressive. Failures tend to occur in this stage and are mainly caused by thermal fatigue, erosion, creep damage, hot corrosion or oxidation (9; 10; 11). Additionally, there are other failure mechanisms related to the great mobility of aircraft and the wide variation of environments they fly in, such as salt laden sea air, erosive sand, dust, volcanic ashes and atmospheric pollution.

Unlike compressor stages, the pressure gradient is larger in turbine stages, which means higher pressure loads on each blade (2). Flow tends to bypass the blade stage by bordering the blade tip from the pressure side to the suction side. These leakages are called tip clearance losses and they reduce the turbine efficiency (6). A common solution to address and reduce tip clearance losses is by using shrouded blades as shown in Figure 1.2. These blades are locked together by a circumferential band that wraps around them through the outside diameter. They also improve the stage stiffness which is weakened during operation due to the high temperatures. In contrast, shrouded blades cause higher inertial loads on both blades and disc, limiting the maximum speed of the shaft and the temperature they work under to avoid creep failure (12; 13).

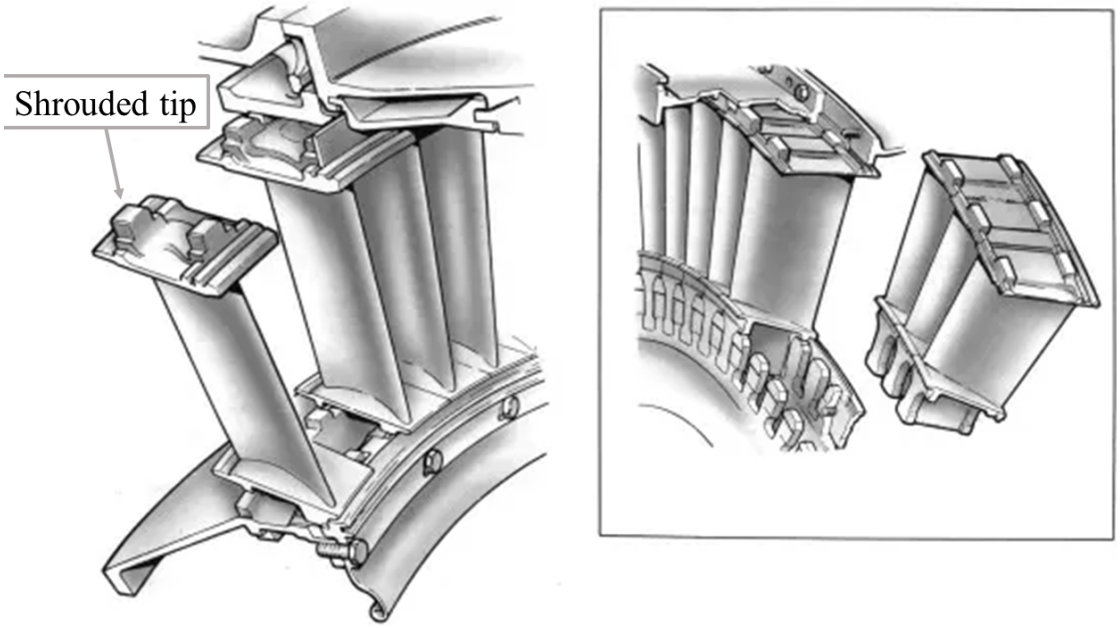

Figure 1.2: Shrouded turbine stage.

Consequently, shroudless blades (Figure 1.2) in turbine stages become more interesting when higher temperatures and higher rotational speeds are required, as they offer a weight reduction and, therefore, lower inertial loads. On the other hand, they are more sensitive to tip clearance losses, demanding an efficient tip sealing control which reduces these tip leakages to the least during every point of an jet engine's operation (14).

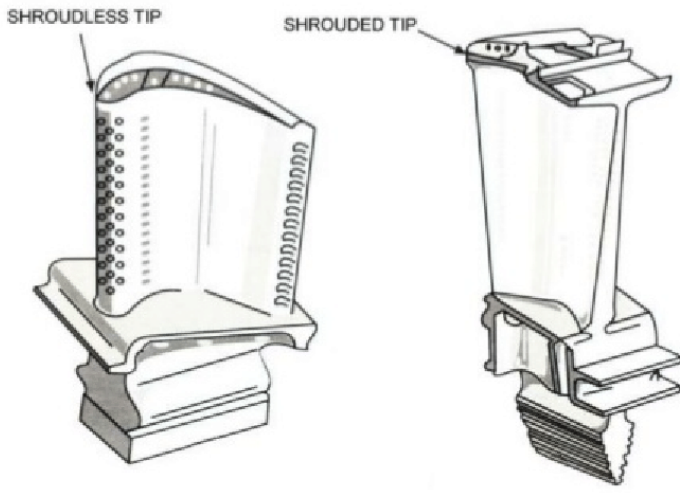

Figure 1.3: Shroudless vs shrouded blade design (15).

The tip clearance between moving and stationary parts does not remain constant

during every stage of an aircraft operation as the casing and rotor undergo radial variations that occur at different rates. These changes in size take place as a consequence of their thermal expansion and, in the case of rotors, aerodynamics, thrust and centrifugal loads (16). ACC (Active Clearance Control) systems compensate for these growths/shrinkages (17) and maintain a tight tip clearance during the entire flight profile, as can be seen in Figure 1.4.

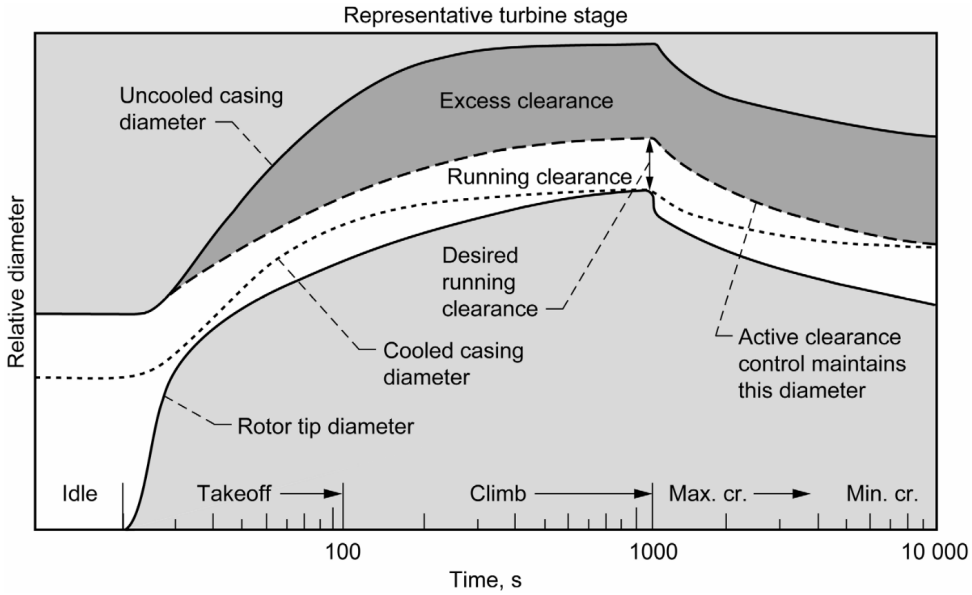

Figure 1.4: Tip clearance control of a HPT during the different stages of a jet engine operation (18; 19).

ACC only succeeds by itself when these variations are uniform and occur at a known controlled rate as a result, for example, of a change in the engine operating point (16; 18). When they occur abruptly and localised, as happens under extreme attack angles, reverse thrust or engine malfunctioning, abradable seal coatings are required to guarantee both a tight tip clearance for minimum losses as well as the engine integrity in case there is contact between moving and stationary parts (20; 21).

1.2 Abradable seal linings

Abradable seal systems are not only employed in turbine sections, but also in compressor sections to minimize the clearance between adjacent rotary and stationary components, guaranteeing their integrity during every stage of the jet engine operation profile. Abradable materials are sprayed onto seal stationary parts as a sacrificial material which prevents any wear on the rotor if contact occurs. It allows near zero

tip clearance, maximizing the engine performance. If abradable linings are not used, tip clearances must be wide enough to prevent any potential contact, thus introducing higher tip losses. In some applications, abrasive linings are deposited also onto the blade tip to ensure the rub compatibility with the abradable and guaranteeing the blade integrity during the contact (22; 23).

The cold build (or minimum) tip clearance is defined during the first run of the engine where the rotating components rub the abradable coating for the first time, leaving a groove on it. For this reason, a stable material cutting of the coating is required. A rough cut of the abradable or the wear of any rotating component resulting from a poor cutting performance would end up in a local oversizing (see Figure 1.5) and therefore in a drop of the engine efficiency or even causing a catastrophic failure in the case of any blade cracks. Once the engine is run for the first time and a groove is generated on the abradable, the tip of the blade sits along this during the regular engine operation (20; 24).

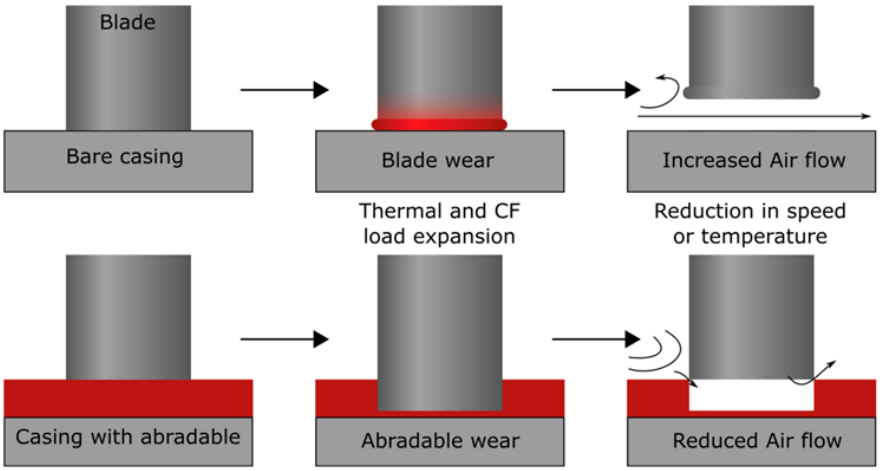

Figure 1.5: Schematic of a single blade rubbing against the casing with and without the use of an abradable lining on it (22).

Despite the track on the abradable lining being produced during the first run of the engine, repeated rubs may occur and blade wear protection is required along the engine lifetime (25). When rubs occur after the first run, they are considered as a malfunction condition which perturbs the engine steady state running and causes irreversible effects by opening the tip clearance (26). These interferences are mainly generated by the combination of aerodynamic loads, thrust bending and the uneven thermal expansion between blades and casing during engine start and aircraft takeoff.

Additional disturbance sources such as misalignment, unbalance, high inertial loads or flow motion forces may also lead to this detrimental situation (26; 16).

Therefore, the main target of an abradable system is the rub compatibility between the abradable lining and the blade tip when contact occurs. A system is considered compatible when the cut of the abradable lining is produced by a brittle fracture mode where material is released without being compacted when the blade passes, generating a smooth end surface with no or minimal impact on the blade (Figure 1.6). However, blade wear, material adhesion, abradable compaction, irregular end surface of the lining produced by spallation, delamination or/and grooves due to an irregular cut are some of the non-desired wear mechanisms that can make the system fail (27; 28; 29; 30). Asymmetric rubs also produce hot points on the coating that may result in destructive cut instabilities (18). Besides rub compatibility, other properties such as resistance against erosion, sintering, corrosion and oxidation are also required (31).

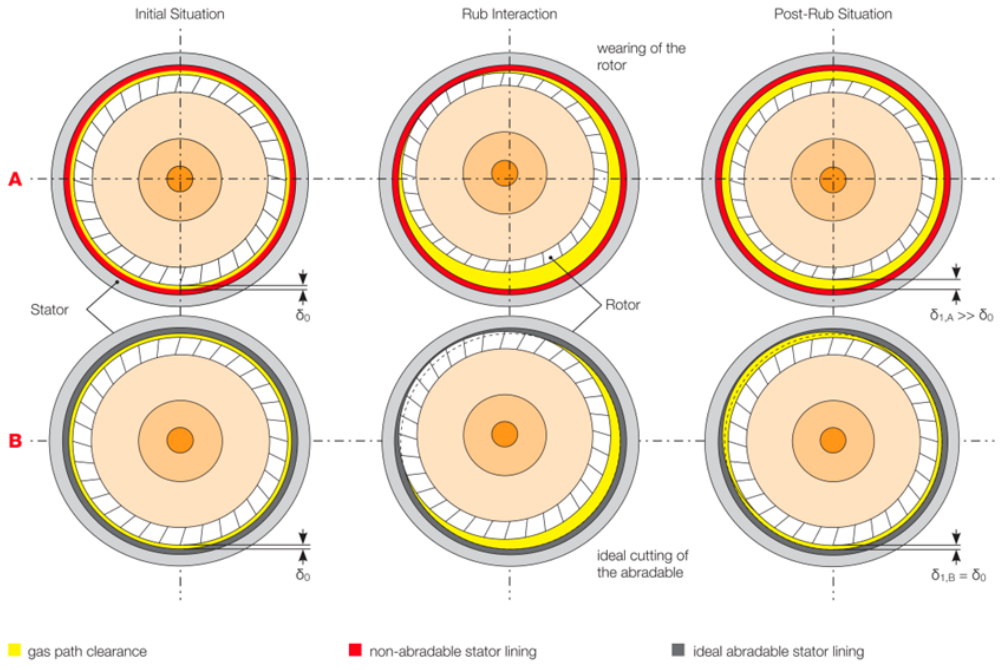

Figure 1.6: Global (top) vs local (bottom) oversizing after rubbing depending on whether an abradable seal system is used (32).

As mentioned, a poor performance of the abradable system when contact occurs means a drop in the engine efficiency. This has been assessed by diverse studies that correlate the tip clearance with the gas turbine efficiency. In the study of effects of turbine tip clearance on gas turbine performance (32), an increment of the tip

clearance by 1% of the blade span in shroudless turbine stages is shown to lead to a leakage of 1-2% of the primary flow and therefore to a 1-3% reduction of the stage efficiency. It is also suggested that a 2% increase of the engine efficiency would be achieved with a 50% reduction of the seal clearances (31). Additionally, narrowing this gap has a direct impact on the decrease of the Specific Fuel Consumption rate (SFC) as it has been reflected through studies in compressor stages (18; 33) and in turbine stages (16), where a decrease by 0.0254 mm in the HPT tip clearance implies a reduction of the SPC by 0.1% and the EGT (Exhaust Gas Temperature) by 1 °C. Furthermore, a 3D computational fluid dynamic model backs up these statements pointing out that through a reduction of the tip clearance by one order of magnitude, both the stage efficiency and power output are improved by 3% (34). There are also other associated costs to the loss of design clearances, if a rub occurs and clearances enlarge, it means that an increment of the fuel burn rate is required to maintain the same engine performances. This increment in fuel consumption makes the TIT increase, compromising the components of the HPT first stage and reducing their lifetime (16).

A wide selection of ceramic and metal-based materials, generally classified by their temperature limitations (35), are used in abradable linings in turbomachinery according to the section of the engine they are used at. Low temperature abradable seals are common in fan and first compressor stage sealing where temperatures are below 400 °C, where Al-Si based alloys with a second phase of a polymeric material or a release agent which provide the abradability property are the most frequent solution (36; 37). For the last stages of the compressor where gas temperatures rise up to around 760 °C, either or both Ni and Co based alloys are normally used instead: NiCrAl, NiCrFeAL or MCrAlY (where M is either Ni, Co or both). Finally, high temperature abradable seals are used for operating temperatures above 760 °C which consist of a porous ceramic, generally Yttria-Stabilized Zirconia (YSZ) or Magnesium Aluminate Spinel (MAS), blended with a fugitive polymeric phase (18; 38; 14; 39; 40). Ceramic coatings' abradability is strongly influenced by the porosity of the sample, the more porous a material is, the easier it is to cut (23). A higher level of porosity makes them more susceptible to erosion wear though. All these coatings are widely applied through thermal spraying techniques which provide a high level of microstructural control. The level of porosity in a thermal spray coating can be manipulated by adjusting key process parameters such as spray distance, particle velocity, substrate temperature, and feedstock material characteristics. (31).

Given ceramic linings are considerably harder than conventional blade materials, abrasive coatings must be applied on the blade tip with the aim of protecting the blade from excessive wear as well as boosting its cutting capability. They consist of protruding hard abrasive grits bonded to a metallic matrix. Particles commonly used include aluminium oxide, zirconia oxide, silicon carbide and cubic boron nitride (18). Being c-BN (Cubic Boron Nitride) the most popular solution thanks to its extreme hardness (back to diamond) and its excellent thermal stability (41). In addition, it has been demonstrated that it possesses the best cutting performance against YSZ ceramic coatings (42).

The main challenge during the last few years has been keeping the abrasive grits fixed to the blade. Electro-deposited MCrAlY, where M is Ni and/or Co, has been the most extensive anchor phase employed to fix c-BN grits to turbine blades in gas turbines (42). Although MCrAlYs have outstanding properties at room temperature as anchor phases, most of the abrasive grits break free from it in a short period of time when temperatures increase over 900 °C, with no sign of abrasive grits when the same tests are conducted at 1100 °C (43). MCrAlYs together with c-BN grits is the current abrasive system employed by Rolls-Royce for turbine sealing in modern engines like XWB-97 or Pearl 15 (44). To overcome the MCrAlYs bonding strength at high temperature, Rolls-Royce engineer the engine tolerance ensuring enough gap clearance to prevent any contact when the blades have lost their cutting capability after the first run stage (45). In response to this challenge, two different c-BN bonding solutions with a more promising temperature range have been developed by Rolls-Royce in order to replace the current MCrAlYs. In contrast to current systems that are deposited by electroplating techniques, these new generation anchor phases are produced by DED (Direct Energy Deposition). The first of these two materials is a Nickel based superalloy whose temperature limit has been reported to be 1150 °C. The second and more complex is a NiAlTaCr Intermetallic with lavas phase strengthening which is supposed to maintain a stable cut up to 1250 °C (44).

The amount of studies about the cutting performance of abrasive coated turbines blade against ceramic abradables linings are extremely limited and not conclusive for multiple reasons. Most studies do not address the wear mechanisms that arise from the contact. Numerous pieces of work have been conducted around compressor cases (36; 27; 22; 46; 29; 47; 48; 49; 50; 51), allowing the comprehension of the contact wear mechanisms for the optimisation of the system cutting performance. However, all these experiments have been done for metal-based abradable materials, bare blades

and no source of heating. The scarce studies about ceramic linings at high temperature have available the pre and post testing samples as isolated results which do not provide enough data to understand the wear mechanisms that come about during the contact (52; 53; 54; 55; 56; 42; 57; 58; 23; 39; 31; 14). Moreover, all these studies are conducted in high temperature test rigs that only focus the heating source on the abradable sample and completely miss the blade as well as there is no information about the tipped blades other than they were c-BN tipped. These experiments are not representative from the blade analysis point of view as the temperature required to weaken the MCrAlY matrix and release the grits is not reached. The only piece of work (40) that achieves a high temperature on the blade is conducted in a small scale rig, whose both linear speed and incursion rate are not high enough to replicate the contact conditions typical of a turbine stage.

1.3 Aims and objectives

The aim of this research is to analyse, from the blade point of view, the cutting performance and wear mechanisms of electroplated c-BN tipped CMSX-4 blades against MAS abradable linings. These abradable seal systems are currently employed, with some limitations, by Rolls-Royce at the HPT of Pearl 15/700/10X and Trent XWB-97 engines. The performance of the next-generation DED c-BN tipped blades which are in development and aims to replace the current electroplated blade solution will also be addressed in this piece of work. The lack of research together with the possibility of enhancing the engine efficiency, the performance and lifetime of these abradable seal systems as well as the reduction of their maintenance are the knowledge gap this projects seeks to address.

In order to conduct this research, a novel high-temperature abradable test rig has been developed in the University of Sheffield. This test rig allows replication of both the incursion conditions and the high temperatures needed on the blade to activate the wear mechanisms reported from engine operation (45).

The objectives of this piece of work can be outlined as:

1. Develop an abradable test rig at the University of Sheffield to extend the current incursion testing capability to high temperature.

2. Further develop the methodologies for the force, temperatures and wear evaluation of the abradable seal system during incursion testing.

3. Develop an analytical tool with the aim to quantify the wear suffered by blade abrasive coatings.

4. Characterise the performance and identify the wear mechanisms of electroplated c-BN tipped blades against MAS ceramic coatings as a function of the incursion rate, incursion depth and temperature.

5. Compare the performance of DED c-BN tipped blades to electroplated c-BN blades at both room and high temperature for a range of incursion condition.

1.4 Thesis layout

Chapter 1 provides an overview of the motivation behind the utilization of abradable seal systems in modern gas turbines and outlines the aims and objectives of the study.

Chapter 2 offers an extensive literature review to contextualize tip sealing approaches in modern gas turbines. It delves into the rationale for using abradable seal systems in the high-pressure turbine stage, examining the requirements of ceramic abradable linings and abrasive-tipped blades employed in that stage. Additionally, it provides a comprehensive review of any prior testing conducted around the ceramic abradable seal systems employed in high-temperature environments.

Chapter 3 introduces the novel high-temperature incursion rig (HTR) specifically developed for assessing the performance of c-BN tipped blades against MAS ceramic abradable linings at high temperatures. It also describes the existing low-temperature incursion rig (LSR) and the set-up required for the initial studies conducted in this research. The chapter further outlines testing and performance characterization methodologies as well as a full description of the different test samples employed in both test rigs.

Chapter 4 details a novel analytical tool developed in Matlab for assessing the wear produced on electroplated c-BN tipped blades from their cutting performance. This tool will serve in the assessment of the performance of such blades in the experimental chapters.

Chapter 5 is the first experimental study, where the performance and wear mechanisms of electroplated c-BN tipped blades against MAS ceramic linings are investigated at room temperature and different incursion conditions in the LSR. The study focuses on investigating the effects of grit density, incursion rate, and incursion depth.

Chapter 6 serves as the second experimental instalment, continuing the methodology established in the previous chapter. This chapter looks into the examination of

the performance and wear mechanisms of two variants of DED c-BN tipped blades against MAS ceramic linings. The investigation is conducted at room temperature in the LSR rig, considering various incursion rates and depths.

Chapter 7 stands as the third and concluding experimental segment. This chapter involves the assessment of electroplated and DED c-BN tipped blades against MAS abradable lining samples at high temperature in the HTR rig. The evaluation includes not only a direct comparison between blade architectures but also an examination of their performance in contrast to ambient condition.

Chapter 8 functions as the concluding section, bringing together the findings from the three experimental chapters and placing them in the broader context of research on ceramic abradable seal systems and the developed rigs for their assessment. This chapter also addresses the limitations of this work and outlines the next steps to further explore the lines of investigation introduced in this study.

Chapter 2

Literature Review

The development of ceramic abradable seal systems for turbine applications, particularly in gas turbines, represents a critical area of research that has yet to receive a comprehensive literature review. These systems play a vital role in improving turbine efficiency by minimizing clearance gaps between rotating blades and stationary components, yet the existing literature lacks a cohesive, in-depth analysis specific to their design and performance. To address this gap, this chapter explores related fields and draws insights from areas that share technological and functional parallels. These include blade tip designs in turbine sections, thermal barrier coatings, and abradable sprayed coatings, with a focus on manufacturer-driven research. Additionally, studies on superabrasive grinding wheels, Rolls-Royce's internal research on abrasive blade coatings, and tribology testing with partial relevance to these systems are examined. By synthesizing findings from these adjacent fields, this review seeks to establish a comprehensive understanding of ceramic abradable seal systems and provide a solid foundation for future research and development in this area.

2.1 Blade tips in abradable seal systems

Abradable lining seals allow the reduction of tip clearances to levels which cannot be achieved by mechanical means in both the compressor and turbine, as well as compensating for casing out-of-roundness or rotor misalignment. These types of seals have been traditionally used only in aviation gas turbines, but advances in abradable materials as well as in the understanding of how the tip of the blade rubs against the abradable coating have caused their popularity to increase in the power generation industry. Without abradable lining seals, tip clearances must be wide enough to prevent any contact during engine service. Large tip clearances would lead to a drop in the engine efficiency caused by leakage flows (18).

Even with liners employed, as long as non-zero clearance between the rotating blade and the stationary casing exists, there will be leakage flows which penalize the stage efficiency. Additionally, the geometry of the blade tip plays an important role in the aerodynamic performance of the seal as well as in the cutting properties of the blade. Different designs for turbine blade tips have emerged over the years to satisfy the need for tip sealing (59). These designs can be divided into two main groups depending whether they apply to either shrouded or shroudless blades (Figure 1.3).

In shroudless blade stages, the pressure difference between the pressure surface and the suction surface of the blade generates a leakage flow around the tip. In shrouded stages, this tip flow is blocked by the shroud, however, a weaker leakage flow over the shroud still occurs, dominated by the pressure difference upstream and downstream of the rotor stage (60).

At the same flow conditions and with a clearance large enough, shrouded stages are aerodynamically more efficient than shroudless stages (60). However, the shroud adds weight which results in an augmentation of the stresses in both the rotor blades and disc. This is especially critical in the HPT where large inertial loads at elevated temperatures lead to creep of the blades (61). Besides that, in shrouded turbines, the cavities of the shroud introduce flow interactions that generate vibrations (62). Therefore, shroudless turbines allow to increase the output power as they can be run faster without compromising the rotor blades or disc.

Contrary to what might be expected, the aerodynamic advantage of shrouded stages decreases when the clearance is reduced. As such, there is a break-even clearance where shrouded and shroudless stages exhibit the same efficiency. If the clearance is reduced further beyond that point, the shroudless stages perform better, with a maximum efficiency difference at zero clearance which is the so-called "offset loss". The windage drag generated by the skin friction of the secondary flow, when it passes between the tip shroud and the casing, and the cavities at the shroud are responsible for this offset loss (60).

Abradable lining seals make possible the downsizing of the tip clearance to almost zero. Therefore, shroudless blades become not only aerodynamically more favourable when they are employed together with abradable coatings but also mechanically more advantageous as the blades are lighter than shrouded ones.

2.1.1 Shrouded blade tip design

Shrouded blades are generally only used on turbine sections where the aerodynamic loads per stage are greater. These blades have a T-shape whose tips interlock together

to form a ring that rotates in close proximity to the casing. Seal teeth are employed over the shroud outer face at different inclinations and orientations to enhance the aerodynamic and cutting properties of the shroud. These seal teeth can be generally split into fins, if they are parallel to the plane of rotation, or fences, if they are perpendicular, as can be observed in Figure 2.1 (63). Whereas fences restrict the swirl circumferential velocity of the leakage flow, fins reduce the flow across the shroud by narrowing the radial clearance between the shroud and the casing. The sealing efficiency of the tip enhances with an increasing number of fins (64).

According to the turbine design, the shroud, in turn, can be straight or flared if the mean radius of the tip increases along the axial direction (65). Flared tips require the casing to similarly flare, which makes the shroud system more sensitive to axial displacements.

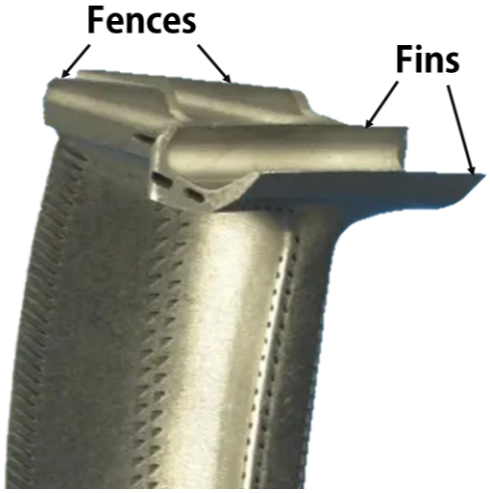

Figure 2.1: Fins and fences on the tip of a shrouded blade.

Although the shroud tips of adjacent blades are not mechanically joined, the shroud-to-shroud interface usually has a Z-lock shape which allows axial displacement of a single blade to be limited (66; 67).

2.1.2 Shroudless blade tip design

Although shroudless blades are employed in both the compressor and turbine, the design of blades, especially the tip, in turbine sections is more complex as they require an internal cooling system to withstand the extreme temperatures. Several tip shapes have been devised and used with successful outcomes. There is not a single design that fits in every turbine and meets all the requirements in an optimized manner (59).

The tiny tolerances achievable by employing abradable liners complemented with an optimized shroudless blade tip design guarantees a high-performance solution for tip sealing.

There are three main design philosophies that govern the shroudless blade tips today: flat cylindrical blade tips, tips with squealer rim seals, and tips with winglet seals. The major advantage of flat cylindrical blades (Figure 2.2) is the simplicity of their cooling system as no protruding parts need chilling. However, in civil and military aviation engines, the limited seal performance of this type of blade tip has more recently given way to the more sophisticated designs with squealer rims (Figure 2.3) and winglets (Figure 2.4), which have been proven to be more efficient (68; 69).

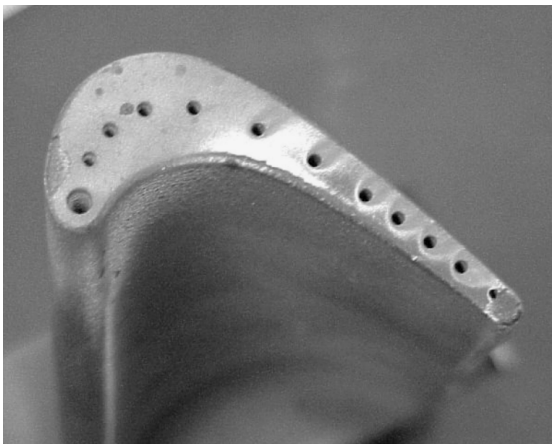

Figure 2.2: Flat cylindrical blade (59).

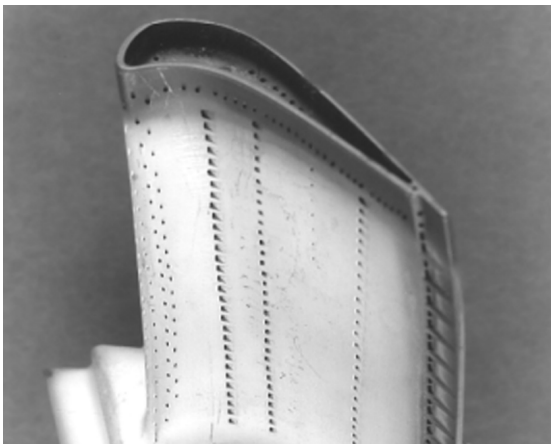

Figure 2.3: Squealer blade (59).

A squealer rim is basically a prolongation of the aerodynamic surfaces of the blade to form a seal strip at the tip (70; 71; 72). Its seal mechanism can be approached as a two-tooth seal labyrinth where the flow is forced by pressure ratio to pass over the first tooth from the pressure side and then expand into the tip cavity. Subsequently, the flow is contracted in the second tooth and leaves the tip by the suction side (59). Different design variants have been proposed such as squealer rims that are opened on either or both leading edge and trailing edge, or an extra squealer rim on the tip cavity (69). The major handicap of the squealer rims is the difficulty to keep them cool and at effective working temperatures.

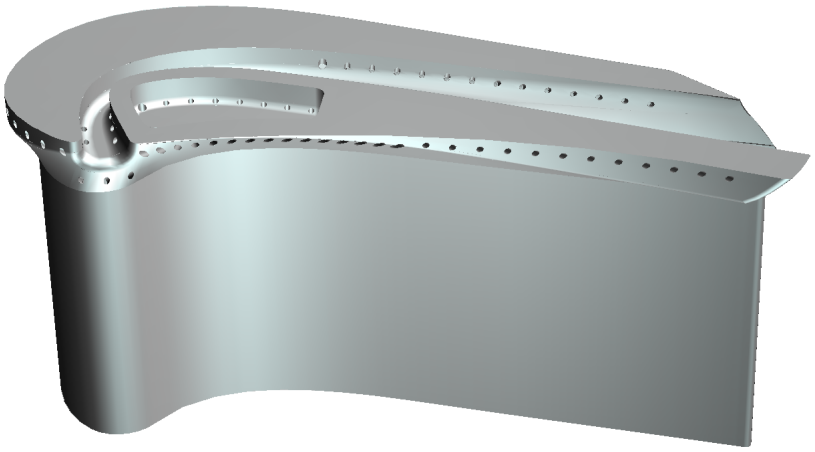

Figure 2.4: Winglet blade concept (73).

The other current trend is the use of winglets on the blade tip to reduce the difference in pressure across the tip. The main disadvantages of this practice are the weight addition and the intensification of the overall heat transfer as the winglets increase the blade surface area (68). Furthermore, winglets can be employed in combination with the squealer rim approach (74). This innovative concept has been investigated by Rolls Royce under the ANTLE program (Affordable Near-Term Low Emissions) where two airfoils overhang both the suction and the pressure side with a passage at the tip from the leading edge to the trailing edge (63; 6).

2.2 Environment and materials

Abradable coatings are applied over the stationary parts in the tip sealing of the fan, the compressor and the turbine sections. The material selection depends heavily on which section they are employed in. In some cases, different materials may be required in the same section as the operating environment varies along it. The main operating parameters that apply to a specific position inside a gas turbine are engine speed, temperature, mechanical loadings, thermal cycling, and velocity, composition, and impingement angle of the gas. The seal material must withstand the most severe operating points as well as endure over the whole engine lifetime. Abradable materials need to be weak enough to be properly cut, but strong enough to withstand the erosive force of the high-velocity gas.

Abradability in seal materials is achieved by using different techniques according to the type of material and the conditions they work under. One of these practices

is built-in porosity that reduces the required specific cutting energy of the coating (75). Some materials also have a second phase embedded which acts as a release agent during the rubbing process (76; 77). Further, there are other abradables, such as fibre metals and honeycombs, that obtain their abradability by using a specific structure that deforms and breaks when the rotative component interacts with it at high speeds (78; 79; 80).

The most usual system for classifying abradable materials is depending on their operating temperature range (Figure 2.5). Low temperature abradables are employed in the fan as well as in the Low-Pressure Compressor (LPC) where service temperatures are below 400 °C. Polymers are applied through casting over the casing for fan tip sealing whereas aluminium-silicon based, and nickel based abradables are used in the LPC. Aluminium-silicon based materials are usually sprayed in combination with a second phase such as a polymer, hexagonal boron nitride (h-BN), or graphite that provide the abradable properties (39). The use of h-BN also enhances the oxidation resistance of the coating (81). In contrast, nickel based abradables are only sprayed with the addition of graphite as a second phase (82). These coatings are suitable for being abraded by either steel, titanium alloy or nickel superalloy blades (83; 84; 82).

Cobalt and nickel based abradables are used for the HPC (High-Pressure Compressor) tip sealing where temperatures reach up to 760 °C. These mid-temperature abradables comprise a primary phase of NiCrAl, NiCrFeAl or MCrAlY plus a second phase of h-BN, a combination of h-BN with a polymer, or bentonite, depending on the matrix material. Different hardness values can be achieved by controlling the ratio of the second phase as well as the in-built porosity (85; 86; 87; 88). Aluminium-bronze with polyester is another alternative which is also used in the HPC (89). However, this material is not suitable for the last stages as its maximum service temperature is 650 °C. In the HPC, the blade material that rubs against the abradable coating is limited by the temperature. Whereas untipped nickel superalloy blades can be employed in the whole HPC temperature range, steel and titanium alloy blades are only appropriate for use up to 550 °C (39).

When temperatures exceed 760 °C, metal-based coatings become no longer feasible for tip sealing and ceramic abradables are applied instead. YSZ, whose chemical formula is ZrO_2-Y_2O_3, has traditionally been the most common abradable ceramic in gas turbines. However, its poor performance at temperatures above 1200 °C has given way to novel abradables such as MAS (14; 90). The abradability of a ceramic coating is attained by adding either or both a polymer phase that is burned out after the spraying process to generate porosity (90) and a h-BN phase which acts as

a solid lubricant. However, the oxidation resistance of h-BN limits the use of this second phase up to 1200 °C (91). In contrast to metal-based abradables, ceramic coatings are significantly harder than the superalloy blade. Therefore, the blade tip needs reinforcing with abrasive particles to ensure blade integrity and a proper cut (31). Although the performance of aluminium oxide, zirconium oxide and silicon carbide against ceramics has been analysed with successful outcomes, c-BN is the most common and successfully proven solution for abrasive tipping (42).

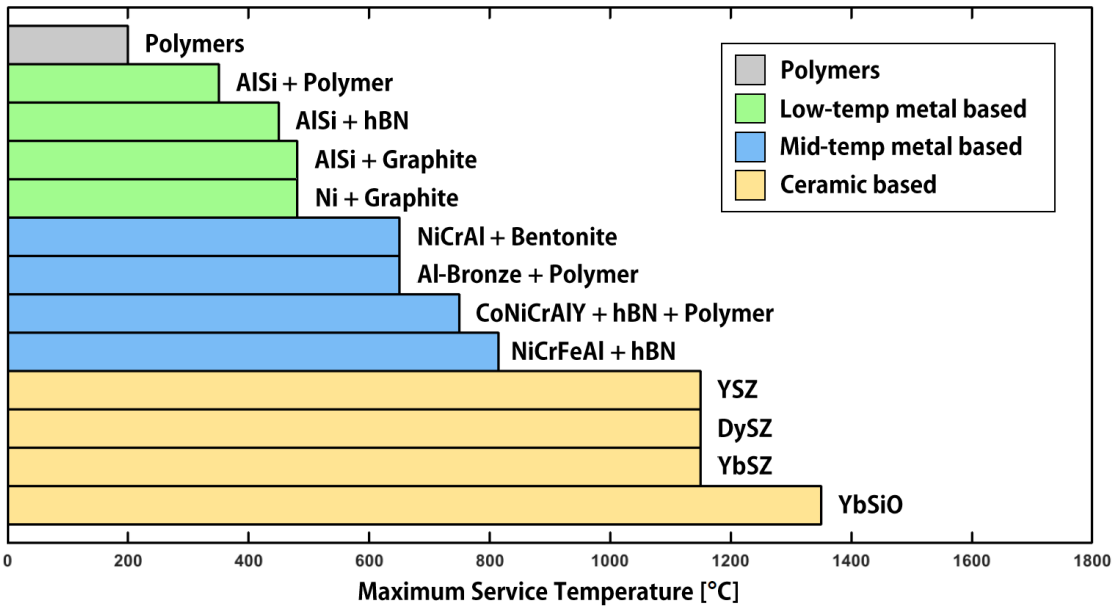

Figure 2.5: Maximum service temperature of the most common abradable sealing materials (73).

2.3 Abradable ceramic linings

2.3.1 Structure, composition and coating process

Abradable linings act as a sacrificial protection that is initially cut by the rotating component during the first run of the engine to set the gap clearance and prevents wear on the blade tips during future undesired contacts. Specifically, refractory ceramic coatings are sprayed at the hottest sections of aero-engines where metal based materials cannot withstand the harsh conditions. These sections comprise the first turbine stages, where temperatures may reach values above 1400 °C.

Abradable ceramic linings can be approached as a TBC where the final ceramic layer has not only insulating but also abradable properties. This approach helps

to explain their thermal-mechanical behaviour and how coatings fail when contact is not occurring. Phenomena that cause a TBC to fail are any of what follows: thermal expansion mismatch, thermal conduction, radiation, elastic, plastic and creep deformation, fracture, fatigue, oxidation, hot corrosion, diffusion and sintering (92).

The structure typically of TBCs consists of four or more layers where each one is made of either metal or ceramic and serves a specifically purpose. These layers are represented in Figure 2.6 and listed as follows: substrate, bond-coat, Thermally Grown Oxide (TGO) and topcoat which, for turbine sealing, fulfils the abradability requirement. In some cases, more than one sublayer is demanded in the topcoat as the final abradable sublayer has a slightly different thermal expansion coefficient in relation to that of the bond-coat, resulting in large residual thermal stresses during high thermal gradient cycling. Therefore, intermediate ceramic sublayers are required for smoothing the transition of this coefficient along layers (93; 94).

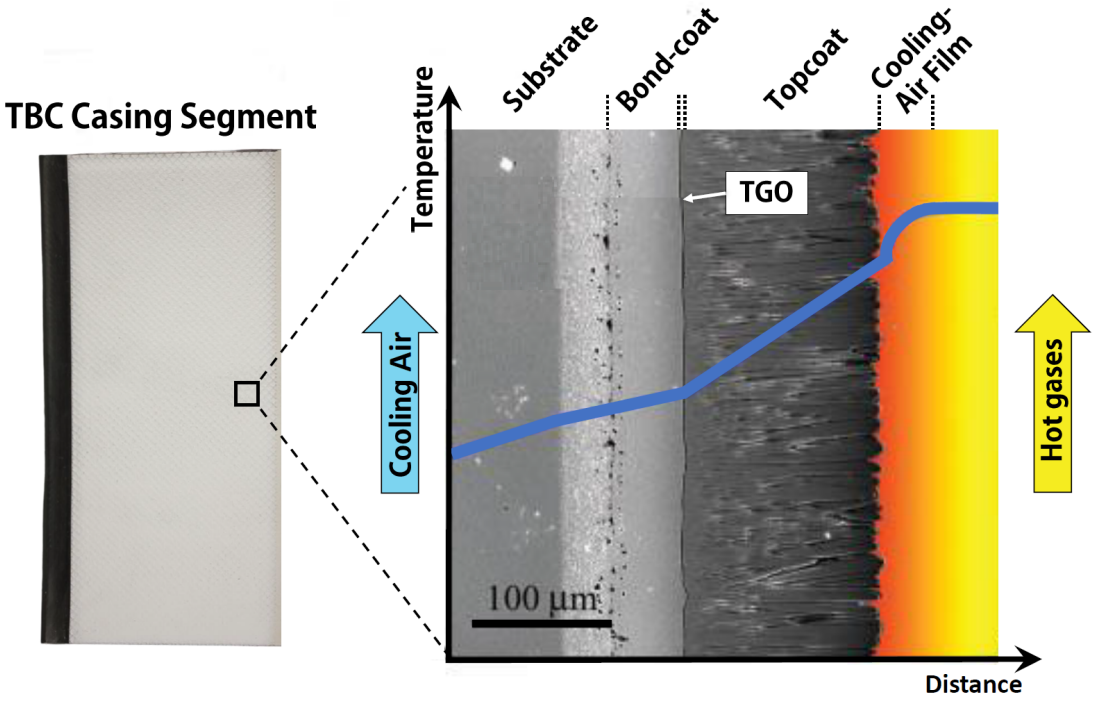

Figure 2.6: Cross section of a TBC turbine blade with internal cooling where the different layers are indicate and the temperature gradient is represented along the section (92).

The substrate is a nickel or cobalt based structural superalloy with the addition of from 5 to 12 other elements to upgrade properties such as strength, ductility, oxidation resistance, hot-corrosion, creep resistance and castability (95). The substrate is air-cooled from inside through internal channels in the case of blades or from the outside

in casing segments. As a consequence, a gradient of temperature arises in-service along the system (96). High temperature cycles in superalloy substrates produce the interdiffusion of elements to the bond-coat (97). It has not been fully studied but the interdiffusion of certain elements such as tantalum, titanium, tungsten and molybdenum may jeopardise the hot corrosion resistance of the bond-coat and weaken the TGO, causing the coating to spall (98; 92). Therefore, abradable linings need to be addressed as time and cycle dependant systems.

The bond-coat is an intermediate metallic layer which fixes the following ceramic layers to the substrate without reacting with the underlaying superalloy and prevents its oxidation by forming an oxide thin film at the ceramic interface, the TGO. The proper design and manufacture of the bond-coat are crucial to ensure the integrity of the coating. The bond-coat is generally made of a MCrAlY, where M is either Ni or a blend of Ni with Co for providing higher oxidation resistance, and it is generally engineered by APS (Atmospheric Plasma Spray) or EB PVD (Electro-Beam Physical-Vapor Deposition). Aluminides of nickel and platinum manufactured by electroplating or chemical-vapor deposition are other materials also used as bond-coats. The principle purpose of this layer is to acts as a reservoir of aluminium to ensure the formation of α-Al_2O_3 as TGO.

The TGO, as it can be observed in Figure 2.7, is a thin film (1 to 10 μm in thickness) generated as a consequence of the oxidation process of the bond-coat due to the oxygen diffusion through the porous ceramics of the topcoat (99). Even if the upper layers were fully dense, the high oxygen diffusivity of those ceramics would also supply it to the bond-coat (100; 101). It has been reported that the TGO spalls when it reaches a maximum thickness from 8 to 10 μm (102). Although the bond-coat oxidation is inexorable, the TGO must grow up as α-Al_2O_3 and it needs to do uniformly, free from defects and slowly to delay as much as possible the coating failure.

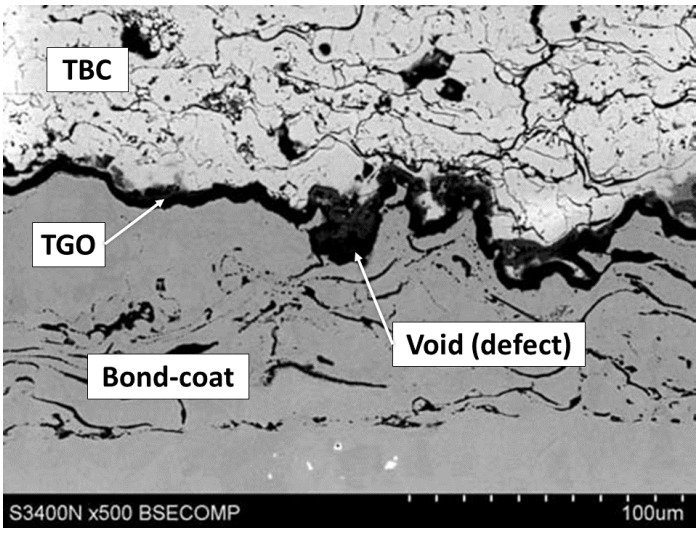

Figure 2.7: Cross section of a specimen where YSZ was sprayed onto a NiCoCrAlY bond-coat and oxidized at 1100 °C for 50 hours (102).

The advantage of using alloys that contain Al as a bond-coat, like MCrAlYs, is the generation of alumina as the TGO. Alumina has excellent chemical and thermodynamic stability against oxidation and hot corrosion, as it is the slowest growing oxide at high temperatures. Its extremely low oxygen diffusivity delays the further oxidation of the bond-coat (103), meaning it performs as an impervious barrier which prevents the diffusion of external elements. It is also important to remark on its outstanding adherence. Although, the TGO growth is usually controlled by the inward oxygen diffusion, sometimes the growth of oxide scales is ruled by the outward diffusion of aluminium (99; 104).

The acceleration of the oxidation process can be affected by the presence of certain elements at the bond-coat such as sulphur impurities which increase the growth rate of the TGO (105; 106) as well as drastically debilitate its adhesion (107; 108; 109). To ensure the integrity of the coating, this element is kept in a minimal proportion (1 ppm). Besides, yttria is added in limited amount to counter the sulphur outcome by reacting with it and forming stable refractory phases instead (107; 105; 104; 110; 111; 112). Chromium has also been found of benefit for high temperature corrosion resistance, however, a high chromium content, as aluminium, leads to a lower melting point and to a reduction of the alloy ductility (113; 114; 115; 112; 116; 117; 118). Similar outcomes have been reported with the addition of rhenium (119). Although this element leads to an improvement of both thermomechanical and oxidation resistances, an excessive amount of rhenium causes an embrittlement of the bond-coat.

Although the addition of other species such as hafnium, platinum, zirconium, silicon or boron is not completely clear to be of benefit as they depend on many factors, there are few studies which gather the excellent high-temperature corrosion and oxidation performances of NiCoCrAlYSiB coatings (120; 121; 116). It has been also reported that the inclusion of hafnium to MCrAlY alloys enhances the adherence of the alumina scales as well as the corrosion resistance (113; 114; 118; 38). These reports are in contrast to (122), where traces of hafnium or silicon are suggested to have a negative impact on corrosion protection.

Previously to spray the abradable ceramic, the bond-coat needed pre-treating to ensure its good adherence with the topcoat. Firstly, the surface is cleaned by chemical or mechanical means removing the impurities and, subsequently, it is roughened by using a grit-blasting process which activates the surface by raising the interfacial free energy. This process doubly enhances bonding as it also increases the surface area of contact for the sprayed material (123; 124). The bonding strength between topcoat and the bond-coat is measured according to the ASTM C633 – 13(2017) standard (125). Although, roughing the bond-coat surface enhances the adhesion of the topcoat, this treatment also affects thermal residual stresses as it has been previously represented.

Although there are diverse methods of depositing ceramic on metal substrates, one of the most reliable and generally used for ceramics is APS due to its low cost and high versatility to achieve all the required properties (126; 127; 124). As represented in Figure 2.8, this plasma spraying process consists of a plasma torch which sprays the supplied powder feedstock over the substrate or a bond-coat in consecutive passes. The powder particles are molten and accelerated when they traverse the torch and, as soon as they splash into the top of the previously sprayed particles, they spread and flatten. Inter-diffusion at high temperature and subsequent solidification cause the interlocking of these splats, resulting in the formation of a lamellar structure. The formation of air sacks, voids, unmolten or partially-molten particles and solidification shrinkages during the process trigger porosity in the coating (128). Porosity can be controlled by the spraying parameters (129), by using a secondary phase which is later burnt out (90) or by using specific feedstocks such as a porous nano-structured particle powder where particles are not fully molten (130).

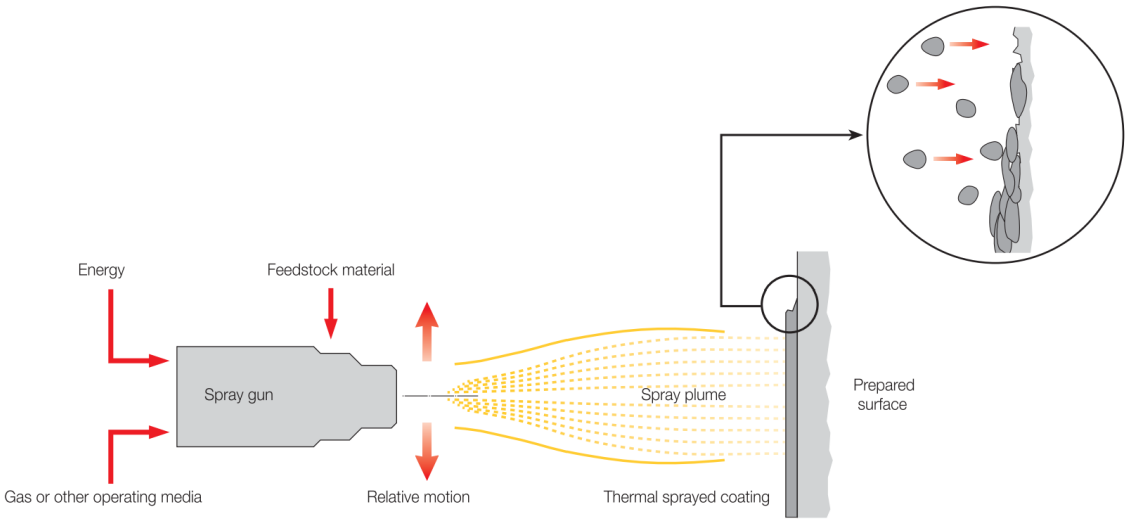

Figure 2.8: Schematic of an Atmospheric Plasma Spraying process (124).

2.3.2 Properties and performance

Apart from a strong and stable adhesion to the bond-coat, abradable ceramics used as the topcoat are challenging to engineer as they simultaneously need to remain stable under high temperature thermal cycling, to match the thermal expansion of the bond-coat, to cope with the growth of the TGO, to provide the substrate and bond-coat with thermal insulation, to have erosion and sintering resistance, and fulfil the abradability requirement as a sacrificial material. It is true that most of the aforementioned wear mechanisms are inevitable but the abradable lining is optimized to minimize the impact of these on its performance. Therefore, it is essential to firstly understand what causes these wear mechanisms.

The oxidation of TGO at high temperatures carries growth strains and induced compressive stresses. The combination of these stresses with the ones produced by thermal expansion mismatch between layers upon cooling are responsible for topcoat spallation (131). In-plane compressions are reorganized in the surrounding imperfections and relieved by out-of-plane displacements, leading either to TGO buckling or to bond-coat yielding (132). These displacements generate tensions normal to the interface that nucleate and grow cracks at the TGO as well as at the topcoat near to the interface (133). When these cracks coalesce, coating delamination occurs (134).

The growth of the TGO brings about two different mechanisms: a rigid solid displacement of the topcoat caused by TGO thickening, and in-plane compressive stresses in the TGO (<1 GPa (135)) that are present at all temperatures (136). Compressions

are due to the lateral constriction of the new oxide formation on the grain boundaries normal to the interface (137). When these stresses are large enough (∼3 GPa (138)), they even inhibit the formation of new intergranular oxides. Moreover, the TGO thickening increases the strain energy density which may end up in producing buckle-driven delamination of the oxide layer. However, at the same time the oxide growth at high temperature makes stresses increase, which are then alleviated through TGO creep (139).

Resulting from the thermal expansion mismatch at cooling, both TGO and topcoat experience residual compressive stresses which reach a maximum at room temperature (2.5 - 4.5 GPa (140)). Compressions at the TGO are one order of magnitude higher than those at the topcoat, inasmuch as the topcoat is relatively more docile to endure strains due to its porosity and has a lower thermal expansion mismatch with the bond-coat (see 2.1). Thermal cycling reduces these residual compressive stresses through their redistribution by creep or yielding of the bond-coat, with tension regions even developing upon further re-heating (141).

Layer	α, Thermal expansion coefficient $[10^{-6}\ K^{-1}]$ at 25 - 900 °C
Typical Ni superalloys	14 - 15 (142)
NiCoCrAlY Bond-coat	16 - 18 (142; 143)
Polycrystalline Al_2O_3	9 (142)
7 wt. %YSZ	10 - 11 (93; 144)

Table 2.1: Thermal expansion coefficients for each layer of a YSZ TBC at 900 °C.

Upon thermal cycling, surface imperfections such as undulations, which are typically required in APS substrates to enhance topcoat adhesion (124), play a crucial role in the generation of residual out-of-plane stresses at TGO interfaces and their surroundings. During cooling, tensile and compressive stresses originate at the undulation crests and troughs respectively, which are also enhanced by the TGO growth (145; 141; 146). Residual tensions nucleate and grow cracks at the oxide interfaces as well as at the nearby topcoat (see Figure 2.9). Moreover, as long as thermal cycling persists, it may lead to reverse the nature of the residual stresses at room temperature, causing tensions at the troughs, which subsequently cause cracking. Stresses at imperfections show a dependency with material properties and with the ratio between

the amplitude and the wavelength of the oscillations (141; 147). During thermal cycling, undulations tend to increase their amplitude by ratcheting of the TGO into the bond-coat, causing an increment of out-of-plane stresses (148).

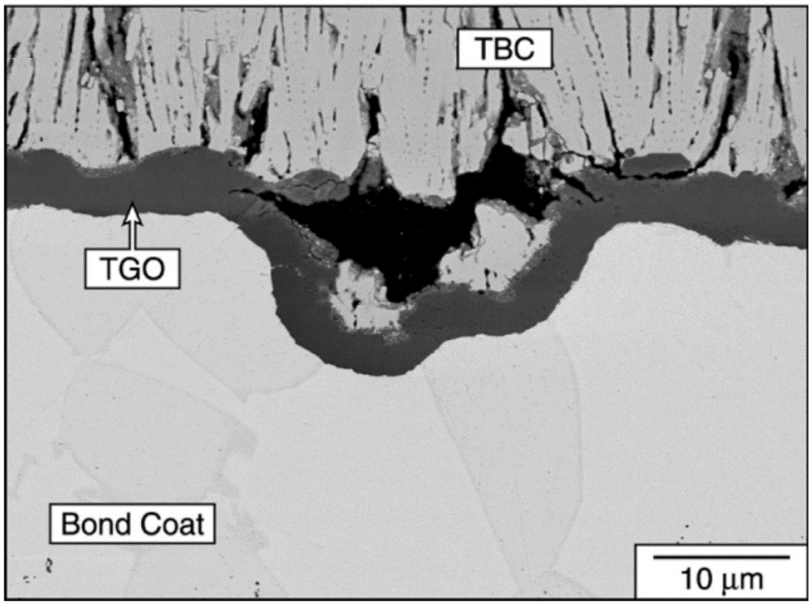

Figure 2.9: Crack nucleation in the interface between the TGO and the topcoat due to residual stresses (131).

Aside from oxidation, hot corrosion also takes place in turbine stages due to the mix of high temperature and the presence of products from combustion such as Na_2SO_4, NaCl and V_2O_5, resulting in an extremely reactive environment. These products might react together, forming a molten salt reservoir at high temperature which will damage the oxide protective layer by dissolving the scales (149). As a consequence, the reservoir of aluminium will be consumed to restore the TGO. The presence of NaCl in the gases leads to acute cracking and subsequently spallation of the layer as NaCl can penetrate into the bond-coat, generating internal voids by means of oxychlorination as well as oxidation cyclic reactions (150; 151; 152; 153; 118). The degradation of the protective layer allows oxygen and sulphate to penetrate into the bond-coat which brings about the formation of internal oxide and chromium sulphide (Cr_2S_3) as shown in Figure 2.10) (151; 154). All of these phenomena will cause an acceleration of the depletion of aluminium reservoir and, consequently, of the corrosion process (155). Accordingly, hot corrosion can be seen as an accelerated oxidation with the addition of internal oxide and chromium sulphide.

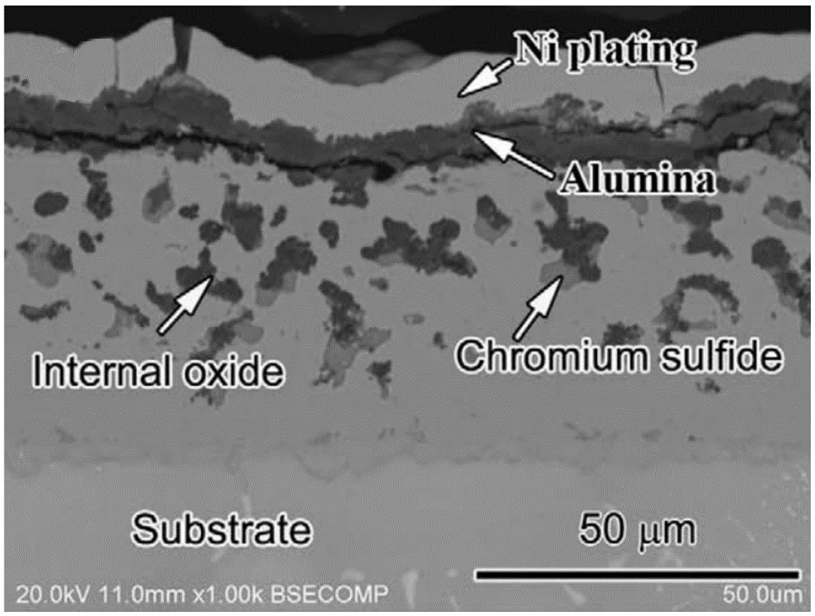

Figure 2.10: Presence of internal oxide and chronium sulfide in the bond coat after corrosion for 100 hours in Na_2SO_4 + NaCl at 900 °C (154).

The abradability performance of the ceramic topcoat is achieved by reducing the required energy for particle detachment. This can be obtained by controlling the matrix particle size, by generating porosity though the manufacturing process or adding a polymer phase which will be subsequently burnt out with heat post-treatment, or by having a second dislocator phase entrapped within the ceramic matrix which acts as a release agent (37; 38). However, only full ceramic coatings are suitable at high temperatures (58). The relation between abradability and porosity has been reported in different studies (156; 23; 129), where, although the evolution of abradability with porosity strictly depends on material and spraying parameters, the trend is repeated in every case: an increment on the porosity percentage means a more effective cut of the coating. Nevertheless, there is an upper threshold where the abradability is not improved in spite of porosity increases (23). Porosity also reduces thermal conductivity and allows for the accommodation of high strains due to temperature variations.

In the same way, abradability has been analysed as a function of the coating surface hardness, better abradable performances are attained with a lower hardness (129; 157; 28; 158). Therefore, it can be deduced that hardness is dependent on the coating porosity and can be used as an indicator of abradability. MAS ceramic coatings samples are analysed in (129) where hardness and porosity exhibit an inverse proportionality. For CoNiCrALY-BN metal based samples (157), the dependency between both parameters follows a non-linear function with a prominent intermediate

linear zone. Despite the potential disparity in trends between materials, it is right to say that abradability, porosity and hardness are directly correlated.

Erosion resistance is one of the abradable coatings main requirements, inasmuch as erosive wear comes about inside aero-engines in many circumstances, for example when an aircraft takes off in a sandy environment or flies through dust clouds. Erosive wear may also materialize as a consequence of debris released from abradable coatings when contact occurs. Similar to other types of wear, erosion resistance is not directly influenced by the material mechanical strength and other properties need considering (159). The influence of surface hardness on erosion resistance has been independently analysed for CoNiCrALY-BN metal based coatings (157), Durabrade™26XX metal-ceramic composite coatings (77) and MAS full ceramic coatings (129). All of these different studies are in accordance with the fact that erosion resistance has a direct proportionality with coating hardness and, consequently, an inverse proportionality with abradability.

Despite the brittle nature of ceramics at ambient temperature, which even may speed up wear, at high temperature where metals become reasonably soft, ceramics exhibit higher ductility, suppressing the brittle fracture mode they have at room temperature. The erosion resistance of abradable coatings is generally assessed in accordance with the General Electric (GE) E50TF121CL-A erosion test (156). In this test, a total of 600 g of alumina particles of 50 μm is sprayed onto the coated surface from a distance of 100 mm and at a 20 °angle. The maximum variation in the coating thickness is measured (38) and the GE number is calculated ass shown in Equation 2.1 (156).

$$\text{GE number} = \frac{\text{Test time [s]}}{\text{Maximum variation of the thickness [in]} \times 1000} \tag{2.1}$$

The GE erosion number represents the time needed, expressed in seconds, to penetrate 24.5 μm of the coating thickness and is measured in s/mm. A higher value of the GE number means a higher erosion resistance. A minimum value of 2 s/mm has been proposed in (77) for this number, below this value the coating erosion resistance is excessively poor. The GE number is a good indicator of abradability and determined on a simple to perform test. Additionally, an upper threshold of 5.5 s/mm is proposed to guarantee the good cut-in performance of the coating (129).

Therefore, a conflict between abradability and erosion resistance arises as ceramics are too hard and in need of a high level of porosity to be properly cut, which implies a low erosion resistance. If hardness drops under a certain level, it compromises the

thermal diffusivity of the protective abradable, producing thermal damage in either or both the rotating blade and the abradable coating as heat from the contact cannot properly dissipate (158). Typical GE number values which fulfil both requirements for YSZ ceramic abradable coatings are comprised between 2 and 5 s/mm (38; 14).

From a material volume standpoint, 7 to 8 wt% YSZ has been one of the most widely used ceramic for abradable linings due to not only its good abradability but also its resistance to thermal-mechanical loads. YSZ provides a good insulation to the underlying layers by reason of its low thermal conductivity (2 W m^{-1} K^{-1} for fully dense YSZ at 1127 °C (160)). Moreover, its thermal expansion coefficient is quite similar to that of the alumina from the TGO and close to those of the substrate superalloys and bond-coat materials (see Table 2.1), which diminishes stresses resulting from the thermal expansion mismatch. However, the good performance of this topcoat ceramic in long-term applications is limited up to about 1200 °C where two main detrimental events arise above that temperature: phase transformation and sintering, which lead to the coating failure (93; 161).

The YSZ phase diagram, as seen in Figure 2.11 predicts a tetragonal (t-YSZ) and a cubic (c-YSZ) phase in equilibrium between 600 °C and 2000 °C, where t-YSZ has a low yttria concentration in contrast to c-YSZ, which has a high yttria concentration (162). Upon cooling down from 600 °C, the tetragonal phase (t-YSZ) undergoes a martensitic transformation to the monoclinic phase (m-YSZ), this phase transformation implies an extensive volume expansion and subsequently crack nucleation as a result of the induced stress (163). However, due to the quenching that splats undergo during the APS process, the time at high temperature is not enough to carry out the compositional readjustment required to form t-YSZ and c-YSZ, but an alternative nonequilibrium tetragonal phase (t'-YSZ) with a high concentration of yttria is generated instead (161). This metastable tetragonal phase is the most desired for abradable applications and may be denoted as non-transformable as it will not turn into the monoclinic phase (m-YSZ) when the coating cools down to room temperature, preventing the volume variation (162).

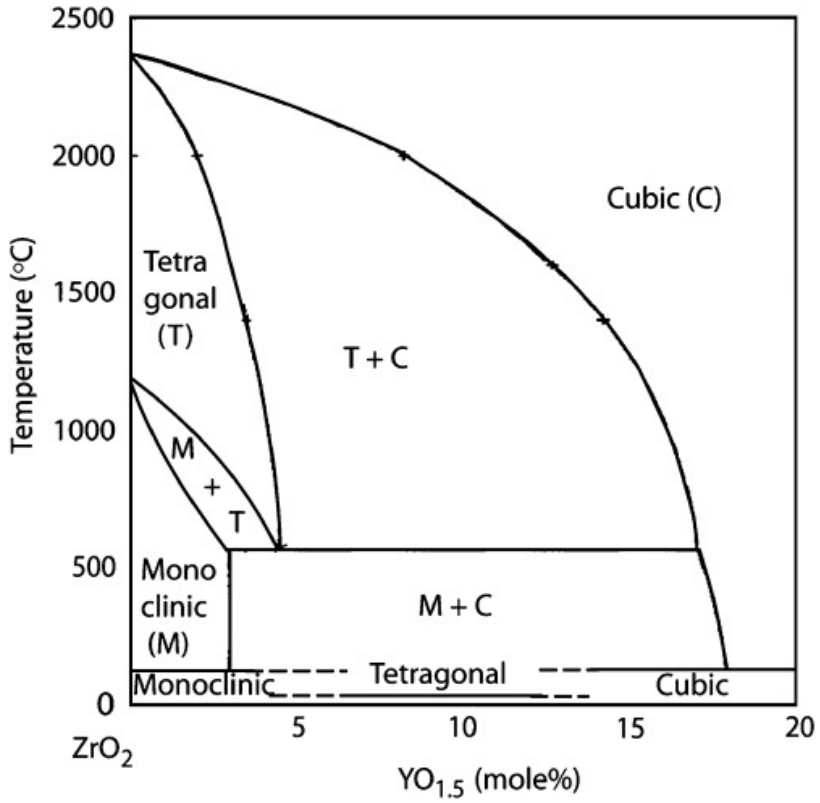

Figure 2.11: Phase diagram of Yttria-Stabilised Zirconia (164).

However, the t'-YSZ phase is unstable at temperatures above 1200 °C where a diffusion phenomenon takes place, transforming this phase into the equilibrium t-YSZ and c-YSZ phases. This process is called annealing and the YSZ phase transformations are represented in Figure 2.12. This newly formed t-YSZ will indeed undergo a phase transformation to m-YSZ upon cooling to room temperature, inducing a volumetric strain in the unit cell by 4% which may result in cracking and coating failure (165; 161).

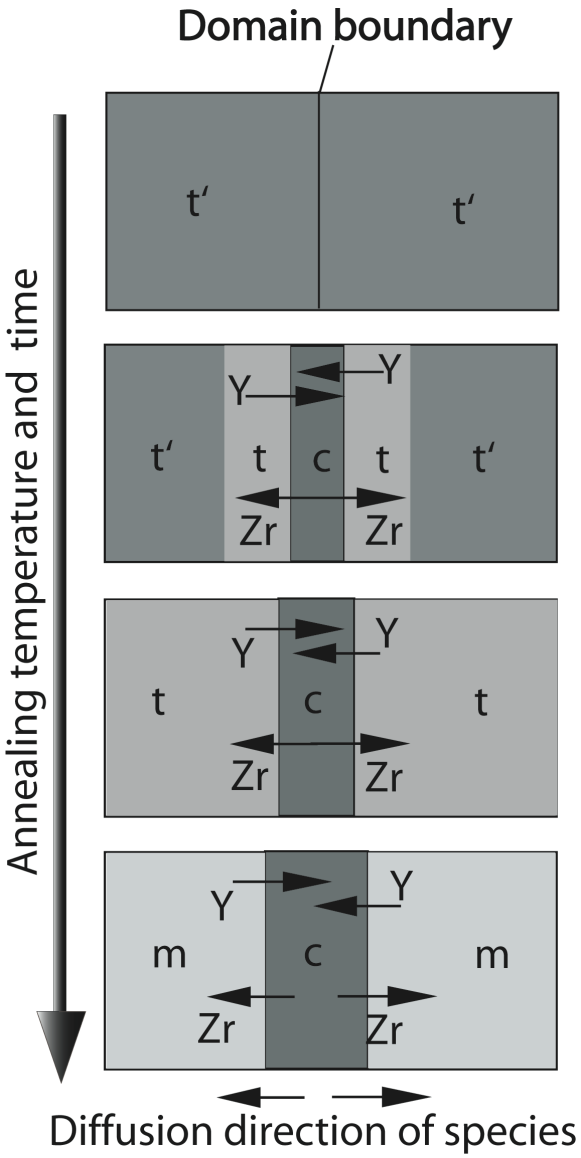

Figure 2.12: Schematic diagram of the phase evolution that YSZ undergoes upon the annealing process (165).

Apart from phase transformation, sintering becomes especially prejudicial in YSZ at high temperatures. This detrimental event leads to microstructure changes, resulting in a reduction in porosity and an increment of the Young's modulus. As a consequence of this densification, the topcoat not only becomes less strain tolerant but also exhibits a loss in abradability. Therefore, sintering alters the mechanical properties of the coating, generating higher stresses under thermal cyclic loadings and diminishes the coating lifetime (93; 161).

This poor performance of YSZ above 1200 °C encouraged Rolls-Royce to look into and optimize a more promising ceramic lining system made of Magnesia Alu-

mina Spinel ($MgAl_2O_4$) (14). MAS is reported to possess a suitably higher thermal conductivity as well as a higher thermal stability compared to YSZ (166). However, unlike YSZ systems, MAS has a considerably lower thermal expansion coefficient (7.9 $\times$ 10^{-6} K^{-1} at 25 - 1000 °C (167)) compared to that of the bond coat, prompting higher stresses during thermal cycling. Layered topcoats are proposed to deal with this limitation by adding one or more intermediate layers that help to smooth the pronounced thermal expansion coefficient mismatch between the bond-coat and the final MAS abradable ceramic layer (93; 14; 94). In this coating system, the intermediate layers are not supposed to be rubbed. YSZ is generally used for these intermediate layers, however, in this case, it does not reach the high temperatures that trigger the aforementioned detrimental mechanisms as they are insulated by the MAS top layer. With the aim of spraying a high-performance MAS abradable coatings, APS process parameters have been analysed and optimised in (129).

The influence of the expansion mismatch for MAS coatings under thermal cycling has been studied in (94). A double-layered system with a YSZ intermediate layer between the MAS layer and the CoNiCrAlY bond-coat sprayed onto an Inconel 738 substrate is compared to a second system where the MAS is directly sprayed onto a substrate made of WHIPOX™ + RBAO (Wound Highly Porous Oxide Ceramic Matrix Composite + Reaction Bonded Aluminium Oxide), whose thermal expansion coefficient ((8.4×10^{-6} K^{-1} at 25 - 1250 °C (168)) is quite similar to that of MAS. Both systems were submitted to thermal cycling, heated up with an oxygen burner up to a maximum surface temperature of 1400 °C and a thermal gradient of 0.2-0.3 K/μm along the sample thickness, and subsequently, cooled down to 100 °C by compressed air. After 500 cycles, the double-layered specimen suffered from minimal spallation (Figure 2.13a) due to residual tensile stresses from the thermal cycling. In contrast, no spallation was observed on the WHIPOX specimen after 1515 cycles (Figure 2.13b, the spallation observed was produced by the sample clamper), where densification instead was noted, resulting from compressive stresses. Both phenomena, backed up with an analytical stress model, are influenced not only by the thermal expansion but also by the thermal gradient along the sample.

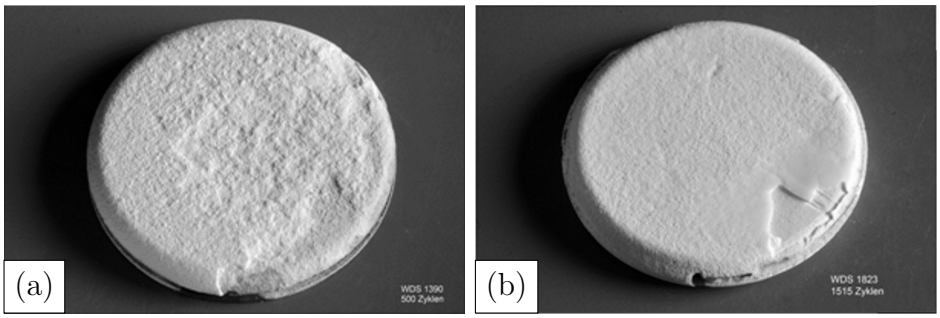

Figure 2.13: MAS coated samples after thermal cycling with identical conditions: (a) MAS sprayed with an intermediate YSZ layer over a CoNiCrAlY bond-coat after 500 cycles and (b) MAS directly sprayed over a WHIPOX substrate after 1515 cycles (94).

To improve the spallation resistance, the addition of a 3D interface between the bond-coat and the double-layered (MAS and YSZ) topcoat in curved segments is analysed in (14), where specimens were heated up above 1300 °C in 120 s cycles with a thermal gradient of 0.2-0.4 K/μm across the coating. The 3D interface structure was deposited by laser cladding over the bond-coat before spraying the ceramics in order to enhance the clamping of the YSZ layer. The 3D structure is made of the same material as that of the bond-coat and its geometry enhances the damage tolerance of the coating by generating vertical cracks which relax thermal stresses. These curved specimens, with and without the 3D interface, were tested in the same facilities and in similar conditions to those of the previous study (94). Whereas the specimen without the 3D interface suffered from spallation of big ceramic fragments before reaching 2000 cycles (Figure 2.14a), minimal damage occurred in the sample with the 3D interface after 3000 cycles (Figure 2.14b).

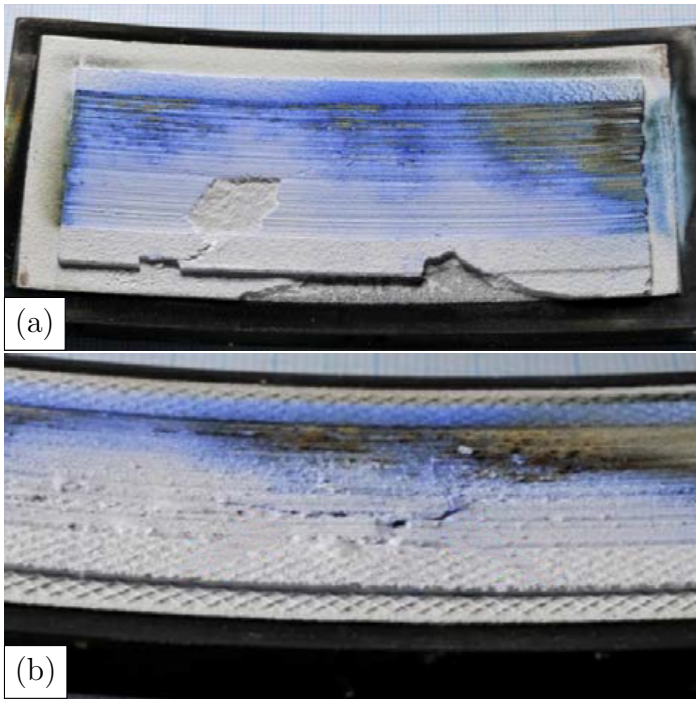

Figure 2.14: MAS curved specimens after thermal cycling with identical conditions: (a) without 3D interface after less than 2000 and (b) with 3D interface after 3000 cycles (14).

2.4 Abrasive blade tip coating

As abradable ceramics are significantly harder than the nickel superalloys used in turbine blades, abrasive coatings are required over the tip of the blade in order to ensure their integrity as well as achieving a high-quality cut of the abradable. Abrasive coatings employed on blade tips consist of protruding superabrasive grains, generally c-BN particles, entrapped in a metal matrix that acts as a bonding system.

2.4.1 Abrasive Particles

Abrasive materials employed in turbine blade tipping do not only require the general properties that apply to typical superabrasives used for grinding wheels such as high hardness, wear resistance, toughness and friability (169), where friability refers to the capacity of the abrasive particles to fracture and generate new sharp cutting edges when the particles become blunt, but must also be resistant to high temperature oxidation and burning, non-reactive with the gas flow or the bonding material, and highly thermally conductive (40; 170). High thermal conductivity is essential to

minimize the temperature on the contact surface as the generated heat dissipates through the abrasive grains (171).

2.4.1.1 Geometry characterization

The performance of abrasive coatings is heavily influenced by the size and shape of the grain utilised on them. The minor and major diameters of a grain projection provide a fundamental measure of its size. Nevertheless, shape is the feature that governs the grain abrasiveness. A sharp-angled grain is generally more abrasive than a blocky round grain but, in turn, more susceptible to fracture. There is also a challenge in quantify how sharp a grain is as there are infinite shapes. This is why numerous dimensionless parameters have been proposed with the aim of linking the geometry with abrasiveness (172). Some of the most used parameters are the following:

- Aspect ratio (AR) describes the grain elongation. It is defined as the ratio of the major to minor diameter. By definition, it is always greater or equal to unity.
- Convexity (C) is closely related to the cutting potential of the particle as well as its strength. It is defined as the ratio between the area of an idealized elastic membrane stretched across the grain projection and the actual area of the projection. Convexity is calculated according to Equation 2.2, where A_m is the projected area of the particle and A_m the area between. An increasing degree of the convexity denotes a higher abrasiveness, but a lower mechanical integrity (173).

$$C = \frac{A_p + A_m}{A_p} \tag{2.2}$$

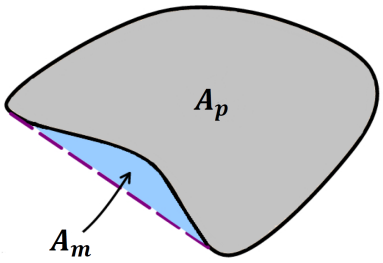

Figure 2.15: Schematic of the projected area of a particle and the area of the idealized elastic membrane across it.

- Sharpness (S) is a parameter that has been specially developed for characterising the wear capability of abrasive grains (174). As abrasive wear rate can be estimated in terms of the angle of a perfect cone-shaped particle and its penetration depth, which is, in turn, a function of the load and hardness of the wearing material (175), grain abrasiveness can be expressed through the correlation between two orthogonal areas (176), Ω and Λ, as illustrated in Figure 2.16a. The functional relationship between these two areas is the so-called "groove function" (Figure 2.16b).

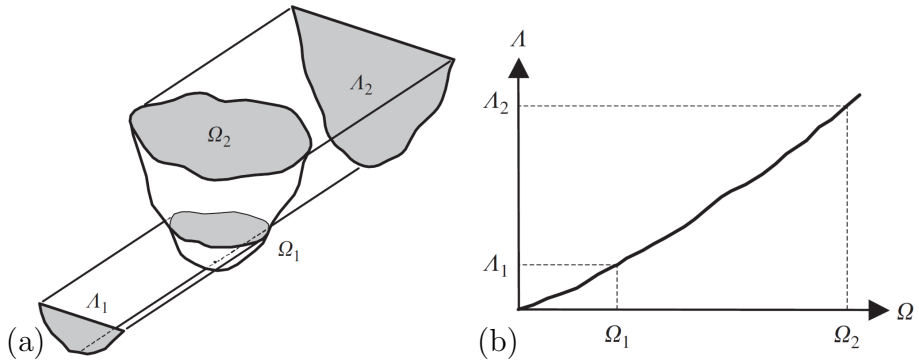

Figure 2.16: (a) Schematic representation of two different set of Ω and Λ and (b) relationship between Ω and Λ for a single particle in a fixed orientation (173).

So far, groove function only applies to one particle at a single orientation. However, the "average groove function" allows to extend the characterization to a sample of multiple particles with their infinite potential orientations (174; 173). In order to obtain a dimensionless parameter for comparing different samples, the average values Ω and Λ areas are divided by the average projection area (A) of the sample of particles, getting Ω_A and Λ_A. The sharpness parameter is obtained as expressed in Equation 2.3 where L is the maximum expected penetration depth in the abraded material.

$$S = \int_0^L \Lambda_A \cdot d\Omega_A \tag{2.3}$$

The influence of the size of abrasive grains on the wear rate in grinding has been widely addressed for metallic homogeneous materials (177; 178). Wear rate linearly increases rapidly with the increment of the particle size until reaching a critical value, which depends on the material. After this critical point, the wear rate curve flattens

or indeed considerably decreases its growth rate as a result of a change in the governing wear mechanism, which turns from microcutting at lower particle sizes into microploughing at bigger particle sizes where the plastic deformation of the worn material becomes more important (179; 180). That said, the research that covers other types of materials such as ceramics or polymers is extremely limited, and a clear pattern between abrasive particle size and wear rate is barely discernible (181; 182; 183).

On the other hand, the dependence of grain shape on wear rate has been investigated for a range of ceramic materials through abrasive wear experiments (184; 173). The experiment results exhibit a positive linear relationship between wear rate and each of the aforementioned shape parameters, where the aspect ratio correlation turned out to be the weakest. Although both convexity and sharpness predict the wear rate with almost identical accuracy, convexity seems to be optimal since it is much more convenient to calculate than sharpness (172).

2.4.1.2 Wear mechanisms

The wear of the superabrasive grains employed in grinding wheels for machining aerospace and automotive components has been widely analysed by both mathematical and experimental methods (185; 186; 187; 188; 189; 190). The outcomes obtained from the research of grain wear in grinding can be extrapolated to abradable seal applications since both tribosystems do not introduce substantial differences (40).

Three mechanisms, represented in Figure 2.17, are recognized as the main causes of wear in abrasive grains (172; 169; 191):

1. Grain fracture occurs when a portion of the grain breaks off, but the rest of the particle remains attached to the bonding system. According to the extent of the remaining portion, fracture wear can be split into microfracture and macrofracture. Properties such as shape, crystal size and morphology, cracks, impurities or inclusions as well as the level and nature of the loads arising during cutting play a major role in the fracture behaviour of the grain.

2. Attritious wear involves dulling of the abrasive grains by forming rounded edges and flat spots. Attritious wear is due to both physical and chemical mechanisms such as plastic deformation, diffusion, degradation and decomposition. These mechanisms are especially aggressive in turbine environments where the high temperature conditions boosts their incidence.

3. Bond fracture occurs when abrasive grains are pulled out from the attachment layer, leaving a void crater behind without cutting capability. This situation arises when the frictional force that is applied over a single particle exceeds the attachment strength of that grain to the bonding system. It is also required to meet the condition that its bonding strength is lower than its fracture strength.

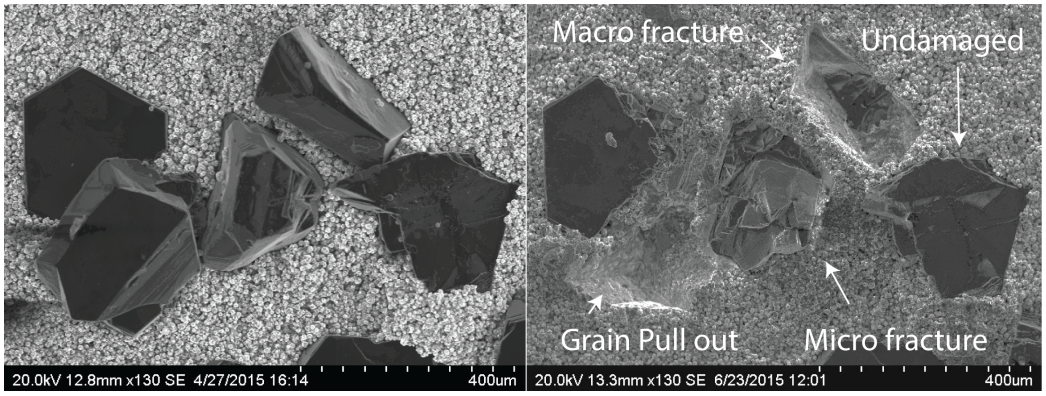

Figure 2.17: Example of the main wear mechanisms in abrasive grains (40).

There is very little research on the wear behaviour of abrasive tipping used in abradable seal systems and mostly limited to electroplated c-BN blades (170; 22; 40). However, the behaviour has been reported to be highly analogous to that of grinding wheels (22), which is divided in three well-defined stages as represented in Figure 2.18 (35; 185; 172; 169; 192). A high-wear initial stage is dominated by the loss of the weakest and most protruding grains, followed by steady state wear ruled by a combination of attritious wear and grain fracture. In the final stage, the wear grows exponentially as a result of grain dulling, contact force increase and subsequently detachment from the anchor phase.

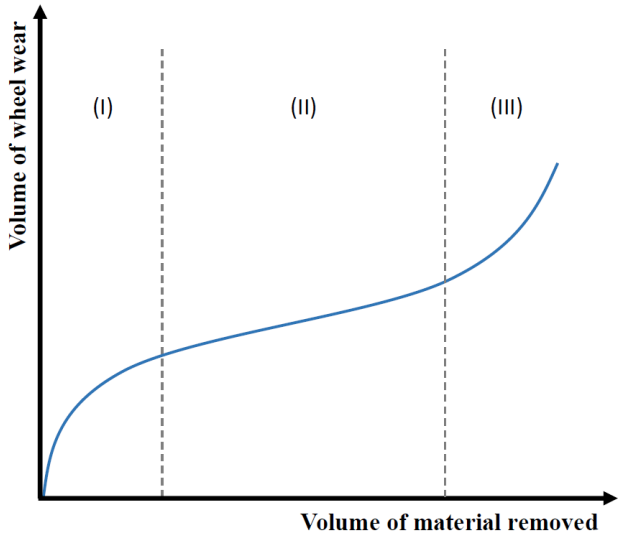

Figure 2.18: Wheel wear trend over time (169).

During the initial stage of the grinding wheel life, the fact that the contact load is only shared by the most protruding grains combined with the weak anchoring of their shallow embedding leads to a high number of grain pull-outs, which has been estimated to be about $60 - 80$ % of the total wear at this first stage (193). Despite the fact bond fracture is the main failure mechanism at this stage, crystallographic defects on grains also have an important contribution to the wear of the grinding wheel. These defects are remarkably detrimental if they are present at the bond level, which may cause grain fracture flat at that level with the total loss of their cutting capability (189). The grain size has been reported to be influential on the principal wear mechanism, where small particles make up a higher proportion of failures as a result of bond fracture, and big particles tend to fail due to grain fracture (194; 186).

When a grain fails by either bond fracture or macrofracture, the subsequent grains are subjected to larger loads which, in turn, make them more likely to fail (40). This chain reaction is especially aggressive at this transient stage and repeats until an equilibrium is reached between the number of active grains and the cutting load distributed between them (186), which gives way to the steady-state wear regime dominated by the combined effect of attritious wear and grain fracture.

During the steady state wear period of the abrasive tip, grain fracture is generally preceded by local attritious wear as a result of the grains rubbing against the workpiece, which involves the dulling of the edges of the grains (193; 188). The occurrence of flat spots on the grains enlarges the friction between the grain and the workpiece,

leading to high contact forces, excessive heat generation and poor cutting efficiency (172). When the stress generated by the contact forces on an abrasive grain exceeds its fracture strength, a part of the grain cracks and breaks, creating new fresh cutting edges (188). The crack initiation may occur due to either tensile or compressive stress at the regions where maximum absolute stresses take place. The subsequent crack propagation and edge renewal take place at these spots when the increasing stress due to attritious wear exceeds the critical fracture stress. The maximum stress for each grain takes place at the rake surface at a finite distance from the cutting edge, which depends on the force ratio and typically ranges from 1.5 to 4 times the contact length. The stress in this zone is tensile in nature and establishes a fracture initiation zone that is illustrated in Figure 2.19. The other common fracture initiation, but smaller zone is located adjacent to the cutting edge where the maximum compressive stress occurs and leads to the crumbling of the cutting edge. Whereas macrofracture tends to occur as a result of aggressive overload and enough crack propagation at the rake surface, microfracture is more frequent and takes place at the compressive zone near the cutting edge (185; 190).

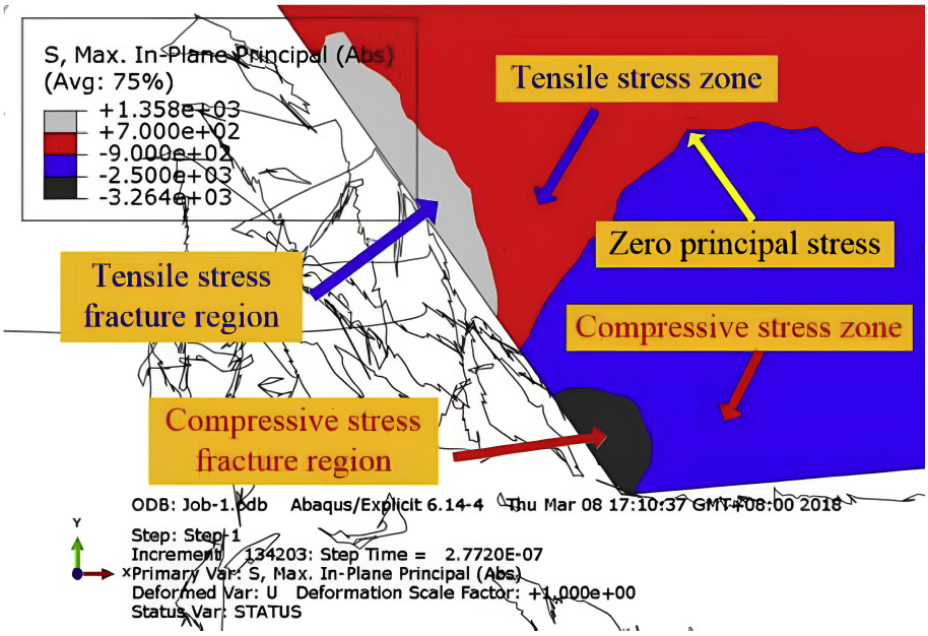

Figure 2.19: Tensile and compressive stresses of an undamaged abrasive grain at contacting the workpiece (190).

Throughout the abrasive process, the number of active cutting points generally increases as a result of grain fracture, from a single fresh cutting edge to multiple active edges that shape an intricate striated surface (190), only evaluable by using

a fractal dimension (195). Additionally, the surface fractal dimension resulting from microfracture has been reported to be higher than that formed by macrofracture (196).

Despite the number of active cutting edges increasing, the ratio of normal force to tangential force increases during the cutting process, which means that the cutting becomes less efficient, especially at the beginning (188). As a rule, an increasing number of active edges implies that the material removal region is divided into thinner and more uneven layers with different removal mechanisms (188; 190). The force ratio increases inasmuch as multiple cutting edges have less protrusion and, therefore, the cutting removal becomes less dominant, fostering rubbing and ploughing (197).

In the third and final stage, the grain wear grows exponentially. The increase of rubbing and ploughing relative to cutting results in an increment of the grinding forces and heat generation, which translates into acute attritious wear and subsequently bond fracture due to excessive loading as well as the weakening of the grain bonding (185; 169), bringing the cutting capability of the blade/grinding wheel to an end. In addition, thermal damage may appear on the surface of the workpiece.

2.4.1.3 c-BN

Cubic boron nitride (c-BN) is a superabrasive material that is extensively employed in blade tipping over other superabrasives such as diamond, aluminium oxide, zirconia oxide or silicon carbide due to its extreme hardness and ultrahigh thermal conductivity. c-BN is the second known hardest material, 61-67 GPa (40), only after diamond. However, c-BN is preferred to diamond since it is more stable at high temperatures (171).

c-BN reacts with O_2 to form a thin but dense protective layer of B_2O_3 (2.4) which prevents further oxidation of the particle at temperatures below 900 °C. However, this oxide layer is no longer stable and protective when temperatures increase above 900 °C (198; 103), due to the acceleration of B^{3+} and O^{2-} diffusion (according to the Arrhenius equation (199)). The cracking and spallation of these oxide scales occurs when the stresses induced by the thermal expansion mismatch and oxide growth are larger than the bonding strength of the oxide scales, exposing the unoxidised grit underneath (200). Cavities are also formed in the diffusion layer as a consequence of the release of N_2 gas, a product of the BN oxidation reaction (Equation 2.4). These cavities increase the total volume of the oxide layer as oxidation continues (104), which considerably weakens the adhesion of the oxide scales and enhances the inward diffusion of O^{2-}. At the same time, no shedding (an unstable thickening of the oxide

layer ocurred) was observed during oxidation at 950 °C for 200 hours, with all c-BN grits then shed at 1000 °C after 200 hours (103). Finally, it is of note that the same test was carried out in (170), where the grits lasted less than 3 hours at 1200 °C.

$$2 \cdot \mathrm{BN(s)} + \frac{3}{2} \cdot \mathrm{O_2(g)} \Rightarrow \mathrm{B_2O_3(l)} + \mathrm{N_2(g)} \tag{2.4}$$

Considering c-BN's thermal properties, high thermal conductivity in abrasive grits is essential to rapidly dissipate the heat from the contact along the grits and then through the matrix interface. Otherwise, extremely high temperatures arise on the tiny contact spots which would end up thermally damaging any of the parts in contact. The c-BN thermal conductivity has been measured to be in the range of 800 – 1600 $\mathrm{Wm^{-1}K^{-1}}$ at room temperature depending on whether c-BN is enriched or not (201).

Finally, although stoichiometrically balanced c-BN is colourless, commercial abrasives feature a range of colours from amber through brown to black in accordance with the level and type of the additive dopants. It is suggested that c-BN becomes black with boron enrichment (172).

2.4.2 Bonding system

In contrast to the mechanical behaviour of grains, much work has gone into researching the bonding of abrasive tipped blades. The bonding system is in charge of holding the abrasive grains rigidly in place. Materials employed as a bonding system require properties that include strength, toughness, hardness, oxidation and corrosion resistance as well as good adhesion of the abrasive particles (169).

2.4.2.1 NiCoCrAlY

NiCoCrAlY is the most common bond material employed together with c-BN particles in turbine blade tipping. However, the combination of different factors related to oxidation, phase transformation, thermal expansion mismatch and thermal weakening has been found to be limiting in their use at high temperature.

At the initial stage of MCrAlY oxidation, the Al from β-(Ni, Co)Al phase reacts with O_2 to form a Al_2O_3 protective layer where both θ- and α-Al_2O_3 phases coexist (202). During further oxidation, the metastable θ phase gradually turns into a stable α phase, which slows down the oxidation rate (103). The depletion of Al in the metal matrix causes the transformation of β-(Ni, Co)Al phase into γ'-(Ni, Co)$_3$Al phase (202). These non-uniform phase transformations involve different degrees of volume

shrinkage that may cause the undulation of the oxide scale and subsequently cracking until spallation (203; 204).

The oxidation process is also aggravated by the thermal expansion mismatch between c-BN (6×10^{-6} K^{-1} at $25 - 1200$ °C (205)) and NiCoCrAlY (19.5×10^{-6} K^{-1} at $25 - 1200$ °C (142; 143)) by creating interfacial clearance between the grits and the metal matrix at high temperature (103). This gap acts as a shortcut for oxygen, accelerating the oxidation process of both the abrasive grits and the bonding system, weakening the bonding between them apart from introducing residual thermal stress.

In order to estimate the stresses in the bonding layer during contact a 2D finite element model was employed in (170). This model consisted of a squared-shape c-BN particle embedded in a NiCoCrAlY matrix with a shear distributed load on the tip. The load was taken in accordance with previous rubbing tests. Different scenarios varying the particle exposed height were analysed. The results predicted a maximum Von Mises stress from 5 to 30 MPa in the bonding system as particle exposure increased from 20% to 75%. Ignoring the creep effects, particles remain attached as long as the yield strength of the matrix material is larger than the stress generated on it during contact.

MCrAlY alloys exhibit a yield strength around 800 MPa at room temperature, far from the estimated stress necessary to pull out a grain, and this strength remains roughly constant up to 650 °C where it begins to drop sharply (206). At 1000 °C, yield strength has values from 50 MPa to 100 MPa, depending on the coating composition (207). Finally at 1050 °C, the yield strength is drastically reduced to around 30 MPa (44). The combination of the material softening at increasing temperature with the stresses resulting from the abradable cutting, cause plastic deformation of the bonding system until particles are unanchored and released.

However, even though stresses during contact are lower than the yield strength of the matrix material, abrasive grits can also fail due to creep damage at high temperature. NiCoCrAlY creep resistance was evaluated for that stress range in (208; 209; 43). In order to asses the amount of time that a bonding system can retain abrasive grits according to the material creep rate, the necessary strain for realising any particle was assumed to be 0.1 in (43). Considering the stress predicted on particles during the contact from (170) at a temperature of 1050 °C, abrasive grits will remain attached from 102 to 104 s before failure. This amount of time will be significantly reduced at 1200 °C, where particles only will last between 1 and 30 s. Although the estimation made at 1050 °C is consistent with the pin-on-disc abrasion tests carried out in the same document (43), no representative test has been conducted

to validate the short operating lifetime of NiCoCrAlY+c-BN abrasive systems at 1200 °C.

The mechanisms exposed above contribute to the deterioration of the NiCoCrAlY bonding layer at high temperature and subsequently release of c-BN abrasive grains which causes the loss of the cutting capability of the system. However, no one has looked into the system behaviour as a whole, i.e. the bonding system plus abrasive grains, and how it cuts at conditions typical of turbine sections.

The most common technique used for depositing c-BN grits with a NiCoCrAlY matrix as an abrasive coating is electrochemical deposition. According to the Tribomet process patented by Praxair Surface Technologies (210), the blade is placed in a mould where abrasive particles are co-deposited with a thin adhesion layer of Ni that fixes the particles to the tip surface. This is carried out together with a high frequency vibration to achieve a uniform particle distribution. The particles are secured with an infill of the NiCoCrAlY powder. Subsequently, the blade tip is heat treated to allow the diffusion of the powder into the nickel matrix to form a homogeneous phase (Figure 2.20).

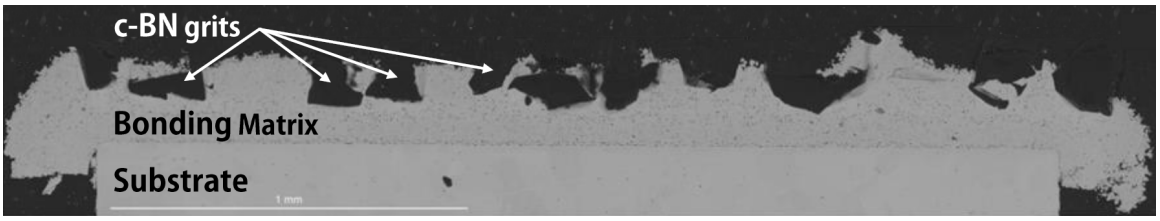

Figure 2.20: BSE image of c-BN grits on a NiCoCrAlY matrix deposited on the substrate by electroplating (211).

2.4.2.2 Inconel 792

Due to the MCrAlY's limitations at high temperature, Rolls-Royce is currently looking into alternative bonding materials for fixing the abrasive c-BN grits to the tip of the blades in the turbine stages of the engine (44). The first of these materials is Inconel 792 which has been proposed as a short term solution as it is a well studied material already employed in the hot sections of gas turbines.

Inconel 792 is a Ni based high-strength polycrystalline superalloy commonly employed for the production of blades and discs of gas turbine engines by reason of its strength and low-cycle fatigue life at high temperature as well as its corrosion resistance in sulphur-bearing environments. However, there is no research about the use of this superalloy as a bonding matrix in abrasive lining, and the available research

as a casting material for blades is scarce and scattered compared to other superalloys (212; 213).

As has been previously presented, the match between the thermal expansion of abrasive grits and bonding matrix plays an important role in maintaining the grits in place during the heating cycles. Because of the non-existence of available studies about the thermal expansion of Inconel 792 at increasing temperature, the coefficient for Inconel 738 has been taken as a comparison instead. Inconel 738 is similar in both properties and composition to Inconel 792 (214). The thermal expansion of Inconel 738 has been reported to be 16×10^{-6} K^{-1} at $25 - 1000$ °C (215), which is slightly lower than the one for MCrAlY alloys (18.5×10^{-6} K^{-1} at $25 - 1000$ °C (142; 143)). On the one hand, this is an advantage as the thermal expansion coefficient is very close to the one for CMSX-4 ($15 - 16 \times 10^{-6}$ K^{-1} at $25 - 1000$ °C (216)), the Ni based superalloy the blades of the turbine stage are usually made of (142), which guarantees the integrity of the bonding matrix adhesion. On the other hand, it does not bring any enhancement to reduce the thermal stresses between the bonding matrix and c-BN grits, as it also occurs with the current NiCoCrAlYs matrix.

Moving to hot strength, Inconel 792 offers a substantial improvement compared to MCrAlYs. Whereas, the yield strength of NiCoCrAlYs at 1050 °C is around 30 MPa, the proposed Inconel 792 has a yield strength of 300 MPa at 1000 °C and a estimated yield strenght of 250 MPa at 1050 °C. This value is at least, an order of magnitude larger than the predicted stresses on the bonding matrix during contact. However, it is expected that this hot strength drastically drops to around the same value as the predicted contact stresses (around 30 MPa) when temperatures reach 1200 °C.

Likewise, the creep behaviour of Inconel 792 has been analysed in (212). Although the maximum temperature considered in this study is 950 °C, it can be directly compared to the data represented (43) for the same temperature on the NiCoCrAlY material. While in contrast to NiCoCrAlY which exhibits a minimum creep rate between 10^{-3} and 10^{-2} s^{-1} at 100 MPa, for Inconel 792 this rate drops to 10^{-8} under the same load, meaning it offers a substantial enhancement of the creep resistance.

Manufacturing the bonding matrix is also a challenge. Electroplating relies on the reduction of metal ions from solution (anode) into solid material on the workpiece (cathode). Typically, only single metals (e.g. Ni) or simple alloys (e.g. NiCo) can be deposited directly from the solution. There is also a limitation based on the reduction potential on what can be deposited, and also what can feasibly be deposited together. In order to manufacture more complex alloys such as NiCoCrAlY the additional

elements are co-deposited as a powder and the resulting coating is thermally treated to homogenise it and develop the desired microstructure. The packing density of the powder is a limiting factor to create a fully dense coating, thus limiting the alloy composition that can be engineered. In addition, there is another limitation associated with the temperature required to thermally treat the coating after deposition. Highly thermally stable alloys such as Inconel 792 require an extremely high temperature (1300°C) to homogenise. This process ages the substrate as well, reducing its certified lifetime (45).

In turn, Direct Energy Deposition (DED) becomes a more convenient technique to deposite Inconel 792 as a bonding matrix due to the aforementioned reasons. DED is a group of Additive Manufacturing (AM) processes where the metal feedstock, either in powder or wire form, is fed onto the substrate surface while the energy source, either a laser, a electron beam or a plasma arc, partially or fully melts the deposited material (217; 218), as is represented in Figure 2.21. DED tecnhiques are usually employed in an inert atmosphere to prevent both the substrate and the metal deposited from oxidizing. For the case of abrasive coatings, the abrasive grits (c-BN) are co-deposited with the alloy, and the power of the energy source is set to partially melt the alloy and not the abrasive grits (45).

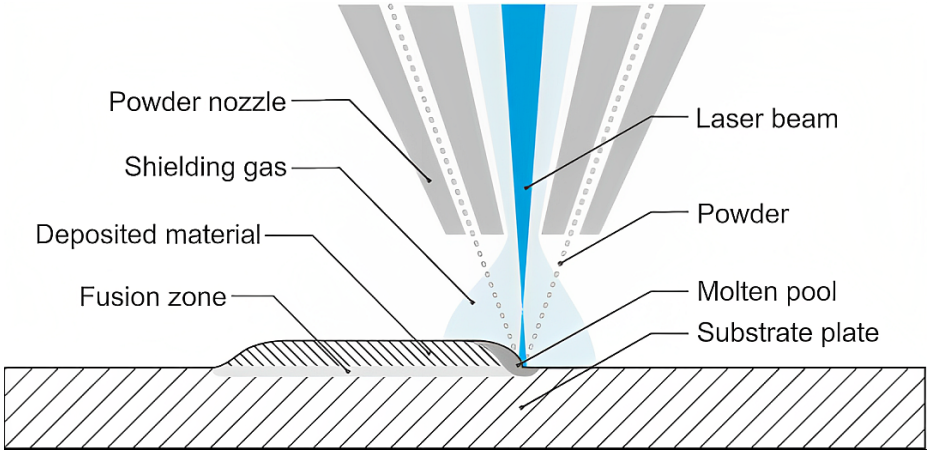

Figure 2.21: Schematic diagram of the DED process (219)

2.4.2.3 IP75

The second promising material proposed for replacing NiCoCrAlY as a bonding matrix is IP75 (NiAl-7.5Cr-2.5Ta), a new intermetallic NiAl based alloy with a precipitated strengthening NiTaAl Laves phase and finely distributed Cr particles. This

material has been developed for high temperature applications. IP75's thermal conductivity is from two to three times higher than Inconel 792, which helps to dissipate the heat from the contact faster. NiAl based alloys also offer an excellent oxidation resistance thanks to this formation of a protective aluminium oxide, Al_2O_3. In contrast to MCrAlYs, NiAl based systems only produce the stable α-Al_2O_3 oxide, thus avoiding the phase transformation and subsequent volume changes which induce residual stresses on the bonding system (220; 221; 211).

Although the thermal expansion of IP75 has not been studied so far, NiAl based alloys with varying volume of a NiTaAl continuous Laves phase have been measured in (43). Considering that the volume of the Laves phase in IP75 is around 14% (45), the thermal expansion coefficient for this amount of continuous Laves phase is 16×10^{-6} K^{-1} at $25 - 1000$ °C, one very close to that previously presented for of NiCoCrAlY and Inconel 738. The thermal expansion coefficient along the typical range of the HPT service temperature was also analysed in (43) and compared to that of CMSX-4 in (211), where both of them exhibit a fairly close trend, thus minimizing again the residual stress on the blade-bonding matrix interface.

IP75 differs from the analogue NiAl-NiTaAl alloys by having a precipitated instead of continuous second Laves phase, which enhances the ductility of the material at room temperature, at the expense of reducing the high temperature strength; as well as by the addition of Cr particles, which also boosts the ductility, avoiding brittle fracture at room temperature (222; 223; 224; 225). In addition, Rolls-Royce has stated that NiAl-NiTaAl alloys are not manufacturable as a bonding matrix through DED techniques (45).

The yield strength of IP75 has been evaluated up to 1200 °C in (221). For this novel material, the high temperature strength has been reported to be up to 200 MPa at 1000 °C, depending on the powder manufacturing process. Even though this value is slightly lower than that of Inconel 792, the yield strength only drops by around 25 MPa when temperature increases to 1100 °C, and the trend suggests that IP75 will undergo a similar reduction from 1100 °C to 1200 °C. Therefore, there is a substantial difference between the expected yield strength at 1200 °C for IP75 and that of Inconel 792, this being 150 versus 30 MPa respectively.

In order to compare the creep resistance of IP75 with the two other alloys, the same load, 100 MPa, and temperature, 950 °C, are considered. According to (220), IP75 exhibits a creep rate of 10^{-6}, four orders of magnitud lower than NiCoCrAlY but two higher than Inconel 792. Considering that the initial cut of the coating lasts from seconds to a few minutes (45) and the later undesired rubs are extremely brief,

the creep resistance of IP75 is high enough to hold the abrasive grits during the engine life time. Finally, as occurred for Inconel 792, the most convenient technique to apply IP75 together with c-BN abrasive grits over the turbine blades is DED (45).

2.5 Previous testing of ceramic abradable seal systems

Wear is generally assessed by means of a standard device called a tribometer. Tribometers replicate friction and wear at the interface between two surfaces under controlled conditions (226). These devices are based on a constant contact interaction and some of them can also replicate adverse environmental conditions like high temperature, vacuum or an inert atmosphere. However, these devices fail at simulating the interaction between blade and casing inside of a gas turbine as the contact between these two bodies is intermittent and occurs at speeds that no tribometer can reach (22; 227). Because of this, specific abradability wear test rigs have been designed and developed over the years to replicate the contact conditions of gas turbine abradable seal systems as well as asses their performance (52; 228; 39; 40; 22; 229).

NASA Lewis Research Center was the first institution to publish documents about the testing of abradable materials at high temperatures (52; 53; 54; 55; 56). These publications date from 1975-1982. The abradability tests were performed in a test rig that was property of Pratt & Whitney Aircraft. The blade tips were mounted on the periphery of a disc driven at the required speed by a compressed air turbine as can be seen in Figure 2.22a. The abradable specimen was attached to a moveable platform which injects the sample radially into the rotor at the required incursion speed. The abradable sample was heated by two oxygen-acetylene torches coupled to the moveable platform (Figure 2.22b). The distance of the torches to the abradable sample could be varied to control its surface temperature. Wear assessment was carried out through the Volume Wear Ratio (VWR) parameter whereby different blade-abradable systems could be compared. VWR was calculated as the ratio of the blade tip wear volume to the abradable sample wear volume, the lower the parameter, the better the abradability of the system.

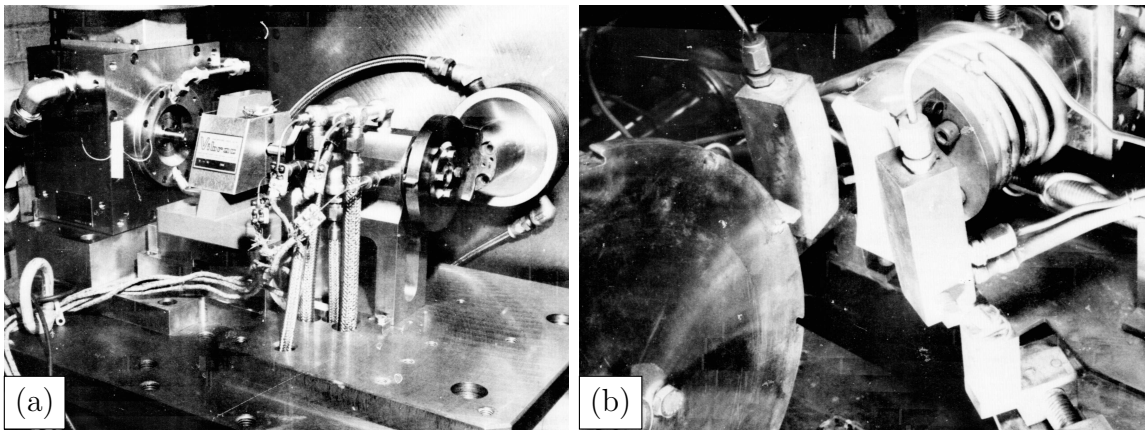

Figure 2.22: Abradability rig developed by Pratt & Whitney Aircraft: (a) rotor and (b) burner (52).

Pratt & Whitney Aircraft conducted two test programs for the assessment of ceramic linings at temperatures of 1093 °C and 1316 °C (52). The ceramic coatings tested in the first of these programs were quartz woven fibers specimens and graded layer systems made of Calcium Stabilized Zirconia (ZrO_2-CaO or CSZ) with CoCrAlY as a bond-coat. The substrates used for both materials were made of a Mar-M-509 Co-based superalloy and the blades employed of a B-1900 Ni-based superalloy. Abradability tests were conducted at various blade speeds up to 305 m/s and an incursion speed of 25.4 μm/s (an incursion speed of 254 μm/s was also assessed but only for the quartz woven fiber study case). Poor abradability was obtained for the CSZ specimens where the blade tips exhibited extensive wear, and no groove was observed on the abradable coating. In contrast, on the quartz woven fiber systems tested at 1093 °C, a complete groove was produced on the sample with no measurable wear on the blades. However, at 1316 °C, the quartz woven fiber coatings were completely disintegrated. Spallation and delamination were observed in both materials as a result of the thermal cycle.

The second program consisted of a set of tests where B-1900 metal blades rubbed against abradable coatings made of YSZ with a CoCrAlY bond-coat. Both a continuously sprayed and a layered configuration for the YSZ/CoCrAlY transition were employed on the specimens. The addition of CeO_2 for preventing material adhesion was also analysed. The test parameters were the same as those employed in the first program. YSZ performed far better than CSZ and quartz woven fibers. The differences in abradability between the coating structures were negligible, where the

addition of the CeO_2 did not provide any visible improvement. In contrast to the first program, no spallation or delamination occurred in any testing.

With the successful outcomes obtained for YSZ, its abradability testing was furthered in (53). In order to simulate the engine conditions more closely and improve the cutting performance of the abradable, the one-bladed rotor from the previous rig was replaced by a twelve-bladed rotor that was accelerated up to 305 m/s. The abradable specimens were heated up to 1335 °C and three different incursion speeds (2.54, 25.4 and 254 μm/s) were studied. The intermediate incursion speed, 25.4 μm/s, presented the best outcomes in terms of abradability with the deepest track on the YSZ sample as well as the minimum blade wear and material adhesion. With a metallographic examination, blade tip adhesion and abradable densification were also observed. It was suggested that better results could be achieved by either increasing the porosity of the ceramic material or using an abrasive material bonded to the blades tips (56).

In contrast to (53), it was suggested in (230) that for a given combination of materials and rub depth, increasing the incursion speed reduces the tip wear since the total number of blade impacts decreases. Testing was conducted on silicon carbide and silicon nitride abradable samples at 1370 °C. However, all the tested coatings collapsed due to thermal stresses.

The research and development of ZrO_2 based abradable seals continued in (228) with a novel test rig built by Sulzer Metco, a division from Sulzer that was later acquired by the Oerlikon Group. The rig was based on a constant coating-to-blade interaction where the coating sample was heated up with a propane-oxygen burner ring up to 1100 °C as illustrated in Figure 2.23. The coating was pressed with a load of 22.55 N against two untipped René 80 Ni-based blades that were accelerated up to 42 m/s. Two variants of zirconia were employed during testing: 20%YSZ and Aluminium-(24%Magnesium Stabilized Zirconia) composite (Al-MSZ). Abradability was assessed in terms of track depth and blade length reduction. In the case of YSZ, no measurable track was produced on the abradable, with a high blade wear resulting from rubbing. Conversely, the abrasive mechanism observed on the Al-MSZ samples was fracture with no material adhesion. The point was also made that due to the many test rig designs and test conditions, results from different studies were hard to compare.

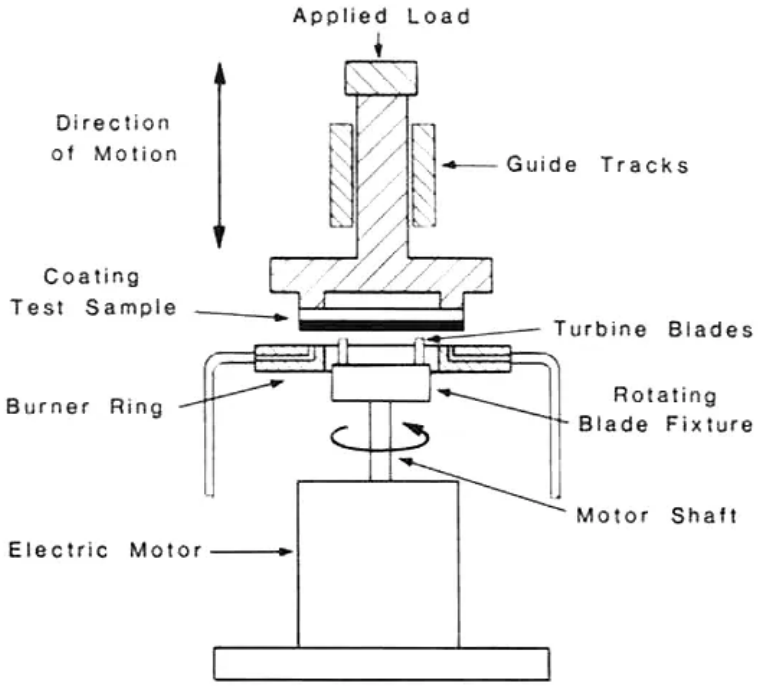

Figure 2.23: Schematic of the constant coating-to-blade interaction rig developed by Sulzer Metco (228)

In 2005, the company Sulzer Metco (now Oerlikon Metco) developed a commercial abradable incursion testing facility (Figure 2.24) in Winterthur, Switzerland (57; 58; 23; 39; 31). The test rig, still operative, heats the abradable sample up to 1200 °C by the use of a high velocity gas stream. Real turbine or dummies blades can be mounted on a turbine disc and accelerated, being able to achieve a linear speed of 500 m/s on the blade tip (31). The incursion speed is controlled by a stepper motor that moves the abradable specimen forward and into the rotor. The incursion speed can be adjusted from 1 to 2000 μm/s (31). Although real turbine blades represent more closely the rubbing contact inside a gas turbine, the use of a dummy blade is representative enough and preferred for systematic investigations.

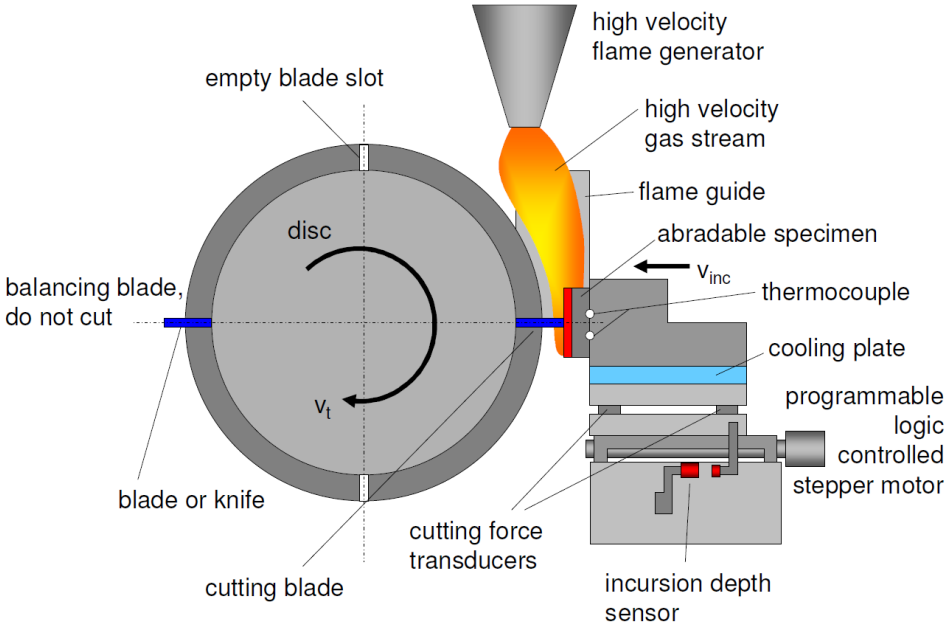

Figure 2.24: Schematic of the commercial abradability rig developed by Oerlikon Metco (39).

In the test rig developed in Winterthur, Sulzer Metco tested the abradability of various ZrO_2 based ceramics stabilized with different Rare Earth Oxides (REO) against c-BN tipped Inconel 718 blades at 1200 °C (57). The three employed REO stabilizers were: dysprosia (Dy_2O_3), ytterbia (Yb_2O_3) and the already tested yttria (Y_2O_3), which form DySZ, YbSZ and YSZ, respectively. Each type of coating was manufactured with an additive of 5 wt% of polyester that was later heat treated to form porosity within the specimens. A porosity of 26.6% was confirmed via metallographic examination on the YSZ, 29.3% on the DySZ and 39.6% on the YbSZ coating. The abradability test parameters were: 250 and 410 m/s blade tip speeds at incursion speeds of 5 and 500 μm/s. An intermediate reference set of parameters was added using 250 m/s and 50 μm/s as a blade tip speed and incursion speed respectively. The results proved that c-BN tipped blades can cut ceramic coatings to a good extent with very limited blade wear or material adhesion. Smoother track surfaces were obtained with both higher blade speed and incursion speeds. Additionally, very slight wear was detected on the blades that were tested against YSZ specimens, which had the lowest porosity. On the other hand, moderate material adhesion to the blade tips was found when testing with DySZ and YbSZ samples.

Under the same test conditions as in (57), YSZ and DySZ ceramic coatings were

tested again, but against bare Inconel 718 blades (58). Whereas two levels of porosity, 24 and 43%, were analysed for the case of YSZ, only 30% of porosity was used on the DySZ specimens. For the lowest porosity samples, poor abradability was found for every condition with a trend toward less coating rupture but heavier blade material transfer with increasing incursion speeds as well as blade speed. For the highest porosity samples, a clean cut with acceptable blade wear (<10%) was obtained for all test conditions selected. However, for the intermediate porosity, wear mechanisms were greatly influenced by the test parameters. A clear tendency towards a clean cut with less blade material transfer and lower blade wear arose with increasing blade speed, but decreasing incursion speed. This statement conflicts with the outcomes obtained from (53; 230; 57) where better performance was achieved for increasing incursion speeds.

The wear mechanisms observed in (58) were summarized in (23) by using the wear maps presented in Figure 2.25. No distinction between material was made on the wear maps, only porosity was taken into account.

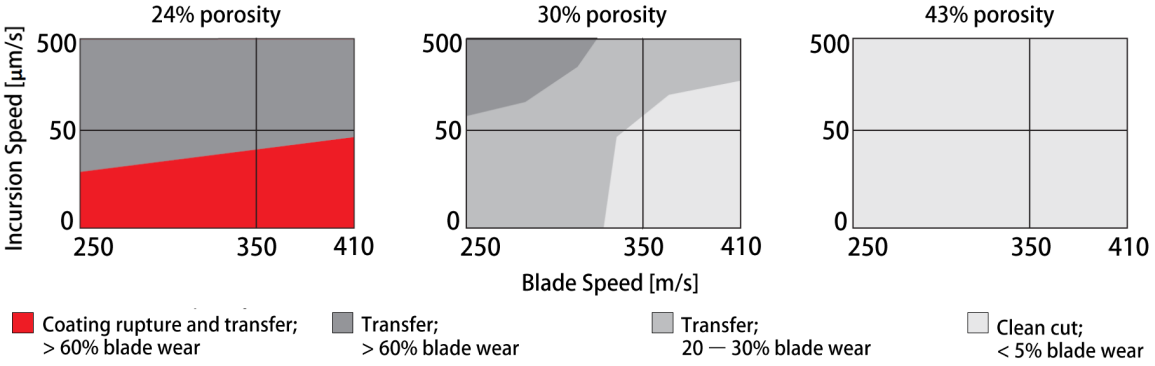

Figure 2.25: Wear maps of the ceramic abradable linings with different level of porosity when rubbed by a Inconel 718 bare blade at different testing conditions (89).

A second set of tests was carried out in (58) to compare the cutting performance between c-BN tipped and bare blades at 850 °C. Whilst a YSZ ceramic coating with 15% of porosity was tested against c-BN tipped blades, a softer version with around double the porosity (31%) was tested against bare blades. The selected test parameters were 250, 350 and 410 m/s at an incursion speed of 50 μm/s. With the use of bare blades, considerable material transfer from the blade to the ceramic as well as severe blade wear (Figure 2.26a) were found for the two lowest speeds. However,

these phenomena were moderate at 410 m/s where a rough track surface was visible. c-BN tipped blades once again provided a clean cut in every condition (Figure 2.26b).

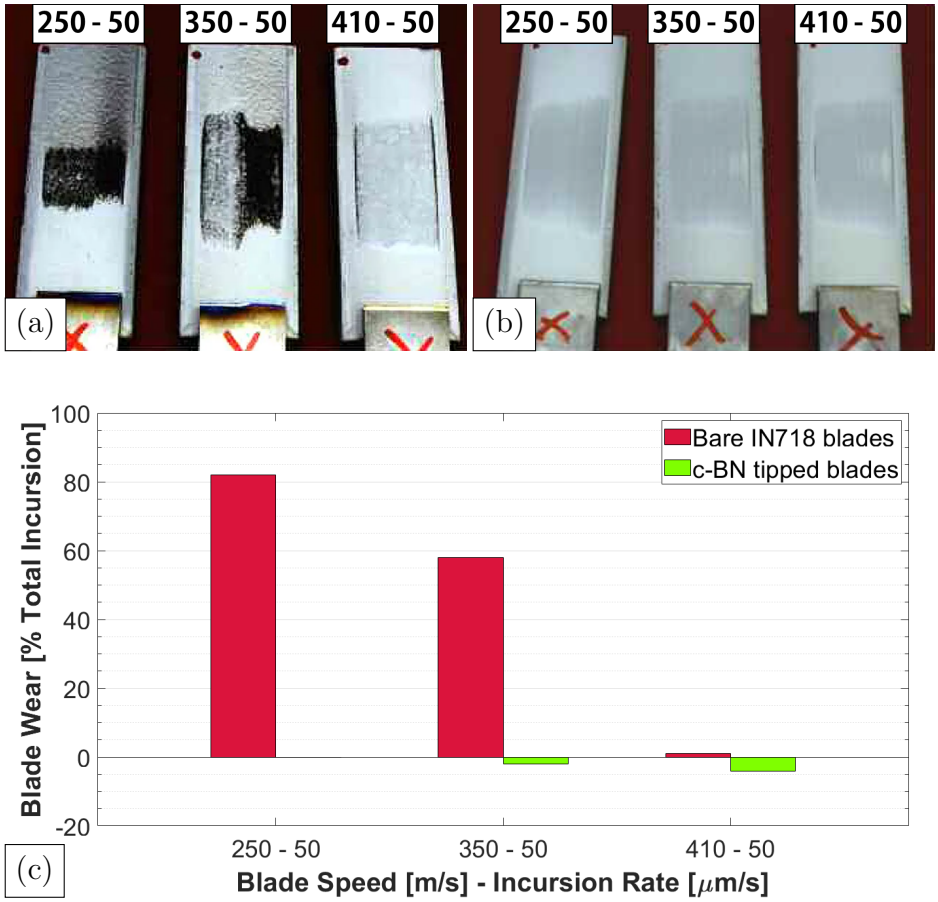

Figure 2.26: Test results of YSZ ceramic samples rubbed by bare and c-BN tipped blades at blade speeds of 250, 350 and 410 m/s and a fixed incursion speed of 50 μm/s: (a) bare blade test specimens, (b) c-BN tipped blade test specimens and (c) blade wear as a total incursion percentage (58).

As such, it is true that increasing the blade speed makes the blade strike the abradable with higher kinetic energy, decreasing the contact normal forces and generating a cleaner cut, as occurs with any grinding tool (134; 171; 231). However, it is important to highlight that the amount of material that the blade has to remove per strike increases when the blade speed decreases at a fixed incursion speed inasmuch as the incursion depth per blade strike is larger. The parameter used for defining this incursion depth per blade strike is called feed, or better known as incursion rate in abradaility testing. It is a function of the blade speed, incursion speed and rotor diameter and is a more representative parameter than incursion speed as it allows a

more accurate comparison between tests at different speed conditions (28). Therefore, the cut improvement in (58) could be also due to a lower and more gentle incursion rate at increasing speeds.

Due to the upward trend of maximum service temperatures in aero-engines over the last decades (232) and the limitations of ZrO_2 based abradables at very high temperature, Rolls-Royce has more recently focused its resources on the development and testing of MAS abradable linings against c-BN tipped blades for use on engine turbine sections (129; 14; 43; 170; 40). However, thus far, research into the c-BN/MAS system performance is still limited and the narrative fragmented. The available studies do not approach the research subject from the same perspective as well as their test conditions are dissimilar, making results barely comparable.

As a starting point, the performance of c-BN was assessed in (170) through a pin-on-disc wear test at 900 and 1100 °C (Figure 2.27). Whereas some abradable adhered to the tip surface with barely blade damage was observed at 900 °C, a great percentage of the c-BN particles were pulled out after 2 min at 1100 °C.

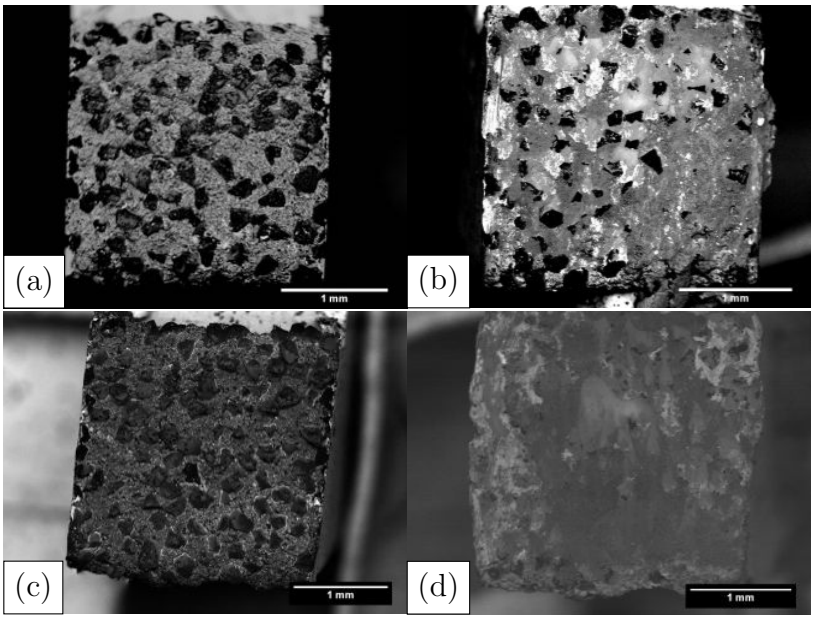

Figure 2.27: Images of electroplating c-BN coated pins from pin-on-disc tests: (a) before test at 900 °C, (b) after test at 900 °C, (c) before test at 1100 °C and (d) after test at 1100 °C (170).

On the other hand, the influence of the hardness as well as temperature on the MAS abradability was analysed at a fixed blade speed (410 m/s) and incursion speed (50 μm/s) in (129). Testing was carried out in the Sulzer Metco incursion test rig. Abradability was measured in terms of blade wear/material adhesion and no difference

was detected within the range of 800-1200 °C. However, abradability presented a great dependence on the abradable coating hardness. As expected, the harder the coating, the higher the blade wear.

Likewise, the influence of a 3D structure underneath the MAS layer to enhance the clamping of the abradable to the substrate was analysed in (14). Both flat and curved specimens were tested at the same conditions (not specified) at the Sulzer Metco facilities. The excellent cutting performance of c-BN against MAS was again demonstrated as presented in Figure 2.28, although no difference was appreciable between the four possible structure combinations (with/out 3D structure combined with a flat/curved substrate).

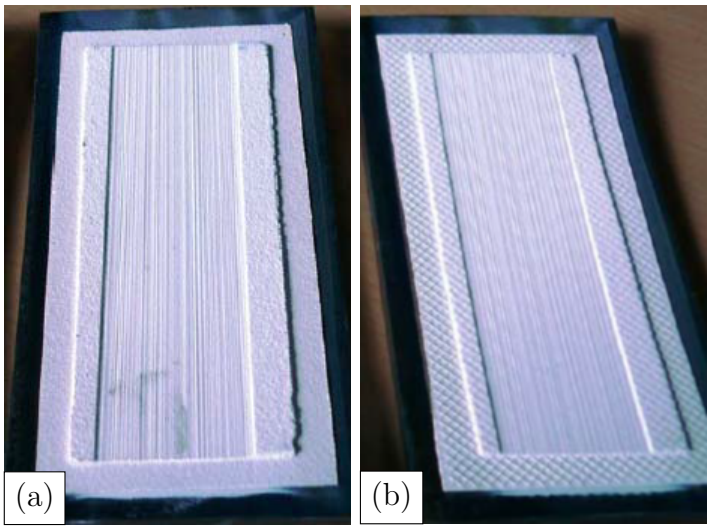

Figure 2.28: Curved MAS specimens (a) with a plain and (b) with a 3D bond-coat interfaces tested against electroplating c-BN blades at the same conditions in the Sulzer Metco rig (14).

All the test rigs described before focus their heating source on the abradable specimen, whose surface temperature is validated by using pyrometers. However, the blade is only heated up at the instant that it passes through the flame, then it cools down by forced convection until the next pass. Therefore, these conditions make the rigs inadequate to study the blade performance at high temperatures. As a consequence, the University of Cambridge developed a small-scale rig that is able to achieve uniform temperature on both the abradable specimen and the blade during the test (40). This rig consists of a spin arm which the blade is attached to and a moveable platform where the coating samples is placed, both enclosed in a split furnace. The furnace maintains a uniform temperature up to 1200 °C on both the blade and the abradable coating. The spin arm is rotated from the outside of the

furnace by a 1kW motor which spins the blade tip at speeds up to 50 m/s. The abradable specimen incursion is also actuated from the outside by a stepper motor connected to a lead screw at incursion speeds ranging from 1 to 200 μm/s. Although this small-scale rig allow both the blade and the abradable specimens to be heated up, it is not possible to achieve either rotary or incursion rates typical of turbine sections needed to trigger some of the wear mechanisms, in addition there was no data recording during the tests (40).

In the University of Cambridge, electroplated c-BN tipped blades were tested against MAS samples at a wide range of temperatures (25, 700, 900 and 1000 °C) and incursion speeds (5, 10, 50 and 100 μm/s), but at a single blade speed of 50 m/s (40). Clean cuts were obtained in every condition. Abradability was measured as the difference between the nominal and the actual track depth. Poorer abradability was observed on the c-BN/MAS systems that were tested at higher temperature. These outcomes conflict with those reported in (129), where only the abradable sample was heated up. The explanation behind this difference is that the temperature increment on the blade boosts the bonding deterioration, and subsequently c-BN grains detach that leading to a loss in the blade cutting effectiveness (40).

Considering the research to date more widely, there is a noteworthy disparity between the test methods developed and employed for each test rig, not only in the heating technique but also in the contact mechanism, which end up in conflicting conclusions. From the standpoint of the contact mechanisms, the results from a pin-on-disc test cannot be directly compared to those obtained from a high-speed incursion test. From the point of view of the heating technique, the currently available abradability incursion rigs that are capable of replicating the contact mechanics focus their heating source on the abradable ceramic specimen, but not the blade. This precludes the blade from reaching the temperatures necessary to start releasing the abrasive grits as a result of the bonding system softening. In addition, the tested specimens are the only results generated, with no data recording during the course of the test as has previously been done for the work conducted around compressor abradable systems (22; 28; 158; 36).

Due to the fact that compressor abradable systems are composed of metal based linings rubbed by either bare titanium or Inconel blades, reviewing their performance and properties is fruitless as the resulting wear mechanisms are unrelated to those arising from the the turbine ceramic linings/tipped blade systems contemplated in this piece of work. However, it is worth considering the methodology and techniques developed by The University of Sheffield in the past few years to monitor and evaluate

the performance of abradable systems throughout the entire course of the tests (22; 28; 158; 36; 233; 234; 235; 236; 237).

The University of Sheffield possesses two currently operative abradable specific rigs whose concept, except for the heating capability, is similar to the commercial rig from Oerlikon Metco in Winterthur. In both rigs, a spindle drives a disc where the blade is mounted and rotated while the abradable coating sample, assembled in a stage driven by another motor, approaches the rotating disc at a specific incursion speed. A dynamometer is placed between the stage and the coating sample to measure the contact forces during the test. The first of these rigs is the Low-Speed Rig (LSR, Figure 2.29a), the disc is cantilevered and the blade can reach a maximum linear speed of 200 m/s (229; 236). In addition, diverse optical devices are available in this rig for recording both the blade and the abradable coating from different angles as well as for measuring temperature. The second rig, the High-Speed Rig (HTR, Figure 3.3.2) has a potential linear speed of 400 m/s (229; 237). However, because the shaft is two-point supported and the closeness of the shielding containment, the amount of optical devices is limited on this second rig.

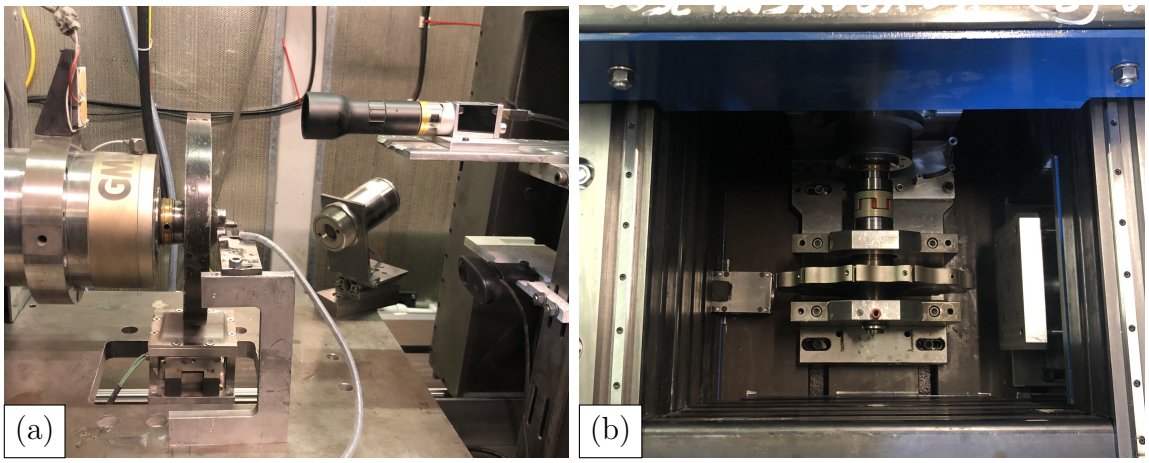

Figure 2.29: Abradable low temperature testing rigs in the University of Sheffield: (a) Low-Speed Rig and (b) High-Speed Rig (237).

To evaluate the performance of the abradable systems, the following measurement instruments can be found in the rigs from the University of Sheffield:

- Dynamometer: placed between the coating sample and the stage, provides measurements of the forces on three independent axes during the contact (22).

- Side top camera: records the maximum length of the blade throughout the test. The maximum blade length is a very useful indicator of the wear rate and material pick-up for bare blades as the entire section generally wears homogeneously. However, when testing tipped blades it becomes impractical as the wear on the abrasive coating occurs locally (22; 236; 237).

- Side bottom camera: allows to record sparks, a sign of non-efficient and high force contact, as well as to observe the material release from the cut (236).

- Front camera: records the blade from a front position at the top position (non-contact). It provides information about the wear and material pick-up across the entire width of the blades (237)

- High speed camera: focusing the contact point on the coating sample, capturing the coating break-up in slow motion. Especially useful, in high porous and heterogeneous materials where DIC techniques can be used to evaluate the compression and crack nucleation underneath the contact point (235).

- Pyrometer: measures the temperature of a single point on the abradable coating from the amount of radiation it emits. A pyrometer is a very convenient non-contact temperature measuring device when temperature is homogeneous along the entire coating surface in contact. This occurs when both the contact occurs homogeneously along the blade and when the abradable coating possesses a high thermal conductivity. When it comes to abrasive tipped blades against ceramic coating the contact is discretized to the grit contact points as well as the high thermal insulation of ceramic materials prevents the pyrometer from being a useful instrument inasmuch as the temperature varies considerably along the contact surface (22; 229; 237)

- Thermal camera: in contrast to a pyrometer, thermal cameras are able to measure and record the temperature across an area. This hardware overcomes the pyrometer limitation at measuring materials with low thermal conductivity and allows identification of the points where the abrasive coating locally fails (233; 235).

The techniques developed by the University of Sheffield provide data to assess how well an abradable lining system performs or, in case that it fails, identify the instant of the test where and why that occurred. The final purpose of these techniques is to establish a standard methodology capable of defining, quantifying and comparing

different abradable systems at different parameters, but by using the same testing methodology.

In summary, the experiments conducted in the University of Cambridge (40; 170; 238) have established the basics for assessing the performance of abrasive tipped blades at high temperature. However, the testing methodology is far from representing the actual contact inside a gas turbine. Furthermore, the evaluating techniques also need further development as post-mortem samples are the only available data which provide little information about how a system is performing during a test. Bringing the techniques developed by the University of Sheffield (22; 28; 158; 36; 233; 234; 235; 236; 237) around the work in compressors to the turbine materials together with a rig capable of testing abradable lining systems at both representative speeds and temperatures would allow to understand, if it fails, under what circumstances the current MCrAlY/c-BN abrasive system does as well as to identify the arisen wear mechanisms that motivates the failure. Due to the limitation of some of the optical techniques when used with abrasive tipped blades, a new technique is required to quantify the damage caused on the abrasive coatings whereby tipped blades engineered by different processes can be straightforwardly compared. Moreover, in order to continue with the development of new and improved bonding systems, the next step would be the evaluation and analysis of the two novel matrix materials, Inconel 792 and IP75 which remain untested as yet, and compare them against the standard NiCoCrAlY system.

2.6 Summary

The studies reviewed in this section highlight a fragmented understanding of ceramic abradable seal system performance in modern gas turbines. To begin, using abradable seal systems to define gap clearances between rotating and static parts is not widely adopted; however, Rolls-Royce employs this technique due to the challenges of defining these clearances mechanically in three-shaft gas turbine engines during cold-build assembly (45). Consequently, research in this area is limited, and adjacent fields have been explored to provide context for understanding the behaviour and performance of these complex ceramic seal systems.

On one hand, research on abrasive coatings for rotating blades in the hot turbine sections has primarily focused on c-BN abrasive grits embedded in an MCrAlY matrix, manufactured by electroplating techniques. This solution has been tested against ceramic abradables using various methodologies, showing generally positive

performance results. However, Rolls-Royce in-service engines have shown premature and excessive wear with this system. While some studies assess the overall performance, they do not examine the specific wear mechanisms at play during contact, as has been recently studied in the compressor section seal systems at the University of Sheffield (22; 28; 36; 234).

Recent studies at the University of Cambridge have taken a material-focused approach to investigate the durability of the c-BN/MCrAlY compound at turbine-section temperatures, finding that the matrix has limited ability to hold abrasive grits in place (40; 170). Consequently, new DED deposited anchor matrices made of Inconel 792 and NiAlTa have been investigated as potential replacements for the MCrAlY matrix (44). However, tests to understand the contact mechanics and wear mechanisms of these alternatives have yet to be conducted. While it remains a priority to understand the intrinsic wear mechanisms of electroplated c-BN in an MCrAlY matrix against ceramic abradable linings, the next step is to gain similar insight into the DED deposited Inconel 792 and NiAlTa matrices, which have not yet been tested on an incursion rig.

On the abradable side, more research exists than on abrasive coatings, often derived from studies on TBC used in hot sections to protect metal parts from high temperatures, but with an added emphasis on abradability (129; 157; 28; 158). This factor, which opposes erosion resistance, requires a balanced solution. MAS ceramic lining has been found to offer good thermal stability, a thermal expansion coefficient compatible with the nickel superalloy used in substrates, and sufficient abradability, as demonstrated in previous tests against c-BN electroplated tipped blades.

Although abrasive tipped blades have been previously tested against ceramic abradable linings, their performance has been superficially assessed, without detailed examination of the contact mechanics (53; 230; 57; 58). Furthermore, methodologies in each study vary, leading to inconsistent and incomparable data. Furthermore, the baseline for high-temperature tests on ceramic abradable seal systems only heats up only the abradable lining, omitting the rotating blade and thereby not triggering the material failure mechanisms recently observed in abrasive coatings. Additionally, there is no data on material performance during the test itself, as only pre- and post-test samples are examined. In recent years, the University of Sheffield has developed methods to assess compressor metal-based abradable seal systems by monitoring contact forces, temperatures, and wear during tests. These methodologies could be adapted and further explored for ceramic abradable systems in turbine applications.

In addition, traditional methods for assessing abrasive tipped blades, such as weight or volume measurements and groove depth analysis, are limited because they assume simpler wear behaviours typical of bare blades (58). Abrasive tipped blades experience complex wear processes, including grain fracture and matrix detachment, which these methods fail to capture effectively. Visual inspection is also insufficient, as it only reveals complete failure without detailing progressive wear and is time-consuming, making it unsuitable for the stochastic nature of abrasive tipped blade performance. The limitations of the traditional methods for assessing blade wear are further reviewed in detail in Section 4.1.

Chapter 3

Materials and methodology

3.1 Planned work

After thoroughly reviewing the available literature on ceramic abradable seal systems and identifying key knowledge gaps (as summarized in Section 2.6), the next step is to outline a targeted approach for advancing this technology.

Before initiating experimental testing, it became clear that a standardized method is needed to assess wear in abrasive-tipped blades. To address this, Chapter 4 introduces an analytical tool designed specifically for evaluating the wear of electroplated c-BN-tipped blades, the baseline solution used by Rolls-Royce. This tool, which will be applied in subsequent experimental chapters, enables efficient assessment of the complex, variable wear characteristics of abrasive coatings—going beyond the visual inspection techniques used in earlier Rolls-Royce-funded studies (170; 40).

Following the development of this analytical tool, the electroplated c-BN-tipped baseline blade will be assessed to both understand its performance and replicate the wear mechanisms observed in operational gas turbines. Although high-temperature testing is the ultimate goal, the initial testing phase will be conducted in a staggered approach due to the availability of test rigs and specific instrumentation. First, the Low Speed Rig (LSR), detailed later in this chapter, will be used to test at room temperature, as it is readily accessible within the research group. The LSR is versatile, allowing for multiple instruments to measure contact forces, abradable temperatures, blade wear, and material ejection, depending on study requirements. Collecting data from diverse sources enables a holistic understanding of wear mechanisms for any given material pair. Establishing a clear understanding of these mechanisms at room temperature is crucial before introducing variables like high-temperature effects that could further impact performance. This process will then be repeated for the novel DED c-BN-tipped blade variants.

Once room-temperature evaluations are complete, high-temperature testing will commence. A new High Temperature Rig (HTR), introduced in detail later in this chapter, was developed during this research to test blades at elevated temperatures, addressing the limitations of rigs that only heat the abradable sample. Commissioned near the conclusion of this scoped research time, the HTR currently has limited instrumentation, constrained by both space and the complexity of its design. Thus, it is essential to fully characterize wear mechanisms at room temperature on the LSR before progressing to high-temperature assessments on the HTR.

The samples used in both the LSR and HTR are simplified representations of the blades and abradable linings used in actual gas turbines. These simplifications reduce manufacturing and design complexities and have been shown in compressor studies to replicate in-service wear mechanisms accurately (22; 28; 229; 36; 234; 237). For the blades, thickness approximates real turbine blade tip edges, and the width exceeds the abrasive grit size, providing sufficient coating on each blade sample. The abradable sample's thickness matches that of industry linings, with widths exceeding blade width and lengths tailored to ensure that, given the rig's disc radius, the ceramic track fully accommodates the abradable depth. Stepped-thickness samples will also be used, as they allow assessment of wear at varying depths within a single test, helping to understand wear progression without interrupting the testing process.

3.2 Test Samples

3.2.1 Blades

The blade samples used in this piece of work are a simplified version of the actual blades employed in gas turbines. Two different designs are considered in this research depending on the rig the blades are tested on. The standard long design (16 mm long), represented in Figure 3.1a, commonly used in previous studies done on the Low Speed Rig by the abradable research group of the University of Sheffield; and a shorter redesign (14 mm long), shown in Figure 3.1b, which has been made to accommodate the blade to the narrow space available in the novel High Temperature Rig.

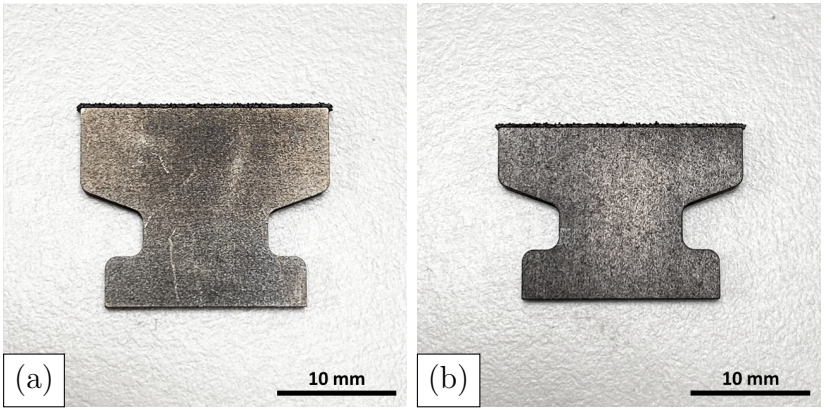

Figure 3.1: Blade geometries: (a) standard design (16 mm) and (b) short design (14 mm).

Blades are made of CMSX-4 nickel superalloy and the tip is coated with the three different abrasive linings considered in this study depending on the test to be undertaken:

- TBT 429: this coating is commercially available from Praxair Surface Technologies, Inc. It comprises 60/80 US mesh single crystal c-BN grits embedded in a NiCoCrAlY matrix. The coating is deposited through an electroplating patented process called Tribomet.

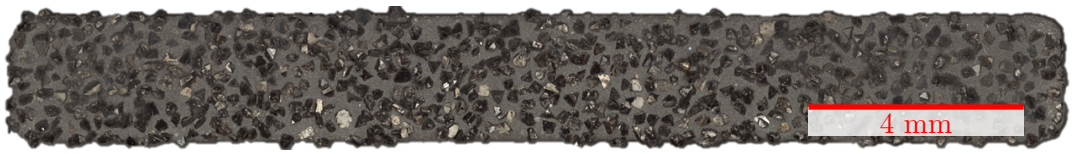

Figure 3.2: TBT429 abrasive blade coating.

- Delta: the second generation of abrasive coating has been developed by Rolls-Royce Corporation and transferred to pre-production source at RPM Innovations. This consists of 60/80 US mesh single crystal c-BN grits embedded in an Inconel 792 matrix. The technique employed for engineering this abrasive coating is Direct Energy Deposition (DED) where grits and the matrix material in powder are deposited together.



Figure 3.3: Delta abrasive blade coating.

- IP75: the third generation of abrasive coatings is also a Rolls-Royce IP applied by IWS Fraunhofer in Germany. Again, it consists of a DED process whereby 60/80 US mesh single crystal c-BN grits are co-deposited with a NiAlTaCr intermetallic matrix on the blade tip.

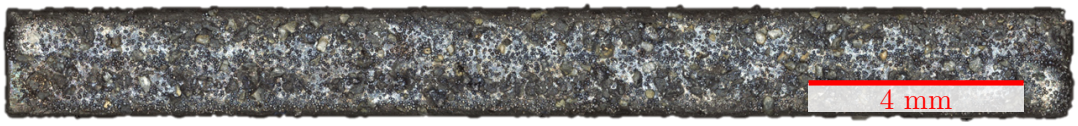

Figure 3.4: IP75 abrasive blade coating.

All blades have been supplied by Rolls-Royce.

3.2.2 Abradable coatings

A single material, but with different geometries and thicknesses has been used as the abradable coating samples, which are manufactured through Atmospheric Plasma Spraying (APS). The material to be tested is Magnesia Alumina Spinel (MAS), but a series of intermediate layers must be sprayed between this and the substrate to ensure a good adherence. The substrate is a 80x80x3mm plate made of 316 stainless steel which has 8 countersunk holes in order to be fixed to the test rig. On top of the substrate, a 150 micro thick metallic layer of CoNiCrAlY is sprayed to act as a bond-coat with the later ceramic ones. Then, an interlayer 7% Yttria-Stabilised Zirconia (YSZ) with a thickness of 200 microns is sprayed over the bond-coat. Finally, the MAS layer is sprayed on top with the thickness required for the test incursion depth. The nominal hardness of the MAS layers deposited on the samples used in this piece of work range from 55 to 66 on the Rockwell hardness scale, using the R15 test method. The two sample design used on this study are the following:

- Standard samples: The arrangement of layers are sprayed on top of the substrate to an area of 60x60 mm, as shown in Figure 3.5a, with a MAS thickness of either 800 μm or 1500 μm. The first of the thicknesses, 800 μm, is the standard thickness employed in Rolls-Royce gas turbines HPT and the second one, 1500 μm, allows a deeper incursion rate to analyse the blade cutting endurance within sensible cost and manufacturing times (45).

- Stepped samples: for this case, the different layers are sprayed to an area of 60x20 mm with a MAS thickness of 1500 microns. Subsequently the width is equally split into three parts, where 500 and 1000 microns of material are removed from two of them to generate a stepped shape as shown in Figure 3.5b.

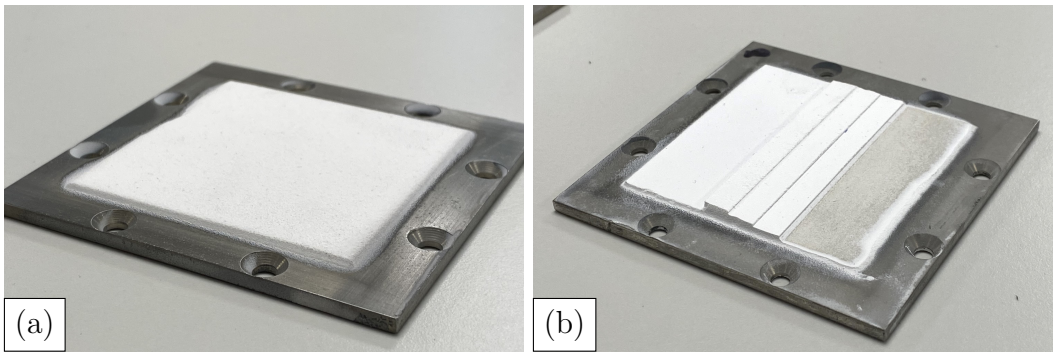

Figure 3.5: MAS abradable samples: (a) standard and (b) stepped designs.

Abradable samples have been supplied by Rolls-Royce.

3.3 Test rigs

The two abradable test rigs used for the incursion tests are the Low Speed Rig and the High Temperature Rig. Whereas the Low Speed Rig has been previously employed for analysing the abradable contact mechanics by the abradable research group in the University of Sheffield (22; 236; 233; 237), the High Temperature Rig has been designed, developed and validated for the purpose of this thesis.

The test procedures for a room temperature test in both rigs are nearly identical. These rigs are located inside a test cell with impact-resistant walls, covered by independent containment and operated from the outside with a control computer. A blade sample is mounted on a custom-made clamp that is inserted and fixed to the rim of a disc, where such disc is driven by a spindle. The abradable sample is fixed to a moveable stage with a dynamometer in between to measure the contact forces. To set up the initial test position, the stage is manually moved to the point where the abradable sample starts interfering with the blade and then retracted by a specific distance to avoid the contact due to vibrations and disc expansion during the disc acceleration. A set of optical instruments, which depend on the rig employed, record different aspects from the contact. These are set up and focused separately prior the start of the test. All these measurement instruments together with the stage and the spindle are controlled by a LabVIEW software code that has been specifically developed for the use of these test rigs. This code controls, synchronises and stores the data recorded by the different instruments.

To begin with the test, the spindle, controlled with the computer, is engaged and speeded up to the rotational speed determined by the required linear blade speed for

the test and the disc radius. Once the disc achieves the required speed, the computer user commands to start the test. All the measuring instruments synchronise, start recording and saving the data in a test folder automatically created. In parallel, the stage commences to approach the rotating disc at the determined incursion speed, given by the disc frequency and the incursion rate defined for the test. At the end of the approach the rotating blade starts contacting the abradable sample which keeps moving forwards until it reaches the incursion depth also defined by the user.

As the abradable samples are flat, the rub length that the blade sweeps increases with every consecutive pass, especially at the beginning of the test, following Equation 3.1, where R_{disc} is the radius of the disc at the tip, ID_{pass} the incursion depth of a given pass and RL_{pass} is the rub length of the pass at a given depth. The increment of the rub length per pass for consecutive pass influences the contacts mechanics as the blade needs to remove more material and the residence time become longer. Forces increase as the blade needs to accommodate more material, and temperature also increases by friction due to higher forces and longer residence times. This increment slows down as the test develops as the difference of rub length between consecutive passes drops but at the same time never reaches a steady state.

$$RL_{pass} = 2 \cdot R_{disc} \cdot arccos\left(\frac{R_{disc} - ID_{pass}}{R_{disc}}\right) \tag{3.1}$$

When the test incursion depth is reached, the stage retracts back to the initial position, away from the rotating blade. The spindle speed is set to zero and the control software waits to finish saving the data before shutting down. A single mechanical E-stop is available to disable every device at any point of the test.

For the case of a high temperature test, only available on the High Temperature Rig, an induction coil is employed to statically heat the blade up before the disc is sped up and it is kept in operation during the test.

Both rigs are broken down more in detail in this subsection. As the High Temperature Rig has been an upgrade of the Low Speed Rig with the further addition of a heating capability, the Low Speed Rig is going to be firstly introduced with the measuring instruments utilised for the tests considered in this thesis. Subsequently, the High Temperature Rig is going to be detailed in, highlighting the differences with its predecessor.

3.3.1 Low Speed Rig

The Low Speed Rig consists of a rotor where the blades are mounted, a stage for the abradable samples, a containment for guaranteeing a safe use and a series of instrumentation devices.

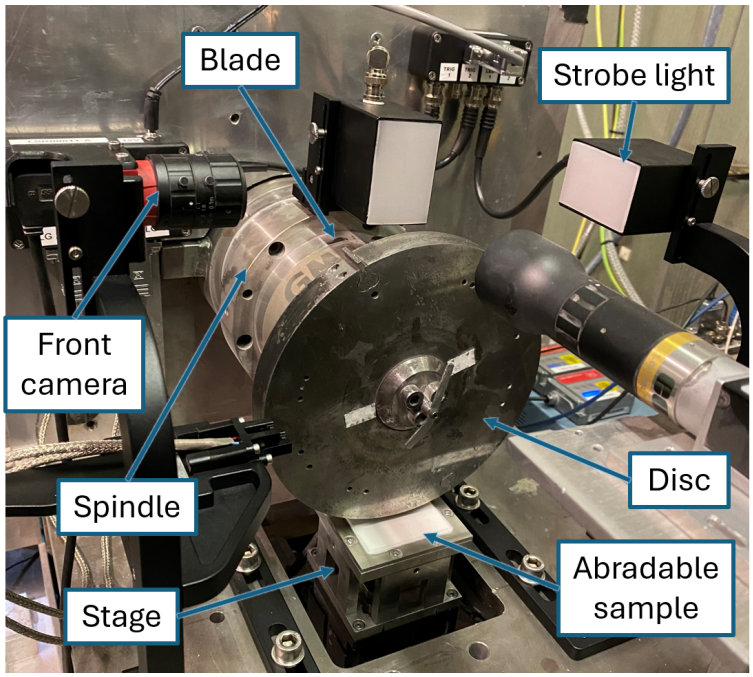

Figure 3.6: Rotor, Stage and Front Camera of the Low Speed Rig.

3.3.1.1 Rotor

On the rotor side, a cantilever disc is directly connected to a spindle (GMN HSP120g - 21000/9) through a rigid coupling (HSK-140). The spindle is controlled by an inverter (Emerson SK3403) which is, in turn, connected to the test control computer. The spindle is cooled down by a 4.5 kW water circulating chiller (Hyfra Chilly 45). The spindle has a maximum power of 9 kW and a maximum rotational speed of 21000 rpm. The testing blade and a dummy blade to counterbalance the weight are mounted on opposite directions on the disc with custom made clamps which are each inserted in and fixed with two grub screws. With the long blades (16 mm), the radius of the disc is 96 and a linear speed on the contact of 211 m/s can be achieved at the spindle maximum speed.

3.3.1.2 Stage

The stage includes a motorized stage guide (SIGMA KOKI SGSP80-20ZF) that reaches linear speeds between 0.1 and 2000 μm/s to move the abradable sample forward to the disc. The stage is commanded by an stage controller (SIGMA KOKI SHOT202) which is connected to the control computer. Between the sample and the stage there is a dynamometer (Kistler Type 9347C), which will be presented later, and an interface plate to fix the sample to it.

3.3.1.3 Containment

The rig containment is made of steel plates and wood. It is mounted over two rails to slide it away to uncover the rig for working on it. On one of the side plates, there is a hole in the line with the contact point for inserting the pipe of an industrial vacuum (Kerstar KEVA 20H) to extract the debris released during the tests. On the other side, there is a window with a glass made of Zinc Sulphide (ZnS) for focusing any optical device on the contact point from the outside as observed in Figure 3.7.



Figure 3.7: Containment of the Low Speed Rig.

3.3.1.4 Instrumentation

The instrumentation used for assessing the performance of the abrasive tipped blades against MAS ceramic coating samples considered in this piece of work are the following:

Dynamometer A triaxial piezoelectric dynamometer (Kistler Type 9347C) is used to measure the forces on the contact between the blade and the abradable sample. The dynamometer independently records the force in three orthogonal directions and its output is a 3 pin cable where each pin corresponds to one axis. The cable is connected to a charge amplifier (Kistler Type 5070A) that turns the dynamometer output charges into voltage which is then read by a digital oscilloscope (PicoScope Series 5000) connected to the test control computer by a USB cable. The digital oscilloscope has 4 independent channels which record the voltage analogue inputs, convert them into data points at 125 MHz and stores them in a buffer where the computer can easily collect the points from and save them in a .tdms file. The force data diagram as described is represented in Figure 3.8 and the data saved in Figure 3.9.

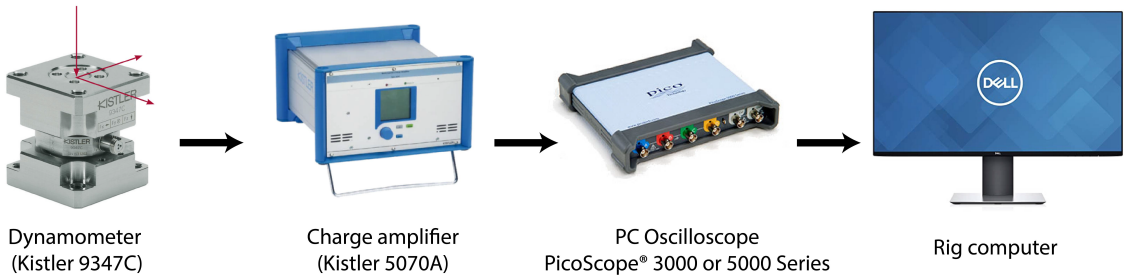

Figure 3.8: Force data diagram (237).

The dynamometer is positioned between the abradable sample and the moving stage, with the addition of an interface stainless steel plate at each side. A thin sheet of rubber is placed between the abradable sample and its corresponding plate to reduce the vibrations between consecutive blade strikes as the stage systems dynamic response is underdamped.

Only two of the three force axes are relevant in this piece of work: the force axis normal to the abradable sample in the inward direction, referred to as normal force, and the force axis in the plane of the direction of the blade rotation, referred to as the tangential force.

The saved data is loaded into Matlab for post-processing. The raw data is as shown in Figure 3.9a, where the negative side comes from the underdamped response of the system. The raw date consists of consecutive peaks where each peak corresponds with each blade strike against the coating sample, Figure 3.9b. For representing the force, the envelope over those peaks is used as the contact force during the test as is shown in Figure 3.9c. More details on how the force are processed can be found in (237).

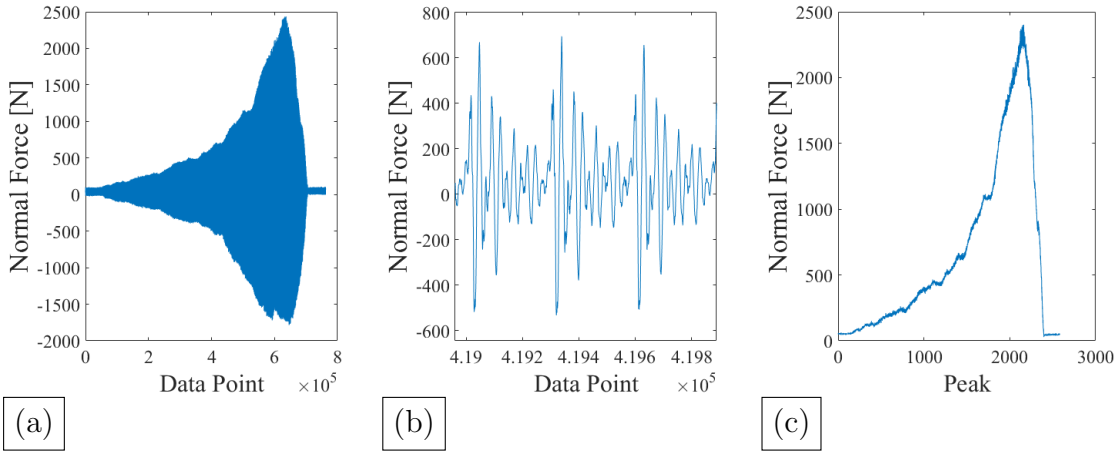

Figure 3.9: Data captured by the dynamometer and plotted in Matlab: (a) raw data, (b) detailed view of peaks and (c) peaks envelope.

Thermographic Camera A thermographic camera (Flir A6751 SLS) is used for measuring the temperature on the abradable surface produced from the contact. This thermographic camera or thermal camera for short, captures radiation in the Long Wave Infrared (LWIR), spectrum more specifically, in the range of 7.5-9.5 μm. The thermal camera manufacturer, Flir, has conducted a custom calibration on the camera to measure temperature in the test range of 150-1300 °C with a 1 % error. For using this calibration, an internal bandpass filter with a wavelength range of 9100-9455 nm must be installed. The camera is set to capture a frame of 320x256 pixels of the abradable sample (Figure 3.10) every time the blade passes, which at maximum speed, records at 350 Hz. The thermal camera is placed in a stand outside the rig containment at a distance of 0.4 m from the contact point and at a viewing angle of 9.78 °C. The camera focuses on the sample through a window in the containment. The glass of this window is made of ZnS, whose transmissivity is 75.51 % and constant in the filter spectral range (9100-9455 nm).

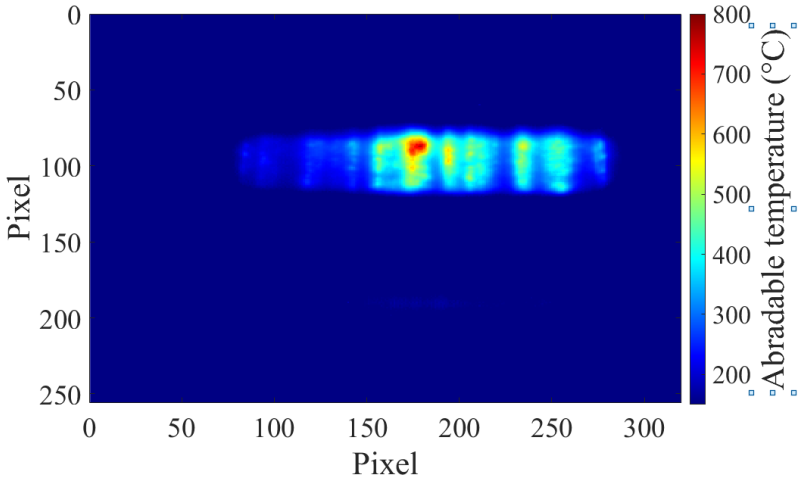

Figure 3.10: Example of a frame captured by the thermal camera from the MAS coating sample during a test.

Thermographic cameras do not directly measure temperature, and instead measure the radiance, L_{BB} (W m^{-2} sr^{-1}), emitted by black bodies, which is then converted into temperature by applying Planck's law for a given wavelength, λ, range. Planck's law is defined in Equation 3.2 where k_b is the Boltzmann constant, $\hbar$ is the Planck constant and c is the speed of light. A series of corrections must be applied to the system as Planck's law considers the energy emitted by a black body (emissivity = 1) throughout an environment with no net flow of matter or energy between the source and the sensor (transmissivity = 1), and no reflected temperature; in other words, a perfect system. Therefore, the measured temperature is as accurate as the corrections considered to characterise the actual system. For that reason, the measured temperatures with a thermal camera are no more than a close estimation of the actual temperature on the measured surface. That said, the temperatures between tests are reliably comparable as the device, materials and corrections remain the same.

$$L_{BB}(\omega, T) = \frac{2\hbar c^2}{\lambda^5} \frac{1}{\exp(\frac{\hbar c}{\lambda k_B T}) - 1} \tag{3.2}$$

The corrections applied can be divided into three groups according to their target: the device, the environment and the object to be measured. The systematic inaccuracy of the device was corrected through a calibration carried out by the manufacturer (Flir), according with NIST, to correlate radiance and temperature. The other two groups of corrections, concerning the environment and the object, are introduced in the thermal camera software (ResearchIR) as parameters or in the later data post-processing. Regarding the environment, the reflected temperature and the

atmosphere transmissivity must be addressed. The first one can be neglected as the surrounding radiations are negligible compared to the one emerging from the contact. Radiation is proportional to the temperature raised to the power four and the minimum temperatures measured in this study are at least 250 °C, much higher than the ambient temperature ($\sim$ 25 °C). The atmosphere transmissivity is dependant on the measuring distance (0.4 m), atmosphere humidity (10 - 20 %) and temperature ($\sim$ 25 °C). Considering those values, the atmosphere transmissivity is 99 %, which means a negligible effect ($\leq$ 1 %) of the atmosphere on the measured temperature. However, the transmissivity of the glass on the containment window which is 75.51 % must be considered.

Considering the object, the principal correction to make is the emissivity of the coating sample. The emissivity of an object is a function of different parameters: wavelength, surface roughness, oxidation, heat treatment, viewing angle and temperature; where some parameters have a greater influence than others. With the aim of validating the emissivity of the MAS abradable samples, an experiment has been conducted with the use of a thermographic paint (LabIR HERP-HT-MWIR-BK-11), whose emissivity has been well studied for different temperature and viewing angles (239).

The experiment consists of painting half of a tested MAS sample (with the groove produced by the blade) with the thermographic paint and putting the sample into a oven at 650 °C for 2 hours. Once the temperature is homogenised, the sample is taken out and put in front of the thermal camera at a perpendicular angle to record the radiance of both bare and painted halves while cooling down as shown in Figure 3.11a. The same experiment is repeated but at an angle of 9.78°. Although the temperature is the same in the whole sample, the thermal camera captures a different radiance from each side as their emissivities are different (Figure 3.11c).

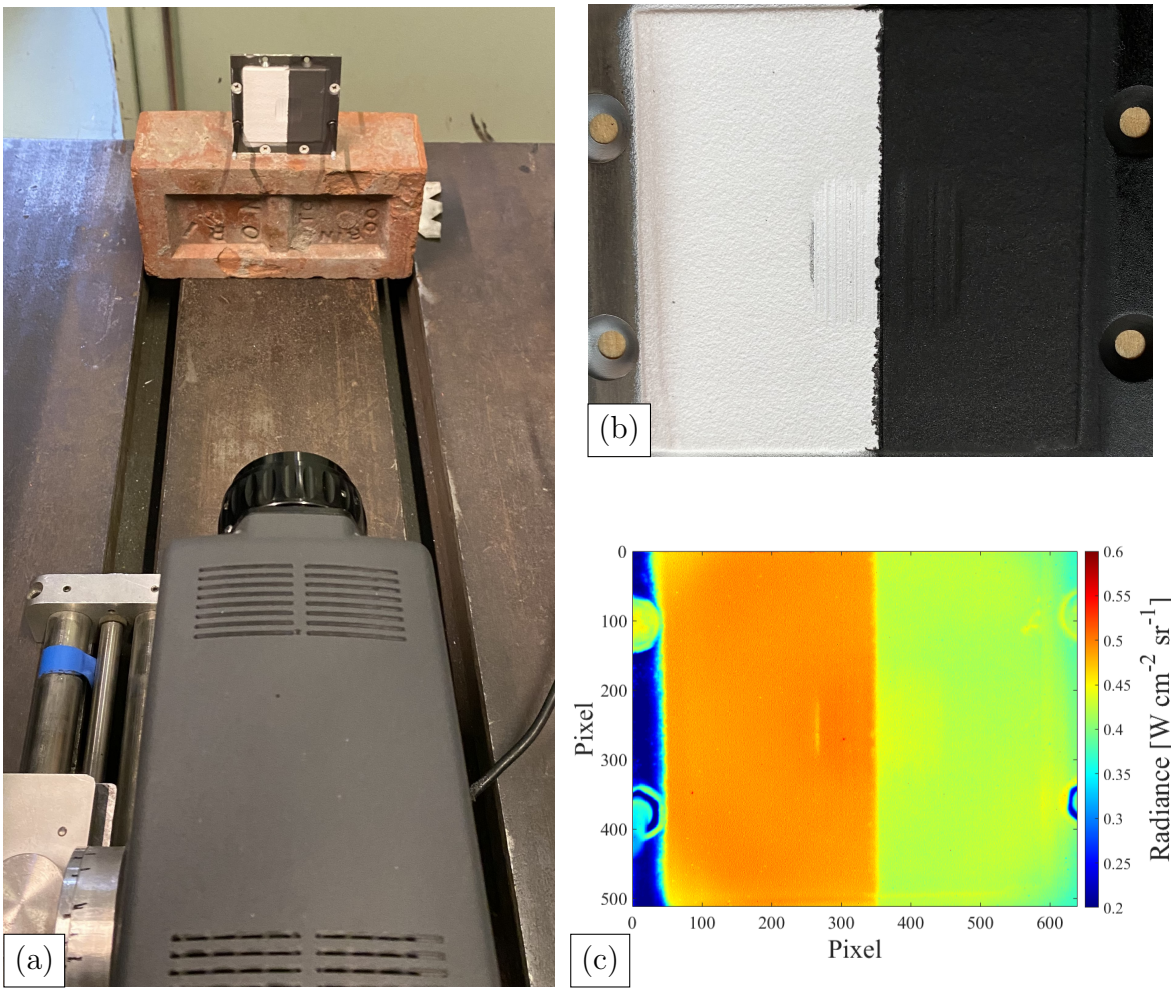

Figure 3.11: Experiment conducted for characterizing the emissivity of MAS samples at 90°:(a) thermal camera set up at 90°and 0.4 from the sample, (b) half painted MAS samples with the blade groove in the middle and (c) radiance measured by the thermal camera for each half.

To correlate both halves, the Stefan-Boltzmann law (Equation 3.3) must be employed. This defines the radiant exitance, M_{BB}, emitted by a black body across all wavelengths for a given temperature, T, and where σ is the Stefan-Boltzmann constant.

$$M_{bb} = \sigma T_{bb}^4 \tag{3.3}$$

The radiant exitance is the radiant flux emitted by a surface per unit area and it is the integral of its radiance over the hemisphere the surface radiates into and defined

according to Equation 3.4 where θ is the zenith angle and dA_s an infinitesimal area over the hemisphere.

$$M = \iint_{hemisphere} \frac{L(\theta)}{r^2} \cos\theta dA_s \tag{3.4}$$

If the radiating object is a black body and, therefore, an ideal diffuse emitter or lambertian emitter which, in other words, means that its radiance is isotropic, the Equation 3.4 leads to Equation 3.5

$$M_{bb} = \pi L_{bb} \tag{3.5}$$

On the other side, the emissivity is defined as the ratio of the radiance emitted by a generic body, L, dependant of different parameters as exposed above and the one emitted by a black-body, L_{bb}, at the same conditions (Equation 3.6).

$$\varepsilon = \frac{L}{L_{bb}} \tag{3.6}$$

Combining the Steffan-Boltzmann law (Equation 3.3) with Equation 3.5 and Equation 3.6, the temperature of any grey body can be directly correlated with its radiance through the emissivity as shown in Equation 3.7.

$$\pi L = \varepsilon \sigma T^4 \tag{3.7}$$

As the temperature on both the painted and non-painted sides is the same after taking it out from the oven, the radiance captured from the thermal camera for each side and their emissivity can be directly related as shown in 3.8.

$$\frac{L_{painted\ side}}{\varepsilon_{painted\ side}} = \frac{L_{non-painted\ side}}{\varepsilon_{non-painted\ side}} \tag{3.8}$$

The emissivity of the paint is known and constant for the range of 500 - 700 °C at a perpendicular angle, where the value according to the paint data sheet is 0.875 (239). By inputting the emissivity of the paint, and the radiance measured at each side at that range of temperature (Figure 3.11c), the emissivity of MAS is calculated and has a value of 0.972 at a perpendicular angle of view in both the rub track and the virgin sprayed material. This value agrees with the one reported for MAS by Rolls-Royce from their internal data base (45) when the measured wavelength range is $9.5 - 11.5$ μm.

The same experiment has been carried out but at the viewing angle for the tests. However, in this case, the viewing angle β between the thermal camera and the track

formed by the blade on the abradable coating varies during the test, and as mentioned previously, emissivity depends on that viewing angle when it is not an ideal diffusive emitter. This angle is dependent on the coordinate along the track as is shown in Figure 3.12 and defined in Equation 3.9, where x goes from $-\sqrt{R_{disc}^2 - z^2}$, $P_1(z)$, to $\sqrt{R_{disc}^2 - z^2}$, $P_2(z)$, for a specific instant during the test when the incursion is z. The closer the viewing angle to the perpendicular, the more consistent the data is as the camera's pixels cover smaller surface areas.

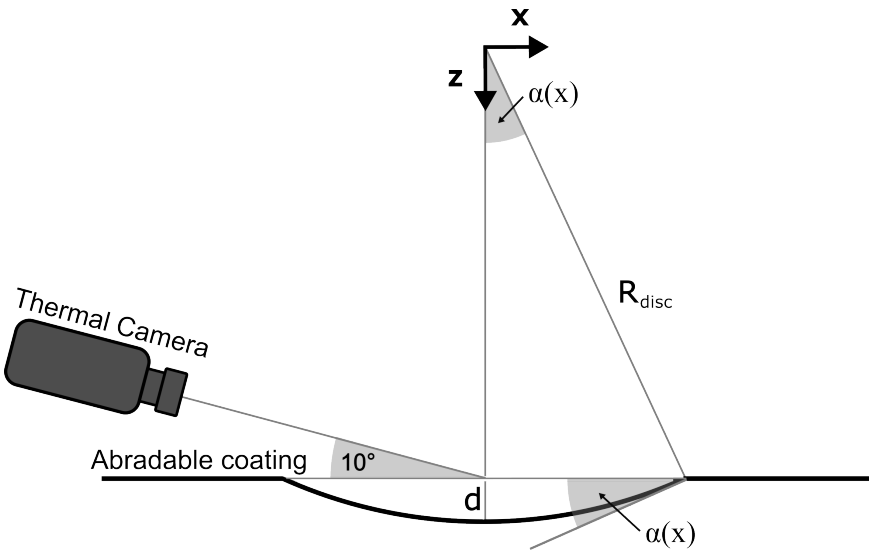

Figure 3.12: Schematic of the thermal camera viewing angle.

$$\begin{aligned}\beta(x) &= \alpha(x) + 9.78^\circ \\ &= arcsin\left(\frac{\sqrt{R_{disc}^2 - \left(\sqrt{R_{disc}^2 - x^2} - R_{disc}^2\right)^2}}{R_{disc}}\right) + 9.78^\circ\end{aligned} \tag{3.9}$$

As shown in Figure 3.13, a radiance variation on the painted side (right) occurs between the off-track area at 9.78° and the track close to P_2 at around 16°, this does not happen on the non-painted side (left). Using Equation 3.8 on the off-track area at 9.78° with the known paint emissivity at this viewing angle (0.692 for the range of 500 - 700 °C (239)), gives a MAS emissivity of 0.977, almost identical to the same for a perpendicular viewing angle. This means that the the MAS abradable coating is very close to a black body as $\varepsilon_{MAS} \sim 1$ with no radiance variation in the range of the thermal camera viewing angles during the tests.

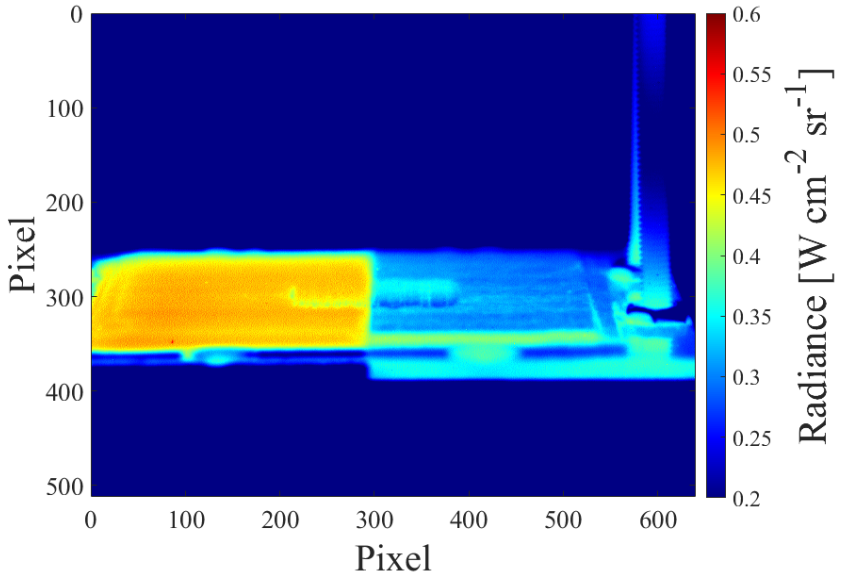

Figure 3.13: Radiance measured from a MAS coating sample at 500 °C by the thermal camera.

All of the aforementioned corrections considered together with the fact that the MAS coating is close to a black body, in both isotropic radiance and emissivity, allow for a relatively accurate measurement of the surface temperature during the tests.

In summary, the thermal camera captures a frame with the radiance of the abradable coating every time the blade passes, with this measurement then turned into temperature according to the corrections mentioned above. In this peace of work, temperature is presented in two different ways. The first of these is simple, but indicative of the blade general performance where the maximum temperature found on each frame is plotted against time or rub length as shown in Figure 3.14b. To avoid defective pixels or misreadings, the pixel with the highest temperature is compared to the surrounding pixels. The second way consists of determining, for every frame, the line across the track on the sample where the averaged temperature of the pixels that define that line is maximum. Then, the most repeated line over the frames is plotted over time or rub length as a 2D map. This 2D map gives a detailed evolution of the blade throughout the test, identifying hot spots (Figure 3.14a).

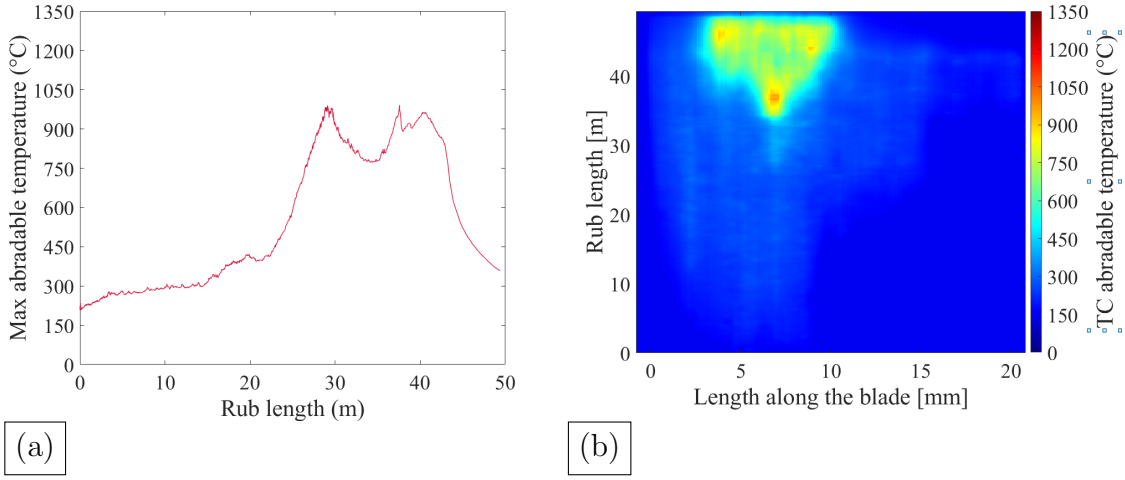

Figure 3.14: Example of the data post-processed from the front camera imaging: (a) maximum abradable temperature and (b) abradable temperature across the blade length throughout the test.

Front Camera A small front camera (Allied Vision Alvium 1800 U-500c) is employed with a fixed focal length lens (Edmund Optics 59-870) to record the length variation distribution of crest-shape DED abrasive coatings during the test. This camera is placed in the blade rotation plane, depicted in Figure 3.6, and records the front of the blade when this is at its highest vertical position. A pair of LEDs with an attached light diffuser are employed as a strobe light which flashes every time the blade passes perpendicular to the camera. The LEDs are triggered by a light gate and produce a white background on the images that highlights the abrasive coating contour as observed in Figure 3.15.



Figure 3.15: Example of a frame captured by the front camera.

The images are processed in MATLAB, where the corners that the disc forms with the blade is first identified and a line is drawn between both corners. This image is then tilted until the drawn line is horizontal. The profile length distribution along

the blade is then calculated from this line which is used as a initial reference. The next step is to calculate the average of the length distribution in the first image and subtract it from every value of the images' length distribution and compile the normalised length distribution row-by-row in a single matrix. This matrix provides the length variation distribution throughout the test as depicted in Figure 3.16a. As the pixel dimension is known, the distribution of each image is averaged and plotted as a 1D variable that defines the evolution of the projected blade area per unit thick variation as seen in Figure 3.16b for a given test. This projected area is then discretised in a single parameter by subtracting the value post-incursion from the initial value in order to compare the damage that DED blades suffer across tests. The root-mean-square roughness of the blade profile, which measures the blade abrasiveness, is also obtained from the profile length distribution for every image.

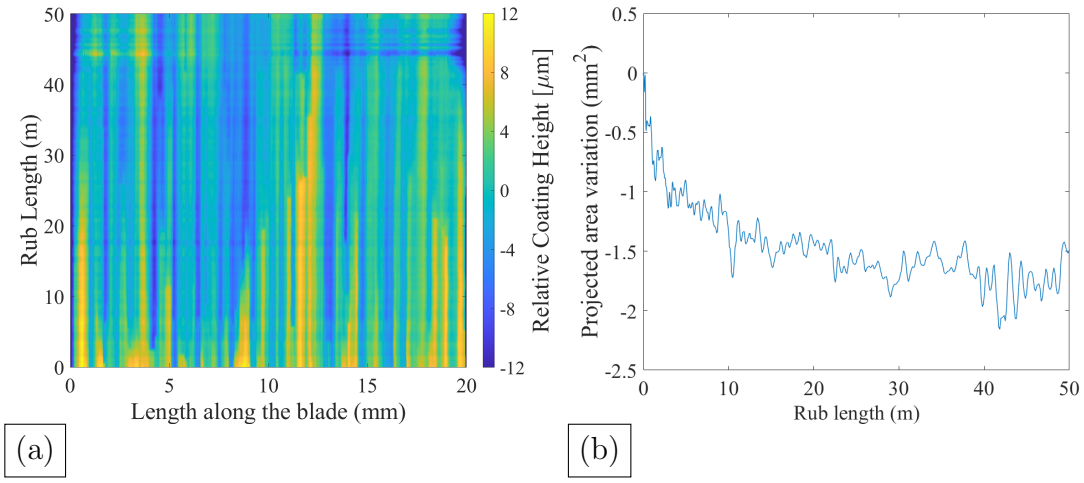

Figure 3.16: Example of the data post-processed from the front camera imaging: (a) blade length variation across the blade length and (b) projected area variation during the test.

This measuring technique is not applicable to electroplated tipped blades due to the in-plane distribution of grits where front grits obscure any damaged produced on the ones at the back.

Video Camera This camera (Logitech C310 HD WEBCAM) is a webcam placed parallel to the disc rotation axis and captures a side view of the contact (Figure 3.17a). The purpose of this camera is to determine the presence of sparks during the contact, where an example of both low and high amounts of sparks can be seen

in Figure 3.17b and Figure 3.17c respectively. When testing metal based abradable coatings against bare metal blades, sparks generally appear even with a low force input due to the nature of the materials (236). However, when testing ceramic based abradable coatings against tipped blades, sparks are an indicator of a malfuncting engagement between both parts.

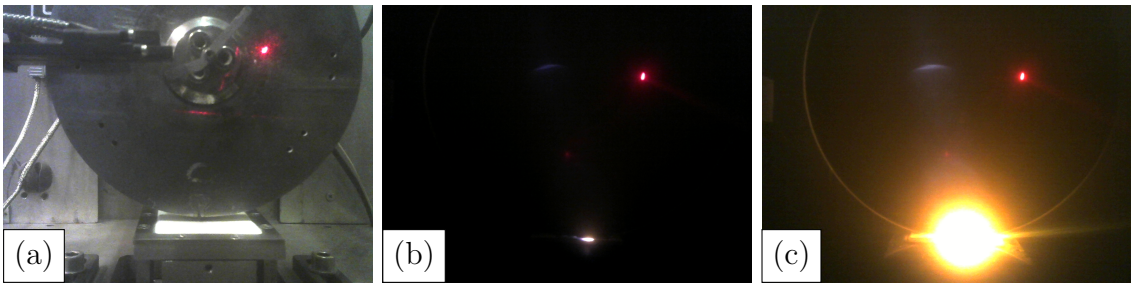

Figure 3.17: Examples of frames captured by the video camera: (a) side view of the Low Speed Rig, (b) a contact with a low amount of sparks and (c) a contact with a high amount of sparks.

3.3.2 High Temperature Rig

The mechanical concept of the High Temperature Rig is the same as the one introduced for the Low Speed Rig, but with the addition of an induction heating system that provides the heating capability. Apart from a rotor which speeds up to the blade achieve the required linear speed and a moving stage which moves the abradable coating sample into the spinning blade, it also consists of an induction coil that wraps the disc and heats the blade up during the test as Figure 3.18 represents.

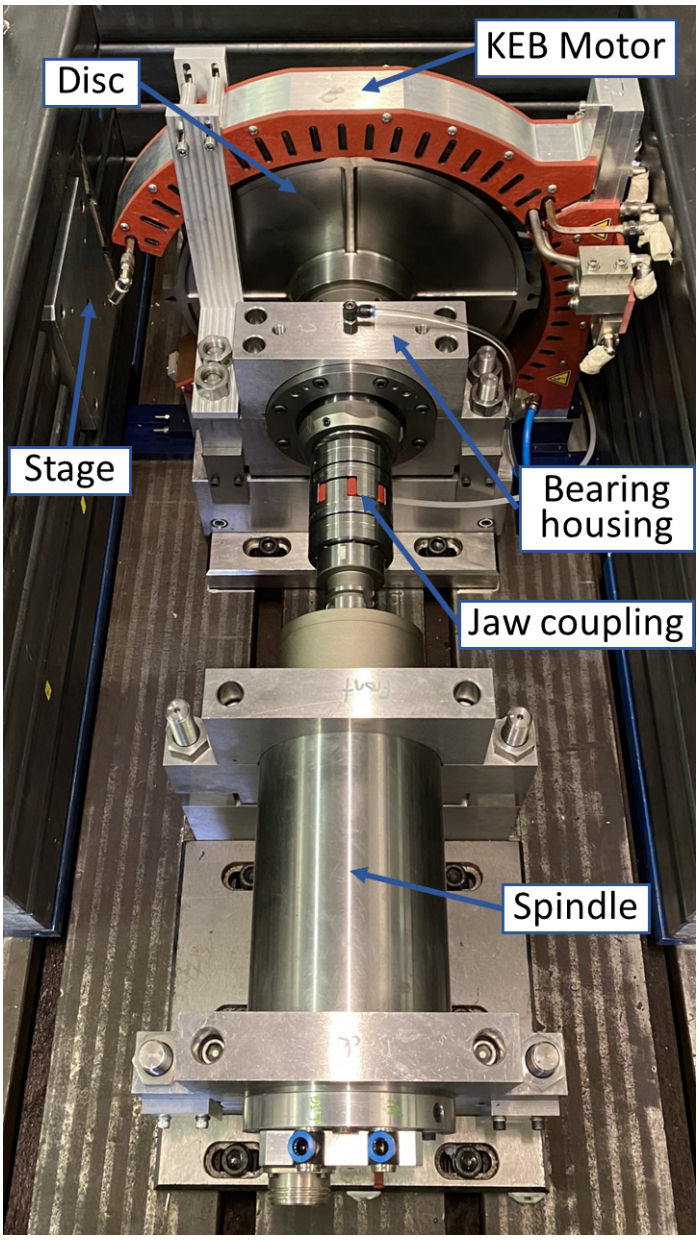

Figure 3.18: Spindle, Rotor, Stage and Induction Coil of the High Temperature Rig (without electrical or piping connections).

3.3.2.1 Rotor

The rotor comprises a disc where the blade samples are mounted, a drive shaft where the disc is assembled and rests onto two bearing arrangements, and a spindle which the shaft is coupled to.

The blade samples are mounted in a 405 mm diameter Ti64 disc which possesses four slots at 90°from each other for inserting the blade clamp. However, only two at opposite directions are used at a time, one for the test blade and the other for

the dummy blade to balance the disc. The disc is assembled in a 476 mm long shaft between two bearing arrangements. The disc is fixed by using a disc shoulder in one side and a precision locknut (SKF KMT 18) on the other side.

Each bearing arrangement is composed of two high precision angular bearings (ICB H 7016 C.T.P4A.UL) in a back-to-back arrangement and two non-contact labyrinth seals (GMN CF 6016 S10). Each bearing arrangement rests against a shaft shoulder and are preloaded with 100 N by using a precision locknut (SKF KMT 15) on the outer side. The bearings are lubricated with an air-oil mixture fed by a lubrication system (Bijur HyperFormance). The excess oil from the bearings is sucked out with compressed air using the venturi effect. Each arrangement is hosted in a bearing housing block assembly and laterally secured by clamping rings that are fixed to the blocks and maintain the seal concentricity. The block assemblies are fixed to the strong floor to ensure the lateral alignment of both bearing arrangement.

The disc and shaft are rotated by a spindle motor (GMN HSP 150G – 18000/9) which is capable of delivering a nominal power of 9 kW at a maximum rotating speed of 18000 rpm. However, due to the windage generated by the current disc, the maximum rotating speed achievable is 12000 rpm. The spindle is fixed to the ground floor, as the rest of the rig, and connected to the shaft though a flexible coupling (KTR Rotex GS 19) which increases the permissible tolerances and absorbs any potential misalignment during operation. The spindle is refrigerated by a 4.5 kW water chiller (Hyfra Chilly 45) and controlled by a power inverter (ABB ACS355-03E-38A0-4). A brake resistor (ABB CBT-H 560 GHT 281 18R) is connected to the inverter to discharge and slow down the spindle quickly in an emergency.

3.3.2.2 Stage

The stage moves the abradable sample forward at the required incursion rate while the rotor is spinning. This system is composed of a servo motor, a right-angle gearbox, a planetary gearbox, a linear actuator and the platform which the sample is attached to (Figure 3.19).

The servo motor (KEB 24.SM-200-42B0) has a nominal torque and speed of 0.72 Nm and 4500 rpm, respectively. This is coupled to a right angle gearbox (Wittenstien LPK 070-M03-30-011) with a reduction ratio of 30:1. This gearbox, in turn, is connected to a planetary gearbox (Wittenstien LP 070S-MF2-50-1D1), whose reduction ratio is 50:1, which results in a total reduction ratio of 1500:1. The planetary gearbox is connected to a linear actuator (EDrive Eliminator HD304) through a flexible coupling (KTR Rotex GS 19). The linear actuator has a 10 mm pitch lead screw

which turns the circular motion from the servo motor into the linear displacement of the platform.

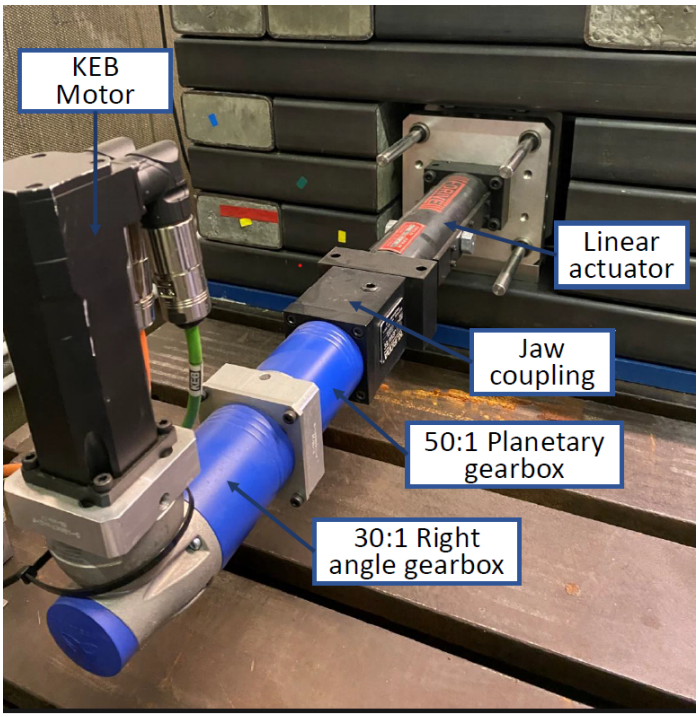

Figure 3.19: Components of the High Temperature Rig Stage

The stage is required to provide a minimum incursion rate of 0.02 μm/pass at 50 m/s and a maximum of 2 μm/pass at 250 m/s. These values imply stage incursion speeds from 0.778 to 389.13 μm/s and motor rotating speeds between 7 and 3502 rpm, which are in the range of operating motor speeds. In the event that higher incursion speeds are required in the future, the 50:1 planetary gearbox can be replaced with a replacement 10:1 planetary gearbox (Wittenstien LP 070S-MF1-10-1D1) which allows to increase the incursion speed up to 2500 μm/s.

3.3.2.3 Induction Coil

To heat the blades, a custom made induction coil is employed. The induction coil consists of a continuos S-shape bent copper tube inside a C-shape aluminium structure which surrounds the disc all around its circumference except for the part where the coating sample approaches the spinning blade. The coil is fed throughout a copper power bar which is connected to a heating station (UltraFlex HS-8), which, in turn, is connected to a control system (UltraFlex UPT-W15/150) capable of delivering 15 kW in the 50 kHz – 150 kHz frequency range.

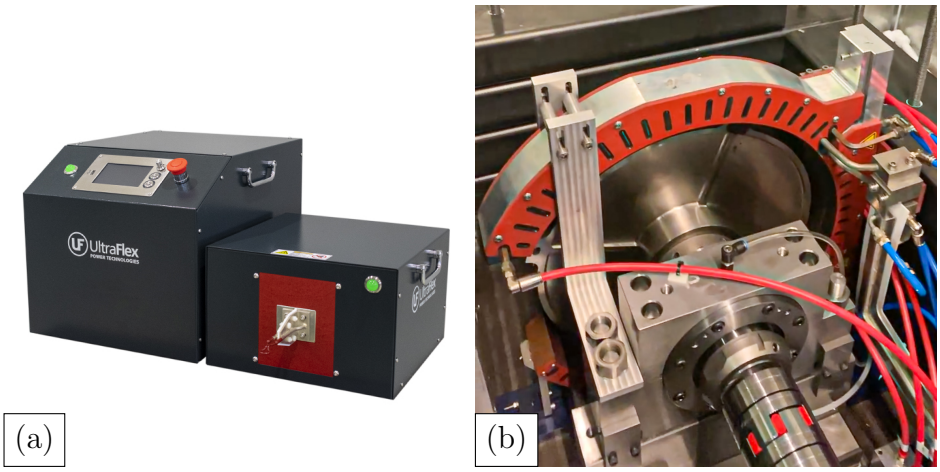

Figure 3.20: Induction Coil systems: (a) control system (left) and heating station (right), and (b) C-shape coil.

The three systems that make up the induction coil are cooled by a circulating pump (Grundfos CMBE 3-93) that provides distilled water from a 180 l tank through three different lines in parallel as shown in the diagram represented in Figure 3.21. The systems are fed with a rate over 6 lpm at a pressure between 3 and 6 bar. The tank is simultaneously connected to an industrial chiller (HYFRA Alpha 16-W) that keeps the water inside the tank at 15 °C.

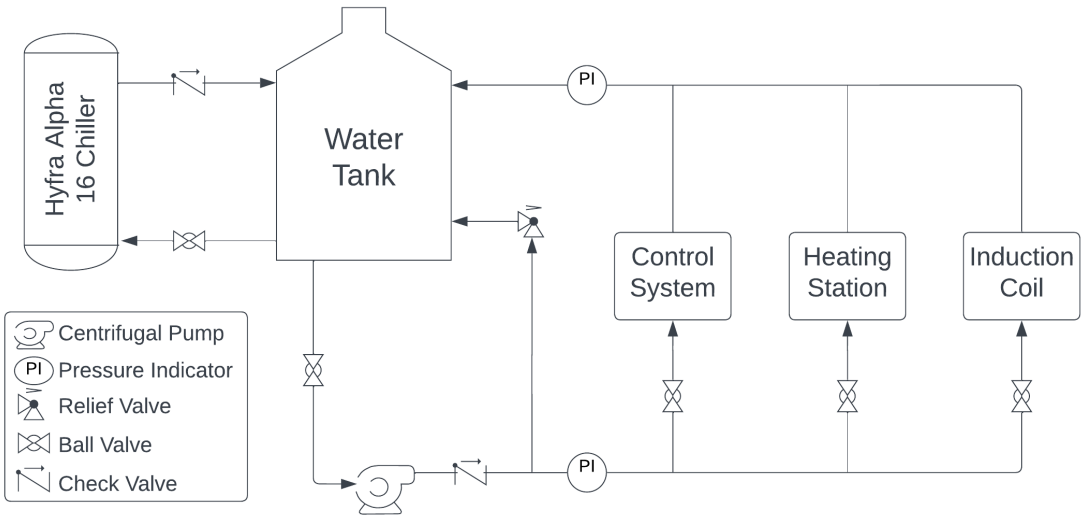

Figure 3.21: Water cooling of the High Temperature Rig

As the tube inside the induction coil is bent in a S-shape, there are optimum angular positions where the heating capability is maximized but others where the

electromagnetic field generated by the coil cancels itself. For this reason, the blades are pre-heated up statically at one of these optimum positions before the disc is sped up. The temperature achieved on the tip of the blade according to the pre-heating time is represented in Figure 3.22.

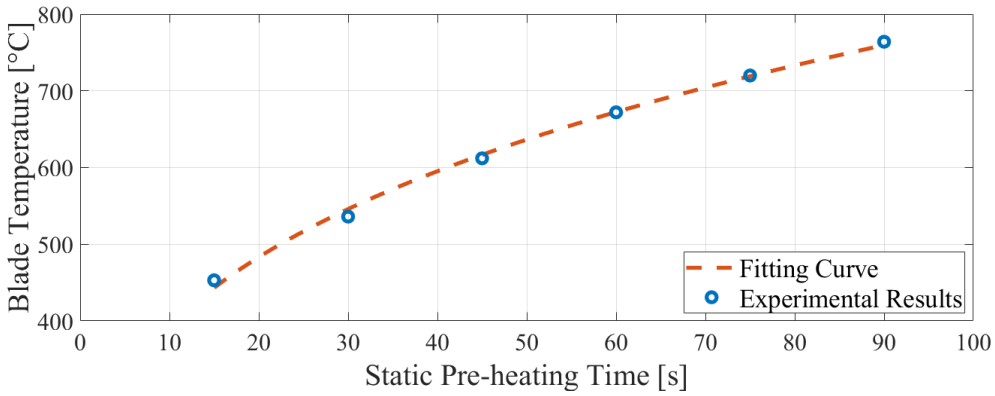

Figure 3.22: Temperature reached by the blade during the static pre-heating at an optimum angular position

3.3.2.4 Containment

The containment consists of a series of hollow steel bars filled with concrete that are piled above each other and cover all except for the spindle side. Each side is fixed to a steel plate on the bottom through threaded rods and the ends of adjacent sides are linked together. On one of the sides, there is a window where the stage is fixed as can be seen in Figure 3.23. On the side of the spindle, there are two aluminium plates with a thick piece of wood in-between instead. These are made with a shape whereby the spindle can stick out from the containment, with there also being enough space for the induction coil power bar to either. On the top, there is a lid made of four bars that rest on a movable platform, which uncovers an aperture underneath for sample change over.

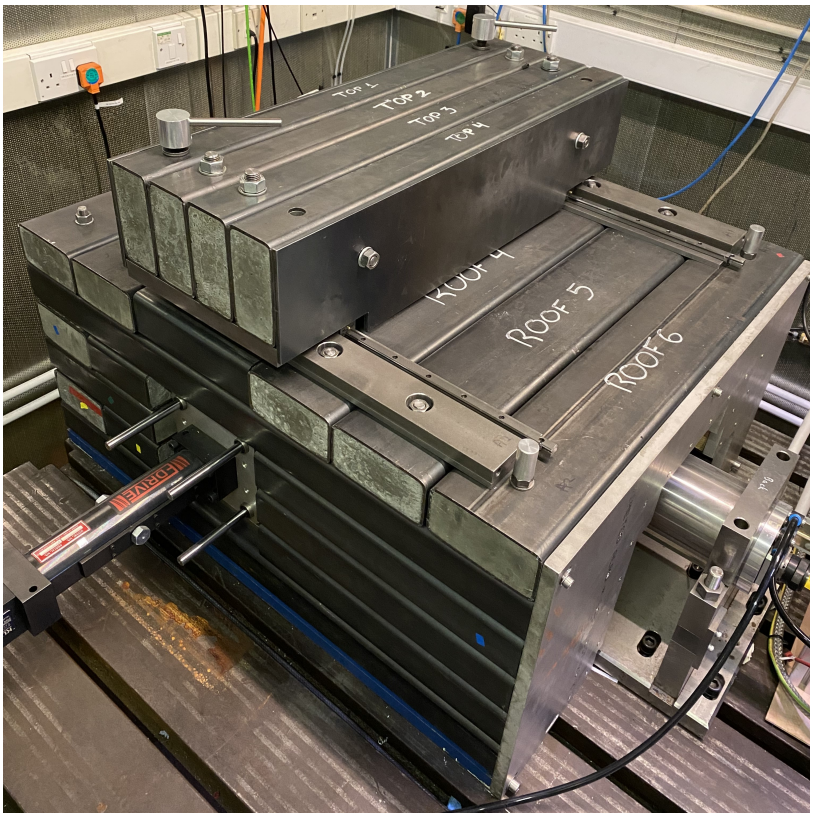

Figure 3.23: Containment of the High Temperature Rig Stage

3.3.2.5 Instrumentation

Dynamometer The same dynamometer as that one used in the Low Speed Rig (Section 3.3.1.4) is employed between the stage and the coating samples to measure the contact forces (Figure 3.24) and force data is equally post-processed.

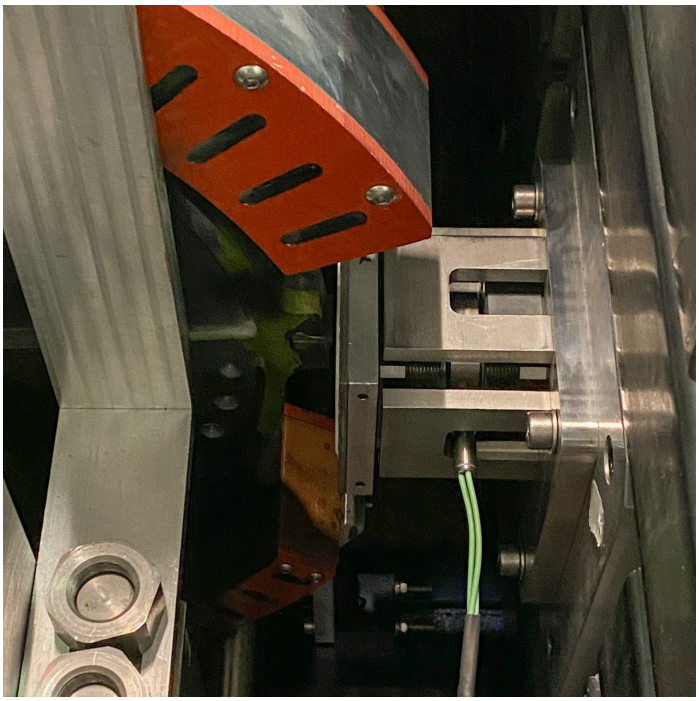

Figure 3.24: Dynamometer used on the High Temperature Rig for measuring contact forces

Pyrometer To measure the blade temperature during the tests, a high frequency pyrometer (Impac IGA 740-LO, Figure 3.25) with a temperature range from 400 °C to 1300 °C is placed perpendicular to disc at 78 mm and record a spot size of 0.3 mm on the side of the blade, approximately 0.5 mm down from the blade tip, when it passes in front of it. Equation 3.10 defines the time window the pyrometer sees the blade, where t_{blade} is the blade thickness, d_{blade} the diameter of the disc at the blade height and ν the disc frequency in Hz. Considering the High Temperature Rig geometry, the pyrometer sees the blade for 19 μs, when the disc spins at 4715 rpm and therefore, the blade linear speed is 100 m/s. The device response time, 6 μs, which is lower than this viewing window and, therefore, the pyrometer can respond to the rapid radiance variation from when it does not see to blade to when it does as shown in Figure 3.26b



Figure 3.25: High frequency pyrometer used on the High Temperature Rig for measuring the blade temperature

$$\text{Pyrometer viewing window} = \frac{t_{blade}}{d_{blade}\,\pi\,\nu} \tag{3.10}$$

The pyrometer captures the radiation emitted by the blade and processes it into temperature according to the emissivity introduced as an input by a control setting. The temperature is then linearly converted into voltage, read by the same digital oscilloscope (PicoScope Series 5000) that is used with the dynamometer. The analogue signal is turned into digital data points at 10 MHz which are stored in the oscilloscope buffer for access by the computer at a slower rate, which converts the points back into temperature and saved them in a .tdsm file which is later processed in Matlab as shown in 3.26. The side of every blade upon which the pyrometer is focused is painted with the thermal paint (LabIR HERP-HT-MWIR-BK-11), whose emissivity is known and roughly constant in the pyrometer measurement range (239).

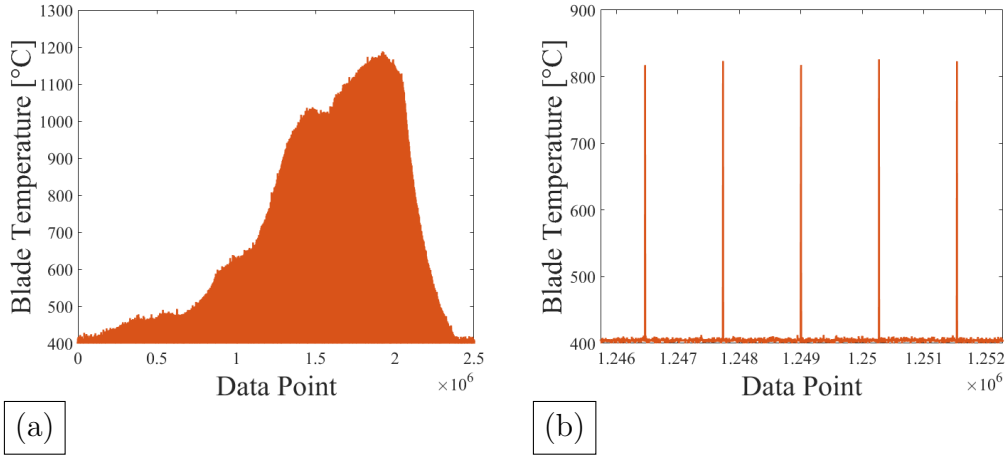

Figure 3.26: Temperature data capture by the high frequency pyrometer from the blade in the HTR and plotted in Matlab: (a) raw data and (b) detailed view of peaks.

Although the measured temperature is not at the blade contact surface where the maximum temperature can be found as a result of the friction generated during the rub, the measurement at the side of the blade provides a very reliable overall blade tip temperature. This measurement enables the determination of whether the blade experiences overheating due to poor cutting performance (Figure 3.27) as well as more generally to compare the blade performance between tests.

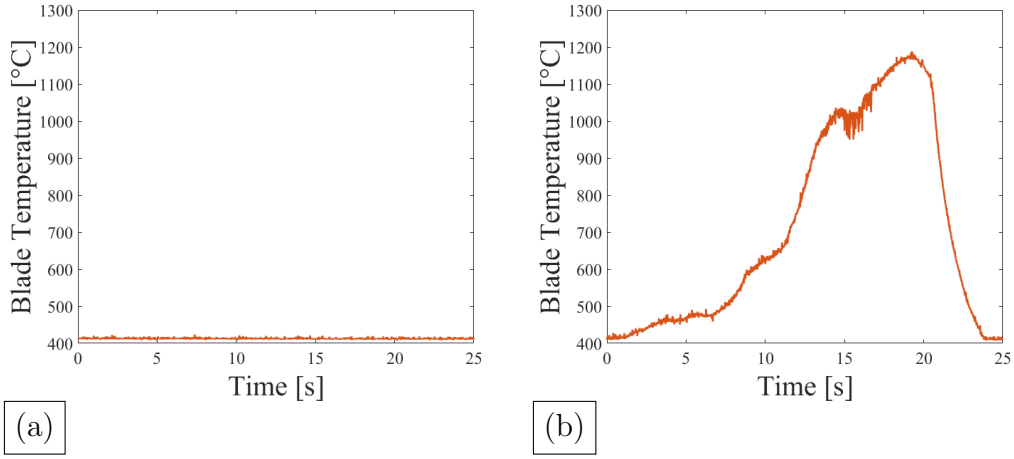

Figure 3.27: Example of the temperature measured on the blade from (a) a good and (b) a poor cutting performance where the blade experience overheating.

As noted the pyrometer is limited to measuring temperatures over 400 °C, and

more generally measuring temperatures under the pyrometer minimum threshold is not insightful for this piece of work and it is preferable to focus on the high temperature range. According to early exploratory tests done in the High Temperature Rig, a good MAS abradable cut with abrasive tipped blades for a given test conditions generates low temperatures (< 400 °C, Figure 3.27a) as well as low forces (< 600 N) with a clean track on the abradable surface. However, when a blade starts failing, the wear mechanisms and both forces (Figure 3.9c) and temperatures (Figure 3.27b) escalate exponentially, and, if that is the case, the pyrometer is able to measure this range of temperature when the blade is underperforming. Blade performance will be broken down in more detail in the next chapters.

3.4 Material Characterization

3.4.1 Optical 3D measuring system

An optical 3D measuring system (Bruker Alicona InfiniteFocusSL, Figure 3.28) is employed with MeasuringSuite software to characterize the abrasive coating on the blade both before and after testing. Tracking the changes occurred during a test enables the assessment of the damage produced when rubbing the abradable sample. How this damage is quantified is later broken down in Chapter 4.



Figure 3.28: Bruker Alicona InfiniteFocusSL system.

The output files obtained are a cloud of points in .txt format that defines the surface extracted from the abrasive coating and its top-view picture as the one shown in Section 3.2.1 (Figure 3.2, 3.3 and 3.4) with a 12000x1800 resolution. The number of points that define the mesh of 20x2 mm blade tip section are in the order of magnitude of dozen million points. The .txt file is later inputted in Matlab where the surface is plotted and subsequently processed.

The optical system is used with a 5x AX length optical objective which provides a vertical resolution up to 400 nm. The parameters set in the software for analysing the blades are a brightness on the lens of 6.00 ms with a contrast of 0.70, a vertical resolution of 600 nm and a lateral resolution of 20 um.

3.4.2 SEM-EDS measurements

Scanning Electron Microscopy (SEM) and Energy Dispersive Spectroscopy (EDS) images of the tested blades were acquired by using JSM-IT300 InTouchScope microscope and Oxford Instrument Xplore AZtec detector, for the SEM and EDS imaging respectively. These analyses facilitate the examination of the wear mechanisms on the blade abrasive coatings. A x50 magnification has been used for the observation of the coating top view in both SEM and EDS techniques. In addition to the x50 magnification, a x250 magnification has been used in the SEM microscope to examinate the blade cross-section.

.

Chapter 4

Analytical tool for quantifying the damage on electroplated tipped blades

4.1 Introduction

This chapter introduces a new analytical procedure developed in Matlab for assessing electroplated tipped blades employed in the abradable tests performed at the University of Sheffield. The two features that are sought to be quantified through this technique are the blades remaining cutting capability as well as the blade wear prior to failure. The performance of abrasive blades is to some degree probabilistic as they are a composite material and need more than one test repetition at specific test conditions to be characterized. Therefore, the high volume of tests required has motivated the development of an automated tool that is fast and easy to operate.

Previous work done around abrasive tipped blades have used the same analysis techniques that have been employed for assessing the cutting performance of bare blades. These techniques are mainly based either on the overall weight or volume difference when tested, or the length/depth of the groove on the abradable sample as well as its visual appearance (240; 23; 14; 44).

Using the overall weight or volume difference as an indicator for the performance of bare blades is appropriate as the material is homogeneous and their behaviour can be simplified as a binary phenomenon. In this case, when bare blades gain weight/volume is due to the material adhesion from the abradable (generally metal based) to the blade tip. On the other hand, a reduction in its weight/volume occurs as a result of a rough contact where the blade tip reaches its melting point and starts to wear down. These parameters can also be directly correlated with the blade height

variation (236). However, when it comes to abrasive tipped blades, the behaviour is no longer binary and provides very little information about its performance. Multiple phenomena that introduce either an increasing or a decreasing weight/volume variation may simultaneously take place on the blade during a test. Whereas only the material adhesion mechanisms can add weight/volume from the abradable sample to the blade; grain fracture, grain pull-out, matrix smearing or partial matrix detachment are some of the most frequent mechanisms that remove material from the abrasive coating (240; 23; 14; 44). Hence, there is a need for finding new ways to assess the wear of abrasive tipped blades.

Likewise, the length or the depth of the groove generated on the abradable sample has been employed as another indicator when compared to other tests at different conditions (blade speed and/or incursion rate) or with its nominal value (23; 40). Again, this measured parameter is appropriate with bare blades as they are expected (to some extent) to wear down in the course of the test (229; 236; 237). Considering the typical size of the c-BN abrasive grits (60/80 US mesh) employed in blade abrasive tipping in the engine (45), the depth variation on the abradable track produced by the fracture of the grits are in the order of tens of microns and such subtle variation are disguised by the the dynamic response of a test rig which may vary at different test conditions, making such variations hardly measurable. In addition, testing on different rigs affects the length of the track as they are subject to their own dynamics (237). Indeed with this approach, it would only have been clearly discernible once the blade had started failing and its cutting capability is minimal (23).

Another technique that has been used to assess the performance of abrasive tipped blades against ceramic abradables is the visual inspection of the groove on the abradable sample. When the abrasive coating has lost all of its cutting capability, generally due to a loss of all of its grits or macrofracture to the bond level, the metal based matrix start smearing the abradable sample, leaving some material on it as a result of the matrix softening due to the increasing temperature from the rub. This phenomenon may occur only at some local areas or intermittently with the effective cut of the abradable when the grits have not been completely removed (23). This technique only provides information about whether the blade has, partially or completely, failed or not, and does not provide any information about the blade status or what led to its failure or when it occurred. Furthermore, more generally this approach fails to consider the blade itself when assessing its performance.

As there is no a standard approach for assessing abrasive tipped blades, the closest analogies that might be applied are the methodologies employed in grinding wheels.

Wear in conventional grinding wheels, manufactured by a cold-press method, is evaluated as the ratio between the volume of the removed workpiece material and either the wheel volume loss or the reduction of the wheel radial length (193; 197). These types of grinding wheel suffer from dressing in which both grits and matrix get removed to unveil new grits underneath and, therefore, make the volume ratio approach suitable for the application. When it comes to superabrasive electroplated grinding wheels, which consist of a single layer of protruding abrasive grains, grain count and power monitoring techniques are employed instead (193).

The work done around developing and testing blades and abrasive coatings in the University of Cambridge has employed a similar approach (40) to the one applied for electroplated monolayers in grinding wheels (193; 187; 197). This approach consists of manually quantifying the amount of microfracture, macrofracture and grit pull-out on the abrasive coating for their correlation with blade performance. However, this methodology is limited to small sampling areas as well as to the repetitiveness of the tests due to the lack of computer-aided tools in order to quantify the features. This procedure becomes very inefficient when large test batches must be considered.

Given the gap in research with regards to the analysis of abrasive tipped blades employed in abradable tests, this chapter introduces a new Matlab-based analytical procedure for evaluating electroplated tipped blades correlated with their performance. The procedure aims to quantify two key features: the remaining cutting capability of the blades and the blade wear prior to failure. Techniques used for bare blades are inadequate for abrasive tipped blades due to their complex behaviour and the presence of multiple phenomena. Manual techniques, such as visual inspection and quantification of fractures and pull-outs, have limitations in terms of sampling areas and efficiency for large test batches. In addition, due to the probabilistic nature of the performance of abrasive blades, multiple test repetitions under specific conditions are necessary for characterization. The need for a high volume of tests has driven the development of a computer-aided tool, with the aim of overcoming the aforementioned limitations.

The proposed process consist in extracting the surface morphology from the abrasive coating of the blade prior of after being tested with an optical 3D metrology scanner. The extracted is then discretised into a cloud of points that can be loaded into a numeric computing platform for its normalisation and later post-processing. The post-processing allow creating measurable parameters that can be decoupled from the measured area, making them directly comparable to other area sizes or blades.

These measurable parameters facilitate the comparison of the wear that blades suffer at different test conditions.

4.2 Data capture

The phases in which the proposed process is divided are presented as: data extraction, normalization of the extracted data, and post processing of the data to construct measurable parameters. Every step is broken down in this section, complemented with examples in order to validate the tool.

4.2.1 Data extraction

The first step consists of the data extraction from any 3D measuring instrument that is able to analyse and export a surface as a 3D point cloud and a 2D high resolution image of the blade top view. In this research, the Bruker Alicona InfiniteFocusSL 3D measuring instrument is employed together with Alicona IF-MeasureSuite software for the extraction of the blade data. Information about the lens and the set of parameters inputted in the Alicona software can be found in Section 3.4.1.

4.2.1.1 3D Data

A blade is mounted in a custom made holder and placed in the device moving stand (Figure 4.1). Next, the volume the system gets the data from is manually defined. Properly defining the space is very important, and in particular the vertical coordinate, as any point out of that space will be omitted when processing the surface. Finally, a horizontal and vertical resolution of 20 μm and 500 nm respectively, is set. The horizontal resolution being an order of magnitude lower than the grits nominal size.

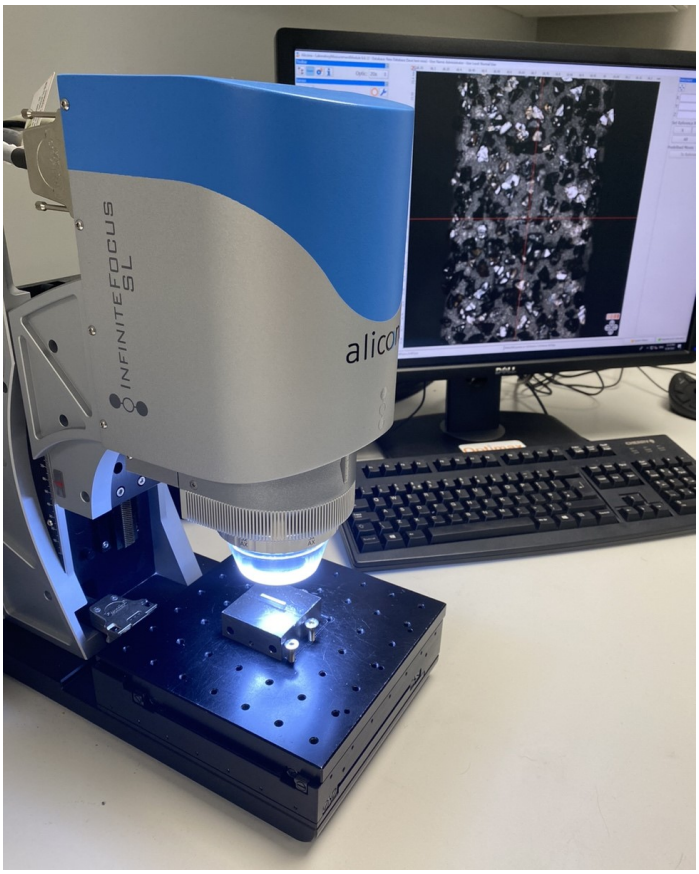

Figure 4.1: Blade set up in the Bruker Alicona InfiniteFocus SL machine.

Once the surface is captured, processed and represented in the software, it is exported as a point cloud in a .txt file where different mesh refinements can be selected. A preliminary analysis has been carried out with this analytical tool in order to study the convergence of the mesh refinement where results highlighted that the second most refined mesh in this software provides enough accuracy (Appendix A.1). This mesh refinement creates around 50 million data points evenly horizontally spaced, for the blade coating surface area which is around 40 mm^2. Each point is defined by the three Cartesian coordinates (x, y and z)

The point cloud saved in the .txt file is exported to Matlab where the unique values of the two horizontal coordinates, x and y, are identified and saved in order inside a $1 \times n_x$ matrix and a $n_y \times 1$ matrix, respectively. Then, for the case of the matrix containing the x values, the initial row is copied on every row until the n_y row. The same process is similarly performed on the y matrix up until the n_x column, resulting in two $n_y \times n_x$ matrices, one with the x coordinate values and the other with the y coordinate values. A third $n_y \times n_x$ matrix is created for the vertical z coordinate, so the x,y and z coordinates for a given data point have the same indexes at each of

the coordinate matrix. The z coordinate of a point that is out of the blade surface is defined as NaN. An example of a raw surface exported as a point cloud and plotted in Matlab with the *surf* function is shown in Figure 4.2.

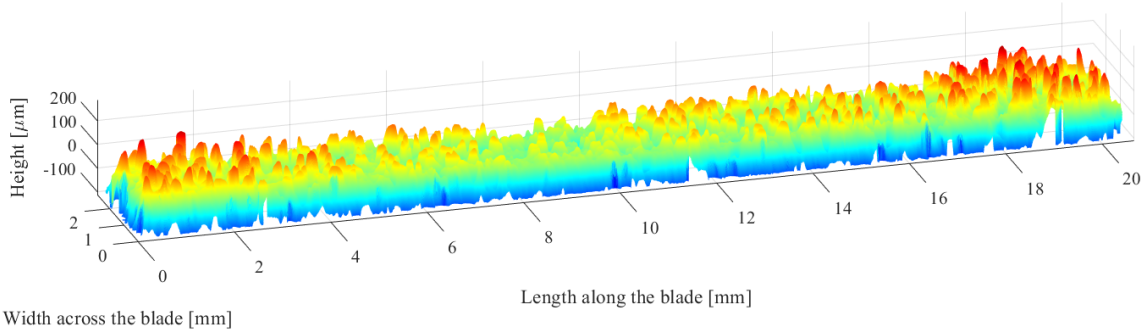

Figure 4.2: Point cloud of the blade surface exported from Alicona software (IF-MeasureSuite) into Matlab.

4.2.1.2 Image

From the same analysis, a 2D image with a very high resolution (11675x1876 pixels) is exported. This image is plotted together with the point cloud during the data processing, helping to identify blade features more clearly. The 2D image is also used for the image processing of the material pick-up which is introduced later. An example of an exported blade 2D image is shown in Figure 4.3

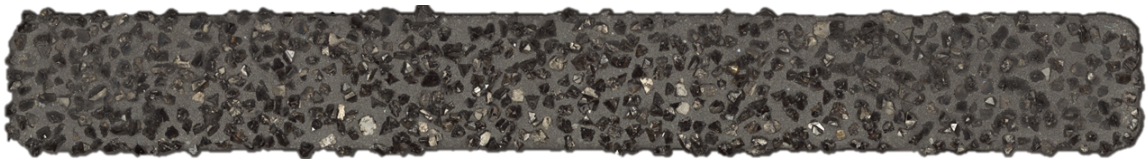

Figure 4.3: 2D image exported from Alicona software (MeasureSuiteSL).

4.2.2 Normalisation of blade orientation

A mounting system is used to place the blades in the same position and minimise the post-processing adjustments needed. However, the point cloud does not reference the same point due to internal software processing when exporting the data. As such, a series of boundary detection and rotation processes are necessary to reference the blades and create a common reference system on the blade centre for their subsequent processing. In addition, slight misplacements on the Alicona system platform make a considerable impact on the later blade processing, and need to be corrected for at the

outset. The orientation processes considered for the blade normalization are rotation, centring, and tilting.

4.2.2.1 Rotation

The blade rotation consists of positioning the extracted surface in such a way that the top and bottom edges, when viewed from above, become parallel to the horizontal axis, and the left and right edges become parallel to the vertical axis. In order to do this, the tool identifies the first and last non NaN values of each column, which correspond to the top and bottom edges respectively. These values are saved in two independent vectors for each edge. A trendline is generated for each vector as shown in Figure 4.4 and the angle with the horizontal line is calculated. The first and last 5 % of elements of each vector are omitted to avoid the interference of the side edges on the trendline generation. Although the difference between the angles of both edges, due to the coating edge irregularities, is reasonably negligible, their values are averaged and the z coordinate is rotated with the *imrotate* command, and as many rows and columns as needed are added to accommodate the rotation.

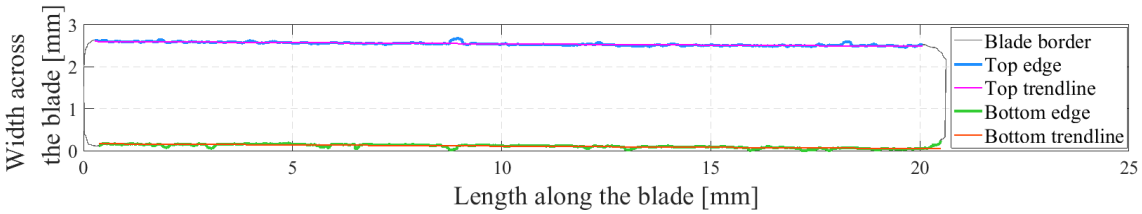

Figure 4.4: Blade edges detection and trendlines employed for finding out the offset rotation.

4.2.2.2 Centering

To find the centre of the blade once rotated, the edges of the blade are identified following the same approach used for the rotation correction. For the top and bottom edges the first and last non NaN values are identified for each column and stored in independent vectors. For the left and right edges, the first and last non NaN values are identified for each row and stored in vectors. The values in each vector are averaged and the centre of the blade is defined as the midpoint between the averaged values for each coordinate.

4.2.2.3 Tilt

Generally, due to blade or base misalignments during the analysis on the Alicona system, the abrasive coating is not completely horizontal for the surface extraction. This ends up with the blade tilted around either or both x and y axes. Two corrections are made to compensate for tilting, one to compensate for the gradient caused by the misalignment along the blade (x coordinate) and another to compensate for the gradient across the blade (y coordinate).

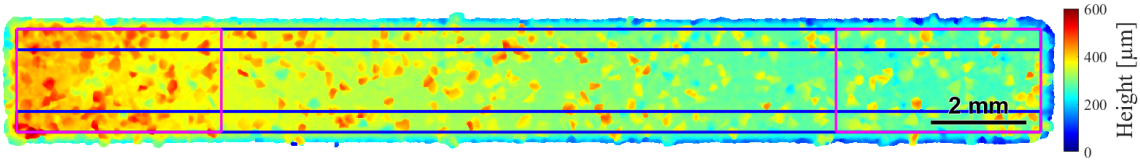

Figure 4.5: Results of the sensitivity analysis of the length of the areas for the blade tilting.

To correct the tilt along the blade, a gradient is determined along each of the two horizontal coordinate axes. Each gradient is defined by the difference between the averaged height of the points contained in two different areas situated at both ends of the corresponding axis over the distance between the centres of the areas. These areas are shown in Figure 4.5 where the magenta boxes are employed to determine the gradient along the x axis, and the blue ones define the gradient along the y axis. A sensitivity analysis has been conducted to determine the length of these areas for each axis (Figure 4.6). The study states that the obtained tilt angle is considerably insensitive to the dimension of the area for the x coordinate (length along the blade) compared to the dependency with the length of the areas for the y coordinate (width across the blade) which converges at 20% of the blade dimension for that axis. Considering the results of this analysis, the length of the areas for each coordinate axis are defined as 30% of the blade dimension for that axis. Finally, the areas start away from the edges to avoid sampling distortion due to the round edges.

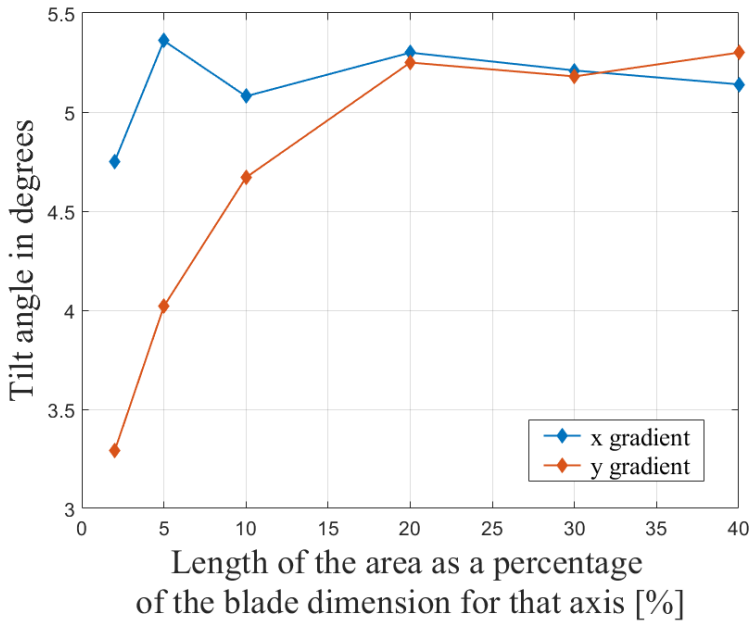

Figure 4.6: Areas employed to calculate the gradient of the offset tilting in both x (magenta boxes) and y (blue boxes) axes.

The calculated gradient for the x (or y) coordinate multiplied by the x (or y) coordinate is then subtracted from the z coordinate to get the corrected z coordinate for each point to make the blade top surface parallel to the horizontal plane as seen in Figure 4.7. Once the tilt correction is applied to the blade, the area to be analysed, defined by the user, is sampled to continue with the post-processing.

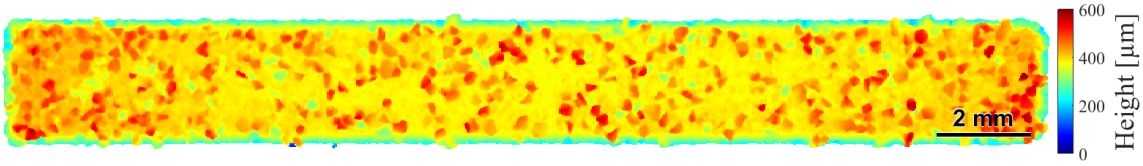

Figure 4.7: Blade after applying tilting corrections and sampled area to be analysed.

4.3 Analytical approach to blade tip classification

In this section, two different approaches are proposed in order to assess both the cutting capability as well as the wear produced on the abrasive coating during a test. The first approach is based on the quantification of the volume, as in traditional grinding wheels, of the abrasive coating in reference to an established reference plane. The second approach follows a procedure whereby different features such as grits and

craters are recognised from the coating by using the coordinates of the extracted points. These two methodologies are affected to some extent by the abradable material picked up by the blade that occurs at some test conditions and is also evaluated in this chapter.

4.3.1 Establishment of the matrix plane

Firstly, defining the matrix of the abrasive coating is essential for running both approaches. The matrix is defined by its surface roughness parameters. Although any surface roughness parameter can be calculated with the available data, only the arithmetic mean of surface height (Ra) which defines the mean plane, the average maximum peak height above the mean plane (Rp) and the average maximum valley depth below the mean plane (Rv) are required for the later identification of grits and voids on the coating.

These parameters are calculated by using the points contained within a set of squared areas that are selected from the matrix by the user as seen in Figure 4.8. The projection of these areas over the coating surface must only contain points from the matrix, and not contain grits. The mean of all the points contained on the areas define the Ra. A percentage of the maximum height values of each area is used for calculating the Rp, Likewise, the same percentage, but taking the minimum values are used for the Rv. Once Ra has been calculated, the z coordinate of each point is normalized as $z' = z - Ra$ in order to set the average height level (Ra) of the matrix in the sampled area as the zero of the vertical coordinate as seen in Figure 4.9.

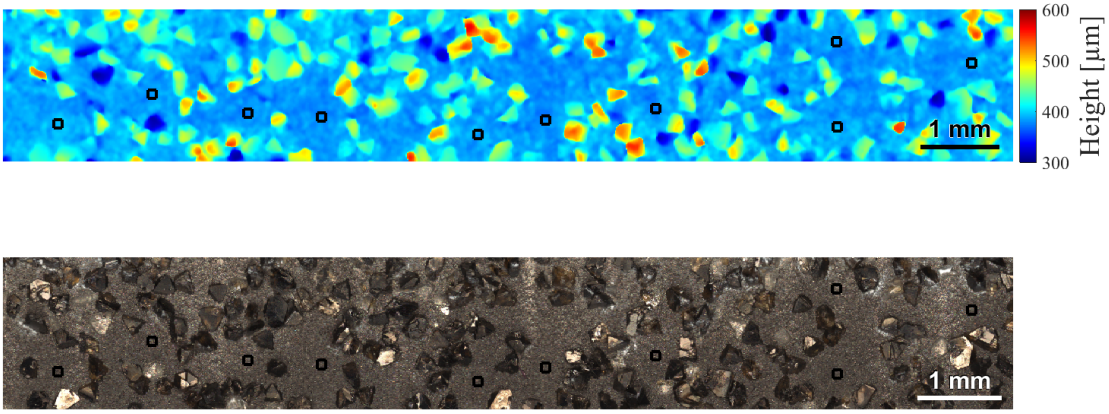

Figure 4.8: Sampled area and selected points to calculate the surface roughness parameters of the matrix

The size of the aforementioned squared areas has been established at 0.1×0.1 mm which is defined by the maximum space available for setting squared areas between grits when analysing TBT 429 electroplated tipped blades with the highest grit density. A square area of 0.1 mm on each side provides around 700 data points. A preliminary convergence study of the Ra, Rv and Rp surface roughness parameters has been carried out to determine the number of areas employed (Appendix A.2). This analysis has reported that more than 10 picked areas for the entire blade surface does not provide any substantial variation on the three surface roughness parameters introduced above.

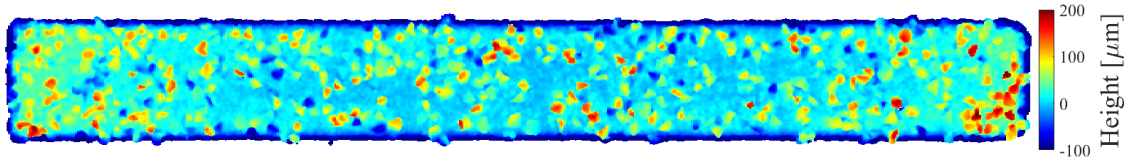

Figure 4.9: Blade surface after being zeroed at the matrix level.

4.3.2 Volume evaluation

Before going into defining the methodology for the volume calculation, a statistical analysis can be done from the raw coordinates of the points which is directly correlated to the volume as it is later introduced. The cutting capability of a blade can be related to the percentage of points whose height is above the matrix level. A higher percentage of points indicates a higher cutting capability of a blade as there are more grits sticking out of the matrix. As the matrix level has been set to zero and the roughness of the matrix is known, positive values over Rp denote the existence of protruding grits as observed in Figure 4.10. On the other hand, negative values below Rv indicate the presence of voids, which are normally generated during the test.

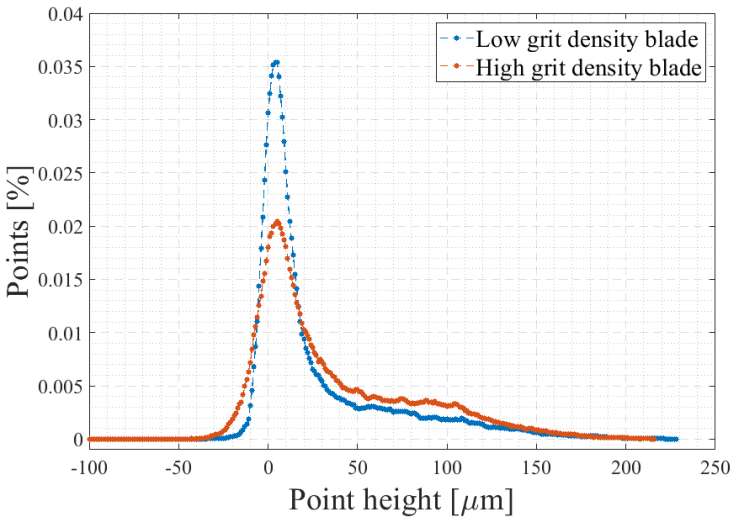

Figure 4.10: Normal distribution of the points height for a high and a low grit density untested blade.

For tested blades, the percentage distribution of point heights is associated with the remaining cutting capability of a blade. An untested blade may present points whose height is large as it comes from protruding grits and would be reduced when tested due to their wear or their failure if it occurs. Although the most protruding grits are the most likely to be worn out first, this effect will not exclusively happen to them. Therefore, points with larger heights always transition to smaller heights when tested as observed in Figure 4.11.

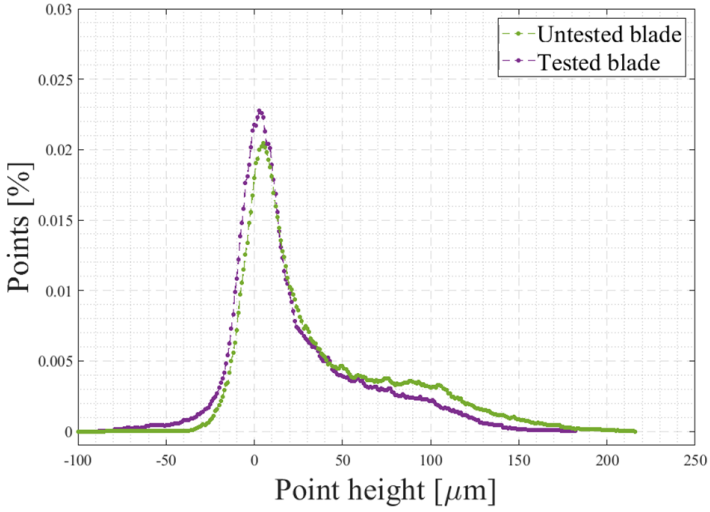

Figure 4.11: Normal distribution of the points height for an untested and a tested blade.

Likewise, there is a direct relationship between voids and the percentage of points whose height is negative and below Rv. As the appearance of voids occur when blades are tested, points with positive height coming from the presence of grits in untested blades transition to negative values when voids are generated during the test, increasing the percentage of negative heights as observed in Figure 4.11. In addition, a few voids may appear from the manufacturing process due to the weak anchoring of highly protruding grits, with this observed in some untested blades.

In addition, the macrofracture of grits at the bonding level can also be identified by analysing the measured height distribution of a blade prior and after being tested. This can be deducted when there is an increase in the percentage of points whose height is in the range between Rv and Rp. This means that technically, there is still a grit anchored to the matrix but its cutting capability is zero.

Although the distribution of the heights of the measured points allows the grit and void distribution on a blade to be understood, it is not comparable between blades as the number of points varies from one to another. As the points horizontal position is known, the volume enclosed between the surface and the already defined and zeroed matrix can be calculated for a given area by using the trapezoidal integration rule. As the point mesh is uniform and equidistant for each in-plane axis, the differential volume enclosed between the surface at that point and the matrix level can be calculated by multiplying the point height by the two horizontal constant distances, in both x and y axis, between points. The total volume is then calculated by adding the differential volumes all together. As introduced with the grit height distribution, only volumes where the points whose height is either positive or negative can be separately added to calculate the volume above or below the matrix level respectively. In this case, volumes, either positive, negative or total, are independent of the number of points for a given area.

As the horizontal distance between points is constant, the volume differentials follow exactly the same distribution as that of the point heights for a given blade and area. Whereas the volume above the matrix level describes the remaining cutting capability on a blade, the volume below the matrix level represents the voids generated when tested. Although, the total volume can only be directly compared between blades provided that the area is the same, this can also be normalized with the area.

Having a single normalized parameter instead of a distribution allows a batch of blades or the variation suffered by a single blade when tested to be easily compared. In addition, it also allows different areas of the same blades to be compared, which is of particular use in helpful for stepped tests.

4.3.3 Feature detection

The second approach for evaluating the cutting capability and wear produced on a blade as a product of being tested consists of directly counting active grits, voids and other features . Although this seems a simple and straightforward way to assess a blade, the challenge is to computerize the process of identifying them. Different techniques for the optical recognition of colours and shapes are employed for post-processing the test data acquired from the optical devices. However, the high reflectivity, different colours and angles of the multiple grit faces as well as the irregularity of shapes between grits, as shown in Figure 4.12 make this approach extremely challenging. Because of this, a dimensional procedure is developed in this research for grit feature recognition.



Figure 4.12: Portion of a blade showing the non-uniformity between grits in terms of colour and shapes.

The method for recognising the active grits consists of incrementally sweeping the positive range of height starting from the highest to finish at the matrix level. Before starting the sweep, two matrices with the same dimensions as the sampled surface matrix are created. The first matrix is a height boolean matrix, reset for each iteration, to store what points from the sampled surface matrix are above the height of the current level, *true* entries, and which are below it, *false* entries. In the second matrix, every point from each grit is saved in the same row and column as it is found in the sampled surface matrix and the value assigned corresponds to a unique ID given for that grit. The process starts with a sweep at the highest point of the sampled surface where only a single point is detected. In the next sweeps, the grits already detected in previous sweeps increase their cross-sectional area, with new grits also emerging (Figure 4.13). Before spotting the new grits, adjacent points to the ones corresponding to already detected grits and the adjacent points to these are inspected, counted as the same grit and saved with the same ID. When all the points that correspond to already existing grits have been checked for a given sweep, new grits are identified. The new grits identified are formed by a group of points where none of these is adjacent to the points that formed already counted grits. When the first of these points is identified, all the adjacent points are inspected and counted

as the same grit. This iterative procedure is carried out for every new grit detected during each sweep.

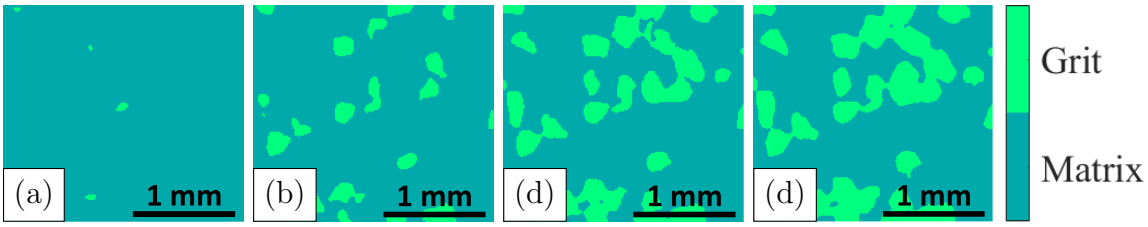

Figure 4.13: Example of the grit detection process for a 1.8×1.8 mm area at (a) 5%, (b) 35%, (c) 65%, and (d) 100% of the process.

The increment between sweeps is defined by the user. The sweep must be small enough to avoid that two grits that are touching each other are considered as a single grit, but large enough to not detected more than one separate cross-sectional area from the same grit. A sixth of the nominal minimum grit size (30 μm) has been proposed and previously tested as the sweep increment for the analysis of TBT 429 electroplated blades considered in this research. The sweeps are carried out until the matrix level is reached, more exactly, when the double of the Rp value of the matrix is reached. Anything below 2·Rp is not considered as an active grit as it is in the range of the matrix level. Finally, he number of active grits can be divided by the sampled area to obtain the grit density.

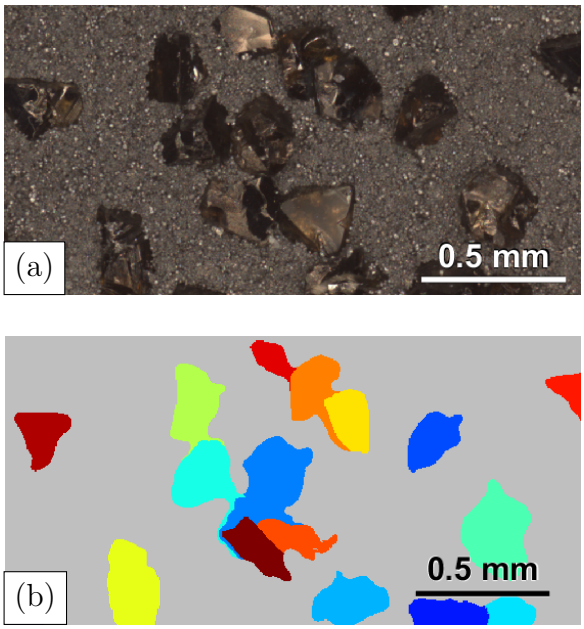

Figure 4.14: Example of grits active detected by the tool: (a) image of the grits on a TBT429 blade and (b) Matlab matrix of what is detected as active grits.

The main advantage of this approach is that the outcome provides the number of the grits which is an intelligible parameter. However, there is a difference between having a given number of grits that were just deposited and protruding significantly, as opposed to having the same number, but where the grits already suffered from dressing, and whose maximum height is closer to the matrix bonding level.

Likewise, the same procedure is employed for detecting voids, but sweeping the negative heights from the lowest point to the matrix level. In this case, the closing height is twice the value of Rv.

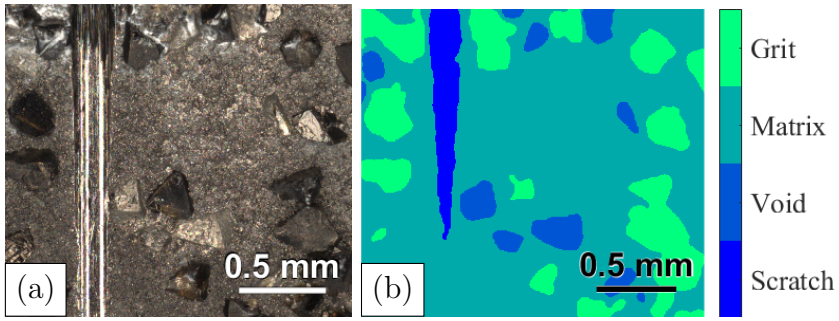

Figure 4.15: Example of the features detected by the tool: (a) image of region of a TBT429 blade and (b) Matlab matrix of the detected features.

When a blade starts to wear down during a test, it has been reported from preliminary work around the performance of electroplated blades that scratches may appear, especially in low grit density blades, in the matrix in the cutting direction as a result of the bare matrix rubbing against the ceramic (241). In the course of the void recognition process of tested blades, scratches are also recognised as voids and corresponding ID's are set to them by the nature of the methodology. After the void recognition is done, a filter is run over every void in which their aspect ratio is evaluated. If the aspect ratio is above a specific value, inputted by the user, the void is counted as a scratch instead. Considering that c-BN grit aspect ratios for TBT 429 blades usually range from 1 to 3, the minimum aspect ratio set in this research for the for recognition of a scratch is 5.

4.3.4 Material pick-up

As noted, tested abrasive tipped blades sometimes suffer from material pick up where material from the abradable sample becomes trapped between the abrasive grits of the blades. This phenomenon, when it occurs, may affect the measurements of the two proposed methodologies. Although it is not possible to isolate the adhered material to calculate its volume, an approach is introduced to estimate the degree of material adhesion a blade exhibits after being tested, and to provided contextual data when assessing the two outlined approaches.

The approach is based on the optical recognition of the bright white MAS material trapped on TBT 429 blades, which aside from this are mainly dominated by gray and dark colours, making the MAS material quite distinguishable. The sampled area is converted from RGB into greyscale by following the Equation 4.1, where I_{Gray} ranges from 0 to 1.

$$I_{Gray} = 0.2989 \cdot I_{RGB-Red} + 0.5870 \cdot I_{RGB-Green} + 0.1140 \cdot I_{RGB-Blue} \tag{4.1}$$

As seen in Figure 4.16, ny pixel whose greyscale intensity is above a threshold value is considered as MAS material pick-up as. The number of pixels above the threshold is then divided by the total number of pixels of the area to obtain the pick-up ratio. The threshold value is set with the aim of detecting the MAS material trapped but minimising the detection of those grits with a whiter colour due to light reflection. Although there is no a clear value that separates both features, as shown in Appendix A.3, at a value of 0.63 the trend transitions from a non-linear to linear rate, where it can be assumed that in the non-linear regions, greyer pixels from the matrix start to

be considered as material pick-up. As such, a value of 0.63 was adopted for this work. At this threshold, the apparent material pick-up ratio measured for untested blades, where there is of course none, is lower than 0.02, further validating the approach.

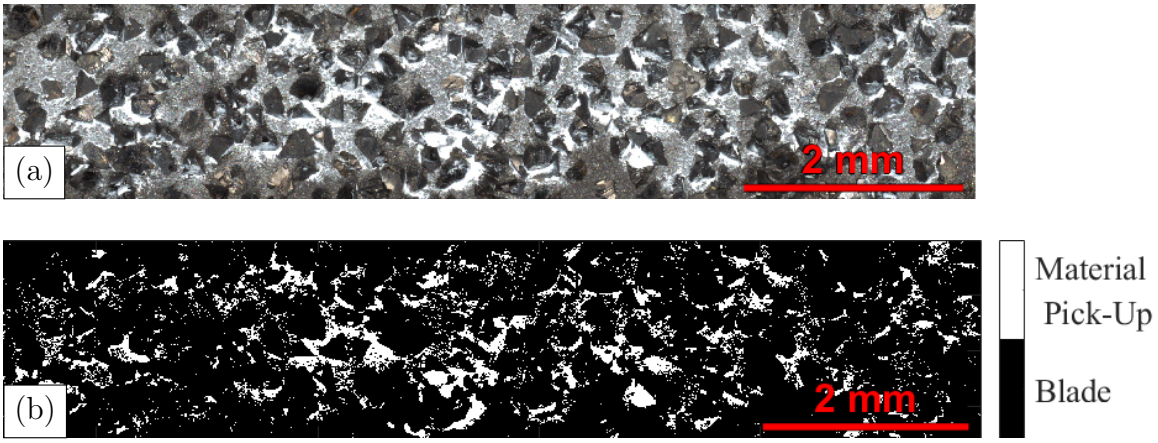

Figure 4.16: Example of material pick-up detected by the tool: (a) image of a TBT429 blade with MAS material adhered to it and (b) Matlab matrix of the detected material.

4.4 Results

For tool validation, a set of blades, both untested and some tested under identical conditions, has been used to correlate the evaluation parameters proposed in the previous section. To assess blade wear, the evaluation parameters are divided into two groups based on their method of determination: volume evaluation and feature detection. In the volume evaluation category, parameters include the volume per area both above and below the matrix level. In feature detection, parameters include grits, voids, and scratches. Although both groups aim to assess blade wear, the techniques used differ, as outlined in the previous section. Additionally, using different techniques enables cross-validation, as they should yield consistent results.

These parameters have been analysed for a set of six blades with different initial grit density (Figure 4.17a in blue) that were tested at the same test conditions of 200 m/s (linear speed), 0.3 μ/pass (incursion rate) and 500 μm (incursion depth) in the Low Speed Rig, with the data solely presented to explore the proposed method as opposed to directly explore the blade wear, as this will come in subsequent chapters. The surface of each blade abrasive coating is extracted as indicated in Section 4.2 and analysed as in Section 4.3 to obtain te required parameters.

When blades are tested, grits experience different types of wear (as seen in Section 2.4.1.2) that either shatter and reduce their size or get completely removed. As shown in Table 4.1, this results in a reduction of both its grit density and the volume above the matrix level. Likewise, the appearance of craters as a result of pull-outs during testing is reflected by the increase of the void density and volume below matrix level parameters.

Blade Status	Grit density [grit/mm^2]	Volume above matrix level [mm^3/mm^2]	Void density [void/mm^2]	Volume below matrix level [mm^3/mm^2]
Untested	15.28	$3.59{\cdot}10^{-2}$	0.05	$2.98{\cdot}10^{-4}$
Tested	9.31	$2.07{\cdot}10^{-2}$	2.55	$3.35{\cdot}10^{-3}$

Table 4.1: Example of the values provided by the two proposed methodologies for a blade analysed before and after being tested.

All tested blades suffered a reduction of both grits and volume above the matrix level as well as an increment of both voids and volume below the matrix level when tested (Table 4.1). Whereas the change in the grit density (Figure 4.17a) and volume above the matrix level (Figure 4.17b) parameters when tested follow very similar trend and show a dependency with the initial value, the relationship between void density and volume below the matrix level is more disparate.

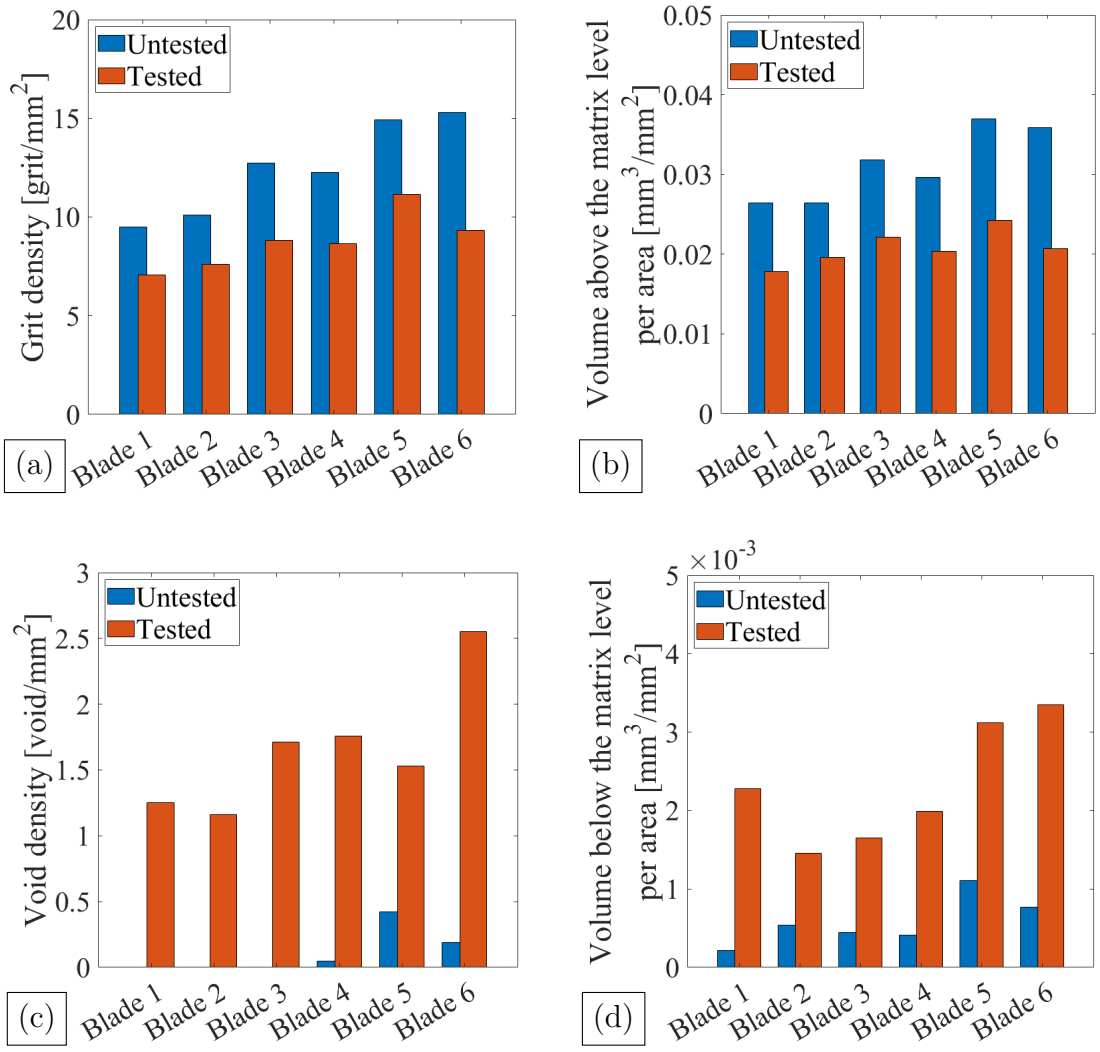

Figure 4.17: Comparison between the analytical parameters for a set of six blades with different initial grit density: (a) grit density, (b) volume above the matrix level, (c) void density and (d) volume below the matrix level.

Considering these results, it is of further interest to cross-plot the developed parameters to account for initial condition. When blades are engineered under the same manufacturing parameters, as shown in Figure 4.18 the initial grit density parameter has a direct relationship with the volume above the matrix level per area parameter. This indicates that the grits deposited during the manufacturing process exhibit an uniform protruding height regardless of the grit density. Finally, as shown in the figure, although some blades exhibit a lower grit density, the majority show a grit density that ranges between 13 and 16 grit/mm^2.

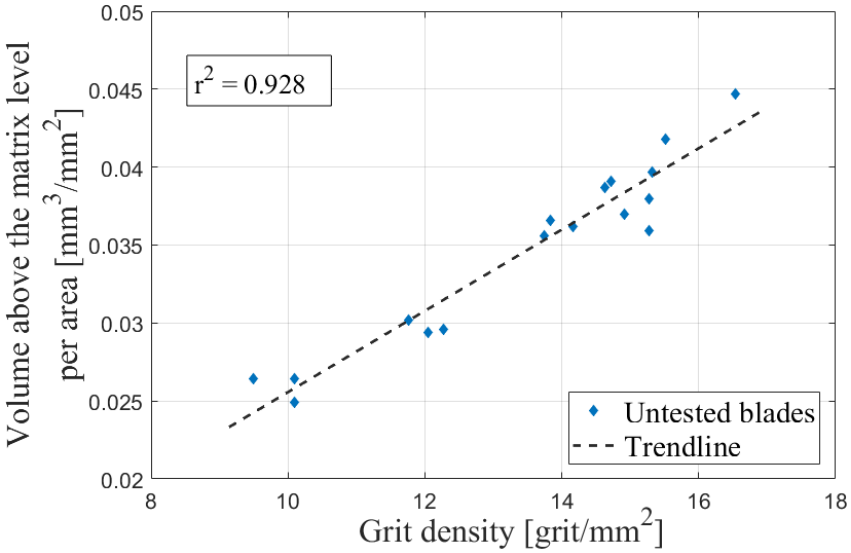

Figure 4.18: Relationship between the volume above the matrix level per area and grit density for untested blades.

The grit density and volume above the matrix level parameters after post-testing can also be correlated and compared to the untested relationship in order to understand how the different wear mechanisms affect this correlation. The data has been investigated in this way as opposed to for example by simply normalising in based on the pre-test grit density, in order to consider the conceptual difference between these two parameters. Whereas the grit density parameter only considers macrofracture and pull out of active grits, the volume above the matrix level per area, apart from accounting for these, also considers localised damage caused by microfracture and attrituous wear mechanisms. The correlations of these two parameters for the blades introduced in Figure 4.17 prior, and after to testing is for the difference between them are shown in Figure 4.19. The fact that the trendline for the untested and tested cases have similar gradients but are offset from one another agrees with the fact that grit microfracture, macrofracture, attritious wear and pull-out occur simultaneously. If only microfracture and attritious wear occurred, blades would maintain the grit density as the number of grits would not vary, but the volume would decrease, with points displaced vertically in the graph. On the other hand, if grit macrofracture (at the bond level) or pull-out mechanisms only occurred the tested and untested trendlines would coincide and the points would diagonally displace to the left along the coinciding trendlines. As such, plotting the data in this way allows both damage mechanisms to be captured. It is also of note that the percentage of volume removed follows the same trend, i.e. it is almost invariant when plotted against the initial grit

density and is approximately one third of the initial volume for a fixed set of testing parameters. At the same time, both tested and different trendlines may differ from these if testing at different conditions.

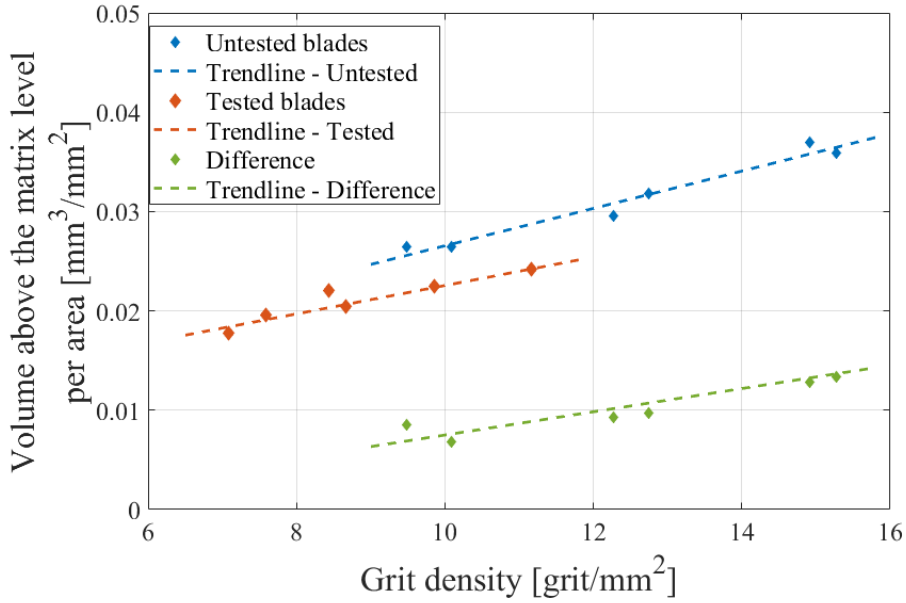

Figure 4.19: Differences in the relationship between the volume above the matrix level per area and grit density for untested and tested blades.

Regarding the voids left behind by the grit pull-outs, both void density and volume below the matrix level per area undergoes an increase subsequent to testing as confirmed in Table 4.18 for a given blade. The volume below the matrix level per area can be equivalently correlated to the void density, as seen in Figure 4.18 for a set of tested blades that have performed under different testing parameters. In this case, the volume below the matrix level cannot be directly correlated with grit density due to the fact that a reduction of the grit density does not necessarily imply a change of either void density or the volume below the matrix level, as it also happens when grit macrofracture occurs.

Exploring this result further, the volume below the matrix level in this case does not correlate with void density as closely as seen in the Pearson Correlation Factor in Figure 4.18 ($r^2 = 0.670$), as grit density did with the volume above the matrix level, especially for increasing void densities. This results from the combination of a lower number of occurrences per area, together with the variability of the embedding of grits, which depends on their shape as well as on the level of infill the grit has on the

matrix, which will determine the emptied volume from the craters left behind when they are pulled out.

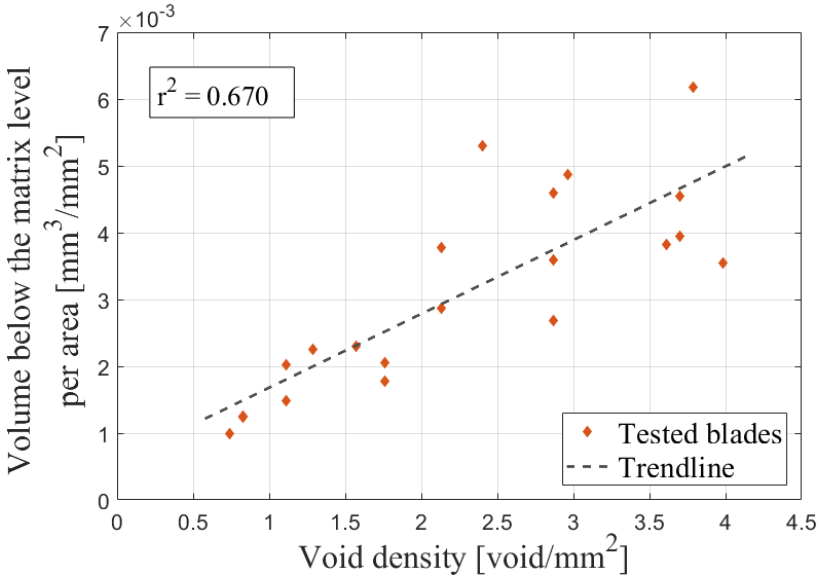

Figure 4.20: Relationship between the volume below the matrix level per area and void density for tested blades.

Finally, both volume above and below the matrix level might be distorted if blades pick up a significant amount of abradable material during testing. Although with the current status of the tool, it is not possible to isolate and quantify the volume of the material trapped on the blade tip, the image processing provides the ratio of the abrasive coating area that has been affected by this phenomenon. The results of a set of 8 blades which suffered from moderate (MPUB1 - MPUB4) and severe (MPUB5 - MPUB8) material adhesion are plotted in Figure 4.21.

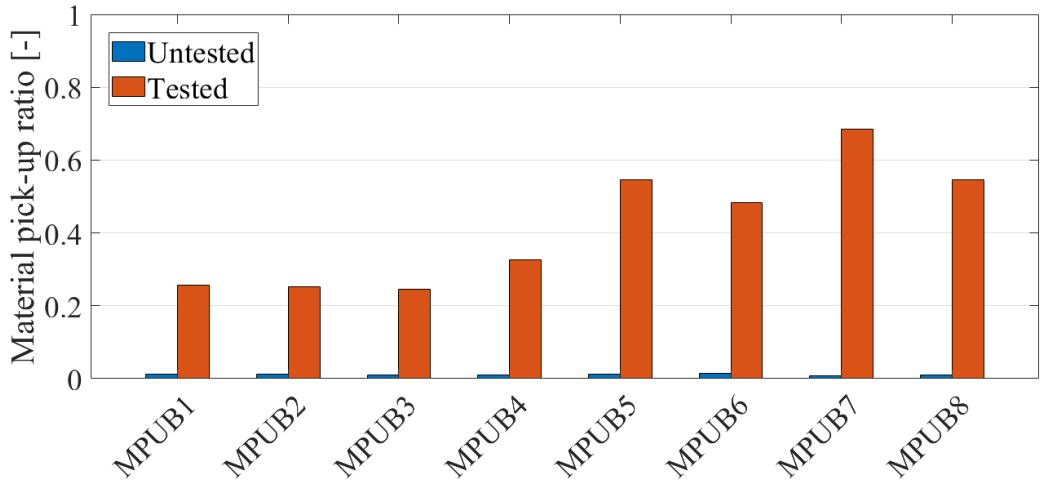

Figure 4.21: Comparison of the apparent material pick-up for a set of eight blades before and after being tested.

The apparent material pick-up from the blades prior to testing is plotted together with the measurement taken from the tested blades. Although there is no material adhered to the blades before being tested, the approach processes the light reflected on the grits as material pick-up because of its white colour and can be considered as a systematic error. The greyscale threshold, which has been set at 0.63, employed for deciding if a pixel contains information of material pick-up provides a systematic error of approximately 0.012 for blades, whose grit density is in the range of 13-16 grits/mm^2. This error also appears in the tested blades but cannot be isolated from the actual material pick-up.

4.5 Discussion

For the assessment of the cutting capability and wear of electroplated tipped blades, two different approaches have been employed and ultimately due to their inter relationship combined. The first approach is to calculate the volume above and below the matrix level per area which requires little post-processing to obtain parameters that capture all the different wear mechanisms - attritious wear, microfracture, macrofracture and pull-out - that abrasive grits undergo during a test. The second parameter is the active grit and void density that requires a more significant post-processing and misses localised grit wear - microfracture and attritious wear - but provides a more comprehensible parameter.

For untested blades, where no type of wear has occurred yet, both volume above the matrix level per area and grit density parameters correlate well (Figure 4.18). This is due to the fact that the grit size and the level of infill in the matrix follows a homogenous distribution among different blades, and number of grits per blade is high. Therefore, any of the two proposed parameters can properly describe the blade cutting capability prior to testing. Furthermore, ending in the same result by using two different approaches supports their validation. When it comes to tested blades, measuring volumes above or below the matrix provides a more robust parameter, as it contemplates all the wear mechanisms that produce damage on the grits as opposed to the grit density parameter which misses microfracture and attrious wear. If grit macrofracture or pull-out was to not occur during an abradable test, the tested blade would provide the same results as it did prior to test, in other words, a false negative on a blade where localised wear - microfracture or attritious wear - might have occurred and has been missed.

The same justification applies to the voids on tested blades, where the volume below the matrix level per area parameter not only takes into consideration that voids have been generated during a test, but it also provides information about the size of the crater left behind. Highly protruding grits require lower forces to be removed as their anchoring is not as firm when compared to a grit deeply embedded into the matrix (43). Hence, bigger craters leading to larger volumes indicate that the blade went through a harsher contact, a phenomenon that is not considered in the void density parameter which does not consider the grit pull-outs in the same way. This together with the low number of occurrences leads to a poorer correlation (Figure 4.20).

However, the main limitation of using the volumes as measuring parameters would be the case where the blade suffers from severe material pick-up. In this case, two phenomena would be simultaneously taking place and which cannot be decoupled from each other. There would be a volume reduction as a result of the grit damage, and a volume increment from the material trapped within the grits. In this case, the grit density parameter would work better as the pick-up material usually gets trapped in the area surrounding grits (Figure 4.16), and in view of how the procedure works, it is considered as a part of the grit. Therefore, if severe material pick-up occurs where there are considerable additions surrounding a grit, grit density comes as a preferable and more convenient parameter in spite of localised wear being left out and allows the direct comparison of blades that have suffered from severe pick-up against blades that did not.

Although this analytical tool has been developed for electroplated tipped blades, it can be used on DED blades with some limitations. DED blades are made of a mixture of grits and matrix deposited together onto the blade as a conglomerate and they do not have a plane matrix to zero the vertical reference system. However, they usually have a thin strip at the trailing edge where the bare blade can be seen underneath. This strip is used as a reference system to apply the corrections and zeroed the measured heights. As grits cannot be picked out from the matrix, only the volume parameter is available for this type of blades, either the absolute volume of the coating or the difference from the untested to the tested blade condition.

4.6 Conclusion

Conventional techniques used for bare blades are inadequate for abrasive tipped blades due to their complex behavior and the presence of multiple wear mechanisms. This has motivated the development of a Matlab-based analytical procedure for evaluating electroplated tipped blades in abradable tests, providing a valuable tool for assessing their cutting capability and wear.

The procedure offers two distinct approaches. The first approach evaluates the volume above and below the matrix level. The second approach uses a more complex procedure to count the number of grits and voids per area. When examining untested blades, both parameters show a high correlation, indicating their effectiveness in describing cutting capability prior to testing.

For tested blades, measuring volumes above and below the matrix provides a more reliable parameter, considering the microfracture and attritious wear mechanisms which are missed in the grit density parameter. Regarding the void generations, the volume below the matrix level per area parameter offers insights into crater size and embedding of grits, while the void density parameter provides a number of occurrences but fails to capture their severity.

However, using volumes as measuring parameters has limitations when severe material pick-up occurs. In such cases, the grit density parameter becomes preferable, as it ignores the material trapped within surrounding grits. Despite omitting localised wear, it allows meaningful comparisons between blades with and without severe material pick-up.

In conclusion, the developed Matlab-based analytical procedure offers an efficient and automated tool for evaluating the cutting capability and wear of electroplated tipped blades. By considering all potential wear mechanisms and accommodating

large test batches, it facilitates accurate characterisation and understanding of these blades with regard to the test condition and will hence be applied in the next chapters.

Chapter 5

Cutting performance and wear mechanisms of electroplated tipped blades

5.1 Introduction

In the examination of electroplated tipped blades within the high-temperature confines of a HPT, a prerequisite comprehension of their performance in cold operational scenarios is paramount. Prior to introducing temperature as a variable, it is imperative to scrutinise the efficacy of these blades during cold runs, as it allows the role of temperature on the cutting efficiency and wear mechanism arising from the contact to be established. This preliminary investigation lays the foundation for a more comprehensive understanding of their operational characteristics in diverse thermal conditions.

Extensive prior research has investigated the details of compressor abradable seal solutions. Notably, experimental setups using abradable incursion rigs have been employed at ambient temperatures (229; 36; 236; 237), yielding valuable data for understanding tribological systems relevant to compressor abradable seals.

This chapter aims to further this research by subjecting TBT 429 electroplated tipped blades to thorough evaluation against abradable ceramic samples, specifically those made of MAS, under ambient conditions. Systematically exploring these interactions provides a more detailed understanding of the tribological nuances in this operational context, forming a basis for informed advancements in the design and application of such blade configurations prior to introducing temperature as a variable to the equation.

For the first set of tests in the chapter, six standard length (16 mm) TBT 429

blades with a low, medium-low and standard grit density (2 blades for each) are tested at a single condition. As introduced in the previous chapter (Figure 4.18), the grit density of TBT 429 blades usually ranges between 13.5 and 16 grits per mm^2. However, some blades from the same batch exhibited both a mildly and a considerably lower grit density. Therefore, the aim is to determine if this reduction in grit density has a later impact on the blade performance.

The blades for the first set of tests are run in the Low Speed Rig at a single condition, considered as the standard condition in this thesis. Focusing on a single test condition enables valuable insights into the effects of grit density on blade performance and establishes meaningful comparisons among the different blade variants. The standard incursion rate is set to 0.3 μm/pass, representative of the same abradable systems inside gas turbine during the RiH (Running in and Handling) manoeuvre whereby the abrasive coating deposited onto the blade cuts the abradable lining on the casing (45). The second parameter to be set is the blade linear speed at the tip. Despite the fact that the LSR cannot achieve linear speeds typical of gas turbines, it has been reported that blade speeds above 50 m/s are capable of triggering the same wear mechanisms that arise inside gas turbines as long as the same incursion rate is achieved (229; 236). Therefore, the maximum linear blade speed that the rig can deliver, 200 m/s, is used for these tests. The last parameter to be set is the incursion depth which is 500 μm, another typical value of the track depth found in the ceramic abradable seals used in Rolls-Royce gas turbines (45).

The interaction between the blade and the abradable sample is influenced by both the blade speed and the incursion rate, which is calculated from the incursion speed, blade speed and blade radius. While the blade speed has a minimal impact once it exceeds 50 m/s (229; 237), the incursion rate becomes the parameter that defines the workload that the blade experience during each consecutive pass. The influence of the incursion rate will be investigated with the second set of tests.

In addition to the RiH manoeuvre, where the incursion rate has been set to 0.3 μm/pass for this piece of work, there are incursion rates from two other manoeuvres — S&C (Slow and Cold) and MTO (Maximum Take Off) — to be replicated at a speed of 200 m/s (45). The S&C manoeuvre is a similar maneouvre to RiH employed on Trent XWB engines and, based on the dimensions, rotational speed during operation, and disc expansion dynamics of the 97K HPT. In this scenario, the blades incur into the abradable at an approximate rate of 0.005 μm/pass towards the end of the incursion. On the other hand, the MTO manoeuvre occurs when the aircraft takes off at the maximum weight the pilot is allowed to attempt it, and in this

case, the blade interferes with the sacrificial lining at approximate 0.7 μm/pass. To explore potential performance compromises when surpassing the values defined by these manoeuvres, additional incursion rates beyond those specified in the engine's performance parameters are further included. The incursion depth remains constant at 500 μm.

Finally, the last parameter to be analysed is the effect of the incursion depth on the blade performance and the wear produced on the grits. Tests cannot be stopped at different incursion depths to analyse the blade as the contact is a dynamic event which builds heat throughout the tests. Stopping the tests would make that dynamic event reset and would not replicate a real cutting scenario. Running a set of tests with different incursion depths is also flawed, as blade damage development cannot be directly compared. Therefore, the solution to address the analysis of a single blade at different incursion depths is by using the stepped design for the abradable samples as introduced in Section 3.2.2. The incursion depth is set to 1250 μm in the test programme, and each step of the abradable sample, whose width is one third of the blade width, sees nominal incursion depths of 1250, 750 and 250 μm. A high to low order will be use when referring to incursion depths from now in advance, as it is the order their corresponding thickness are contacted, and it also is the order when looking at the samples from left to right. The incursion rates have been defined from the engine manoeuvres as per the second set of tests with an extra incursion rate of 2 μm/pass which is added to observe the degree of damage caused on the blade at this aggressive incursion rate when compared with the moderate rates of 0.3 and 0.7 μm/pass.

The following sections will present results for each of these parameters to be studied before a final discussion where the findings from each section will be brought together to holistically build up a narrative capable of describing the performance and wear mechanisms of electroplated tipped blades.

5.2 Grit density

Building upon the analytical tool developed in the preceding chapter, which successfully identified variations in grit density within a batch of electroplated tipped blades, attention is now directed towards the evaluation of the impact of differing grit densities on the cutting performance and wear mechanisms of these blades during testing.

In this set of tests, the primary objective is to comprehensively characterize and compare the performance of a specific set of TBT 429 blades. These blades exhibit

varying levels of grit density, and the aim is to understand how this variability influences their cutting performance when tested against MAS abradable lining samples.

5.2.1 Materials and methodology

The grit density of the blades employed in this analysis together with the test conditions are summarized in Table 5.1. Even though the standard grit density corresponds to the standard high grit density, the groups of blades are defined as low, medium and high grit density for convenience with this classification. On the other side, the abradable samples employed in this analysis are standard MAS abradable samples whose top abradable layer has a nominal thickness of 800 μm.

Test	Blade	Blade grit density		Blade speed (m/s)	Incursion rate (μm/pass)	Incursion depth (μm)
		Group	Value (grit/mm^2)			
EPGDT01	TBT429	Low	9.49	200	0.3	500
EPGDT02	TBT429	Low	10.09	200	0.3	500
EPGDT03	TBT429	Medium	12.59	200	0.3	500
EPGDT04	TBT429	Medium	12.27	200	0.3	500
EPGDT05	TBT429	High	14.91	200	0.3	500
EPGDT06	TBT429	High	15.28	200	0.3	500

Table 5.1: Test matrix for the grit density analysis.

5.2.2 Results

Figure 5.1 shows the post-test images of the blade and abradable resulting from the six tests conducted under identical conditions. As shown in the figure, all tests demonstrate a clean cut of the abradable, with no indication of material adhesion from either side. On the blade side, grey marks aligned with the cutting direction can be discerned within the matrix of the low (Figure 5.1a and 5.1b) and medium grit density blades (Figure 5.1c and 5.1d). Notably, the EWM1T1 test blade (Figure 5.1a) exhibits these marks most prominently. On the abradable side, tracks are a result of the grooves left by the indentations of the grit particles during the final stage of the cut, thereby producing the distinct striped pattern.

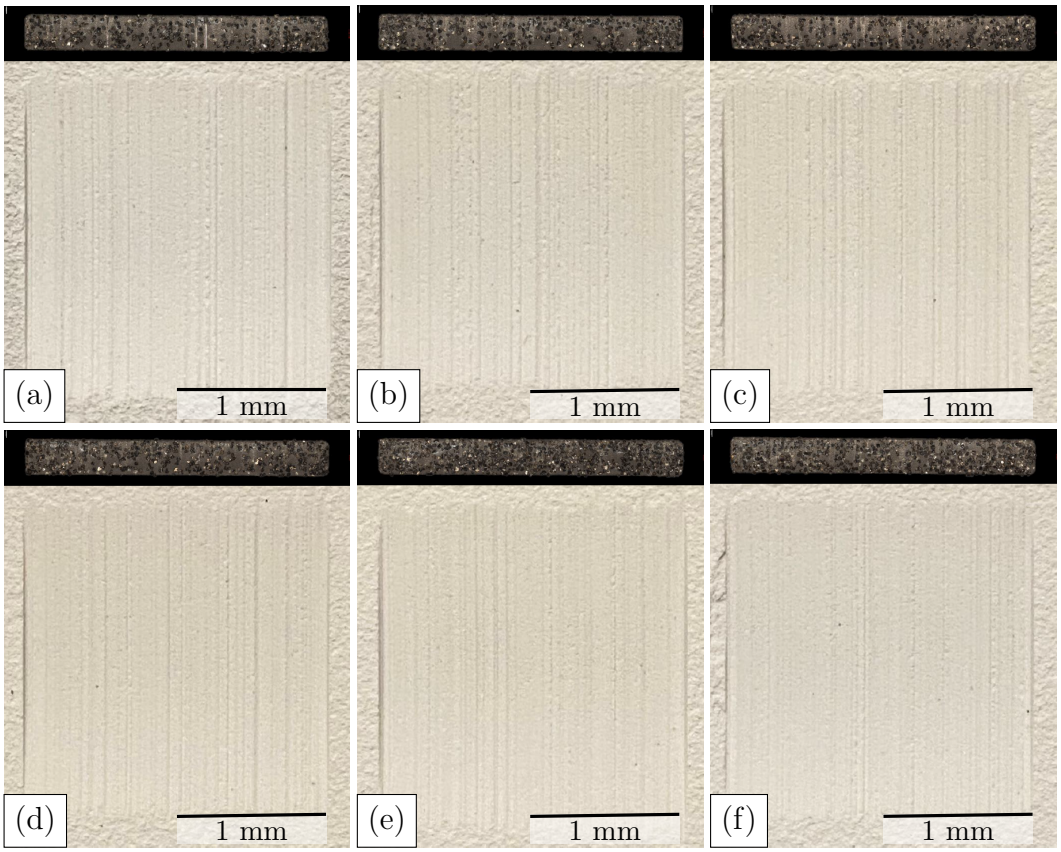

Figure 5.1: Post-test images of the abradable samples the TBT429 blades (top view) tested at 200 m/s and 0.3 μm/pass up to 500 μm with different grit density blades: (a,b) low, (c,d) medium and (e,f) high grit density.

The force and abradable temperature generated during the tests are shown for these six tests in Figure 5.2. The tests performed with the medium (Figure 5.2c and 5.2d) and high (Figure 5.2e and 5.2f) grit density blades quickly stabilise to a point where normal and tangential forces increase at a slow rate over the rub length. For the low grit density blades, both forces and temperature do not transition particularly smoothly, with multiple peaks evident during the early stages of the rub, sooner and with higher values than for the other two groups of blades, where the maximum values take place at the end of the tests.

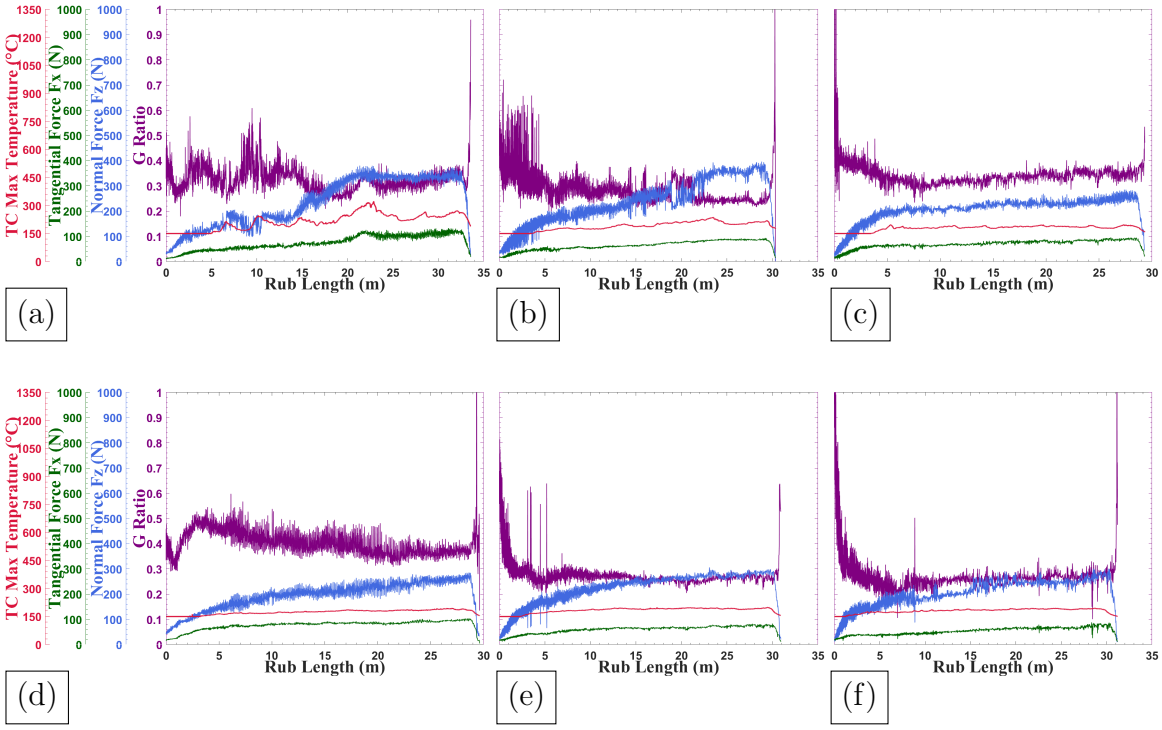

Figure 5.2: Force and temperature data for the tests performed with TBT429 blades at 200 m/s and 0.3 μm/pass up to 500 μm with different grit density blades: (a,b) low, (c,d) medium and (e,f) high grit density.

G ratio is defined as the ratio of the tangential force over the normal force, and ranges in value from 0 to 1. Practically, it is an indicator of how the cutting mechanism develops in a test (242; 28; 36). When a test starts, higher G ratios indicate a more effective cut as more energy from the contact goes into the shear component, with this related to the main material removal mechanism. On the other hand, lower G ratios indicate that most of the energy goes into the normal component, compacting, and cracking the ceramic abradable, and sometimes producing material removal. This compaction, in turn, increases the load as the material does not have any way to escape. The material removal due compaction takes place once the blade has passed as a result of the elastic energy stored from the material compression that may produce some bonding detachment and subsequent debris release (23). However, any damage produced on the blade would also increase the tangential force as the friction coefficient also increases. Therefore, although the G ratio is useful to understand how the performance develops during a test, it cannot be directly compared between tests given its dynamic behaviour and dependency on the friction coefficient. That said,

for this set of tests, excluding the initial contact accommodaton phase, the G ratio was maintained at the same level in each case (Figure 5.2).

In order to have a direct comparison of the blade performance for a set of tests, the maximum normal force and maximum abradable temperature can be compared, with this shown in Figure 5.3, where tests are grouped according to their grit density. These two parameters provide a clear indication of the most aggressive contact condition that the blades suffer during a test, which usually takes place at the end of the test because of blade wear and the rub length increase per pass. Whereas there is no difference between the tests where medium and high grit density blades were used, the two tests with the low grit density blade exhibited a 27% and 42% average increment of the normal force and temperature, respectively.

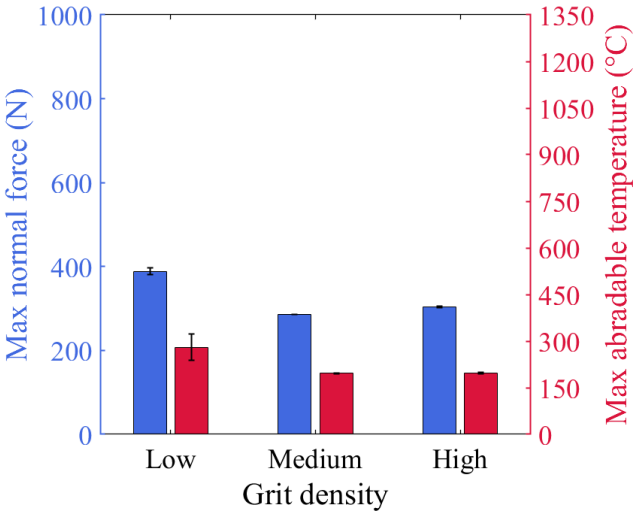

Figure 5.3: Comparison of the maximum normal force and maximum temperature recorded on the abradable surface between the tests performed with TBT429 blades at 200 m/s and 0.3 μm/pass up to 500 μm with different grit density blades.

To understand where the higher abradable temperatures come from in the tests performed with low grit density blades, the data captured with the thermographic camera for the EWM1T1 tests is plotted as a 2D map (Figure 5.4d) with this data processed as described in Section 3.3.1.4, where the x axis represents the blade length and the y axis the temperature progression of a line in the centre of the contact recorded at each pass. The thermal map is plotted together with an image of the test blade (Figure 5.4a), where the lighter marks mentioned before correspond to scratches or their initiation, that were produced during the tests. As shown in Figure 5.4c and 5.4d, the scratches can clearly be identified as hot lines in the thermal map.

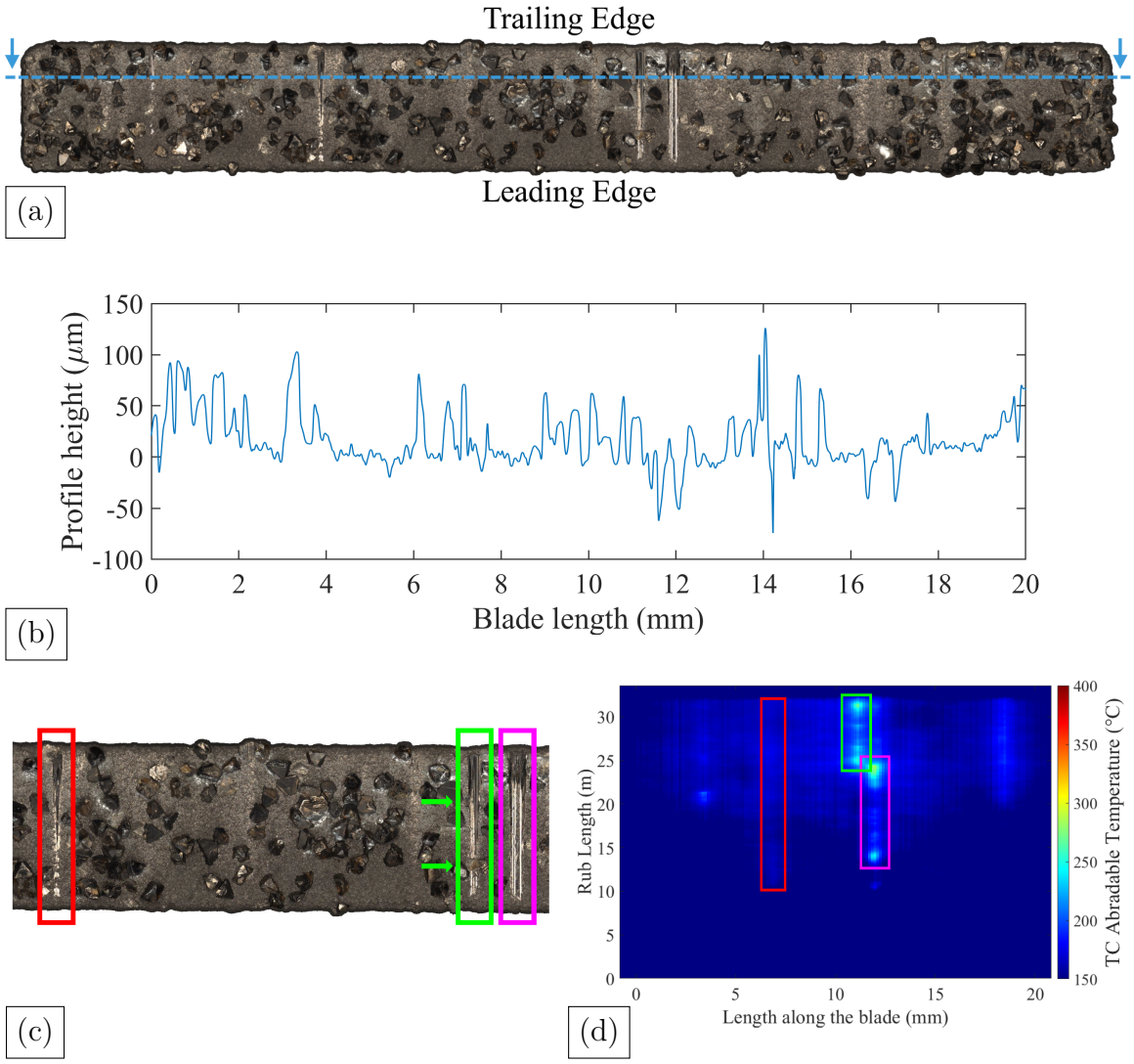

Figure 5.4: Scratches produced on the matrix due to the lack of grits for the EWM1T1 test: (a) EWM1T1 blade with profile cut (b) blade height profile, (c) scratches and (d) thermal map during the test.

The three scratches marked in Figure 5.4c and their corresponding hot lines in 5.4d represent three different scratch mechanisms: (red) a shallow scratch that was generated early in the test, but barely progressed, (magenta) a deeper scratch that also initiated early but ceased to develop further in the middle of the test and (green) a deeper scratch initiated in the middle of the test as a result of grit pull out, which continued its evolution until the end of the test. As can be seen in Figure 5.4c, scratches are generated due to the absence of grits in the cutting direction or their pull out over the course of the test. However, MAS is a ceramic material and as with any ceramic, it fractures and breaks according to where the cracks are nucleated

when the grits hit it (23). Hence the surrounding grits make an impact on the scratch development on an unoccupied line, as occurred in the scratch marked in red, where although it initiated earlier, it did not grow as much as the other two (Figure 5.4b). In contrast, it can be observed that the scratch marked in magenta does not have as many surrounding grits as the previous one. In this case, the scratch grew deeper, generating more heat on two specific ocassions (Figure 5.4d), where the second instant approximately matches the rub length where the maximum temperature was recorded for that test (Figure5.2a). Whilst agreement was observed on this occasion, the rub lengths between the maximum temperature and thermal maps do not necessarily need to match as the thermal maps use the data from a single line as defined in Section 3.3.1.4. During the test, this scratch marked in magenta stopped generating heat as a result of disengagement with the abradable, produced by a local break in the contact. Finally, the scratch marked in green started at the middle of the test because of grit pull out, intermittently generating high temperature spots on the abradable. In turn, this scratch grew deeper as it was present at the end of the test, where the scratch marked in magenta was wider due to the longer contact of the bare matrix against the abradable. This indicates that although scratches progress during the test, they may do it intermittently with periods of saturation and their growth may be stopped or, at least, paused, as a result of the rupture of the ridge left on the ceramic at the scratch line. Otherwise, no scratch would ever stop growing.

There is a combination of events that leads to the saturation periods that, in turn, give way to the scratch nucleation at the trailing edge and its evolution toward the leading edge. The first of these events is the absence of the grit to effectively remove abradable material. The second is the very nature of the test where the incursion motion is continuous, which progressively increases the load while blade and abradable are in contact during a pass. In addition, if the blade struggles to evacuate the cut material, forces and temperatures will similarly rise during a pass as a result of the inefficient cut due to the material entrapped. As a consequence, the normal load that the blade experiences is higher when it leaves the contact than when it enters it for each pass.

With the specific reference to the cut material, some of it is collected by the blade, getting trapped underneath (236) and moving towards the trailing edge, not only compacting and increasing the normal load, but also reducing the protrusion of the grits and creating a three-body abrasion environment. If the incursion keeps progressing, those zones without grit that cannot cut material see an increasing load and local temperature, aggravated at the trailing edge by these mechanisms, which

result in the formation of a scratch. The scratch continuously develops longer, deeper and wider unless the uncut ridge of material on the abradable sample breaks and ceasing engagement with the blade for a limited period. In addition to scratches, some greyer areas are produced on the matrix (Figure 5.4a) by the abrasion of the particles released from the contact. This phenomenon can also be observed on the medium density blades (Figure 5.1c and 5.1d).

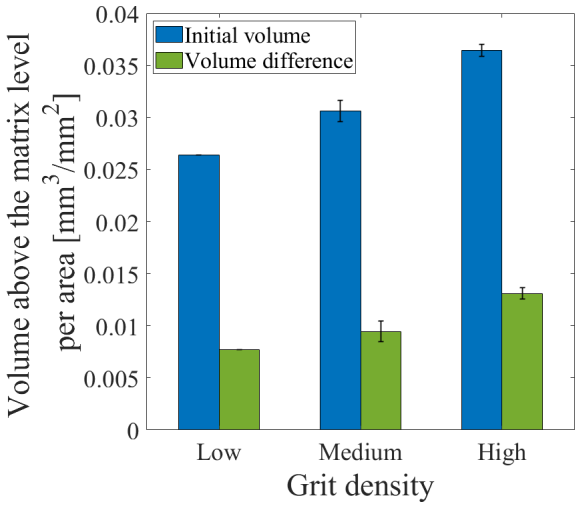

Figure 5.5: Comparison of the initial volume above the matrix level and its reduction during the tests performed with TBT429 blades at 200 m/s and 0.3 μm/pass up to 500 μm with different grit density blades.

With regards to blade wear, Figure 4.19 shows both the initial volume above the matrix level and the reduction of this during the test, where the latter is approximately one third of the initial volume. That said, for the same amount of volume reduction, the damage becomes more significant in the low grit density blades where the wear has extended to the matrix also due to the lack of grits. Considering that only one test condition has been contemplated in this analysis, the next question to answer is how changing the test condition affects the blade performance and its wear.

5.3 Incursion rate

In the previous analysis, the focus was solely on a single test condition, specifically replicating the RiH manoeuvre for the Rolls-Royce Trent XWB HPT. However, it is important to recognize that the interaction between the blade and abradable lining of the seal system is not limited to this particular manoeuvre. There are other critical engine manoeuvres where contact between the blade and abradable occurs, although

the specific conditions of these scenarios may be challenging to determine due to engine malfunctioning.

To gain a comprehensive understanding of the performance of TBT429 blades against MAS at various operating points, it becomes imperative to extend our analysis. In this next phase, blades with a sufficiently high grit density, which ranges between 12.5 and 15 grit/mm^2, are subjected to different incursion rates, allowing a wider range of operating conditions to be investigated.

5.3.1 Material and methodology

The test conditions for this second of set of tests are summarized in Table 5.2, where two repetitions are performed per test condition.

Test	Blade	Blade speed (m/s)	Incursion rate (μm/pass)	Incursion depth (μm)
EPIRT01 (a)	TBT429	200	0.001	500
EPIRT02 (b)	TBT429	200	0.001	500
EPIRT03 (c)	TBT429	200	0.005	500
EPIRT04 (d)	TBT429	200	0.005	500
EPIRT05 (e)	TBT429	200	0.3	500
EPIRT06 (f)	TBT429	200	0.3	500
EPIRT07 (g)	TBT429	200	0.7	500
EPIRT08 (h)	TBT429	200	0.7	500
EPIRT09 (i)	TBT429	200	1.5	500
EPIRT10 (j)	TBT429	200	1.5	500
EPIRT11 (k)	TBT429	200	2.0	500
EPIRT12 (l)	TBT429	200	2.0	500

Table 5.2: Test matrix for the incursion rate analysis.

The blades employed in this set comes from a batch whose initial grit density ranges between 12.5 and 15 grit/mm^2. As determined in the previous analysis, this density has been shown to be sufficiently high to prevent the occurrence of scratches resulting from a scarcity of grit particles, at least until the blades are eventually pulled out during contact. With regards to the abradable specimens, a batch of samples,

whose top MAS layer has again a nominal thickness of 800 μm, have been sprayed to standard parameters.

5.3.2 Results

The post-test images of the samples are shown in Figure 5.7. As shown in the figure, almost no difference was found between the samples tested at different incursion rates. The only difference found was a modest amount of material pick-up on one of the blades tested at the maximum rate (Figure 5.6). Minimal coating rupture was also found in the final track surface (Figure 5.7j) and on one of the edge (Figure 5.7k) for higher incursion rates.

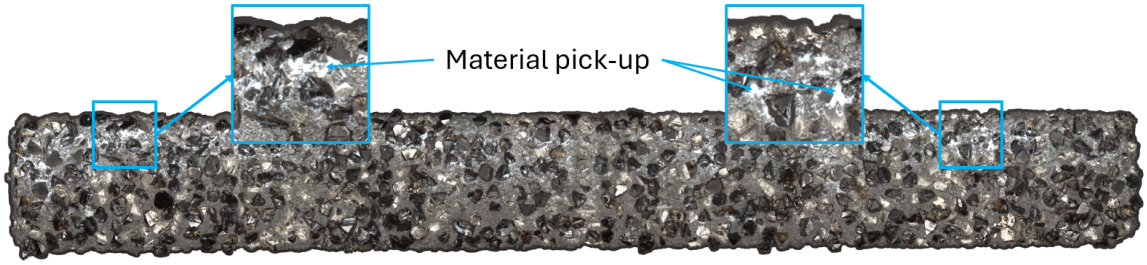

Figure 5.6: Details of material pick-up observed on one of the TBT429 blade tested (EPIDT9 (i)) at 2 μm/pass up to 500 μm.

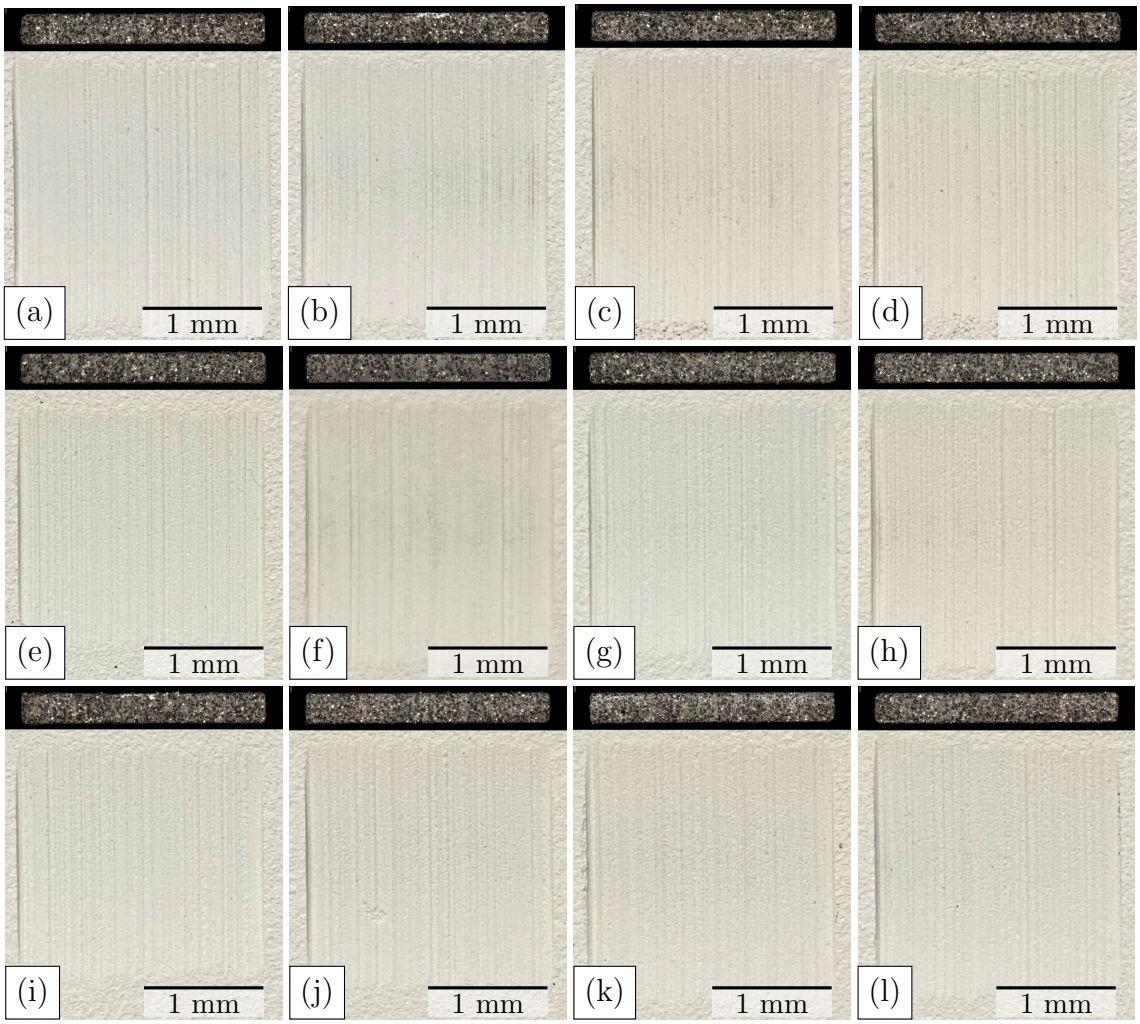

Figure 5.7: Post-test images of the abradable samples and the TBT429 blades (top view) tested up to 500 μm at 200 m/s and different incursion rates: (a,b) 0.001 μm/pass, (c,d) 0.005 μm/pass, (e,f) 0.3 μm/pass, (g,h) 0.7 μm/pass, (i,j) 1.5 μm/pass and (k,l) 2.0 μm/pass.

The force and abradable temperature data obtained from the twelve tests conducted for this analysis are shown in Figure 5.8. For the lowest incursion rates of 0.001 μm/pass (Figure 5.8a and 5.8b) and 0.005 μm/pass (Figure 5.8c and 5.8d), whilst forces generated from the contact are low and barely distinguishable from the noise caused by spindle vibrations and disc windage, a low level cyclic behaviour can be observed where the normal force starts to increase until it reaches a peak before returning to the noise threshold. This suggests that at these incursion rates, damage accumulation is required to trigger material removal and that the chunks of the abradable removed are larger than the length the stage travel per pass. Likewise,

these low force contacts generate temperatures below the thermal camera threshold (150 °C), and as such cannot be measured.

For higher incursion rates, both tangential and normal forces exhibit a consistent pattern across the higher incursion rates. Initially, there is a steep increase in forces, followed by a nearly constant increase as the rub length progresses, reaching the maximum value towards the end of the test. This observation aligns with the previous set of tests where no scratches occurred. Furthermore, the magnitude of the linear increases becomes more significant as the incursion rates increase. The maximum temperature recorded on the abradable follows a similar trend, albeit with a more subtle rate of increase.

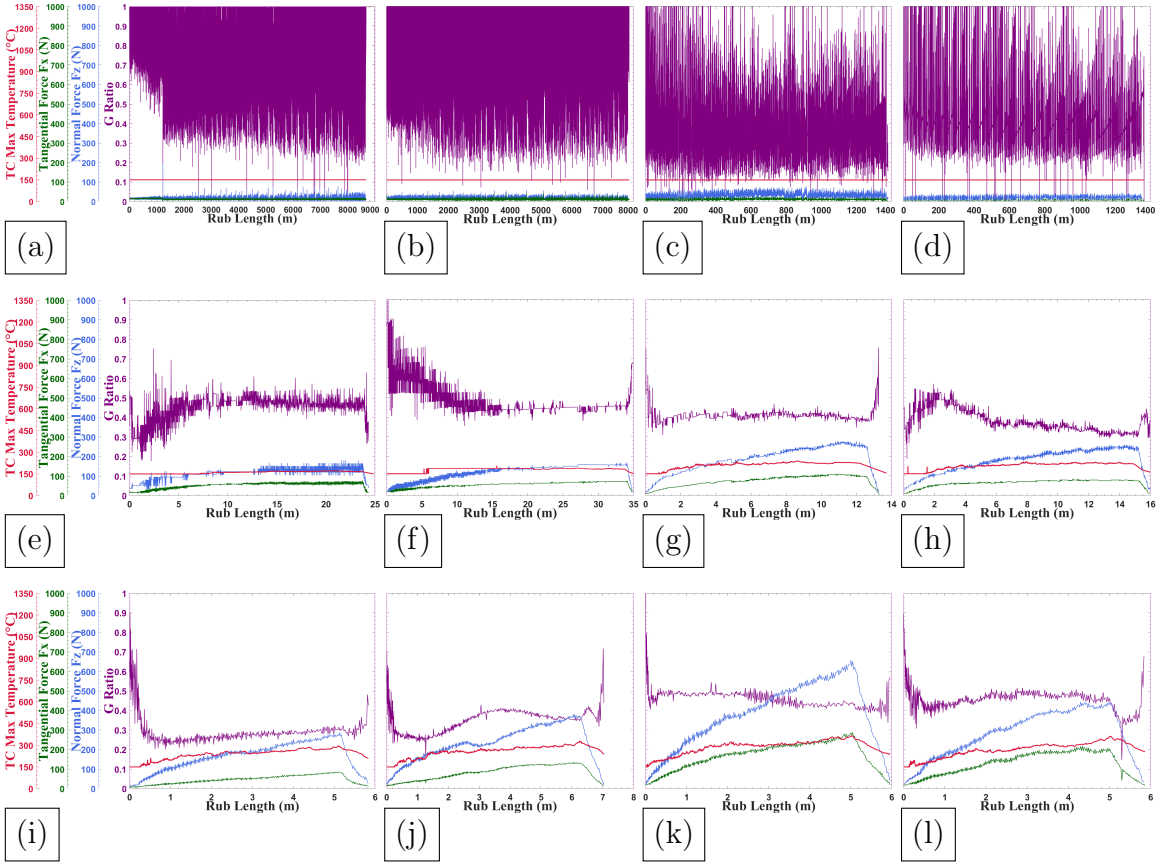

Figure 5.8: Force and temperature data for the tests performed with TBT429 blades up to 500 μm at 200 m/s and different incursion rates: (a,b) 0.001 μm/pass, (c,d) 0.005 μm/pass, (e,f) 0.3 μm/pass, (g,h) 0.7 μm/pass,(i,j) 1.5 μm/pass and (k,l) 2.0 μm/pass.

The maximum force and abradable temperature recorded for each test are plotted in Figure 5.9. As the incursion rate increases, there is a consistent and incremental rise in these parameters, supported by the fact that the workload experienced by

the blade increases as more material needs to be removed per pass. At the same time, the end surfaces of the abradable tracks exhibit no significant variation across the range of incursion rates tested. These observations suggest that the material removal mechanisms resulting from the blade-abradable contact remains unchanged apart from at the low incursion rates (0.001 and 0.005 μm/pass), where a cyclic process takes place.

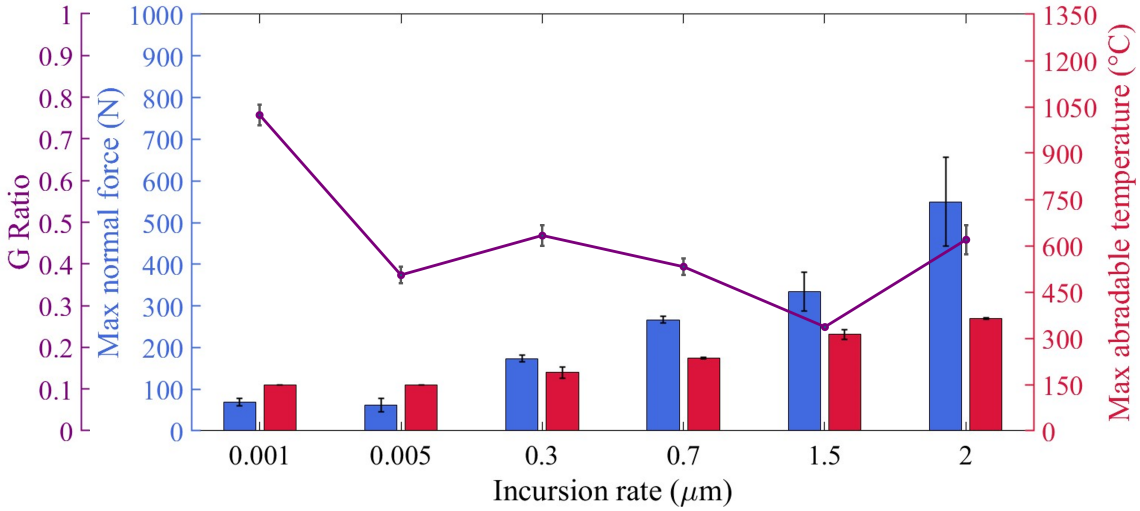

Figure 5.9: Comparison of the maximum normal force, G ratio and the maximum temperature recorded on the abradable surface between the tests performed with TBT429 blades up to 500 μm at 200 m/s and different incursion rates.

As previously noted, blades used in this set of tests were carefully selected to meet real engine standards, with a grit density falling within the medium to high range defined in the previous chapter. As noted, these represent grit densities high enough to avoid scratch formation because of a lack of grits in a given area.

For the analysis, only post-test volume measurements were taken, which are presented in Figure 5.10. The remaining cutting capability of a blade, defined as the volume above the matrix level, consistently decreases as the incursion rates increase, whereas the incursion rates increase, the blades operate under higher loads (Figure 5.8). This load leads to increased damage on the grits post test, reducing their volume as a result. Conversely, the volume below the matrix level, which defines the degree of grit pull-out, increases with higher incursion rates. The low variability observed between the two tests conducted under each condition, along with the clear trend across the range of incursion rates tested, suggests that the workload defined by the incursion rate has a greater influence on the remaining blade cutting capability than

either the total number of passes or initial blade grit density, provided this density is not low enough to trigger an alternative failure mode as demonstrated in Section 5.2.

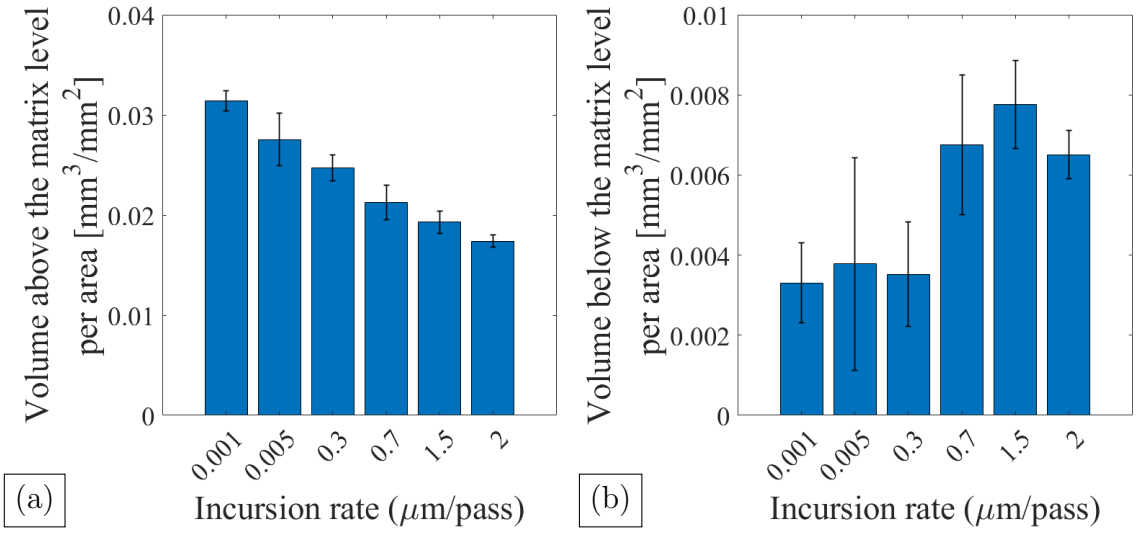

Figure 5.10: Volume above and below the matrix level measured after the tests performed up to 500 μm at 200 m/s and different incursion rates.

All parameters point to a consistently poorer performance at increasing incursion rate, except for the ratio between the tangential and normal forces (Figure 5.9). When comparing G Ratio as a single parameter among different test conditions, three assumptions need to be set:

- It defines the ratio between the tangential and the normal force when the incursion initiation has already stabilised but not further developed.
- No damage has been produced on the blade during the initial interaction with the abradable.
- The grit density is high enough to ensure a homogenous contact.

In turn the G ratio can be used to determine how efficient the interaction is between blade and abradable. Ideally, this parameter should be as close to the unity as possible, which would indicate that forces are mainly tangential, coming from the shear of the cut. Although the G ratio has been plotted for the two lowest incursion rates, it is not indicative as the force values drops below the noise threshold.

When evaluating the G ratio for higher incursion rates, G ratio decreases with increasing incursion rates until it reaches the maximum incursion rate considered

in this study, where the G ratio suddenly increases (2 μm/passs). From a contact mechanics perspective, this trend indicates that the blade struggles to accommodate higher rates of material removal, increasing material compression, which then gets alleviated at the highest incursion rate (2 μm/pass). Upon comparing the G ratio curves in Figure 5.8, it becomes aparent that they remain roughly constant for almost every test, indicating that the blade does not suffer enough damage to alter the contact mechanics present.

Test	Incursion rate (μm/pass)	Blade cutting capability (mm^3/mm^2)	Abradable Profile Rq (μm)
EPIRT06 (f)	0.3	0.0234	33.81
EPIRT08 (h)	0.7	0.0198	31.56
EPIRT09 (i)	1.5	0.0204	31.37
EPIRT12 (l)	2.0	0.0180	25.75

Table 5.3: Remaining blade cutting capability and 1uadratic mean (Rq) of the abradable sample profile at the deepest point for different incursion rates.

The blade remaining cutting capability is analysed together with the root-mean-square roughness of the abradable profile at the deepest point for one of the tests (the one with the most stable cut of the two repetitions) for each incursion rate. As shown in Table 5.3, tested blades get more damaged with increasing incursion rates as the blades require to undertake heavier workload per pass and the resulting track on the abradable surface is smoother because of the blade losing abrasiveness. The stepper drop at the highest considered incursion rate can be better understood in combination with the G ratio analysis. The G ratio sudden increase at the highest incursion rate indicates that the contact become more efficient, transition from a third body abrasion mechanism to a direct cut of the material due to the high incursion rate. This cutting mode transitioning boost the blade wear as it directly contacts the abradable and, hence, the resulting abradable surface becomes considerably smoother due to the lack of abrasiveness.

Overall, understanding the behaviour of blades under different incursion rates is vital for optimizing their performance and durability in practical applications, and has been achieved in the preceding section. However, further investigation is needed to explore the effects of sustained wear at deeper incursions and its implications on

blade functionality are also required to establish the boundaries of the applications and functionalities of the more complex systems they are employed in.

5.4 Incursion depth

Although the wear experienced by the blades and their cutting performance in the two previous sections showed a dependency with both the blade grit density and the incursion rate, wear was not high enough to trigger the blade failure. To reach the ultimate blade capability limit and to understand how this occurs, stepped tests with deeper incursions are performed at targeted incursion rates.

5.4.1 Material and methodology

The blades employed in this batch of tests follow the same standards defined in the previous analysis where grit density was in the range between 12.5 and 15 grit/mm^2. The conditions tested are then summarized in Table 5.4.

Test	Blade	Blade speed (m/s)	Incursion rate (μm/pass)	Stepped incursion depths (μm)
EPIDT01 (a)	TBT429	200	0.005	1250-750-250
EPIDT02 (b)	TBT429	200	0.005	1250-750-250
EPIDT03 (c)	TBT429	200	0.005	1250-750-250
EPIDT04 (d)	TBT429	200	0.3	1250-750-250
EPIDT05 (e)	TBT429	200	0.3	1250-750-250
EPIDT06 (f)	TBT429	200	0.3	1250-750-250
EPIDT07 (g)	TBT429	200	0.7	1250-750-250
EPIDT08 (h)	TBT429	200	0.7	1250-750-250
EPIDT09 (i)	TBT429	200	0.7	1250-750-250
EPIDT10 (j)	TBT429	200	2.0	1250-750-250

Table 5.4: Test matrix for the incursion depth analysis.

5.4.2 Results

Once again, the images of both the blades and the abradable samples post test are shown in Figure 5.11. However, this time, clear damage on both samples occurred on

the the side that incurred the deepest for those tests run at 0.7 μm/pass (Figure 5.11g, 5.11h and 5.11i) and 2.0 μm/pass (Figure 5.11j). Severe material adhesion is also found on the abradable side as a result of the blade failure. At the highest incursion rate (2.0 μm/pass), coating rupture took place and propagated to the middle section of the stepped samples. On the contrary, the cut for the standard (0.3 μm/pass) and the lowest incursion rate (0.005 μm/pass) was clean with no visual difference between the different sections. The stripped darker marks at the deepest point of the track (Figure 5.11a, 5.11c and 5.11d) are due to the YSZ intermediate layer underneath which has a yellowish tone and begins to become exposed when the MAS topcoat thickness is thinned.



Figure 5.11: Post-test images of the abradable samples and the TBT429 blades (top view) for the stepped tests (1250, 750 and 250 μm) performed at 200 m/s and different incursion rates: (a,b,c) 0.005 μm/pass, (d,e,f) 0.3 μm/pass, (g,h,i) 0.7 μm/pass and (l) 2 μm/pass.

The damage on the blade is clearly visible at a macroscopic level depending on

the incursion rate they were run at, being consistent and repetitive for each given condition. As such blade damage can be classified by incursion rate as follows:

1. 0.005 μm/pass (Figure 5.12): at this incursion rate the only discernible visible difference is very limited material pick-up (as detailed in Figure 5.6) from the abradable at the section that cut up to 1250 μm deep. Grit fracture and pull-outs occurred, but further analysis is required to quantify the level of damage for each section.

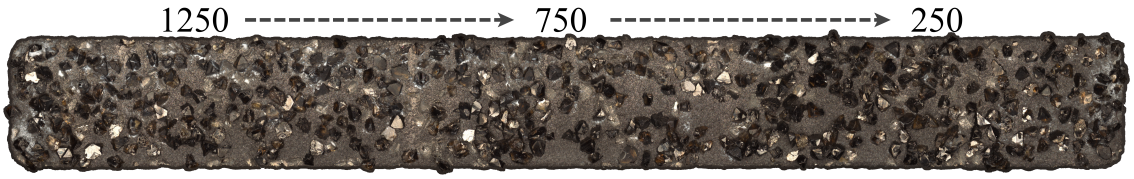

Figure 5.12: Details of one of the TBT429 blade tested (EPIDT02 (b)) at 0.005 μm/pass up to 1250, 750 and 250 μm.

2. 0.3 μm/pass (Figure 5.13): when tested at the standard conditions, abradable material pick-up begins to be more noticeable, especially when moving towards the section that cut the deepest. This material adhesion starts at the trailing edge as can be seen in the middle section and then propagates to the leading edge as the incursion continues, as occurs on the side that cut up to 1250 μm deep.

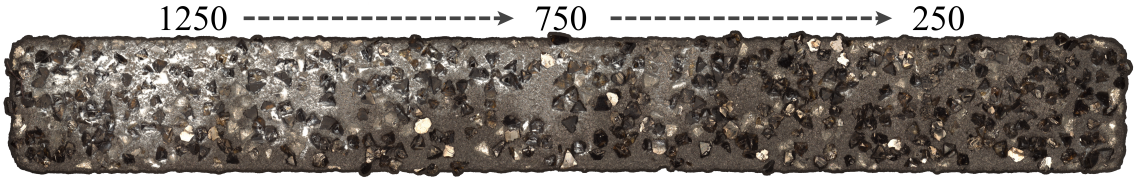

Figure 5.13: Details of one of the TBT429 blade tested (EPIDT06 (f)) at 0.3 μm/pass up to 1250, 750 and 250 μm.

3. 0.7 μm/pass (Figure 5.14): when blades run above the standard incursion rate, the middle section which cuts up to 750 μm deep starts showing a considerably higher level of material adhesion, which is extended to the whole width of this section. At the section that runs the deepest (1250 μm), the coating has failed with no sign of abrasive grits and a stripped patern resulting from smearing of the base metal. This coating failure began to propagate to the middle section.

The abrasive coating at the very edge still remains attached to the blade, suggesting that this failing mechanism did not start at the blade edge. The portion of the blade that only ran to a depth of 250 μm remains undamaged apart from the unavoidable grit wear mechanisms that will be further analysed later in this section.

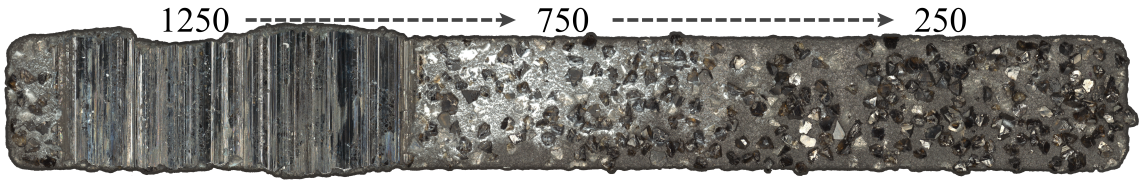

Figure 5.14: Details of one of the TBT429 blade tested (EPIDT03) at 0.7 μm/pass up to 1250, 750 and 250 μm.

4. 2 μm/pass (Figure 5.15): the coating failure that just started to propagate to the middle section at 0.7 μm/pass, almost reaches the side of the blade that cut the shallowest for the most severe test condition. Where the blade did not fail yet, but cut up to 750 μm, considerable material pick-up can be observed which then disappear for the section that went just up to 250 μm deep. Again, the failure mechanism did not occur on the very edge of the blade, which suggests that the failure started in an intermediate section. The stripes on the middle section generally have a wide variety of grey tones with a few almost white, due to the adhesion of the ceramic. As happens at the previous incursion rate, when moving to the section that runs the deepest, the stripped pattern becomes less noticeable and the tones darker. This failure mechanism is further analysed with SEM microscopy techniques in Chapter 7.

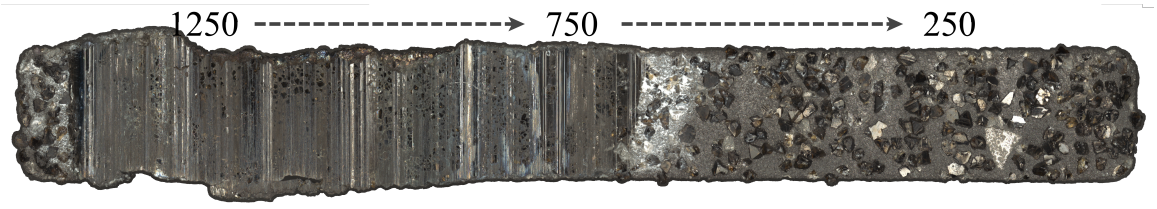

Figure 5.15: Details of one of the TBT429 blade tested (EPIDT10 (j)) at 2 μm/pass up to 1250, 750 and 250 μm.

The coating failure comes together with a significant loss of the blade cutting capability as there is no grit available in the surface to produce an effective material removal mechanism, increasing contact forces and temperature.

In this case, force graphs do not provide a full insight of the blade performance, as in stepped tests forces are dependant on the length of the blade in contact with the specimen. In addition, because of the heterogeneous nature of abrasive coatings on blades, the transition between steps occurs progressively. However, if the blade fails, forces can still be used to determine the instant and failure severity. This failure initiation can be discerned from the force and temperature data in Figure 5.16, where for the 0.7 and 2 μm/pass incursion rate tests, these parameters spike up towards the end of the test.

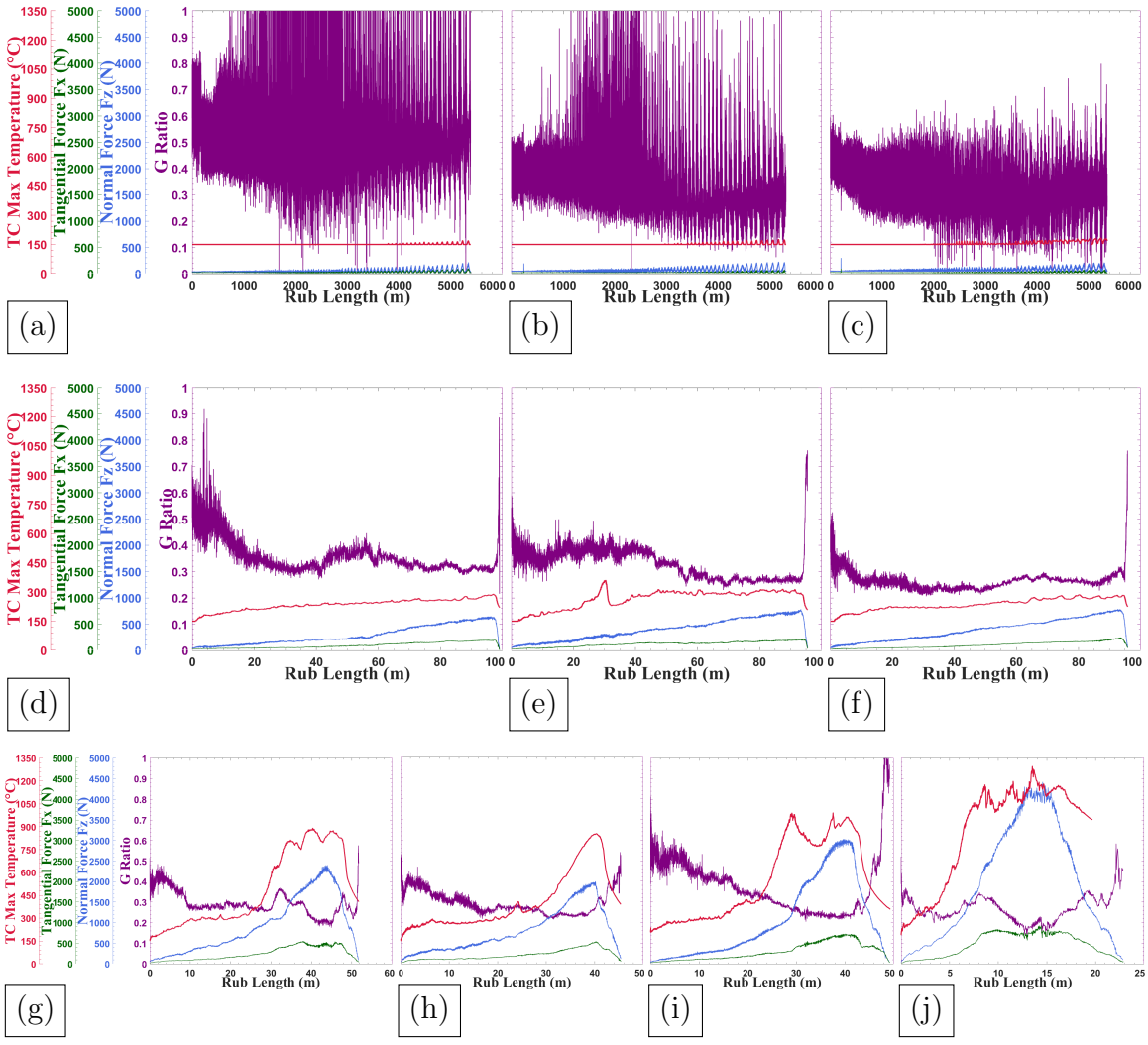

Figure 5.16: Force and temperature data for the stepped tests (1250, 750 and 250 μm) performed with TBT429 blades at 200 m/s and different incursion rates: (a,b,c) 0.005 μm/pass, (d,e,f) 0.3 μm/pass, (g,h,i) 0.7 μm/pass and (l) 2 μm/pass.

Considering the force data further, it could be expected that forces would show two changes, from the steps on the abradable samples, in their growing rates since the

contact area of the blade increases as the test proceeds. However, for the 0.005 (Figure 5.16a, 5.16b and 5.16c) and 0.3 (Figure 5.16d, 5.16e and 5.16f) μm/pass incursion rates, where the blade did not fail at any of the repetitions, force data did not show such a noticeable change. This is likely due to the the different variables within the test such as the blade initial test position, vibrations, grit height distribution and abradable roughness making the transition between steps smooth and progressive, and hard to distinguish. As temperature is recorded as the maximum temperature on the abradable, it is independent of the contact area, and as such transitions can similarly not be observed

For the incursion rates that made the blade fail, 0.7 (Figure 5.16g, 5.16h and 5.16i) and 2 μm/pass (Figure 5.16j), it can be clearly observed that both forces and temperature start to rise towards the end of the tests, indicating a turning point where the mechanism that leads to blade failure initiated. The following peak defines the failure stage where it propagates and forces, and temperature as a result, keep increasing until the test finishes. When considering absolute values, it can be observed from Figure 5.17 that both averaged normal forces and abradable temperature per test condition increase considerably for those incursion rates (0.7 and 2 μm/pass) where the blade failed. During this failure phase, G ratio follow a bathtub shaped curve, which is an indicator of a poor cutting mechanism (Figure 5.16).

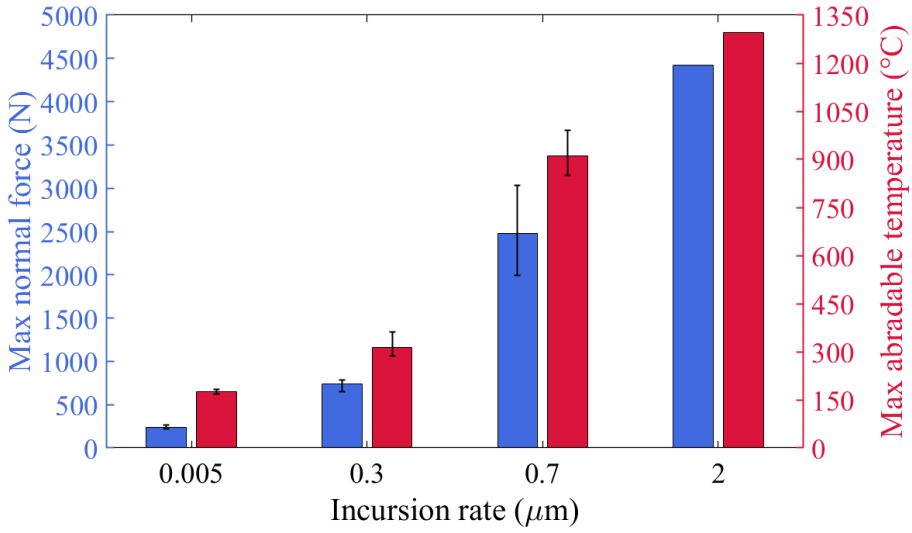

Figure 5.17: Comparison of the maximum normal force and the maximum temperature recorded on the abradable surface between the stepped tests performed with TBT429 blades up to 500 μm at 200 m/s and different incursion rates.

How the blade fails can be further investigated by using the abradable 2D tem-

perature maps processed from the thermal camera data. These maps are presented aligned with an image of the tested blade for the EPIDT07 (g) and EPIDT10 (j) tests in Figure 5.18.

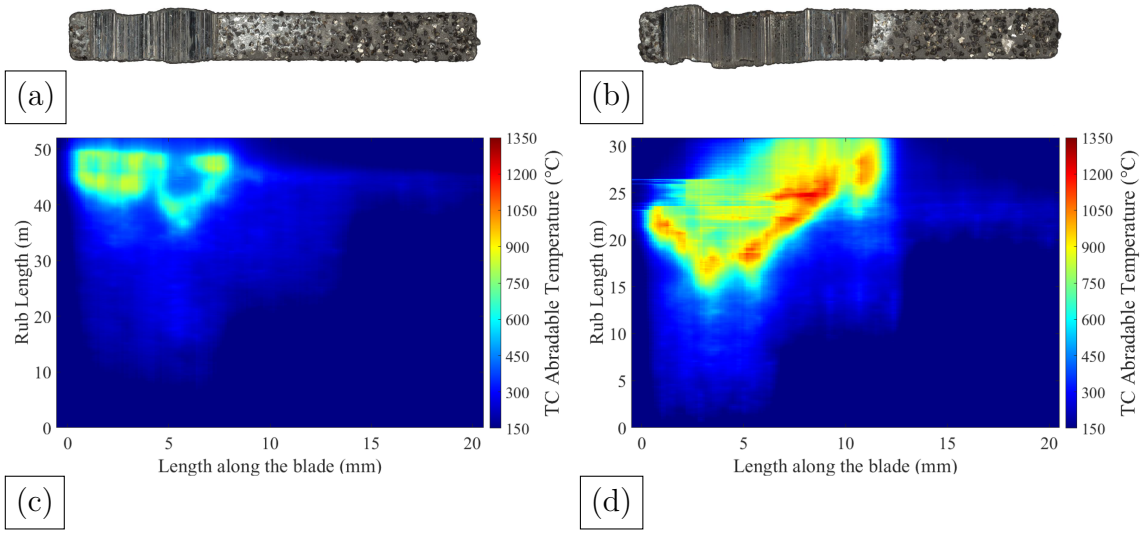

Figure 5.18: 2D thermal maps and blade images of the stepped tests performed at (a,c) 0.7 and (b,d) 2 μm/pass.

For the blade performed at 0.7 μm/pass (Figure 5.18a and 5.18c), a large increase in temperature on the section that cuts the deepest occurred towards the end of the test. This increase initiated at two different points: at 5.43 mm from the left side the blade when the nominal rub length was 36.13 m, and at 2.47 mm when the rub length was 40.06 m. These regions then propagated independently. For the test at 2 μm/pass (Figure 5.18b and 5.18d), increases in temperature once again occurred at two independent points: at 3.28 and 5.65 mm from the left side at a rub length of 13.96 and 14.62 m respectively, which in this case unified and then propagated together much more abruptly and reaching higher values than in the previous condition. On the left side of this region there is a noisy area with a drop in temperature caused by the abradable coating rupturing (Figure 5.11j). Although the measured temperature is on the abradable sample and does not provide information of the blade temperature, it provides accurate information on how the scratches, spotted in Section 5.2 as a result of the poor interaction between the bare matrix and the abradable, further develop and propagates to the surrounding when the incursion continues and eventually leading to the blade failure as investigated in this section. In addition, the temperature map aligns very precisely with the damaged region of the

blade due to the MAS low thermal conductivity. It is worth noting that the damage propagation did not extended to the very edge of the blade for any of tests where the blade went through an abrasive coating collapse.

Once abrasive coating rupture occurred, only the remaining non-failed regions (if any) can be assessed with the analytical tool in order to quantify the remaining cutting capability. Figure 5.19 presents the remaining blade volume above the matrix level per unit area for each of the different depth sections. For those zones where the abrasive coating was damaged and partially removed, only the remaining undamaged part was considered for the analysis. The sampled damaged areas provide a good estimation as they are still considerably larger than the grit scale. Results show a consistent trend where the remaining blade cutting capability decreases when the blade cuts deeper as well as for increasing incursion rates. This trend is also evident in Figure 5.10 where a higher number of incursion rates were considered. Finally, the variation seen in the results is likely caused because of using smaller areas for the analysis together with analysing the remaining absolute volume instead of the difference against to the blade volume prior being tested. That said, the approach still provides good insight in terms of the mechanism taking place.

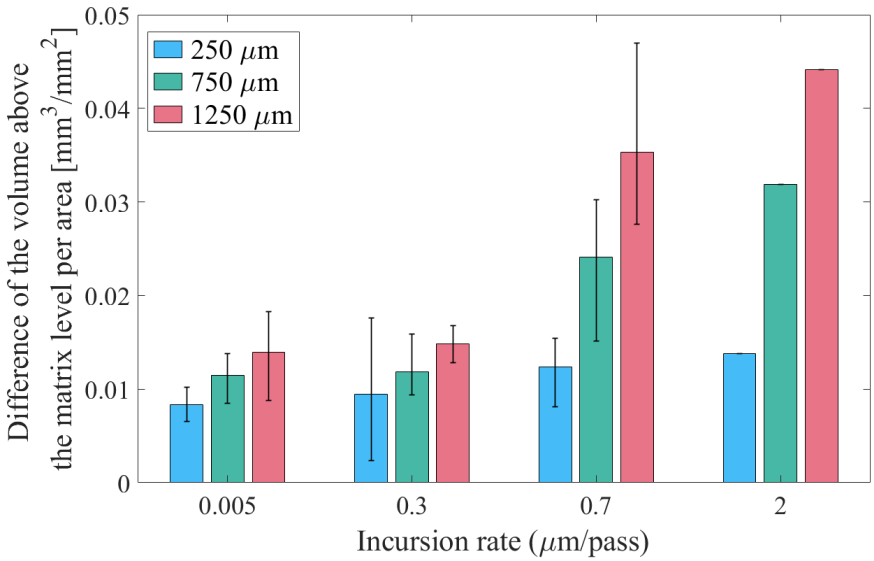

Figure 5.19: Difference of the volume above the matrix level per area for the stepped tests performed at 200 m/s and at different incursion rates, and divided by the three stepped incursion depths.

The grit wear analysis combined with the 2D temperature maps of failed blades clearly explains how electroplated tipped blades fail. Blades have a limited life that

is consumed faster or slower depending on the test conditions (Figure 5.19). It is worth noting that although the material removed is the same for every test, the grit wear is considerably reduced at decreasing incursion rates. Once the blade matrix starts to become damaged, seen as scratches (Figure 5.4), these develop and expand exponentially if the matrix keeps contacting the abradable, increasing temperatures and causing the surrounding areas to collapse (Figure 5.17). This failure process will be looked into in more details in the discussion section.

5.5 Discussion

In the investigation of blade failure observed in electroplated blades, it became evident that the root cause lies in the nucleation of scratches. These scratches stem from the bare matrix rubbing against ceramic samples due to the loss or absence of grits in a given cross section of the abrasive coating. This phenomenon is illustrated in Figure 5.4. The lack of grit results from either poor manufacturing or grit wear during the test, which is directly affected by the test conditions. When increasing the incursion rate, the blade experiences a higher workload (denoted from the force and temperature increase in Figure 5.8) as it needs to remove more material per pass. These elevated forces and temperatures intensify the grit wear, which can be broken down into either fracture mechanisms or grit pull-out when the stress condition is satisfied (as explained in Section 2.4.1.2).

As the test progresses and a given cross-section depletes its active grits, the matrix begins to rub against the ceramic, generating high temperatures. This thermal effect softens the surrounding matrix area, making the remaining grits more susceptible to detachment. The release mechanism due to matrix softening aligns with findings in (170), where grit anchoring became problematic at high temperatures. Once the failure mechanism initiates at a single scratch, it propagates on both sides until the end of the test or until the abradable coating breaks, losing engagement with the blade (Figure 5.11j). The thermal maps in Figure 5.18 underscore the severity of this as the temperature on the blade is higher than the one measured on the abradable. This is caused by the split of the heat generated by friction which leans towards the blade due to the extremely high thermal conductivity conductivity of c-BN and MCrAlY when compared to the MAS sample conductivity (43). In addition, the thermal camera is recording a single spot on the abradable samples whereas the blade travels over the whole contact arc, increasing its temperature by friction as it travels along the rub track.

Continuing on to the abradable side, no substantial difference is observed as long as the abrasive coating on the blade remains in place. In the second set of tests, the roughness of the track produced on the abradable was compared for different incursion rates. A noteworthy observation is the smoother profile of the track as the incursion rate increases, indicating a correlation with the decreasing cutting capability of the blades and a lower protruding profile due to grit wear. The change in G ratios (Figure 5.8) at the highest incursion rate suggests a variation in the dominant cutting mechanism.

When bare blade rubs against ceramic abradable, particles from the ceramic material that are in contact with the blade can either be sheared by the leading edge or compressed (240). If compression is high enough, it would make the particle detach from the matrix and release after the blade has passed. Abrasive coatings introduce an uneven surface where multiple points can either fracture the abradable or compress it. If ceramic material is fractured by the blade's leading edge, the material is shot forward (236). If the blade partially passes over and particles are sheared closer to the trailling edge, they cannot escape easily until the blade has exited the contact. Higher incursion rates imply more material need to be evacuated. The material not evacuated increases the normal forces due to compressive effects and introduce a third body abrasion mechanism that also contributes to both the blade wear and the abradable cut. In addition, higher grit densities aggravate the evacuation of the fractured abradable particles as there is less space to move freely and leave the interface between blade and abradable lining. This phenomenon of inefficient particle evacuation is also common in grinding wheels due to poor cooling, leading to overheating and wheel clogging (243).

Deeper incursions also intensify this phenomenon, due to the amount of material available to be collected, and the length to be travelled before releasing the trapped particles for a given pass. The fact that the profile of the abradable track becomes smoother at the same time as more material get trapped, suggests that apparent grit protruding heights become decreased, reducing the blade cutting efficiency, due to the trapped material forming an intermediate layer between the abrasive coating on the blade and the first layer of still attached material on the abradable sample. Some of the trapped material, variable with the test conditions, gets attached to the blade matrix as was observed in Figure 5.7 and 5.11. The changes in G ratio seen from the second set of tests (Figure 5.8) suggest that the blade gets more congested at increasing incursion takes until a upper threshold is reached where the rate is so elevated that the material is mainly removed by shear. In turn, blade congestion leads to a

third body abrasion mechanism which is inefficient, generates high amounts of heat and leads the blades to fail because of particle detachment triggered by overheating (Figure 5.11). This failure sequence aligns with the finding obtained from c-BN tipped blades against metal-based abradable linings (229) and c-BN grinding wheels with limited cooling and chip removal (243).

On the other hand, cyclic patterns in forces and temperatures arise for the lowest incursion rates (0.001 and 0.005 μm/pass) which indicate that the blade is far from saturated, as the blade disengages for several passes. The cyclic disengagement limits the material trapped at each pass, which helps to prevent, together with the low temperatures from the contact, the adhesion of ceramic material to the blade.

While wear mechanisms are highly dependant on incursion rate when using bare blades against metal-based abradables, where a lower incursion rates does not necessarily imply a smoother cut and lower damage produced on both the blade and the abradable (229; 236; 237), the performance of abrasive tipped blades against ceramic abradables directly correlates with the incursion rate and hence the workload that the blade experiences. Reducing the incursion rate produces a stable cut even though it occurs cyclically, and reduces the wear of the grits and material adhesion on the blade.

In terms of experimental conditions, the blades used in the three sets of tests adhere to Praxair Tribomet 429 standards and come from the same manufacturing batch, ensuring minimal variability. On the other hand, although MAS samples have been engineered under the same spraying parameters, the raw powder was not from the same batch between sets, which introduces variability with regards to the sample hardness. Although the influence of hardness is beyond the research scope, Table 5.5 demonstrates its impact on force and temperatures under standard test conditions. A corrected force value for stepped tests has been calculated for comparison, and shows values of force three halves those recorded when the blade was at 500 μm deep. With regards to the temperature, the hottest spot on the abradable is independent of size of the contact area and, therefore, does not need any correction.

Test set	Average Sample Hardness (R15N)	Maximum Force (N)	Maximum Abradable Temperature (°C)
Grit density	63.0	294.71	197.12
Incursion Rate	60.5	173.09	188.72
Incursion Depth	66.0	632.77 (Corrected)	312.76

Table 5.5: Abradable sample hardness, maximum force and maximum temperature averages of the tests performed at the standard condition (0.3 μm/pass and 500 μm) for each of the three analysis.

Whilst the influence of hardness on the wear mechanisms cannot be directly demonstrated with the sets of tests as sample hardness was not a considered variable. However, considering the direct relationship between forces/temperatures and wear mechanisms, hardness must aggravate the wear mechanisms and anticipate the blade failure as incursion rate and incursion depth increments do. This assumption about the effect of hardness on the blade has been made according to the outcomes from the research conducted on compressor abradable seal systems which pointed in that direction (229; 237). As such, the variation in hardness is irrelevant for the study of the wear mechanisms.

5.6 Conclusion

This study investigates TBT429 electroplated tipped blades against MAS ceramic abradables in cold operational scenarios as a precursor to elevated temperature analyses. Through a sequential analysis, scratch nucleation, resulting from absent grits in specific coating areas, has been identified as the root cause of blade failure for electroplated abrasive coatings. test conditions, especially incursion rate, significantly influence this phenomenon, intensifying forces, temperatures, and grit wear which become aggravated as the test progresses. The study establishes a correlation between incursion rate and cutting performance, emphasizing the need for incursion rate control as it defines the blade cutting mode and the associated blade damage. While maintaining controlled conditions, the study notes potential influence of sample hardness on forces and temperatures, suggesting future investigation opportunities. Overall, this

research advances our understanding of electroplated tipped blade behaviour, providing insights for design enhancements and prompting further exploration at more representative conditions of HPT environments with the addition of temperature as a variable.

Chapter 6

Cutting performance and wear mechanisms of DED tipped blades

6.1 Introduction

The current electroplated tipped blade solution, TBT429, exhibits some limitations when exceeding the standard conditions of both incursion rate and incursion depth simultaneously. Abrasive coatings on blades, as they occur in grinding wheels, have a limited lifespan. This threshold for failure has been reported to drop with temperature (170; 45). As soon as the cutting capability of a given blade is lost due to the depletion of grits in a certain region, the blade starts to fail as a result of the matrix contacting the abradable. The damage then develops and propagates exponentially as the matrix cannot withstand such elevated temperatures from that inefficient contact.

DED abrasive coatings, such as DELTA and IP75 blades, come as alternatives to overcome the electroplated limitations. Higher thermally stable materials, Inconel 792 for the DELTA solution and NiAlTaCr for the IP75 solution, are used for the matrix to retain the grits in place at higher temperatures. In terms of the abrasive coating structure, electroplated blades can be schematised as a flat layer of matrix where grits are deposited on top and get partially embedded (Figure 3.2). However, DED abrasive coatings form a crest where grits and matrix are all mixed together (Figure 3.3 and 3.4)). Grits stack up above each other, and the local rupture of the coating reveals fresh grits as it occurs in cold-pressed grinding wheels as it is represented in Figure 6.1. Therefore, understanding how this new structure performs, and more importantly, how it wears, is essential before establishing comparisons with electroplated blades or adding a new variable such as temperature to the system.

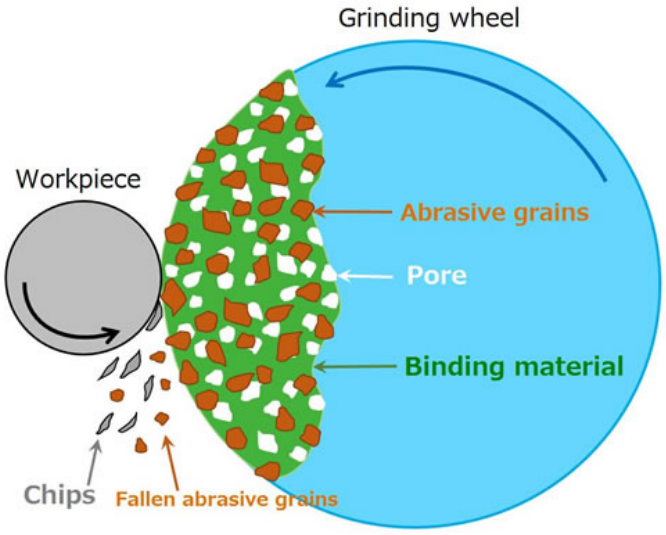

Figure 6.1: Schematic of abrasive grains stack-up in cold-pressed grinding wheels (171)

Due to the structure of the abrasive coating, the analytical tool developed in Chapter 4 cannot be used, because of the absence of a flat matrix as a reference plane. This leads to an inability to geometrically decouple the grits from the matrix for analysis. Additionally, the fact that new grits are exposed with coating rupture, further undermines the applicability of the approach. Nevertheless, a front stroboscopic camera is set to monitor the change in the blade profile for every pass. Post-processing of the captured images provides the variation of the projected area, which is a representative measurement of the blade wear considering the crest shape of DED blades. As the camera captures an image every pass, stepped samples for sampling blade wear are not required for the evaluation of the blade wear development.

The chapter is split into two parts according to the incursion depths tested. In the first part, the blades incur the standard depth of 500 μm at different incursion rates to assess cutting performance. In the second part, the blades are pushed to a deeper incursion of 1250 μm, at the same incursion rates as those in the first part of the chapter, with the aim of triggering failure mechanisms. Splitting the chapter into two parts with different incursion depths rather than using stepped samples is encouraged for various reasons:

- The blade wear can be monitored throughout the incursion without the requirement of stopping the test.

- It minimises the influence of the inherent heterogeneous character of abrasive tipped blades when the blade is partially in contact.
- It reduces the high cost of modifying sprayed samples due to the hard, but very brittle nature of sprayed MAS ceramic material.

As was previously detailed, the incursion rates considered in this chapter are based on the ones employed in Chapter 5, which represent incursions from the HPT sealing system in Rolls-Royce civil engines. However, the two lowest incursion rates, 0.001 and 0.005 μm/pass, have been replaced by a slightly higher rate of 0.02 μm/pass, as the forces were hardly distinguishable from the noise coming from backgrounding vibrations. On the other end, the highest incursion rate, 2 μm/pass, has also been omitted as little change was found compared to, 1.5 μm/pass, which is already over the typical values of the worst-case scenario (45).

In summary, the main goal of this chapter is to understand and assess the performance and wear mechanisms at room temperature conditions of abrasive tipped blades engineered by DED. The secondary goal is to compare the use of the two different matrix materials, Inconel 792 and NiAlTaCr, proposed by Rolls-Royce as solutions for abrasive tipped blades in HPT high-temperature environments.

6.2 Standard incursion test

For this first set of tests, both DED blade variants, DELTA and IP75, are tested at standard incursion conditions to understand and assess the performance of these new variants at different incursion rates representative of actual engine conditions.

6.2.1 Materials and methodology

The blades used in this section come from two independent batches manufactured according to the blade variant, DELTA and IP75. On the other hand, all the MAS abradable coating samples for this test have been sprayed in the same batch with a nominal thickness of the MAS layer of 800 μm.

The blades used together with the conditions they were tested at are summarised in Table 6.1.

Test	Blade	Blade speed (m/s)	Incursion rate (μm/pass)	Incursion depth (μm)
DEDIRT01 (a)	DELTA	200	0.02	500
DEDIRT02 (b)	DELTA	200	0.02	500
DEDIRT03 (c)	DELTA	200	0.3	500
DEDIRT04 (d)	DELTA	200	0.3	500
DEDIRT05 (e)	DELTA	200	0.7	500
DEDIRT06 (f)	DELTA	200	0.7	500
DEDIRT07 (g)	DELTA	200	1.5	500
DEDIRT08 (h)	DELTA	200	1.5	500
DEDIRT09 (i)	IP75	200	0.02	500
DEDIRT10 (j)	IP75	200	0.02	500
DEDIRT11 (k)	IP75	200	0.3	500
DEDIRT12 (l)	IP75	200	0.3	500
DEDIRT13 (e)	IP75	200	0.7	500
DEDIRT14 (f)	IP75	200	0.7	500
DEDIRT15 (g)	IP75	200	1.5	500
DEDIRT16 (h)	IP75	200	1.5	500

Table 6.1: Test matrix for the incursion rate analysis with DED blades.

6.2.2 Results

6.2.2.1 DELTA

Post test images of the DELTA blades and their corresponding abradable liner are shown in Figure 6.2. Images show a clean cut of the abradable with no material adhesion, although a smoother surface roughness at increasing incursion rates is evident.With regards to the blades, no signs of wear can be observed at this macroscopic level.

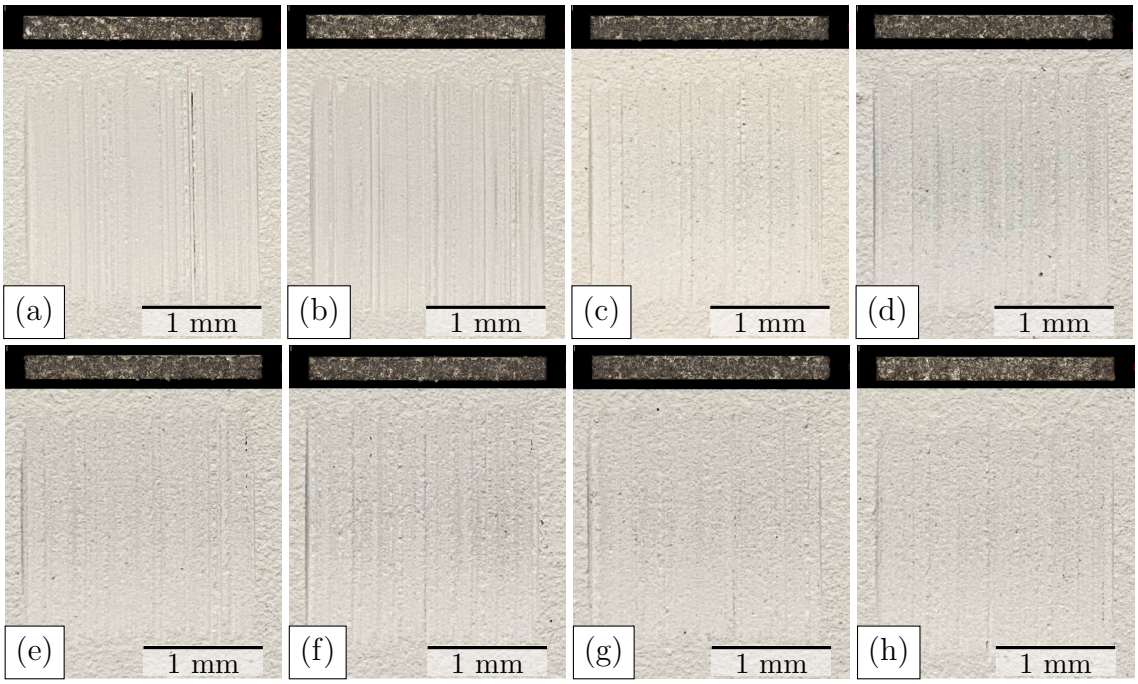

Figure 6.2: Post-test images of the abradable samples and DELTA blades (top view) for the tests performed up to 500 μm at 200 m/s and different incursion rates: (a,b) 0.02 μm/pass, (c,d) 0.3 μm/pass, (e,f) 0.7 μm/pass and (g,h) 1.5 μm/pass.

Due to nature of DED blades, where grits and matrix form together a conglomerate, identifying blade wear mechanisms by visual inspection is not as elementary as it is on electroplated blades. However, some local features are identified when focusing on specific areas of bladea as shown in Figure 6.3. Whereas no damage can be visually recognised on the blade at the lowest incursion rate (0.02 μm/pass, Figure 6.3a), local abradable material pick-up and matrix abrasion start to occur at increasing incursion rates, which is then maximised at the highest incursion rate (1.5 μm/pass, Figure 6.3b).

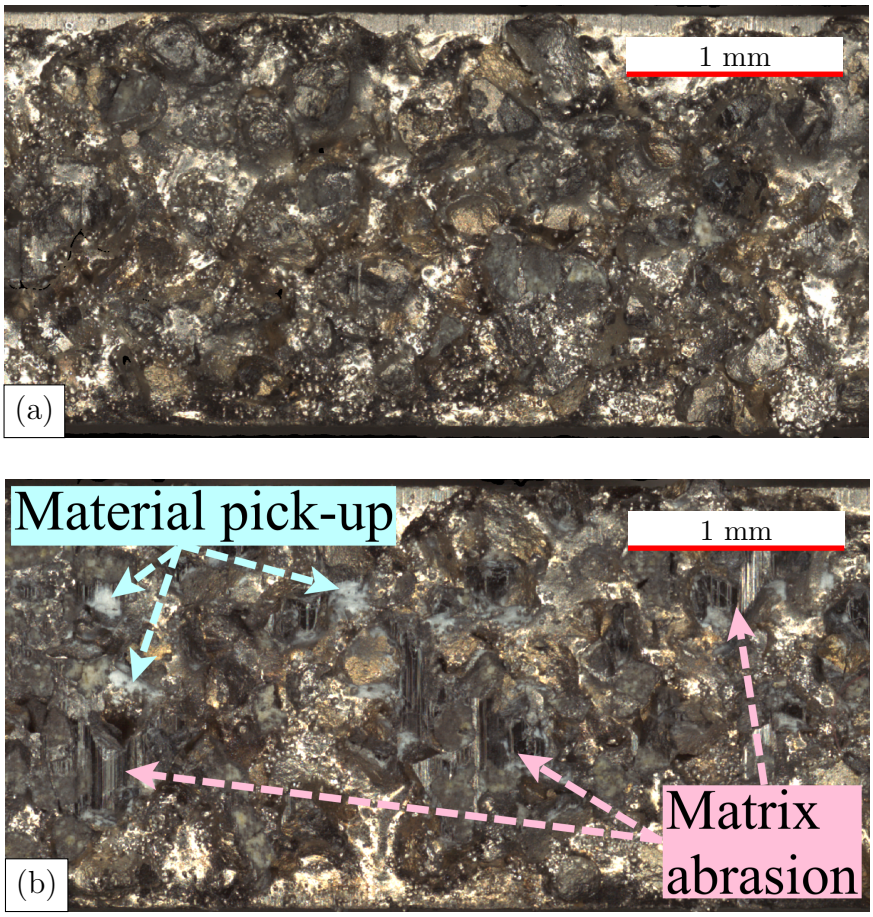

Figure 6.3: Wear features on the post-test DELTA blades for both ends of the studied incursion rate range: (a) 0.02 μm/pass and (b) 1.5 μm/pass.

With regards to the dressing mechanisms, Figure 6.4 shows how grits that were initially covered by either other grits or the metallic matrix (Figure 6.4a) get exposed during the test (Figure 6.4b). This dressing mechanism only takes place in DED coated blades and generates fresh grit edges during the contact that leads the cut.

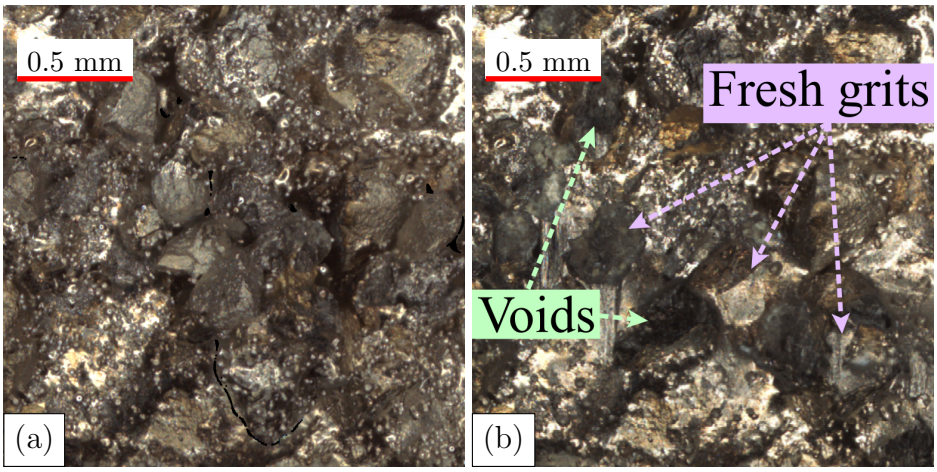

Figure 6.4: Example of the fresh grit exposure on DELTA blades as a result of the dressing mechanism: (a) pre and (b) post test images from the DEDIRT01 test blade.

As observed in Figure 6.5c and 6.5d, an initial rapid increase characterises the progression of forces and temperatures at the standard incursion rate, followed by a more gradual rise as the test unfolds. This initial increase corresponds to the non-linear increase of rub length at each pass in relation to the incursion depth, following equation 3.1. The intricate interplay of forces and temperatures during these initial stages is subject to potential influence from the dynamics inherent in the rig, and particularly within the short strikes of the initial passes. Figure 6.5a and 6.5b show how this increase occurs more progressively at the lowest incursion rate.

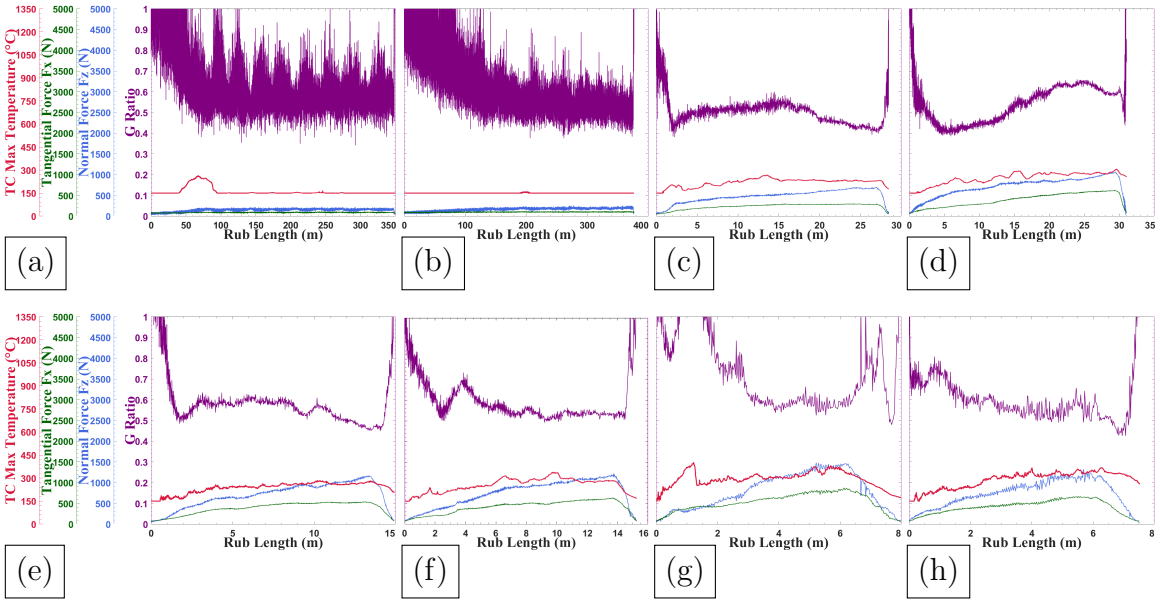

Figure 6.5: Force and temperature data for the tests performed with DELTA blades up to 500 μm at 200 m/s and different incursion rates: (a,b) 0.02 μm/pass, (c,d) 0.3 μm/pass, (e,f) 0.7 μm/pass and (g,h) 1.5 μm/pass.

At increasing blade workload, defined by the incursion rate, forces and temperatures not only are higher, but also show an overall linear increase punctuated by intermittent peaks and valleys. These fluctuations aligned with the local damage and material pick-up found at increasing incursion rates as shown in Figure 6.3. To further understand the development of abradable temperature arising from contact, an examination of thermal map from the rub track is crucial. The overall trend of the thermal maps generated by DED blades, shown in Figure 6.6, is for hot spots spread out along the blade length to occurwhich further develop throughout the test and become more severe at increasing incursion rate. The thermal map from the DEDIRT07 (g) test, conducted at 1.5 μm/pass and shown in Figure 6.3b, highlights the development of an intermittent contact inferred from the presence of hot spots which align with the abrasion features observed in Figure 6.3.

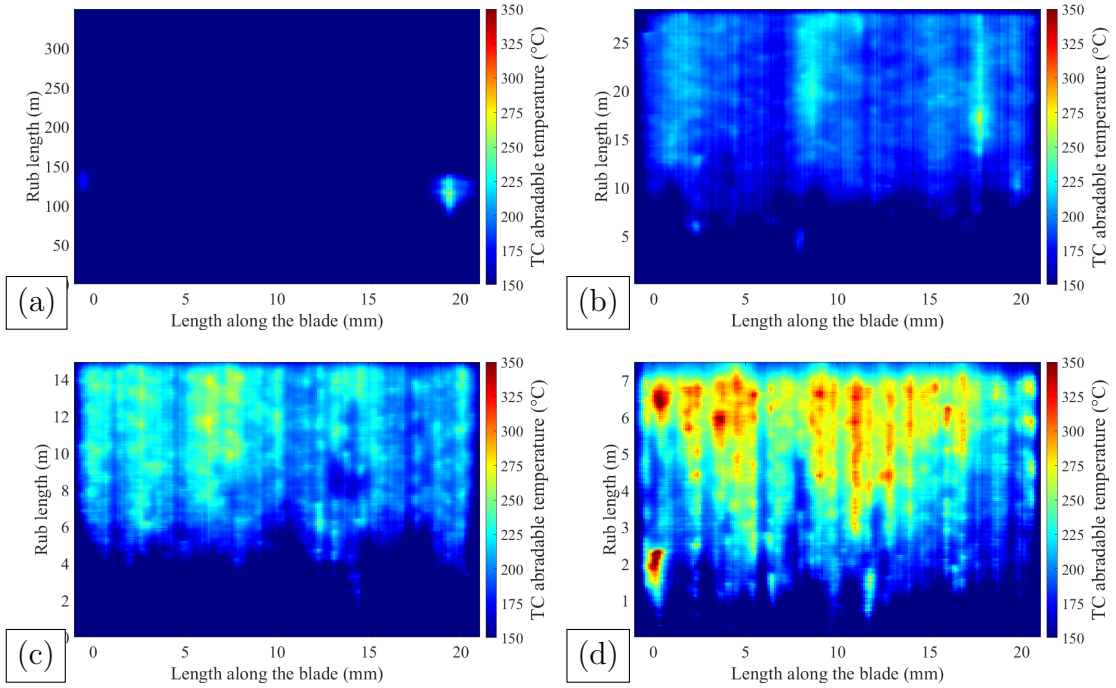

Figure 6.6: Abradable thermal maps from the tests performed with DELTA blades up to 500 μm at 200 m/s and different incursion rates: (a) DEDIRT01 - 0.02 μm/pass, (b) DEDIRT03 - 0.3 μm/pass, (c) DEDIRT05 - 0.7 μm/pass and (d) DEDIRT07 - 1.5 μm/pass.

These instances indicate that the blade intermittently experiences a more aggressive and less efficient interaction with the abradable, which then ceases because of localized ruptures in either the blade abrasive coating or the abradable. Analysing these thermal maps, and considering the interconnected relationship between temperature and forces through friction (244), suggests that hot spots occur together with a local force increase which is barely recognizable in Figure 6.5 due to the small size of the hot spots.

Although these intermittent contact occurrences are more severe at the highest incursion rate, they also occur at the lower incursion conditions (Figure 6.6). The DEDIRT01 test (Figure 6.5a), run at 0.02 μm/pass, exhibits an isolated increase of this temperature at the beginning of the test. When observing the thermal map of this test in Figure 6.6a, there is a region where the contact blade-abradable is more intense for a limited time, producing temperatures on the abradable track that exceed the minimum threshold for the thermal camera to record the temperature. This temperature rise fades away and no other hot spot appears again at that region.

Further processing the force data, the G ratio serves as a metric to quantify the severity of this intermittent behaviour throughout the test. At medium incursion rates (0.3 μm/pass, depicted in Figure 6.5c and 6.5d; and 0.7 μm/pass shown in Figure 6.5e and 6.5f), excluding values at the initial and final stages of the test attributed to contact engagement and disengagement, the G ratio remains relatively stable with occasional progressive incremental or decremental trends. However, at the highest incursion rate (1.5 μm/pass, as illustrated in Figure 6.5g and 6.5h), the G ratio exhibits greater fluctuation, which aligns with the thermal gradient observed in Figure 6.6d.

That said, considering the same assumptions taken in Section 5.3.2 to evaluate the G ratio as a single parameter across different test conditions, the values, represented in Figure 6.7, reveal no overall significant variation. This finding suggests that the same contact mechanics are maintained across the range of assessed incursion rate.

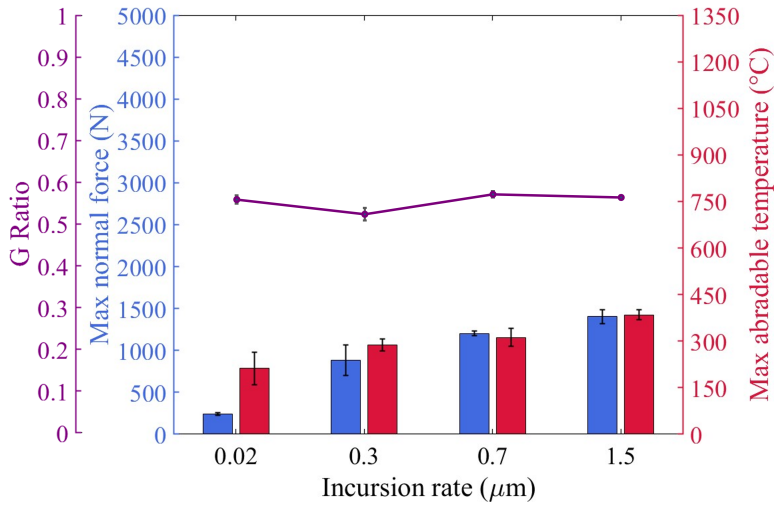

Figure 6.7: Comparison of the G ratio, the maximum normal force and the maximum temperature recorded on the abradable surface between the tests performed with DELTA blades up to 500 μm at 200 m/s and different incursion rates.

Comparing maximum normal forces and maximum temperatures across incursion rates in Figure 6.7, there is a notably lower maximum normal force at the lowest incursion rate (0.02 μm/pass), which then increases at 0.3 μm/pass and remains relatively stable at increasing incursion rates. Thereafter, considering this result in combination with the thermal maps from Figure 6.6, it can likely be deduced that these maximums occur locally at isolated areas of the blade.

When viewed altogether, the low variability in both the maximum normal force and maximum abradable temperature together with the similarity in starting G ratios

at increasing incursion rates, as depicted in Figure 6.7, suggests that the contact does not significantly intensify and the same contacts mechanics are preserved beyond the standard test condition of 0.3 μm/pass.

Figure 6.8a shows the wear produced on the blades as a result of the cut as well as its remaining abrasiveness. These results have been determined from the images captured by the front camera and following the data post-processing methodology introduced in Section 3.3.1.4 for DED blades. These findings indicate an increase in blade damage from 0.02 to 0.3 μm/pass, which then stabilizes into a relatively constant area variation up to the maximum incursion rate. This trend aligns with the observations made regarding the maximum forces and abradable temperature as it was initially anticipated. It is important to highlight that when DED abrasive coatings suffer a variation in the projected area, it does not necessarily occur due to grit damage, as matrix may be either detached or the blade suffer wear as a result of matrix abrasion as depicted in Figure 6.3b.

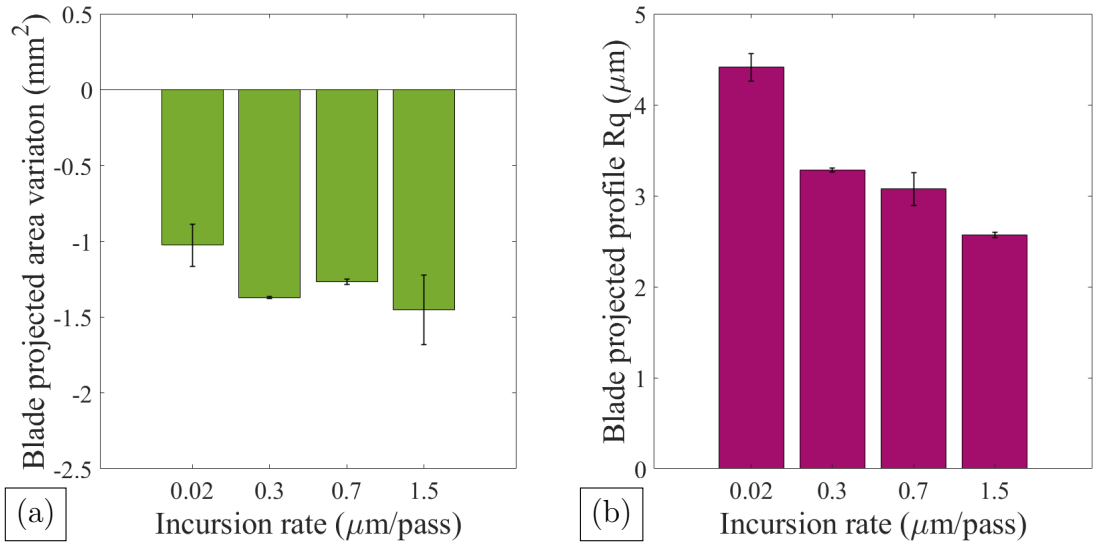

Figure 6.8: Measurements of the (a) projected area variation and (b) projected profile root-mean-square roughness (Rq) of the DELTA blades tested up to 500 μm at 200 m/s and different incursion rates.

The abrasiveness of DED blades can be further investigated by evaluating the root-mean-square average of the final projected profile roughness, Rq. This parameter reveals a noticeable smoothening of the profile with increasing incursion rates, as depicted in Figure 6.8b, which aligns with the higher level of matrix abrasion found for increasing incursion rates (Figure 6.3). In contrast to the volume of blade wear,

DELTA blades demonstrate a close relationship between the workload, defined by the incursion rate, and how they wear, measured by the profile roughness which subsequently influences local cutting performance.

Table 6.2 presents Rq values for the track profile of one rub track at each condition with DELTA blades, along with its corresponding blade profile Rq value. Both the blade and abradable roughness show a decreasing trend with increasing incursion rate, consistent with the visual observation of the roughness on the rub tracks shown in Figure 6.2. The disparity between blade and abradable values arises from the blade profile being a projection where multiple grits are superimposed on top of one another, whereas the abradable value is derived from a single cross-sectional profile.

Test	Incursion rate (μm/pass)	Blade projected Rq (μm)	Abradable Rq (μm)
DEDIRT01 (a)	0.02	4.564	64.006
DEDIRT03 (c)	0.3	3.261	44.320
DEDIRT05 (e)	0.7	2.893	42.897
DEDIRT07 (g)	1.5	2.544	36.627

Table 6.2: Root-mean-square roughness of the projected DELTA blade and the abradable track profile for one of the tests performed with DELTA blades up to 500 μm at each incursion rate.

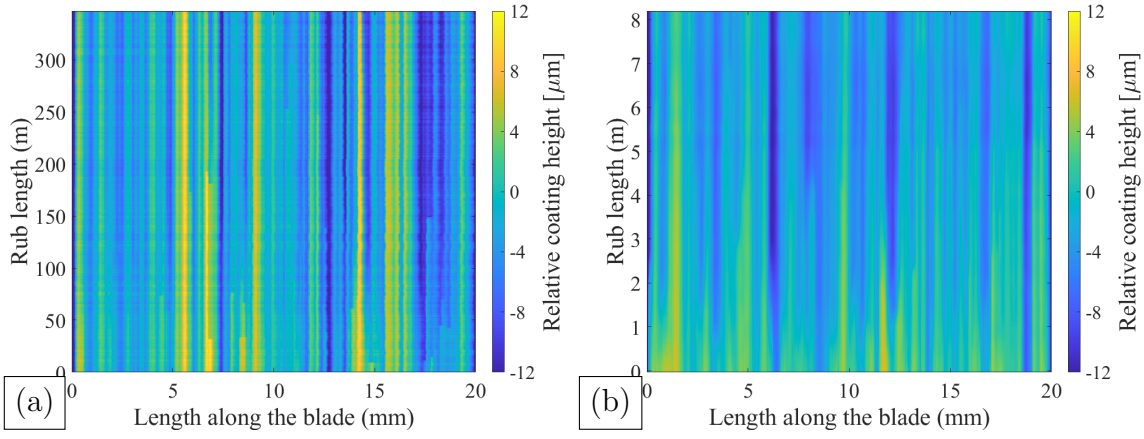

Figure 6.9: Relative profile height maps of the DELTA blades tested up to 500 μm at 200 m/s and different incursion rates: (a) DEDIRT01 - 0.02 μm/pass and (b) DEDIRT07 - 1.5 μm/pass.

Although the wear volume of the blade abrasive coating barely increases at higher incursion rates, the blade does become duller. Figure 6.9 shows how the blade profile develops through test. On the one hand, Figure 6.9b exhibit how the blade profile height becomes smoother throughout a test conducted at the highest incursion rate. In contrast, Figure 6.9a shows how the blade sharpness is preserved at the lowest incursion rate, although material removal still occurs. This variation in behaviour shows consistency with the wear mechanisms observed in Figure 6.3a.

6.2.2.2 IP75

In contrast to DELTA blades, IP75 blades demonstrated a poor performance. Post-test sample pictures in Figure 6.10 show that blades were completely abraded for the two incursion rates they were tested at. The following tests were omitted as the contact becomes rougher at increasing incursion rates and no valuable outcome would have been obtained from an imminent failed blade. In addition, totally failed blades compromise the rig's integrity as a consequence of the elevated contact forces present. Abradable samples show a very irregular track across the cutting direction with strong blade adhesion. When the amount of material adhesion is compared across the two incursion rates, a heavier impact of this mechanism is clearly observed at the lower incursion rate of 0.02 μm/pass (Figure 6.10a and 6.10b).

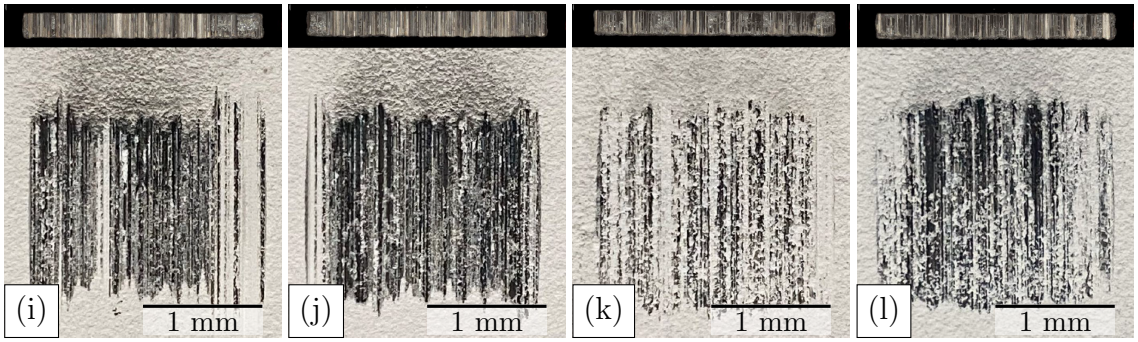

Figure 6.10: Post-test images of the abradable samples and IP75 blades (top view) for the tests performed up to 500 μm at 200 m/s and different incursion rates: (i,j) 0.02 μm/pass and (k,l) 0.3.

Figure 6.11 depicts the high-force and high-temperature environment that these tests result in and lead to the severe damage suffered in both samples. At the lower incursion rate of 0.02 μm/pass, force and temperature show a non-uniform cyclic behaviour. In turn, Figure 6.11a and 6.11b show how both variables increase very

rapidly, suggesting blade underperformance since the beginning of the test, followed a cyclic behaviour where short-duration valleys and peaks succeed each other. Valleys and peaks indicate moments when the blade minimizes contact with the abradable and a maximum blade/abradable interaction respectively.

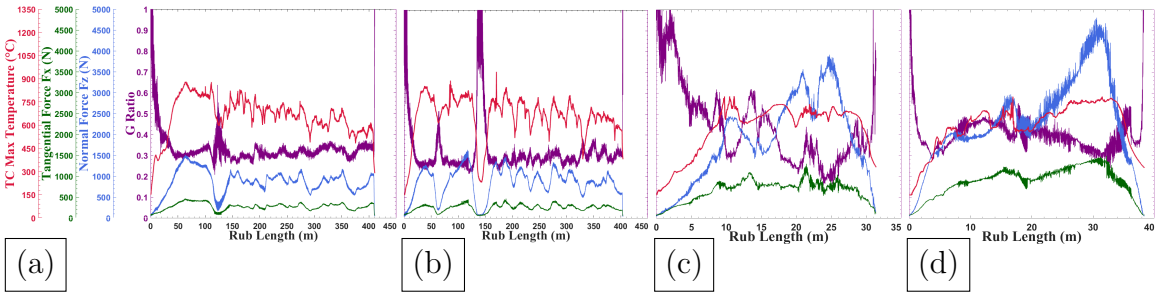

Figure 6.11: Force and temperature data for the tests performed with IP75 blades up to 500 μm at 200 m/s and different incursion rates: (a,b) 0.02 μm/pass and (c,d) 0.3 μm/pass.

A thermal map for each condition is shown in Figure 6.12, with distinct trends evident. At the lowest incursion rate, Figure 6.12a shows clearly distinguishable cyclic behaviour. The cyclic trend is preceded by a build-up period, where the whole section of the blade is in contact and the abradable temperature rises considerably. The blade then ceases contact all of a sudden and the aforementioned cyclic behaviour initiates, where the contact is intermittently ruled by the sides or the centre of the blade. Conversely, Figure 6.12a shows that this cyclic interaction do not take place at the standard incursion rate of 0.3 μm/pass, where a constant temperature gradient along the blade is maintained throughout the entire test.

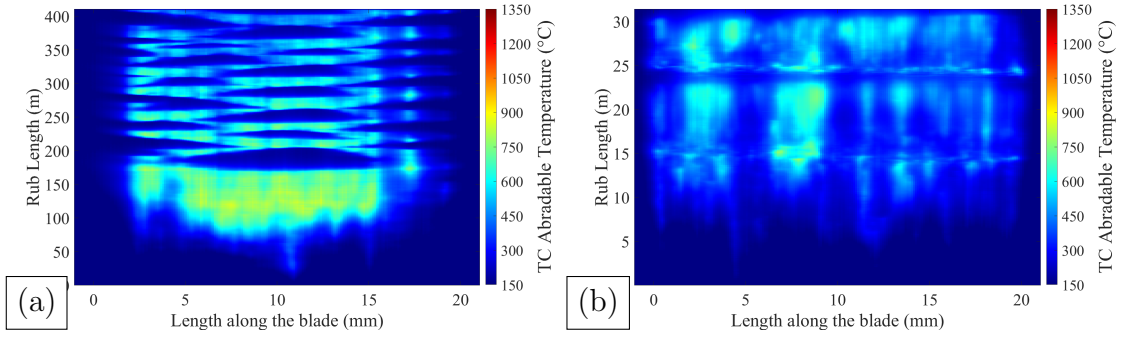

Figure 6.12: Abradable thermal maps from the tests performed with IP75 blades up to 500 μm at 200 m/s and different incursion rates: (a) DEDIRT09 - 0.02 μm/pass and (b) DEDIRT11 - 0.3 μm/pass

.

As shown in Figure 6.13, when comparing maximum normal force and maximum temperature on the abradbale, a relationship occurs where force increases, but temperature decreases at higher incursion rates. Whilst this result is unusual, these results can be understood when analysed together with the blade wear resulting from each incursion rate, which are shown in Figure 6.14.

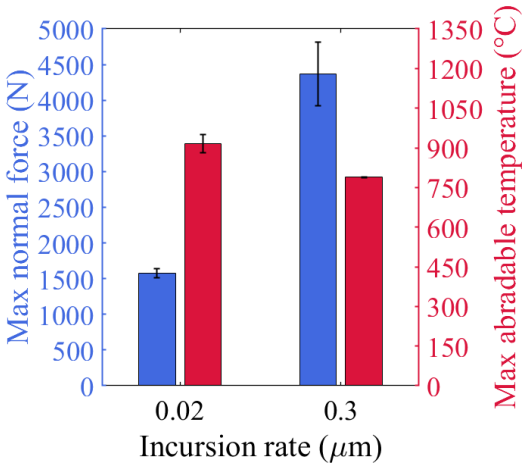

Figure 6.13: Comparison of the maximum normal force and the maximum temperature recorded on the abradable surface between the tests performed with IP75 blades up to 500 μm at 200 m/s and different incursion rates.

As shown in the figure, IP75 blades show significantly higher wear than DELTA blades when tested at equivalent incursion rates, aligning with previously observed IP75 blade failures. Blade wear remains consistent even during failure. A notable, more prolonged wear is evident in IP75 blades at the lower incursion rate when compared between the two rates. Despite the gentler incursion with the abradable at 0.02 μm/pass, the lack of cutting capability, illustrated by high contact forces in Figure 6.2, coupled with a slow incursion lead to a build-up cyclic pattern as depicted in the thermal data in Figure 6.12a. This is further supported by the poor G ratio at this incursion rate (Figures 6.11a and 6.11b). The suboptimal cutting performance significantly increases contact temperatures, which result in considerable blade wear as confirmed by the stripped pattern found on the surface of the IP75 blades (Figure 6.10).

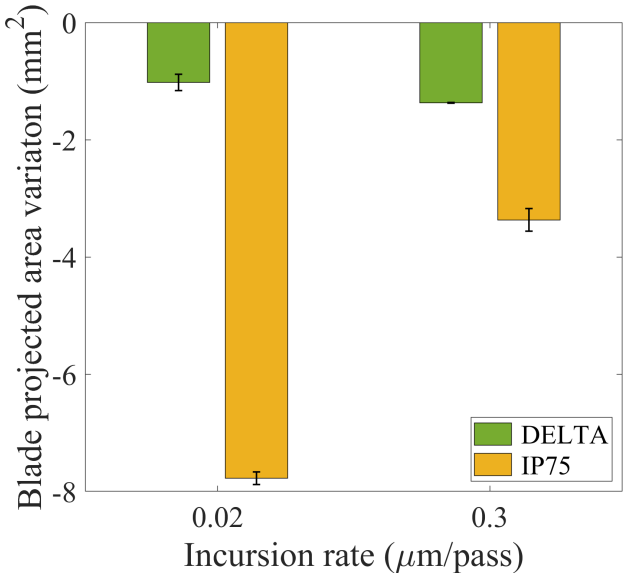

Figure 6.14: Comparison between the variation of the blade projected area suffered by the DELTA and IP75 blades, both tested up to 500 μm at 200 m/s, and 0.02 and 0.3 μm/pass.

Despite sharing the same manufacturing process, DELTA and IP75 blades exhibit vastly different cutting performances. IP75 blades performed poorly at both tested conditions, 0.02 and 0.3 μm/pass, resulting in substantial blade wear and material adhesion from the blade to the abradable sample. In contrast, DELTA blades delivered clean cuts with limited wear, aside from the inevitable and beneficial self-dressing, which increased at higher incursion rates. The 0.02 μm/pass rate demonstrated the most efficient cutting performance among the considered rates. Beyond the low incursion rate test conditions, DELTA blades show low sensitivity to incursion rate in terms of forces and blade wear but a noticeable reduction in blade abrasiveness was identified. As no indications of imminent failure were observed in DELTA blade tests, the next phase involves increasing the incursion depth to assess whether these DELTA blades experience or approach a failure mechanism.

6.3 Deep incursion test

The shallow incursion tests performed up to the standard incursion rate provide insights into their performance and wear mechanisms in DED blades, where the DELTA variant outperformed IP75, which catastrophically failed at the two incursion rates considered for this variant.

As the DELTA blades showed no signs of imminent failure, they are now tested to a deeper incursion depth, seeking the initiation of wear mechanisms that lead to failure. This investigation helps to understand the wear mechanisms that arise if the blade keeps interfering with the abradable longer than it is designed for.

Considering that the IP75 abrasive coating has already failed at the standard incursion rate and depth, testing them at deeper incursions lacks inherent significance. Therefore, they are omitted in this second part of the chapter.

6.3.1 Materials and methodology

The DELTA blades in this set come from the same batch as those used in the previous set, allowing a back-to-back comparison of the blades. However, another set of MAS abradable samples have been sprayed with a nominal thickness of 1500 μm to reach the new incursion depth of 1250 μm. Test conditions and blade details, in this case just DELTA, are summarised in Table 6.3.

Test	Blade	Blade speed (m/s)	Incursion rate (μm/pass)	Incursion depth (μm)
DEDIDT01 (a)	DELTA	200	0.02	1250
DEDIDT02 (b)	DELTA	200	0.02	1250
DEDIDT03 (c)	DELTA	200	0.3	1250
DEDIDT04 (d)	DELTA	200	0.3	1250
DEDIDT05 (e)	DELTA	200	0.7	1250
DEDIDT06 (f)	DELTA	200	0.7	1250
DEDIDT07 (g)	DELTA	200	1.5	1250
DEDIDT08 (h)	DELTA	200	1.5	1250

Table 6.3: Test matrix for the incursion depth analysis with DELTA blades.

6.3.2 Results

Figure 6.15 displays post-test sample images from the second set of DELTA blade tests, extending up to 1250 μm rub depth. An evident change in track smoothness is identifiable in the abradable samples. Figure 6.15a and 6.15b show well-defined and finely cut grooves are observed at the lowest incursion rate of 0.02 μm/pass, which gradually blur at higher incursion rates, leading to localized and limited spallation. Additionally, Figure 6.15e, 6.15f, 6.15g and 6.15h show that the edges of the track,

originally presumed to be outside the blade path, undergoes fracture as incursion rates increase above the standard one.

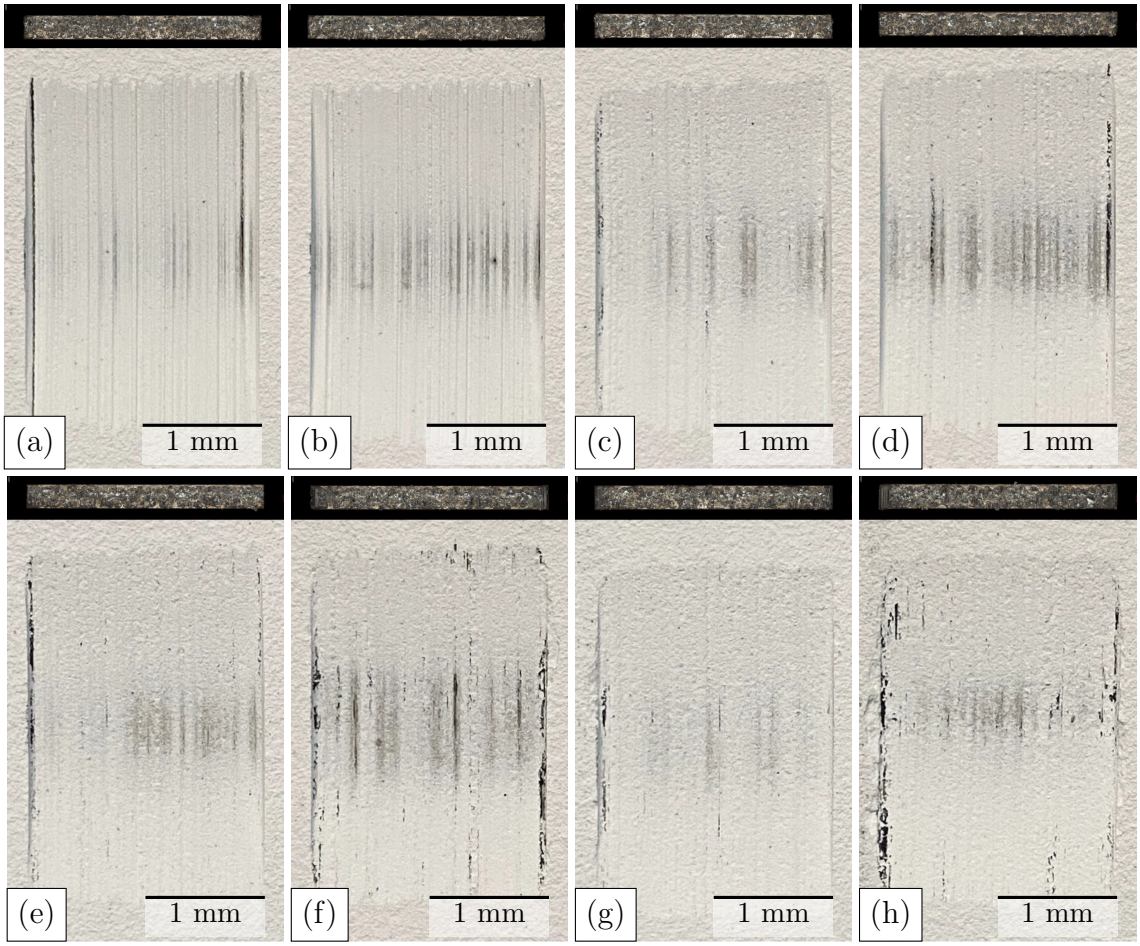

Figure 6.15: Post-test images of the abradable samples and DELTA blades (top view) for the tests performed up to 1250 μm at 200 m/s and different incursion rates: (a,b) 0.02 μm/pass, (c,d) 0.3 μm/pass, (e,f) 0.7 μm/pass and (g,h) 1.5 μm/pass.

Considering the images further, material adhesion occurs to varying extents in every test and presents in two distinct ways. The first involves blade-wide material adhesion at the center of the track, not extending to either the beginning or end of the rub track. The second, with a darker appearance, is confined to one or more lines in the cutting direction. The lighter material adhesion observed at the centre of the abradable maintains a constant length across all incursion rates.

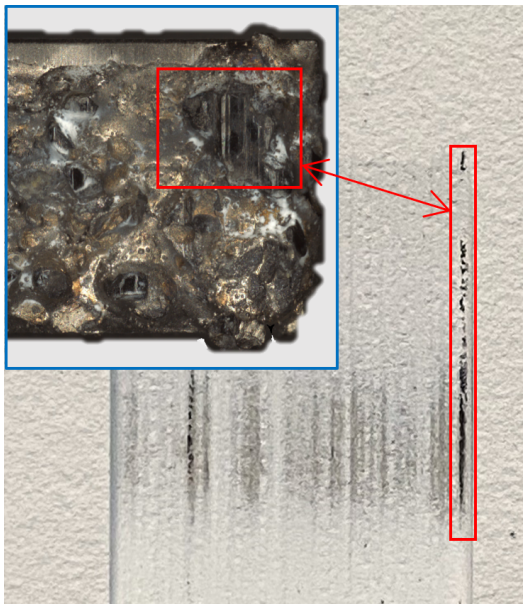

Figure 6.16: Details of the matrix abrasion produced on the blade and the material adhesion left on the abradable sample in DEDIDT04 test.



Figure 6.17: Post test images of the blades from the tests performed with DELTA blades up to 1250 μm at 200 m/s and different incursion rates: (a) DEDIDT02 - 0.02 μm/pass, (b) DEDIDT04 - 0.3 μm/pass, (c) DEDIDT06 - 0.7 μm/pass and (d) DEDIDT08 - 1.5 μm/pass.

Moving to the blade, the blade images in Figure 6.17 show minimal material pick-up for every incursion rate, with negligible differences observed across the considered range. Conversely, matrix abrasion significantly increases with higher incursion rates. Although matrix abrasion occurs across the entire blade section, it becomes more pronounced at the edges of the blade, as can be observed in Figure 6.17c and 6.17d.

The force and temperatures for this set of tests are plotted in Figure 6.18. As expected, both parameters increase with the incursion rate. At the lowest incursion rate (0.02 μm/pass), Figure 6.18a and 6.18b show a stable force development, where the maximum temperature on the abradable has occasional peaks, attributed to localized matrix abrasion causing a temporary temperature rise. Given the localized nature of this phenomenon within a finite area, the overall force of the contact is negligibly impacted.

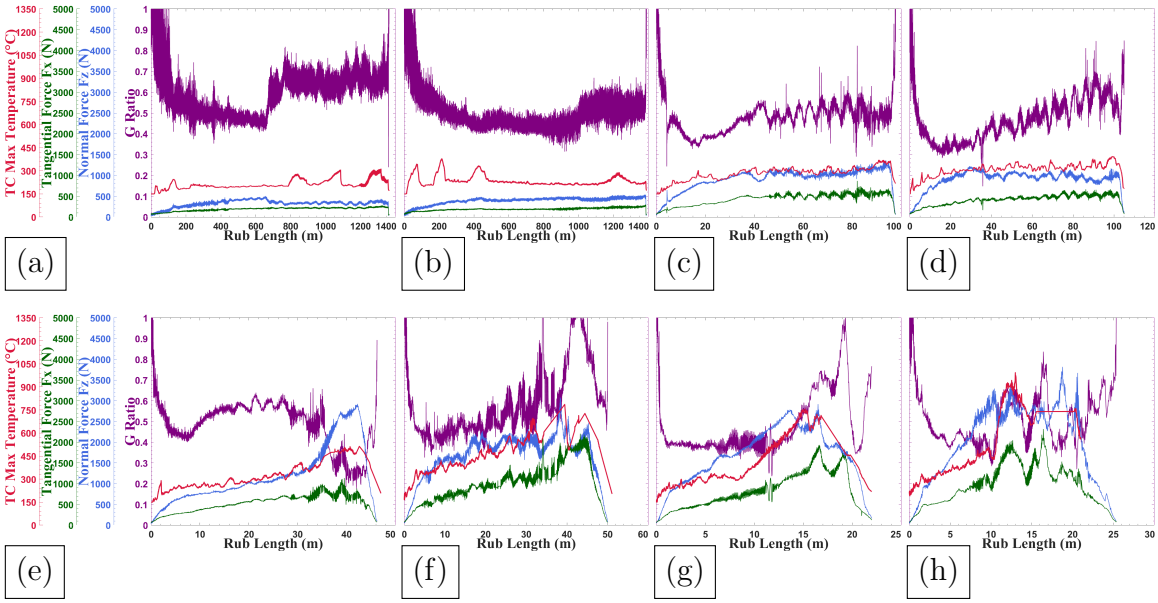

Figure 6.18: Force and temperature data for the tests performed with DELTA blades up to 1250 μm at 200 m/s and different incursion rates: (a,b) 0.02 μm/pass, (c,d) 0.3 μm/pass, (e,f) 0.7 μm/pass and (g,h) 1.5 μm/pass.

Under standard conditions (0.3 μm/pass), it is observed in Figure 6.18c and 6.18d that the contact rapidly stabilizes, resembling the behaviour at the lowest incursion rate. However, around halfway of the total incursion depth, cyclic behaviour emerges with a low peak-to-peak force value. This cyclic behaviour together with the matrix abrasion becomes more noticeable at this incursion rate (Figure 6.17) suggesting that forces and temperature go through an intermittent behaviour led by this abrasion mechanism. Additionally, there is a gradual increase in the G ratio during the tests,

indicating that higher tangential forces are generated due to a poorer interaction between the blade and the abradable.

Upon increasing the incursion rate beyond the standard condition (Figure 6.18e, 6.18f, 6.18g and 6.18h), the cyclic behaviour becomes overshadowed by other phenomena that induce high-force interactions as a result of the increase in the blade workload per pass. At 0.7 μm/pass, distinct behaviours emerge in each test. In the DEDIDT05 test (Figure 6.18e) the G ratio exhibits cyclic behaviour similar to that observed at the standard incursion rate. The divergence of the tangential force curve from that of normal force towards the end of the test, coupled with the clean cut observed on the abradable, suggests that the blade gets congested, promoting a three-body abrasion mechanism.

Conversely, when analysing the forces of the other test conducted at 0.7 μm/pass, Figure 6.18f, the tangential component dominates and intercepts the normal forces (increasing the G ratio) at the test's conclusion. The blade from this test experiences significant abrasion on the edges as previously observed in Figure 6.17c.

Thermal maps from the tests DEDIDT04 and DEDIDT06 are shown in Figure 6.19 to highlight the transition in the force data from 0.3 to 0.7 μm/pass. The abradable thermal map for the DEDIDT06 test in Figure 6.19b reveals hot spots intermittently develop near the edges on both sides, where abrasive wear has been identified. In contrast to the outcomes from the DEDIDT04 test, neither significant matrix abrasion in Figure 6.17b nor hot spots in Figure 6.19a are observed.

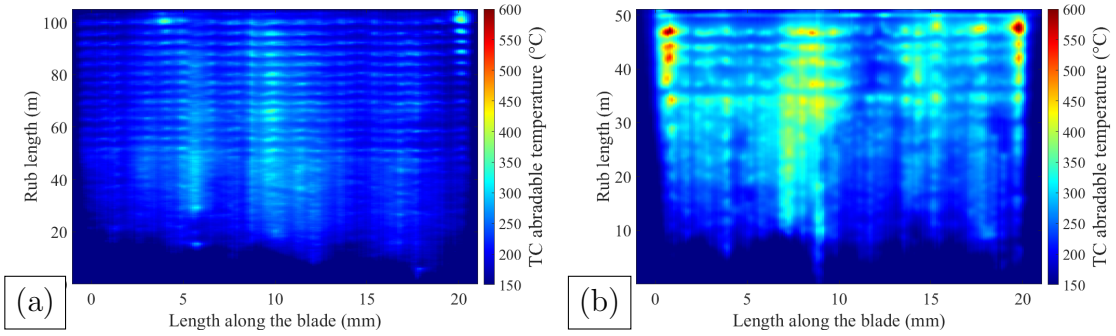

Figure 6.19: Abradable thermal maps from the tests performed with DELTA blades up to 1250 μm at 200 m/s and different incursion rates: (a) DEDIDT04 - 0.3 μm/pass and (b) DEDIDT06 - 0.7 μm/pass.

As shown in Figure 6.18g and 6.18h the variation in force data and wear mechanisms seen between the two repetitions at 0.7 μm/pass also takes place at 1.5 μm/pass.

At the highest incursion rate, forces considerably increases and significant spallation and rupture of the abradable take place, especially on the track edges, as seen from the DEDIDT08 test samples in Figure 6.15h. Figure 6.20 clearly shows the discrepancy between repetitions, highlighted by the error bars at the two highest incursion rate tested.

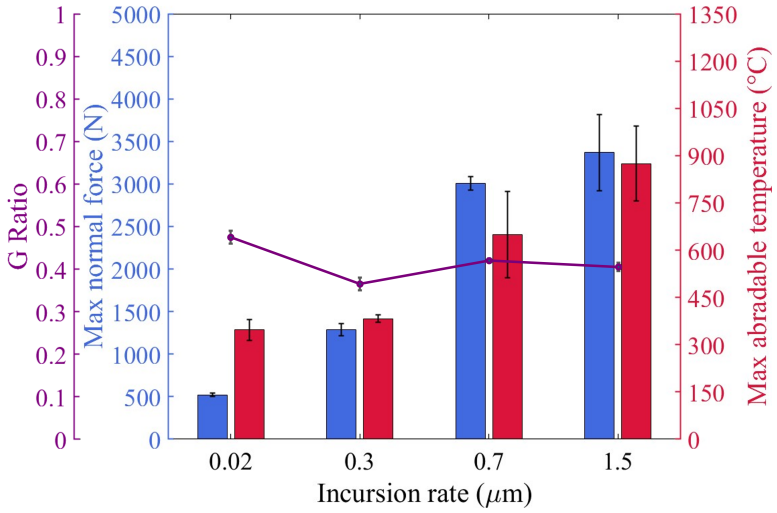

Figure 6.20: Comparison of the maximum normal force and the maximum temperature recorded on the abradable surface between the tests performed with DELTA blades up to 1250 μm at 200 m/s and different incursion rates.

Although G ratios experience considerable variation as the test progresses for this deep incursion, they still can be compared as a single parameter following the same assumption considered in Section 5.3.2. This definition of the G ratio determines the interaction between blade and abradable at the beginning of the test once contact is stabilised and he blade has not suffered significant damage. As might be expected, Figure 6.20 represents the G ratio trend which does not differ from the one obtained for the standard depth test, as the incursion depth does not affect it. That said, the absolute values are offset from the ones obtained in the previous section because of using abradable coating samples coming from a different manufacturing batch.

Blade wear, defined as the variation in the projected front area, has been measured and plotted in Figure 6.21a. The results correlate with the degree of material adhesion observed in Figure 6.18. Higher material adhesion on the abradable corresponds to increased wear on the blade. This trend provides confidence in the alignment between post-test images and the development of the G ratio in determining whether the abrasion mechanism is third-body abrasion or matrix abrasion.

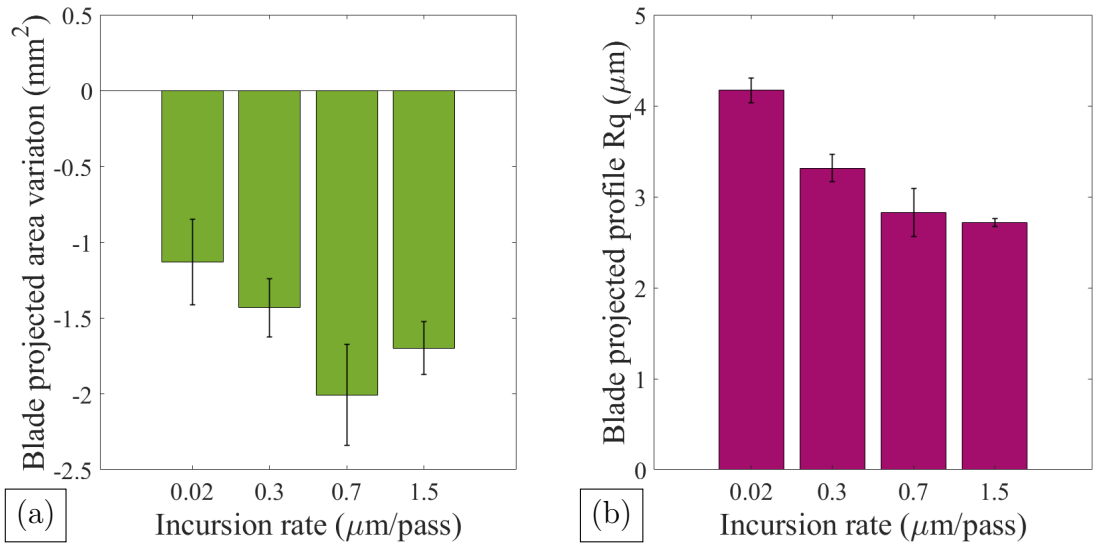

Figure 6.21: Measurements of the (a) projected area variation and (b) projected profile root-mean-square roughness (Rq) of the blades tested up to 1250 μm at 200 m/s and different incursion rates.

In contrast, Figure 6.21b shows the abrasiveness of the blade coating after testing, measured as the Rq surface roughness of the front projected profile, which exhibits a stronger dependence on the incursion rate. Despite experiencing a higher degree of wear at 0.7 μm/pass, the blade retains its abrasiveness slightly better than when tested at 1.5 μm/pass. This abrasiveness also correlates directly with the Rq roughness of the abradable profile, as illustrated in Table 6.4 for one test at each incursion rate.

Test	Incursion rate (μm/pass)	Blade projected Rq (μm)	Abradable Rq (μm)
DEDIDT2 (b)	0.02	4.035	46.021
DEDIDT4 (d)	0.3	3.162	39.313
DEDIDT6 (f)	0.7	3.092	37.071
DEDIDT8 (h)	1.5	2.759	31.737

Table 6.4: Root-mean-square roughness of the projected DELTA blade and the abradable track profile for one of the tests performed with DELTA blades up to 1250 μm at each incursion rate.

The performance of DELTA blades at deeper incursions has been shown to be

dependent on the incursion rate, with both three-body abrasion and matrix abrasion mechanisms coexisting, with which mechanism dominates incursion rate dependent. The heterogeneous architecture of DELTA blades also adds complexity, blurring the transition between these mechanisms. While setting a clear threshold is challenging, the test outcomes clearly indicate which type of abrasion had a greater impact on the contact. Additionally, though limited damage was observed on the edges of the blades, none of the blades approached imminent failure.

6.4 Discussion

The tests conducted with DELTA blades reveal a overall good performance with clean cut of the abradable aover the range of incursion rates considered in this chapter. Forces, temperatures, and the wear on the blades show low dependency on the workload, defined by the incursion rate during the shallow tests. However, this dependency becomes more critical as the DELTA blades incur deeper. Elevated forces and temperatures, resulting from an increasing incursion rate, are mainly generated in areas where the bare matrix contacts the abradable. This view is determined from the structure of DED abrasive coatings, where the grits are mixed with the matrix and do not necessarily protrude over it. These localized contacts create hot spots on the abradable, recorded by the thermal camera, indicating high friction due to inefficient cutting interactions and local blade abrasion.

The generation of hot spots is an intermittent mechanism that develops and increases in severity until either the abrasive coating or the abradable undergoes a local fracture. When a fracture occurs on the blade, fresh grits below the first layer engage with the abradable lining, a mechanism known as dressing. This dressing mechanism, reminiscent of grinding wheels manufactured by cold or hot press, renews grits by locally fracturing the abrasive material after the protruding grits have worn out (191). On the other hand, if the abradable coating breaks, that local damaged area on the blade re-engages the abradable as the test progresses and will reinitiate an inefficient local cut.

The dressing mechanism observed is highly influenced by the incursion rate, despite the amount of wear having been similar for every incursion rate considered in this study. Lower incursion rates produce rougher blade profiles and lower amounts of matrix abrasion which, therefore, generate lower forces and temperatures not only because the blade has to remove a lower amount of material per pass, but also because the interaction between blade and abradable is more efficient. Lower incursion rates

lead to lower forces and temperatures because of the reduced material to be removed per pass. Although, it is not possible to know the temperature of the blade in the LSR, this temperature is higher than the one recorded on the abradable due to the difference between the thermal conductivities as modelled in (43). Higher temperatures on the abrasive coating promote softening of the metal-based matrix which leads to a more ductile fracture that ends up producing the local abraded areas. In contrast, keeping the temperature from the contact low, encourages a more brittle fracture which produces new fresh edges as it has been demonstrated with the low level of abrasion and high post-test abrasiveness found in the blades from the low incursion rate tests. At the same time, a lower incursion rates implies a higher number of passes to remove the same volume of material. The considerably higher number of passes at the lowest incursion rate (0.02 μm/pass) suggests that the abrasive coating undergoes a fatigue mechanisms where cracks occurs and develop through consequent strikes.

None of the DELTA blades experienced total or partial failure at any of the incursion rates or depths. However, a failure mechanism initiated in the deepest tests for the two highest incursion rates, 0.7 and 1.5 µm/pass. The abrasive coating began to deteriorate at the edges of the blade, exhibiting slightly higher inward development for the highest of the two incursion rates, as depicted in Figure 6.17c and 6.17d. This mechanism initiates due to a local inefficient cut where the matrix ends in contact with the abradable, as explained earlier. The occurrence specifically at the blade's edges is attributed to the generation of heat not only by the contact of the normal face, but also from the side faces rubbing against the walls generated on the abradable track. This adverse thermal environment prompts the abrasive coating to fail sooner. A similar pattern of the sides of blades leading the failure initiation was also observed and further explained in compressor sealing solutions where bare blades rub against metal-based abradable coatings (229; 237).

On the abradable side, two distinct types of material transfer from the blade to the coating track were observed during the deeper incursion tests with DELTA blades. The first, had a darker appearance, following single cut lines due to local matrix abrasion on the blade. The second, with a lighter appearance, occurred across the entire width of the track for every tested incursion rate. This is believed to be a result of unintentionally approaching the intermediate layer of YSZ beneath the MAS topcoat which is denser and therefore harder (45).

Moving to IP75 blades, they underperformed at the two conditions they were tested at, 0.02 and 0.3 μm/pass, in contrast to DELTA blades which exhibited a

completely clean cut and constant forces and temperatures for the same conditions. From the experience gained throughout DELTA tests, the wear mechanisms and blade damage do not vary from the standard condition at previously considered increasing rates, they only become more severe. Therefore, higher incursion rates were omitted to avoid compromising the rig integrity.

Although IP75 blades failed shortly after the start of the test at the two considered conditions, the failure process was slightly different. Whereas, the material adhesion on the abradable and blade wear was significant at the standard incursion rate, these phenomena intensify at the lowest incursion rate where a gentler interaction could have been expected. This poorer performance at low incursion rates is likely due to the low heat release with the low amount of material removed per pass. This outcome has also been observed in compressor tip sealing systems when the blade do not remove the abradable material effectively and keep building up heat in the abradable coating (236; 237). The cyclic behaviour observed at the lowest incursion rates also promotes the temperature increment as no or little material is removed during the build-up process, allowing the heat travel reaching deeper layers. In addition, reaching higher temperatures enhances the material deposition on the abradable due to high temperatures on the blade.

Comparing the performance of the two versions of the DED manufactured abrasive coatings which share the same type of grits but use different matrix material, it is clear that IP75 did not perform at the same quality that DELTA blades did. Assuming that both types of blade have been manufactured appropriately, the only difference is the material employed for the matrix whose function is to hold the grits in place while the contact occurs. Considering the early failure of the IP75 blades, it suggests that the matrix does not succeed at holding the grits which are easily released as soon as the contact starts, leading to the unfavourable situation where the bare matrix rubs against the abradable. At the same time, according to material properties, IP75 bonding possesses higher strength and thermal stability compared to DELTA maatrix as reviewed in Section 2.4.2. To understand why the grits are easily released in IP75 blades, futher investigation on the grit matrix interface under aggressive thermal environments is required as was done for electroplated TBT429 blades in (43; 40; 238).

Likewise it was highlighted in the previous chapter, that the hardness of the two batches of MAS samples tested in this chapter are also different as they were manufactured separately, making results not comparable across the two different set of test. That said, considering the hardness relationship with forces and temperature drawn

in Section 5.5 together with the fact that the same material is used for the abradable samples, higher hardnesses are expected to produce higher forces and temperatures, as well as to trigger the failure mechanism more rapidly.

With the performance of both electroplated and DED tipped blades analysed as well as how the wear mechanisms lead them to their end of life at room temperature investigated, the next step in this research is to test these blade architectures at both room and high temperature condition, understand the temperature effect on the the wear mechanisms and compare the architectures' performance across the same batch of MAS sample.

6.5 Conclusion

In summary, the exploration of DED abrasive coatings, specifically DELTA and IP75 blades, provides valuable insights into their performance and wear characteristics in high-temperature environments.

Structural differences between electroplated and DED coatings play a crucial role in wear behavior, highlighting the necessity of understanding the unique crest structure formed by DED coatings. This structural difference, discussed in detail in the literature review in Section 2, played a pivotal role in influencing wear mechanisms and performance outcomes.

The tests with DELTA blades revealed consistent results, where forces, temperatures, and wear shows a low dependency with incursion rate during shallower tests but becoming critical at deeper incursions. During the abradable cut, blades wear and suffer either or both from local fracture or abrasion. Due to the DED coating structure, local fracture produces a dressing mechanism, where fresh grits are revealed and continue cutting the abradable. Lower incursion rates enhance the dressing mechanisms as a result of maintaining a low temperature on the blade and a fatigue mechanism. On the other hand, higher incursion rates promote abrasion spots on the matrix due to the elevated temperatures generated from the contact. Matrix abrasion is an indicator of poor interation.

For IP75 blades, underperformance occurred at the shallower tests. The comparison between DELTA and IP75 blades suggests that matrix material employed in IP75 fails to hold the grits effectively, leading to early failure. For a deeper understanding of why NiAlTaCr fails at holding the grits during the contact, in contrast to Inconel 792 (DELTA), further material focused research is required.

Chapter 7

TBT429 vs DELTA blade performance at high temperature

7.1 Introduction

The cutting performance of electroplated and DED-tipped blades has been assessed across a spectrum of incursion rates and depths in the preceding chapters, all conducted under ambient temperature conditions. In these chapters, an in-depth analysis of the local wear mechanisms occurring during interactions with an abradable lining has been successfully explored. The understanding of these wear mechanisms and their relationship to a series of key variables has led to a comprehensive characterization of overall blade performance. In the preceding tests, the performance of the blades was evaluated in isolation from external sources of heating, a departure from the conditions encountered in gas turbines where both sides of the abradable seal are subject to heat transfer from the hot gas flow. Nonetheless, the isolation of variables in these intricate tribological systems is imperative for establishing relationships between performance and test conditions. The insights obtained from the tests on electroplated and DED-tipped blades under cold conditions have laid the groundwork for understanding their cutting behavior before introducing temperature as a new variable.

As the LSR does not posses any capability to introduce an external source of heating, the High Temperature Rig (HTR) has been developed to introduce such capability in the abradable research group in the University of Sheffield. The HTR (full description available in Section 3.3.2) heats up the blade by means of an induction coil as the hot gasses would do inside a gas turbine. There is no need to heat the MAS liner as its properties have been reported invariable for the HPT range of temperature

(166). The induction coil surrounds the disc circumference except for the section where the stage with the abradable lining moves towards the spinning blade.

The two main objectives of this chapter are motivated by the introduction of this new heating capability. The first aim is to assess the impact that an external source of heating on the blade has on the general blade/abradable lining interaction as well as to consider temperature as a variable in the context of incursion, where the latter has been demonstrated to be critical.

The second of these objectives is to analyse and compare the performance of both TBT429 blades and DELTA blades, which have been demonstrated to be a much better DED alternative than IP75 when tested against MAS lining samples at ambient condition. This back-to-back evaluation under the same batch of MAS lining samples will allow the feasibility of new DED variants against the current electroplated tipped blade baseline to be assessed.

7.2 Materials and methodology

In this set of tests, both TBT429 and DELTA blades are tested at 100 m/s up to a depth of 1250 μm at a range of incursion rates and two heating condition. Although the blade speed at every test performed in the LSR was 200 m/s, which is closer to the typical blade tip speeds in gas turbines (45), the HTR cannot currently deliver speeds above 100 m/s efficiently. That said, studies about abradable systems in compressor stages have report that the blade speed influence is minimum when it exceeds 50 m/s (229; 236; 237).

Although the temperature of the blade is accurately controlled and measured during the static pre-heating, this is not the case when the blade starts spinning. The induction coil is used at maximum settings, but the windage the blade experiences at 100 m/s manages to cool the blade surfaces down. Nevertheless, the core is assumed to remain hot from the soaked heat and creates a temperature gradient across the blade. As the infrared pyrometer records the temperature from one of the blade side, the pyrometer reading is always lower than the averaged blade temperature. However, this measurement enable blade temperatures to be compared between different tests as long as the blade speed remains the same. The test sequence is optimised to engage the contact with the abradable as soon as the blade has reached the set speed, thus minimising the heat loss due to windage. Once the contact starts, the heat released from friction together with the heat sunk into the blade and blade holders during the pre-heating phase helps to raise the surface temperature back again. The HTR is

currently commissioned to pre-heat the blade up to 760 °C according to Figure 3.22 as it is the maximum temperature achievable without compromising the disc integrity. Higher temperatures will not be achieved during the pre-heating phase as the Ti disc is compromised by the heat sunk into it during the pre-heating stage and high-stress regions experience a yield strength reduction (45).

Due to the complexity in maintaining a constant temperature on the blade throughout the test, only two heating conditions will be considered in this test batch: no pre-heating nor heating during the test, and a second condition of pre-heating up to 760 °C according to Figure 3.22 and keeping the induction coil heating at maximum power during the test.

Regards to the incursion rates, the blades are tested at 0.3, 0.7 and 1.5 μm/pass, where the latter case was the incursion rate at which TBT429 blades started to develop failure wear mechanisms at the same incursion depth in Chapter 5 and no performance improvement is presumed to occur at the hot condition. Likewise, the lower incursion rates considered in the other chapters are omitted in this case as the interactions were excessively smooth and no failure mechanisms are expected to be triggered even at the hot condition. Additionally, an extra test point at 1.0 μm/pass is added for resolution. Given the high-stress and high-temperature conditions to which the disc is subjected during the hot tests, a total of 50 tests have been authorized, by a Rolls-Royce stress analyst. These 50 tests are distributed among various projects; consequently, the test matrix for this chapter must be thoughtfully selected.

7.3 Results

7.3.1 TBT429

The test performed with TB429 blades are summarised in Table 7.1. Considering the consistency and good performance observed with TBT429 blades at 0.3 and 0.7 μm/pass in the cold tests (as it will be introduced shortly in Figure 7.2), the number of repetitions was reduced to a single one at cold condition for higher incursion rates. At the same time, due to blade failure in hot condition at the highest incursion rate, 1.5 μm/pass, as observed in Figure 7.1m, no repetition was conducted to preserve samples at conditions where a total blade failure is identified. In addition, total blade failures introduce unstable dynamics out of the force range the rig is designed for, and as such should be avoided where possible.

Test	Blade	Test type	Blade speed (m/s)	Incursion rate (μm/pass)	Incursion depth (μm)
HTEPT01 (a)	TBT429	Cold	100	0.3	1250
HTEPT02 (b)	TBT429	Cold	100	0.3	1250
HTEPT03 (c)	TBT429	Hot	100	0.3	1250
HTEPT04 (d)	TBT429	Hot	100	0.3	1250
HTEPT05 (e)	TBT429	Cold	100	0.7	1250
HTEPT06 (f)	TBT429	Cold	100	0.7	1250
HTEPT07 (g)	TBT429	Hot	100	0.7	1250
HTEPT08 (h)	TBT429	Hot	100	0.7	1250
HTEPT09 (i)	TBT429	Cold	100	1.0	1250
HTEPT10 (j)	TBT429	Hot	100	1.0	1250
HTEPT11 (k)	TBT429	Hot	100	1.0	1250
HTEPT12 (l)	TBT429	Cold	100	1.5	1250
HTEPT13 (m)	TBT429	Hot	100	1.5	1250

Table 7.1: Test matrix for the analysis of the influence of temperature and incursion rate on the performance of electroplated (TBT429) blades.

The overall images of the blade and abradable samples are displayed in Figure 7.2. As observed in Figure 7.1a, 7.1b, 7.1e, 7.1f, 7.1i and 7.1l a clean cut with no or very limited damage on the blade was obtained for all the incursion rates in the cold tests. In the hot tests, material adhesion originated as a result of blade failure, and was observed for incursion rates above the standard value, 0.3 μm/pass as depicted in Figure 7.1g,7.1h, 7.1j, 7.1k and 7.1l. The proportion of the blade that fails at the hot condition enlarges at increasing incursion rates, which ends up in a total blade failure at the maximum incursion rate as observed in Figure 7.1m. The differing appearance of the sample is due to the blade substrate rubbing against the abradable sample, probably as a result of an early stage tip detachment, instead of the bare abrasive matrix as occurs in the other tests with a partial failure.

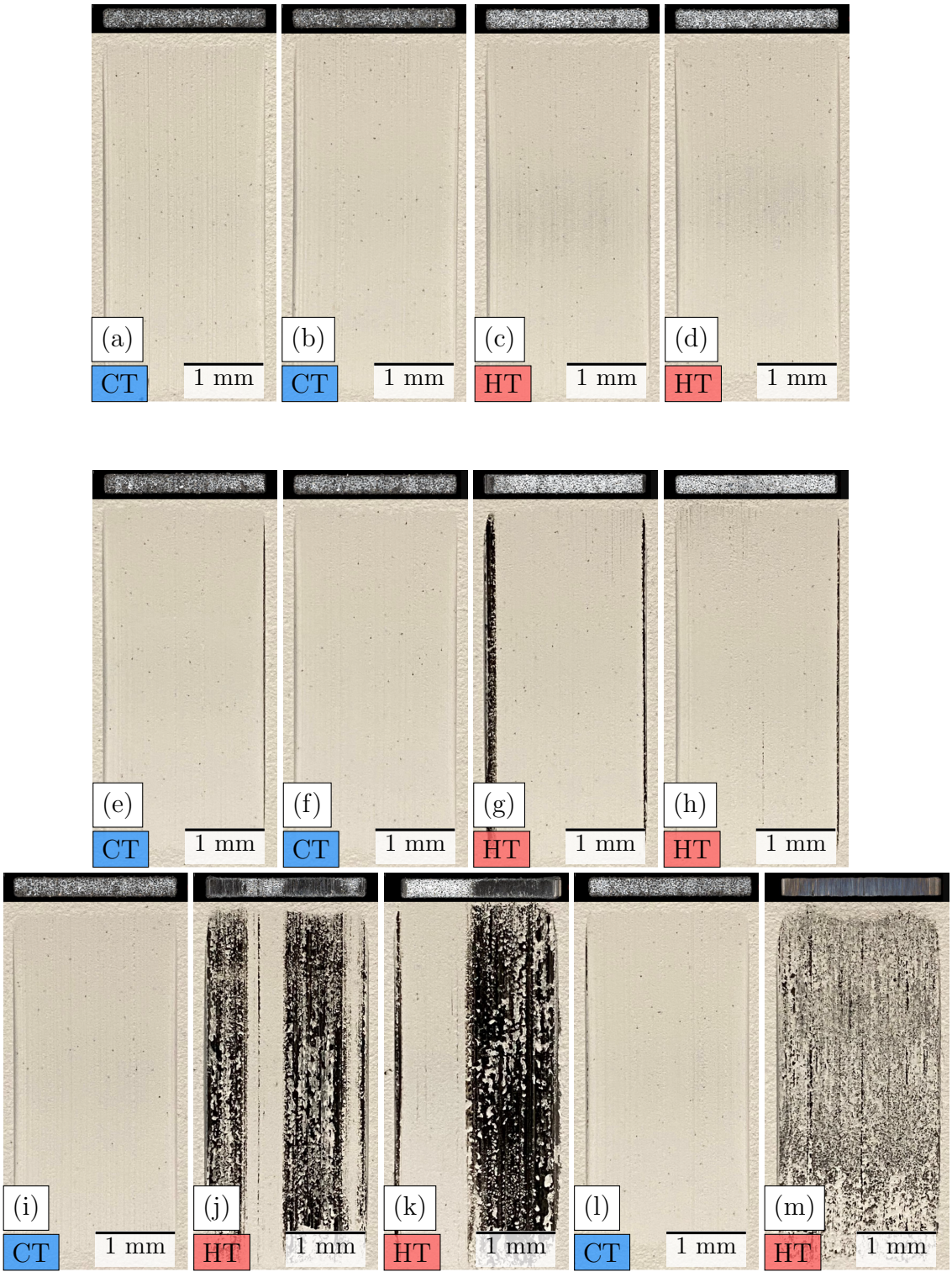

Figure 7.1: Post-test images of the abradable samples and TBT429 blades (top view) for the cold and hot tests performed on the HTR up to 1250 μm at 100 m/s and different incursion rates: (a,b,c,d) 0.3 μm/s, (e,f,g,h) 0.7 μm/s, (i,j,k) 1.0 μm/s and (l,m) 1.5 μm/s.

Figure 7.2 shows composite images of hot and cold blades, assembled to contrast wear behaviour. A direct relationship arises between the two variables considered, incursion rate and temperature, considered and the severity of the wear mechanisms that are visible at macroscopic level, material pick-up and blade failure.

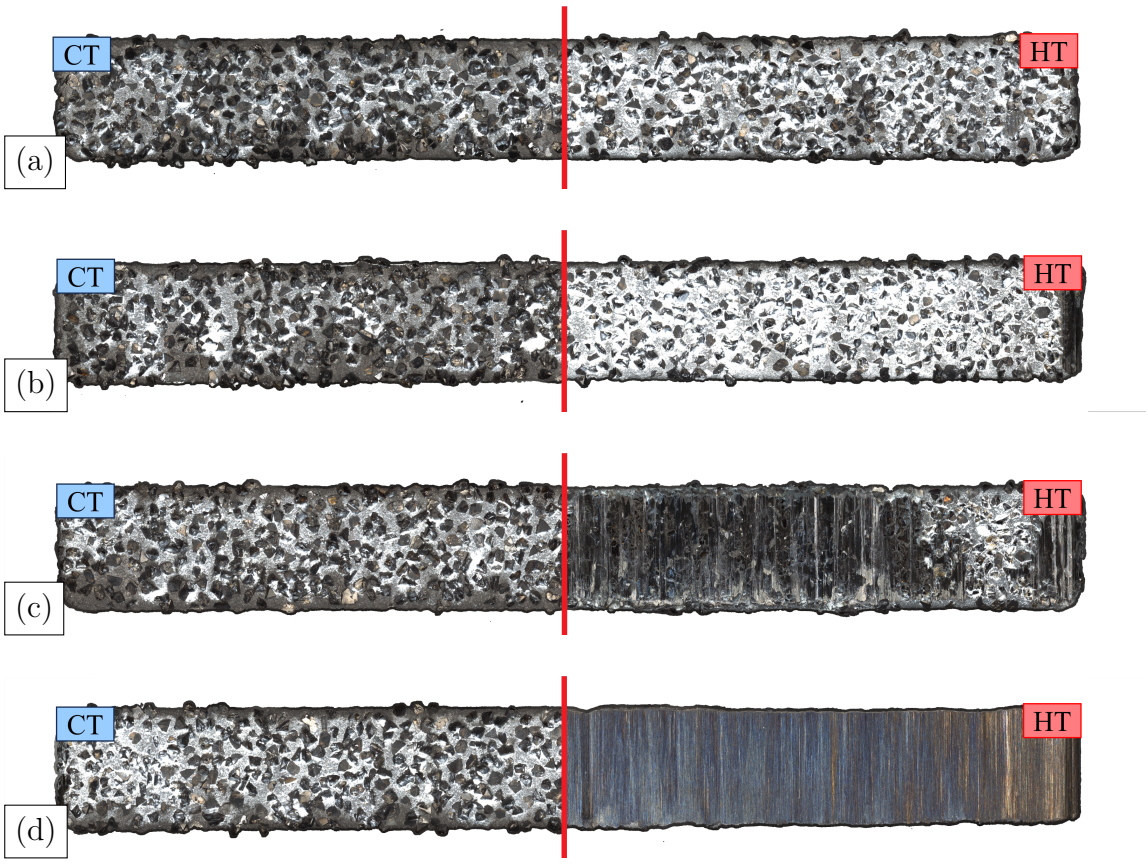

Figure 7.2: Detailed view of one of the TBT429 blades tested at each incursion rate and at both cold and hot condition: (a) 0.3 μm/pass - HTEPT01 and HTEPT03, (b) 0.7 μm/pass - HTEPT05 and HTEPT07, (c) 1.0 μm/pass - HTEPT09 and HTEPT10, and (d) 1.5 μm/pass - HTEPT12 and HTEPT13.

On the one hand, no blade failure, but increasing material pick is visible at increasing incursion rate for cold tests. On the other hand at the hot condition, Figure 7.2a-HT shows significant material pick-up at the standard incursion rate, which is more severe than that from the highest incursion rate at the cold condition, shown in Figure 7.2d-CT. This material pick-up saturates at increasing rates until the blade start to show failure regions at 1.0 μm/pass (Figure 7.2c-HT). This failure region has a dark appearance with grits either broken or embedded in the matrix and some traces of abradable material as detailed in Figure 7.3. In Figure 7.2d-HT, the blade

shows a total failure at the highest incursion rate of 1.5 μm/pass, accompanied by metal discolouration, which is typical from thermal damage of metals.

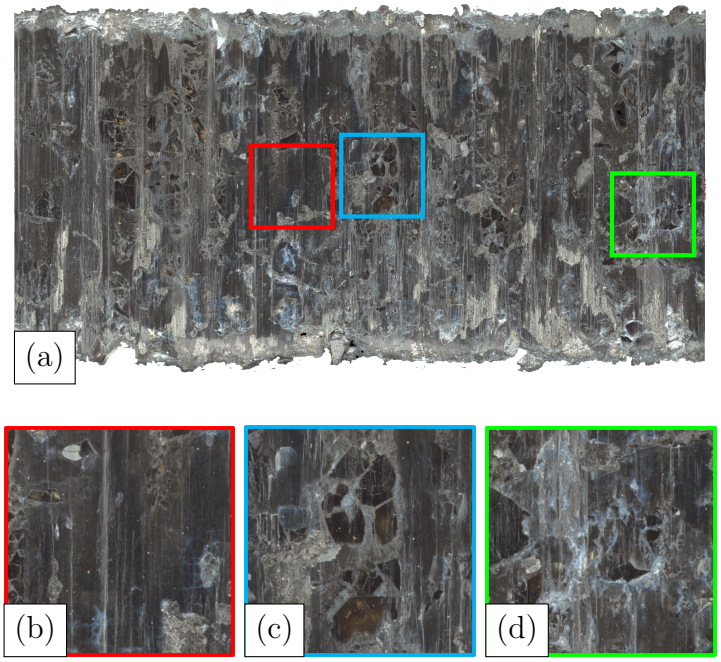

Figure 7.3: Wear features of a section from the HTEPT10 blade that failed when tested at 1.0 μm/pass and hot conditions. Wear features: (a) matrix abrasion, (b) fractured/embedded grits and (c) abradable material entrapped in the matrix.

The analytical tool developed in Section 4 to analyse blade wear has been employed to quantify the material pick-up area ratio according to the methodology defined in Section 4.3.4. The results from such material pick-up analysis are represented in Figure 7.4a. The trend of these results aligns with the visual inspection of the blades in Figure 7.2: increasing incursion rates lead to larger amount of trapped material which intensifies considerably at hot conditions in comparison to cold tests. High variability in the results is found between those blades which exhibit a substantial failed area as only the non-failed area is considered, HTEPT10 blade (Figure 7.1j) and HTEPT11 blade (Figure 7.1k).

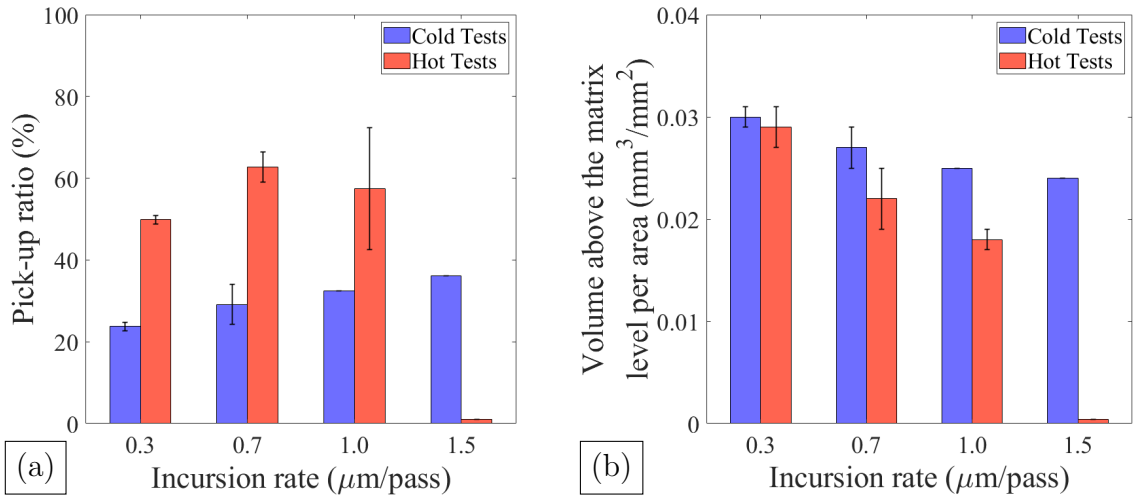

Figure 7.4: Comparison of (a) the material pick-up ratio and (b) the remaining blade cutting capability between the tests performed with TBT429 blades up to 1250 μm at 100 m/s and different incursion rates for both cold and hot test conditions.

Even though the efficacy of the analytical tool is compromised due to the high level of material pick-up as explained in Section 4.5, it has regardless been employed to quantify the remaining cutting capability/wear of the TBT429 blades. Results, displayed in Figure 7.4b, show a direct relationship between remaining blade capability and incursion rate which becomes stronger when tested at hot conditions.

The normal and tangential forces from the dynamometer together with the blade temperature from the high frequency pyrometer are shown for each test in Figure 7.5. The first thing to notice is that the blade temperature decreases below the pyrometer minimum threshold during the disc spin up phase prior to the contact. Commencing at the cold condition, forces remain low, temperatures below the pyrometer operating range and no remarkable event can be highlighted during the test as seen in Figure 7.5a, 7.5b, 7.5e, 7.5f, 7.5i and 7.5l. However, the cutting interaction no longer remains constant at hot conditions when incursion rates increase above the standard rate, Figure 7.5g, 7.5h, 7.5j, 7.5k and 7.5m.

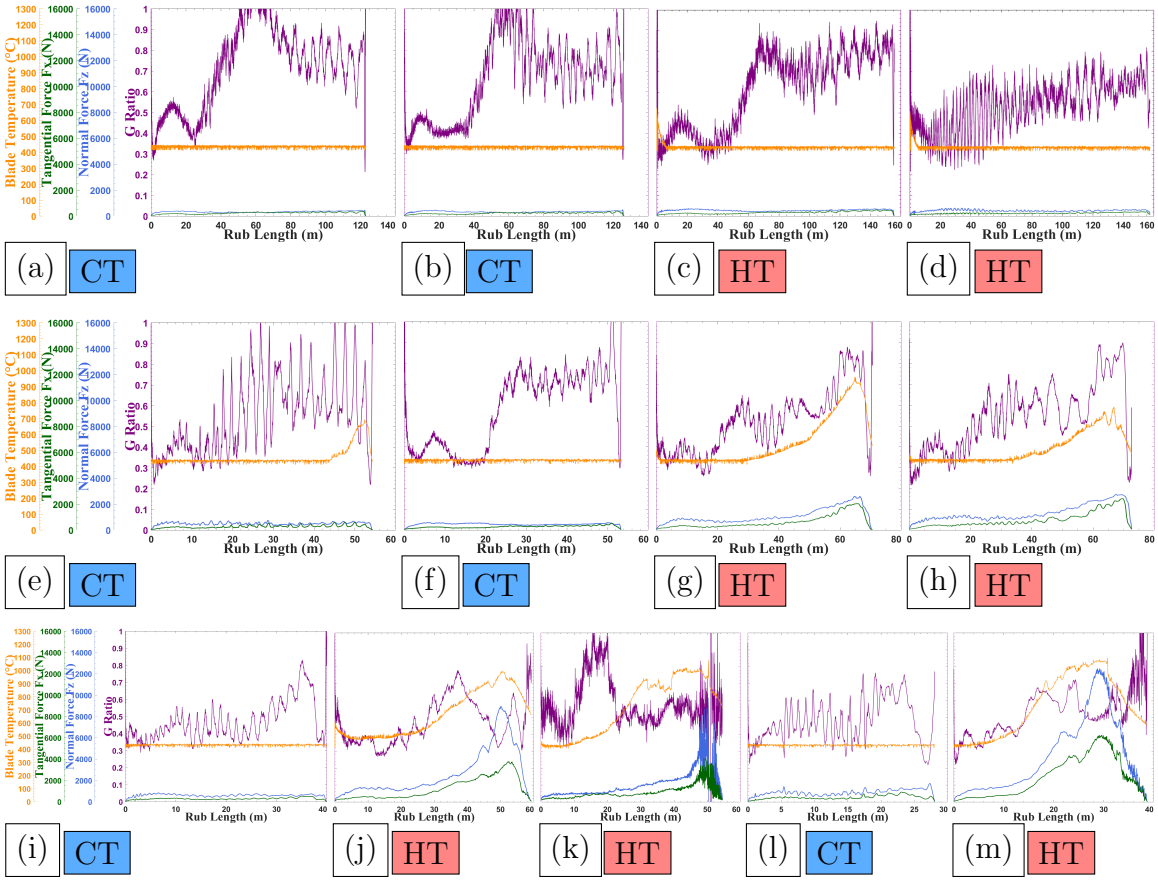

Figure 7.5: Force and temperature data for the tests performed with DELTA blades up to 1250 μm at 100 m/s and different incursion rates: (a,b) 0.02 μm/s, (c,d) 0.3 μm/s, (e,f) 0.7 μm/s and (g,h) 1.5 μm/s.

At the standard incursion rate, 0.3 μm/pass, no forces or temperature differences are visible between the cold, Figure 7.5a and 7.5b, and hot tests, Figure 7.5c and 7.5d, which agrees with the wear produced during the cut (Figure 7.4b). On the other hand, the pick-up ratio is doubled in value for the hot condition.

When the incursion rate is increased to 0.7 μm/pass, a gradual progressive ramp-up can be observed of both forces and blade temperatures at the end of the hot tests (Figure 7.5g and 7.5h) which is increased then at 1.0 μm/pass (Figure 7.5j and 7.5k), with a much larger peak value for both the normal force and the blade temperature. Although this increase begins to happen progressively and much sooner, it is not until towards the end of the test when both normal force and blade temperature experience a more significant rise. Conversely, the tangential force does not undergo any remarkable increase at 0.7 or 1.0 μm/pass. Finally, at the highest incursion rate of 1.5 μm/pass, Figure 7.5m shows early increases in force and temperature and

significantly higher peak values for both forces. In contrast, the blade temperature increase is more modest compared to the preceding incursion rate.

The maximum values for both forces and blade temperature are shown in Figure 7.6, detailed in two distinct graphs representing cold and hot conditions. As observed previously, forces and temperatures maintain significantly lower and at more consistent levels during cold conditions in comparison to the hot tests. Figure 7.6b shows a notable increase in both maximum normal force and temperature when exceeding the standard incursion rate in hot conditions. However, once this threshold is surpassed, the sensitivity of the maximum values for normal force and temperature to the incursion rate variable diminishes.

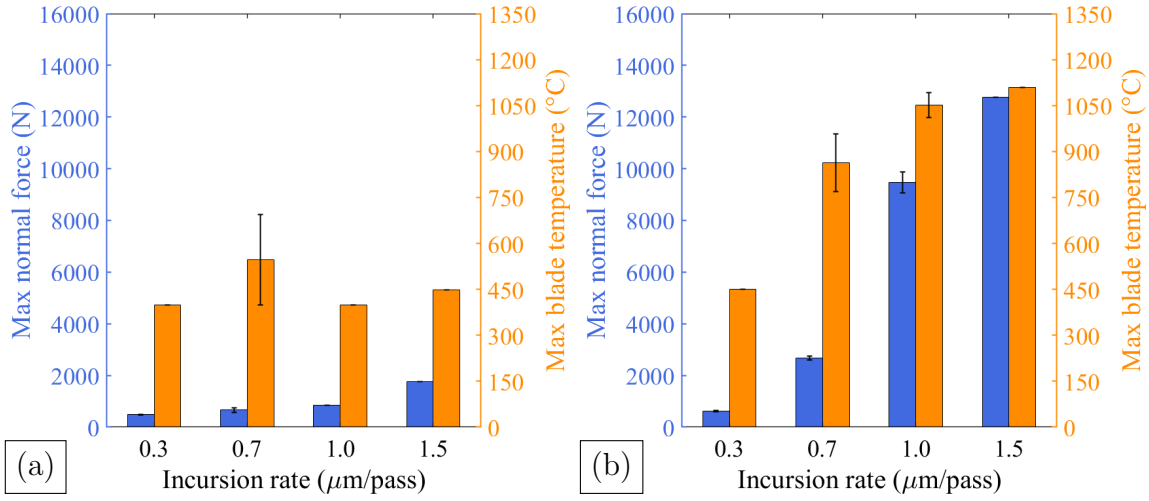

Figure 7.6: Comparison of the maximum normal force and the maximum blade between the tests performed with TBT429 blades up to 1250 μm at 100 m/s and different incursion rates for both (a) cold and (b) hot test conditions.

In order to analyse the tests further, the surface roughness of the abradable material has been examined to validate the influence of blade wear on its cutting effectiveness. As shown in Figure 7.7, the surface profile tends to become smoother with an increasing incursion rate, observed in both cold and hot conditions. This trend is mirrored in the remaining cutting capability, as illustrated in Figure 7.4b, where the incursion rate shows a more pronounced impact on profile roughness during hot tests. As expected, there is a closely correlation between blade cutting capability and the roughness of the abradable surface, with the latter being a consequential outcome of the former.

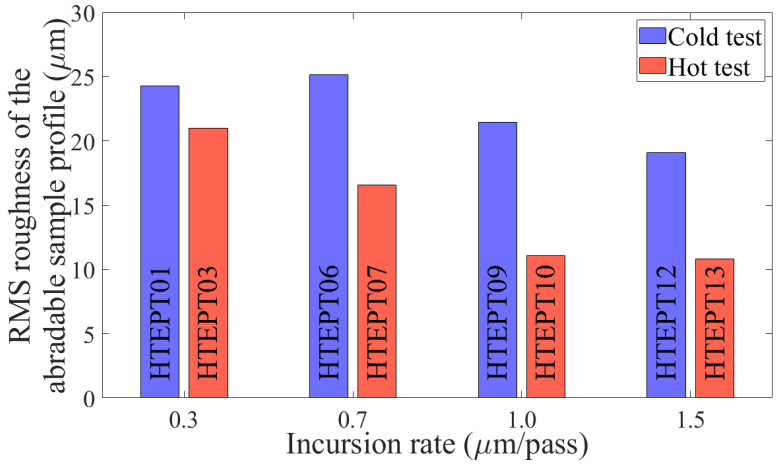

Figure 7.7: Comparison between the Root-Mean-Square roughness of the abradable sample profile at the lowest point for one test per condition of the TBT429 test batch conducted at the HTR.

To summarise the different analysis performed on the TBT429 blades, all of them point in the same direction. Incursion rate produces a rougher contact between abradable and blade, increasing the damage on the tip. Furthermore, this dependency becomes more critical when the hot condition is introduced, aggravating the wear generated on the blade and therefore, compromising the interaction with the abradable.

7.3.2 DELTA

The initially planned matrix for TBT429 was intended to be replicated in the DELTA blade testing. However, the DELTA blades experienced a complete failure at a lower incursion rate of 1 μm/pass. Additional valuable insights would not be gained from blades experiencing a total failure at higher incursion rates, and as such the test matrix was truncated. All tests performed with DELTA blades and the test conditions details are listed in Table 7.2.

Test	Blade	Test type	Blade speed (m/s)	Incursion rate (μm/pass)	Incursion depth (μm)
HTDEDT01 (a)	DELTA	Cold	100	0.3	1250
HTDEDT02 (b)	DELTA	Cold	100	0.3	1250
HTDEDT03 (c)	DELTA	Hot	100	0.3	1250
HTDEDT04 (d)	DELTA	Hot	100	0.3	1250
HTDEDT05 (e)	DELTA	Cold	100	0.7	1250
HTDEDT06 (f)	DELTA	Cold	100	0.7	1250
HTDEDT07 (g)	DELTA	Hot	100	0.7	1250
HTDEDT08 (h)	DELTA	Hot	100	0.7	1250
HTDEDT09 (i)	DELTA	Cold	100	1.0	1250
HTDEDT10 (j)	DELTA	Hot	100	1.0	1250
HTDEDT11 (k)	DELTA	Hot	100	1.0	1250

Table 7.2: Test matrix for the analysis of the influence of temperature and incursion rate on the performance of DELTA blades.

The series of images in Figure 7.8 provides a sequential overview of the test samples. At the standard incursion rate, depicted in Figures 7.8a, 7.8b, 7.8c, and 7.8d, a clean cut is evident, with no discernible distinction between cold and hot conditions. Upon increasing the incursion rate to 0.7 μm/pass, Figures 7.8e and 7.8f reveal blade damage, along with noticeable material adhesion on the abradable sample in hot conditions. In contrast, Figure 7.8d displays a clean abradable cut at the cold condition for the same incursion rate. These wear characteristics intensify significantly at 1 μm/pass, where Figures 7.8j and 7.8k demonstrate pronounced material adhesion on the abradable and a blade that has essentially failed under hot conditions. In the cold tests, both material adhesion and blade damage are visibly reduced, as observed in Figure 7.8i.

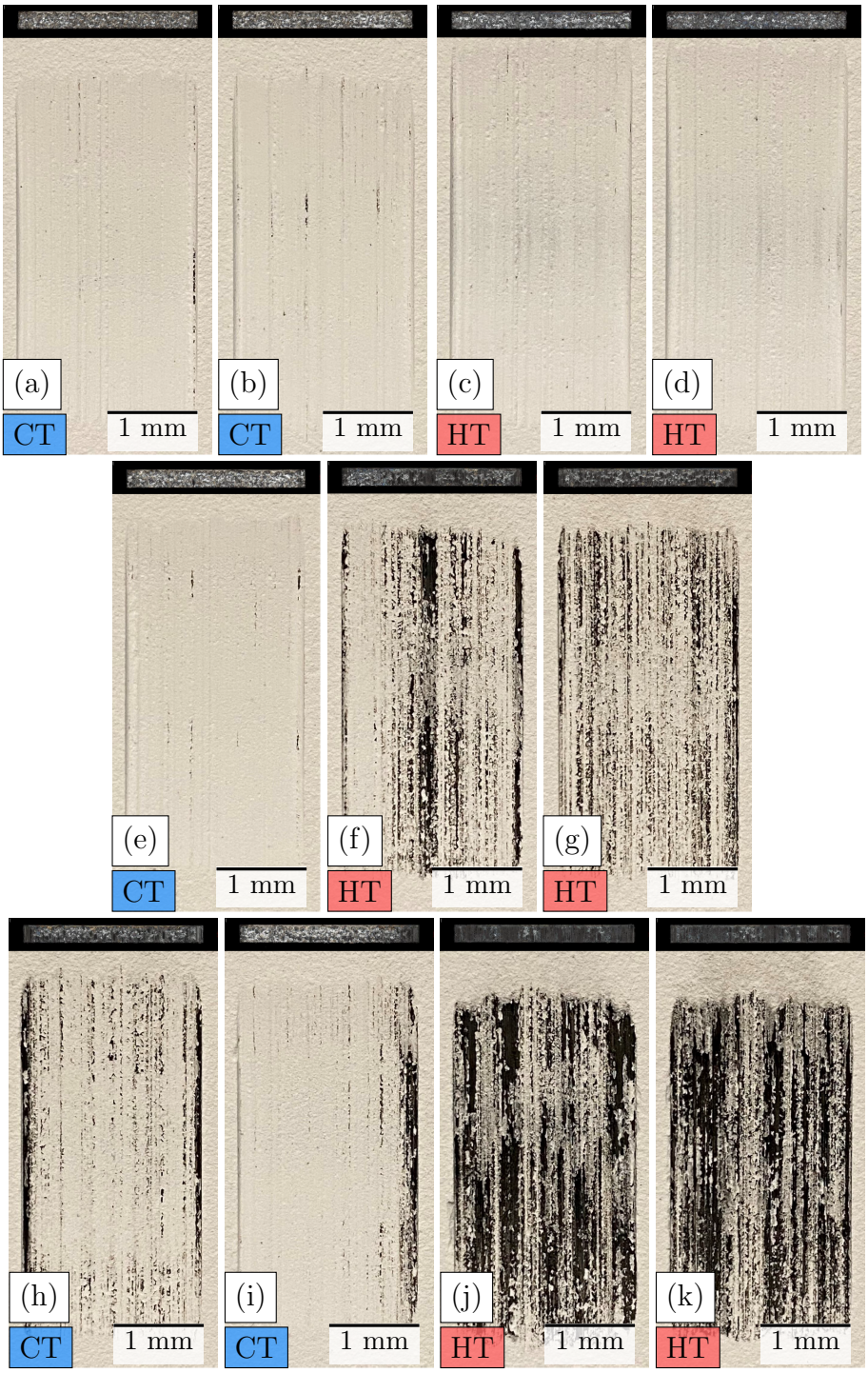

Figure 7.8: Post-test images of the abradable samples and DELTA blades (top view) for the cold and hot tests performed on the HTR up to 1250 μm at 100 m/s and different incursion rates: (a,b,c,d) 0.3 μm/s, (e,f,g) 0.7 μm/s and (h,i,j,k) 1.0 μm/s.

Similar to the approach taken for TBT429 blades, Figure 7.9 shows composite

images of the DELTA blades obtained from both cold and hot tests, enabling a direct comparison of wear features. Abradable material pick-up is recognisable and similar for every condition (if failed areas are not considered). Because of the light appearance of DELTA abrasive coatings, it is not possible to quantify the percentage of area that is covered by entrapped material with the methodology developed for TBT429 blades, although given the severity of the failure it can easily be visually determined

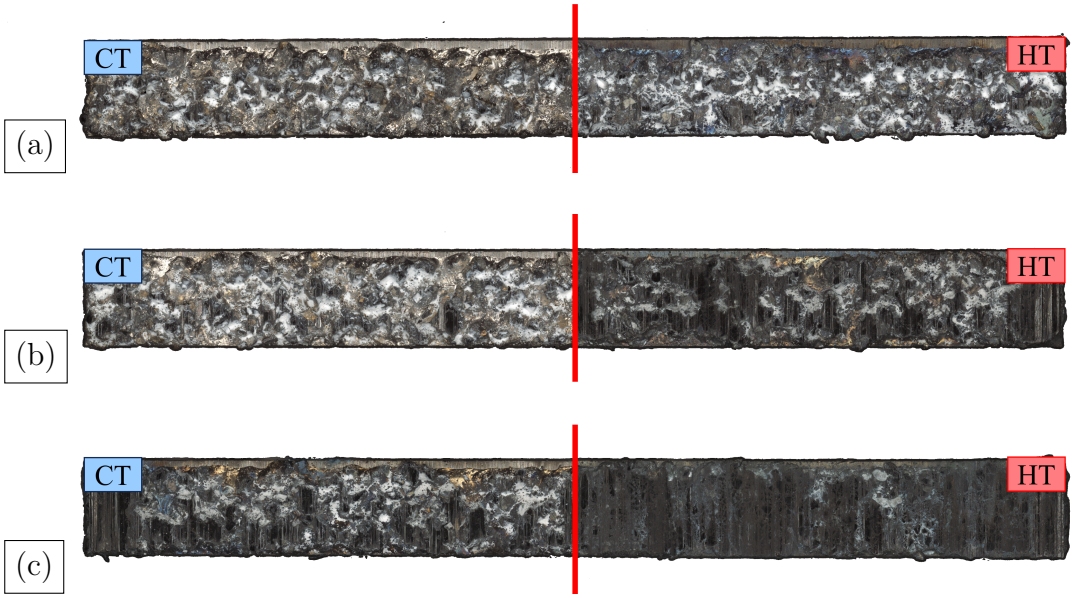

Figure 7.9: Detailed view of one of the DELTA blades tested at each incursion rate and at both cold and hot condition: (a) 0.3 μm/pass - HTDEDT01 and HTDEDT03, (b) 0.7 μm/pass - HTDEDT05 and HTDEDT06, and (c) 1.0 μm/pass - HTDEDT8 and HTDEDT10.

Another discernible wear feature evident in Figure 7.9 is the thermal discolouration, which becomes more pronounced with increasing incursion rates and is particularly notable on blades subjected to hot conditions (Figure 7.9a-HT, 7.9b-HT, and 7.9c-HT). This thermal discolouration is accompanied by an increase in matrix abrasion for blades tested at 0.7 μm/pass (Figure 7.9b-HT) and 1.0 μm/pass (Figure 7.9c-HT) under hot conditions (with similar damage seen in Figure 6.3). That said, Figure 7.9a-HT shows that no major abraded areas are discernible at the standard incursion rate, where blades also exhibit this thermal damage. Meanwhile, matrix abrasion partially overwhelms the blade abrasive coating, as depicted in Figure 7.9c-CT for the highest considered incursion rate, 1.0 μm/pass, at cold conditions. In turn, Figure 7.9c-HT shows an extension of these abraded areas to the entirety of the section when conducted at hot conditions. This difference in matrix abrasion between

cold and hot tests is also evident at the middle incursion rate (Figure 7.9b). The extension of the abraded area for each condition aligns with the degree of material adhesion found on the abradable samples in Figure 7.8.

Thermal discoloration arises from oxidation processes occurring at elevated temperatures (245; 246), and its severity increases with higher temperatures and prolonged exposure times. Figure 7.10 shows the temperatures experienced by the blades in each test, along with the corresponding forces responsible for the temperature generated through frictional contact. In the comparison of cold (Figure 7.10a and 7.10b) and hot (Figure 7.10c and 7.10d) tests at the standard incursion rate, continuous minor fluctuations in forces are observed at both temperature conditions, with no apparent distinctions between them. Blade temperature barely exceeds the pyrometer's minimum threshold in Figure 7.10b (cold test) and Figure 7.10c (hot test). This observation suggests that the thermal discoloration observed in Figure 7.9a might be attributed to the initial preheating, as no significant force and temperature differences are discernible between cold and hot conditions at 0.3 μm/pass.

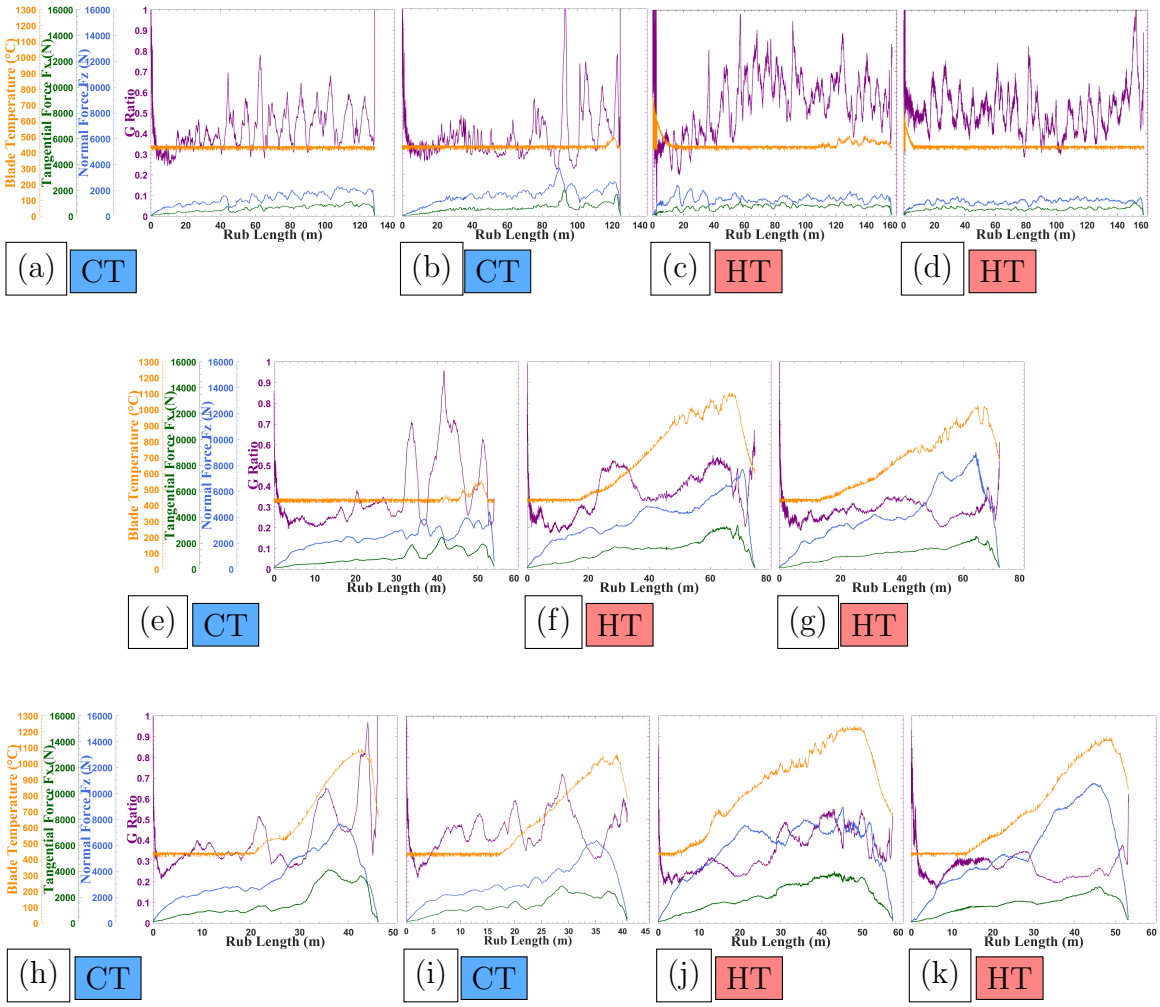

Figure 7.10: Force and temperature data for the cold and hot tests performed on the HTR with DELTA blades up to 1250 μm at 100 m/s and different incursion rates: (a,b,c,d) 0.3 μm/s, (e,f,g) 0.7 μm/s and (h,i,j,k) 1.0 μm/s.

Moving to the next incursion rate of 0.7 μm/pass under cold conditions, Figure 7.10d shows that, although forces demonstrate limited fluctuations, they remain relatively constant throughout the entire test. Blade temperature experiences a gradual rise towards the end of the test, not accompanied by a concurrent force increase. This suggests that the temperature increment is a continuous, gradual process, becoming measurable only when exceeding the pyrometer threshold. In the hot condition for the same incursion rate, as illustrated in Figure 7.10f and 7.10g, the temperature rise is more substantial. This temperature increase is followed by a significant augmentation of both normal and tangential forces at a similar proportion, as can also be observed in the G ratio for both hot tests. The progressive increase in temperature and forces until the end of the test supports the notion of a gradual process accumulating heat,

and consequently wear, on the blade, rather than a sudden failure event.

At the highest incursion rate (1.0 μm/pass) the DELTA blades were tested at, Figure 7.10h and Figure 7.10i show that the gradual build-up of heat also occurs for the cold tests, reflected in both forces and blade temperature, which reach similar peak values to those reached at the hot condition for lower incursion rate (Figure 7.10f and 7.10g). This peak value comparison among incursion rate and temperature condition is better shown in Figure 7.11, where the maximum normal force and maximum blade temperature are summarised for each condition. Moving to the hot test for this incursion rate of 1.0 μm/pass, Figure 7.10f and 7.10g show higher maximums for both forces and blade temperature, which are summarised in Figure 7.11. The blade temperature exceeds the pyrometer range threshold much sooner and the transition from cold to hot condition is not as noticeable as happened at 0.7 μm/pass. Test data displayed in Figure 7.10 highlights that both increasing incursion rate and the heating condition facilitate the heat build-up in the blade, which also coincides with the wear features observed in Figure 7.9.

As briefly introduced in the previous paragraph, Figure 7.11 gathers the maximum values of normal force and blade temperature from each test, separated in cold tests, Figure 7.11a, and hot tests, Figure 7.11b. Both parameters show a direct relationship with incursion rate. At the hot condition, this relationship becomes less sensitive to increasing incursion rate, likely as a consequence of blade saturation and failure initiation as observed on the Figure 7.9b-HT and its subsequent whole section failure observed in Figure 7.9c-HT. Similarly, the resemblance between the maximum values recorded in the cold tests at 1.0 μm/pass and the hot test at 0.3 μm/pass also corresponds to a similar degree of abrasion observed in Figure 7.9c-CT and 7.9b-HT, respectively. Thus, it is evident that there exists a close interdependency between forces, blade temperature, and the extent of wear the blade undergoes, with each factor influencing and being influenced by the others.

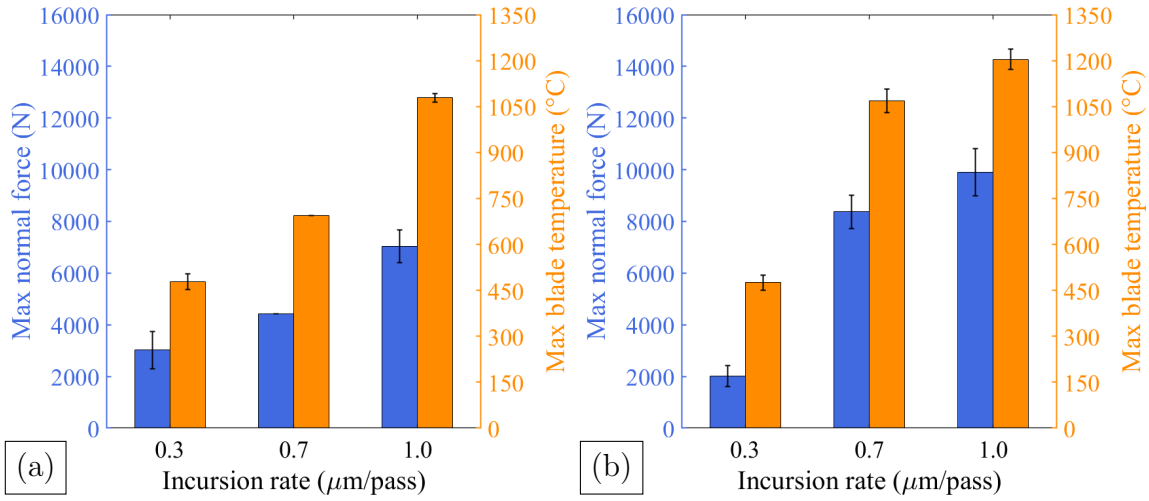

Figure 7.11: Comparison of the maximum normal force and the maximum blade between the tests performed with DELTA blades up to 1250 μm at 100 m/s and different incursion rates for both (a) cold and (b) hot test conditions.

Although further tools are not available to analysed the wear on DELTA blades in comparison to these that have been employed in the investigation of TBT429 blades, the data obtained from the tests and post sample images, in addition to the outcomes from testing them in the LSR, enables a full picture of their performance in both cold and hot conditions to be determined. This overall picture of DELTA blades is going to be further discussed and compared to the baseline TBT429 blades in the next section.

7.4 Discussion

Before proceeding into the discussion of the performance between the TBT429 and DELTA blades, it is worthing highlighting that, in contrast to tests in Chapter 5 and 6, these tests has been conducted in the HTR which is limited to a blade speed of 100 m/s. When comparing back to comparable tests on the LSR, the larger HTR disc diameter provides longer rubs at each pass for the same incursion depth. Consequently, the blade travels longer rub lengths, removes more material per pass, and in turn experiences a higher level of damage for the same incursion rate and depth. In addition, the residency time in a pass is also larger as the blade speed has been reduced from 200 m/s in the LSR to 100 m/s. However, the frictional dynamic does not keep varying when a speed threshold is exceeded (247), which for the incursion tests has been reported to be at 50 m/s (229; 236; 237).

TBT429 and DELTA blades have been tested in hot conditions at 100 m/s at a range of incursion rates in order to compare between the two blade variants and with their respective performance in cold condition. Although the surface temperature of the blade falls below the minimum threshold of the pyrometer at the beginning of the test, it is evident that the utilisation of the induction coil during the pre-heating phase and throughout the test significantly impacts the performance of the blade.

At the standard rate of 0.3 μm/pass, a clean cut was obtained with no sign of damage on any of the blades for both types at either cold or hot condition. Temperatures were either below or slightly above the measurable minimum threshold of the pyrometer, rendering their comparison impossible. Figure 7.12a and 7.12b exhibits the mean normal forces and temperatures according to the blade type and test condition, where DELTA blades consistently produced, in both cold and hot tests, around three times higher forces than TBT429 blades. Considering that heat generation due to friction is directly dependent on the normal force when the contact area is maintained (244), higher temperatures must arise in DELTA tests. However, the comparison of temperatures is not possible due to the pyrometer's minimum threshold.

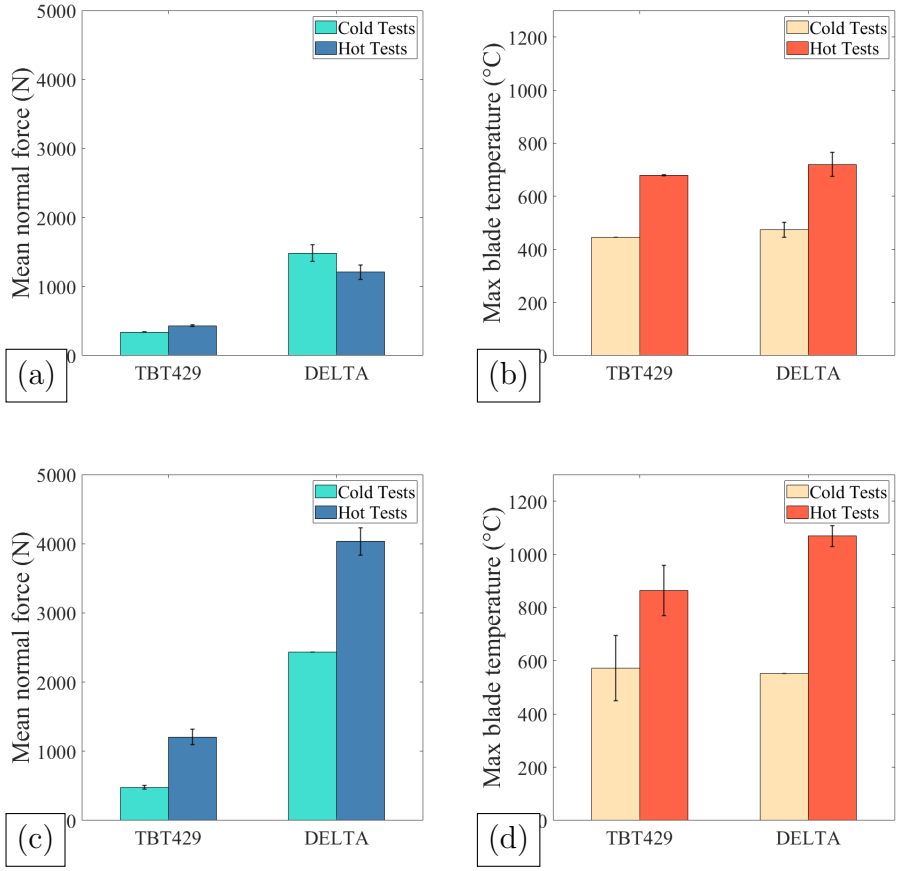

Figure 7.12: Maximum mean normal force and maximum blade temperature comparison between blades and temperature condition for a given incursion rates: (a,b) 0.3 and (c,d) 0.7 μm/pass.

During testing at 0.7 μm/pass, Figure 7.12c illustrates that the mean normal force continues to display a consistent ratio between TBT429 and DELTA blades, similar to what is observed at the standard incursion rate (Figure 7.12a). Once again, maximum blade temperatures are very similar and do not follow the trend seen in forces. In this case, the temperature similarity can be explained by examining Figure 7.13, where TBT429 blades experience very localized abrasion, and subsequent higher local temperatures, on the sides from which the infrared pyrometer takes measurements. Higher temperatures at the edges of the DELTA blades were also previously seen on the LSR in Section 6.3.2, confirming this hypothesis.

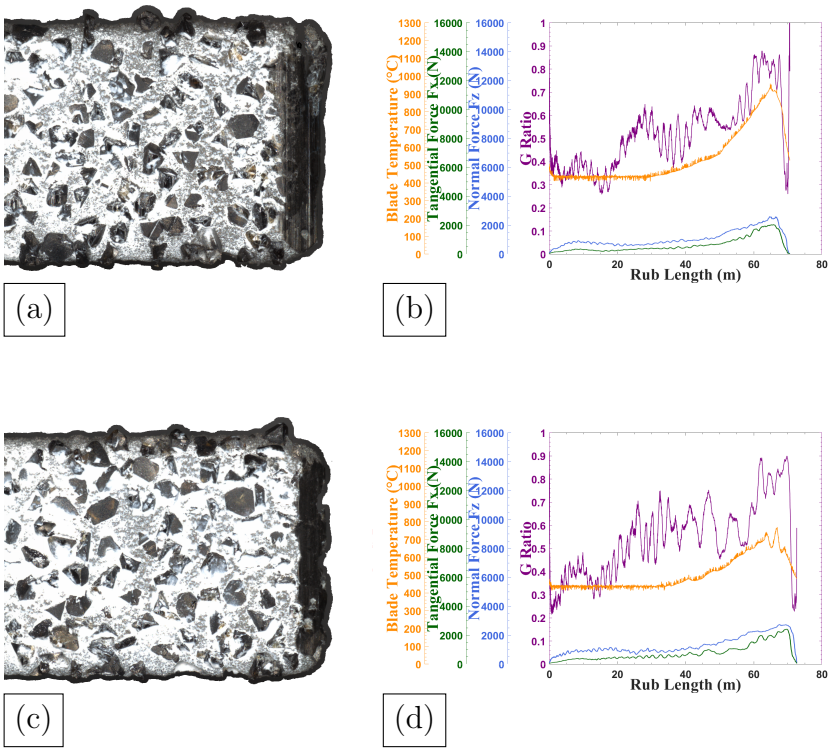

Figure 7.13: Damage produced on the TBT429 blades and recorded temperatures for the two repetitions at 0.7 μm/pass and hot condition: (a,b) HTEPT09 and (c,d) HTEPT10.

When moving to 1.0 μm/pass, where no abrasion was detected on TBT429 blades (Figure 7.1i and 7.2c-CT), DELTA blades displayed high degrees of deterioration (Figure 7.8h and 7.8i). This partial deterioration becomes a full blade failure in the hot test (Figure 7.8j and 7.8k), whereas TBT429 only showed partial damage as shown in Figure 7.1j. On this part, it is of note that incursion rate had to be pushed to 1.5 μm/pass to obtain a similar degree of damage on TBT429 blades as shown in Figure 7.1m and 7.2d-HT.

Blade failure initation for electroplated blades, TBT429, and DED blades, has been investigated in Chapter 5 and 6 respectively. Although the sequence of events depends on the blade morphology, the trigger mechanism is the same, heat accumulation. The accumulation of heat is a consequence of contact friction, which intensifies at higher incursion rates and is further augmented when externally supplied by the induction coil. This heat buildup elevates the temperature of the blade, leading to the softening of the matrix and a weakening of the grit anchoring. In the absence of grits to guide the cutting, the exposed matrix rubs against the abradable, resulting

in increased forces, the release of more heat, and a further rise in temperature.

The main difference between TBT429 and DELTA blades is that in DELTA blades, due to how the abrasive coating is engineering, both the grits and the matrix are simultaneously in contact with the abradable. As the matrix is significantly less abrasive then the grits, the regions where the matrix is in contact lead to a much less efficient contact. These local poor interactions generate matrix abrasion which results in hot spots, even at the beginning of the test. These hot spots were detected by the thermal camera on the abradable coatings in the tests performed on the LSR (Figure 6.6). This global lack of abrasiveness means higher forces are required to penetrate and fracture the abradable as shown by dynamometer measurements detailed in Figure 7.12a for the standard incursion rate tests where no failure mechanism governed the blade performance. The required higher forces to cut the abradable also result in higher temperatures due to friction. DELTA blades are engineered to withstand higher temperatures, but fails at a lower incursion rate than the baseline TBT429 as their thermal stability enhancement is outweighed by the overheating produced by the abrasion mechanism. In other words, the pursuit of more thermally stable matrix materials such as Inconel 792 (DELTA), whose strength at high temperature is enhanced in comparison to the NiCoCrAlY superalloy used in the baseline (TBT429), is overshadowed by their morphology. This morphology is limited by the manufacturing technique these materials are deposited onto the blade with (45).

In contrast to DELTA blades, TBT429 blades provide a clean cut with relatively low forces and manage the heat generated by friction efficiently up to 1.5 μm/pass in cold conditions. No sign of blade failure was visible for any of the cold tests. On the other hand, abradable pick-up by the blade is noticeable at increasing incursion rates, which becomes far more severe for the hot tests (Figure 7.2). This adhesion phenomenon is temperature and not force governed, considering that the pick-up ratio from the cold tests at 1.5 μm/pass increased by 52% over the same cold condition at the standard rate but forces did by 166%. In contrast, the pick-up ratio at the standard incursion rate of 0.3 μm/pass from the hot tests was on average 101% higher than the one obtained from the cold tests at the same rate, whereas the normal forces only increased by 27%. That being the case, the external heat, provided by the induction coil in this rig, is the main cause of material pick-up on the blades. These outcomes align with the findings obtained from testing the interaction between these same materials inside a furnace at 25 and 900 °C but at much lower incursion rates, and consequently lower forces, (170).

Material pick-up reduces the cutting capability and abrasiveness of the blade, demonstrated by the increasing contact forces, abradable surface roughness reduction and increasing material pick-up at higher incursion rates. The process, further explained in (240), starts with the abradable material fractured by the blade, which is then either ejected or compressed underneath it (240; 236). The compressed material is then prone to adhere and gets trapped within the grits. In turn, the trapped material exhibits a dependence on forces and temperature, as shown in Figure 7.2, with the blade diminishing its cutting capability due to the loading of material. Consequently, the forces needed to remove the material increase, further aggravating the blade loading. Moreover, any external heating source, such as the hot gases in gas turbines or the induction coil in these tests, elevates the overall blade temperature, thereby enhancing the collection of material. Congestion of abrasive coating is also common in electroplated c-BN grinding wheels, where increased loading raises both contact forces and temperature (248).

As the test progresses, TBT429 blades reduce in their cutting capability due not only to the trapped material but also the damage produced on the grits. While this process is also influenced by the incursion rate, temperature has a more limited role, with this shown in Figure 5.19. As a result, temperature increases throughout the test until either the test finishes, the blade runs out of grits or gets congested in an local area which triggers a failure mechanism and expands to the rest of the blade as discussed in Section 5.5. The failure of blades in the hot test, contrasted with the intact blades in the cold test, suggests that blade congestion plays a more significant role than grit failure at elevated temperatures. This is indicated by the stronger dependency on the pick-up ratio rather than on blade wear when transitioning from cold to hot conditions (Figure 7.4). Additionally, the higher overall temperatures on the blade, which weaken the matrix as studied in (170), lower the threshold for triggering failure.

A SEM-EDS (Scanning Electron Microscopy-Energy Dispersive Spectroscopy) analysis has been performed on the boundary of a failed region of the HTEPT10 blade to understand how the damage propagated once the blade is congested and fails at a hot condition. The area that has been analysed is shown in Figure 7.14 where the right side shows an abraded region, a healthy region on the left and a transition zone in-between.

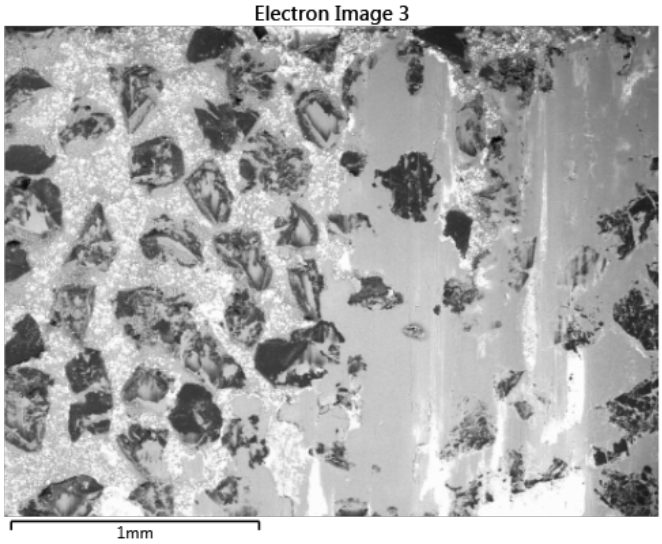

Figure 7.14: SEM Image of a portion of the HTEPT10 blade tested at 100 m/s, 1.0 μm/pass and 1250 μm.

The major elements comprising the TBT429 blade are illustrated in Figure 7.15, where B and N constitute the grits, and Ni and Co are the two primary elements constituting the NiCoCrAlY matrix. Figures 7.15a and 7.15b clearly show that the grit elements, B and N, are distinct on the healthy side but begin to diminish as one moves towards the abraded side. This contrasts with the SEM image in Figure 7.14, where the grits are still visible beneath a layer of material that contains traces of the matrix elements, as observed in Figures 7.15c and 7.15d. Combining this results with Figure 7.14 suggests that the entire grits or parts of them become buried beneath the matrix when the matrix becomes abraded, as opposed to being removed, and the grits elements are not detected may be due to them being below the surface

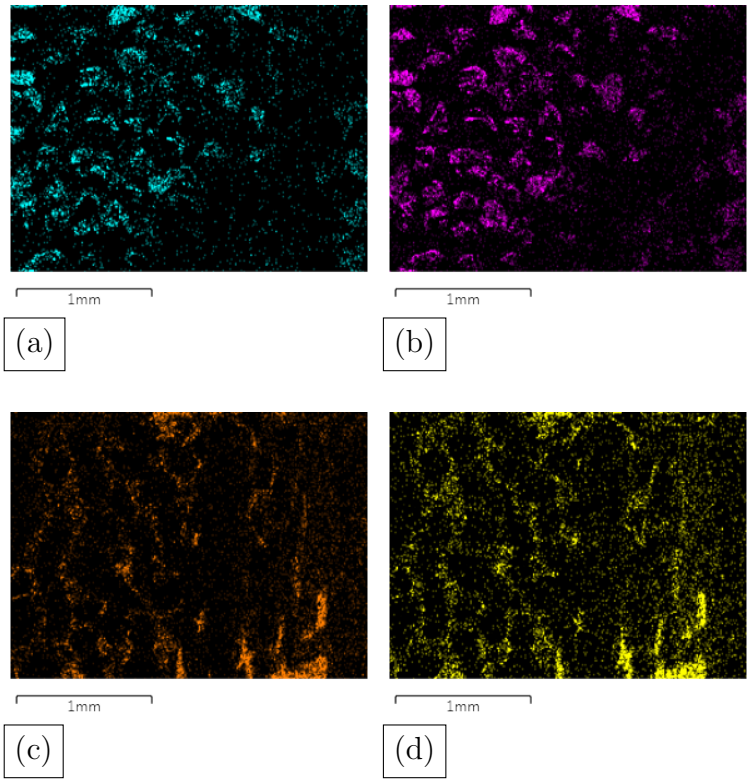

Figure 7.15: 2D SEM-EDS elemental mapping of (a) B, (b) N, (c) Ni and (d) Co on the surface of the HTEPT10 blade post test.

As done for the main blade elements in Figure 7.15, Figure 7.16 shows the main elements of the MAS abradable coating (Mg, AL and O) analysed by EDS. As expected, traces of the three elements are found on the healthy area where the MAS is easily recognisable by visual inspection on the samples (Figure 7.1j). However, an even higher density of these elements are found on the abraded region which is not visually recognizable as the failed region has a dark appearance as seen in Figure 7.2c-HT, in contrast to the whitish one of the MAS. This implies that when the matrix gets abraded as a result of the blade failure, abradable particles mix with the softer matrix, forming an homogenous layer that covers and buries the surrounding grits. The compatibility between the abraded NiCoCrAlY with and the MAS abradable is unknown thus far and would require further investigation to understand the impact of MAS particles blended with the metal.

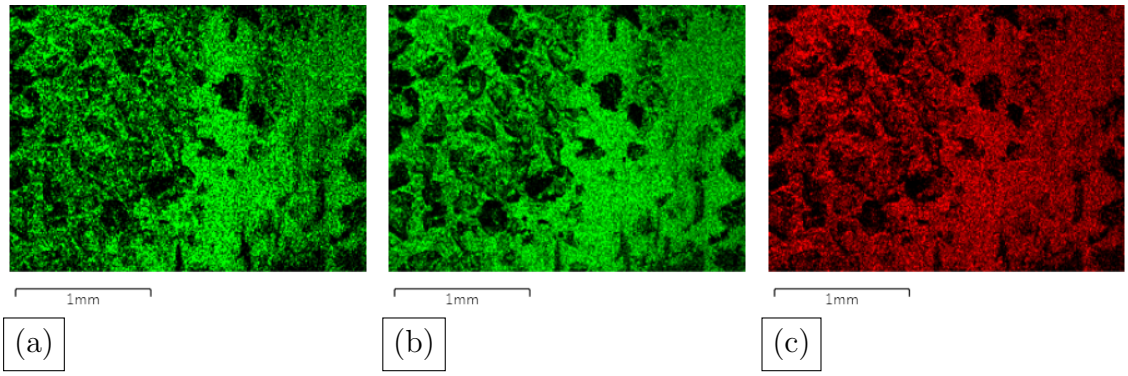

Figure 7.16: 2D SEM-EDS elemental mapping of (a) Mg, (b) Al and (c) O on the surface of the HTEPT10 blade post test.

The results outlined in previous paragraphs indicate the presence of grits embedded into the matrix on the side of the blade that already failed. However, the analysis of the abrasive coating top surface is not enough to identify the integrity of the grits. For this reason, the blade has been sectioned and a SEM image is taken from both healthy and failed regions, as shown in Figure 7.17a and 7.17b respectively.

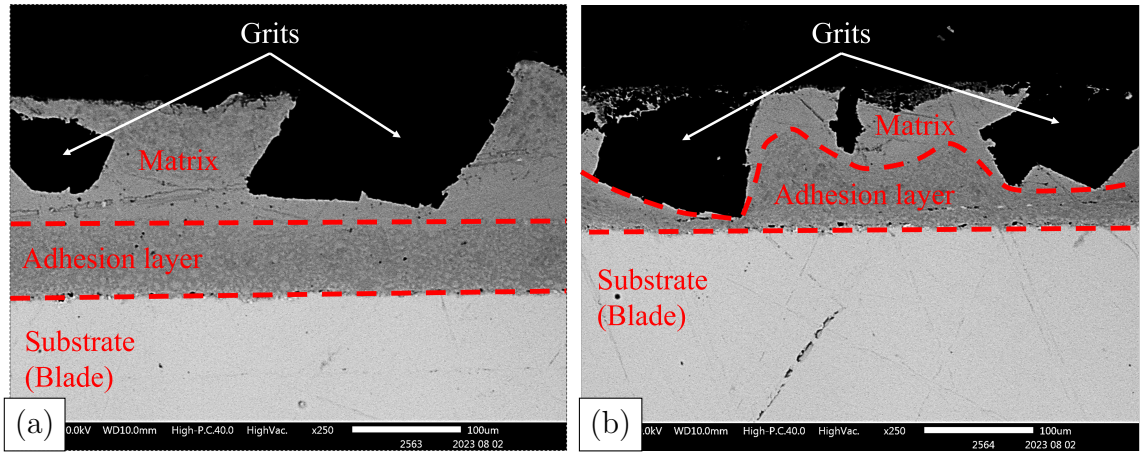

Figure 7.17: SEM images of the HTEP10 TBT429 blade depicting the abrasive coating structure at regions where the blade (a) did not fail and (b) did fail after test.

The healthy region depicted in Figure 7.17a displays three distinct material layers: the substrate (blade), an adhesion layer, and the matrix. The interfaces between these layers are perfectly horizontal. The grits are partially embedded in the top layer, the matrix, and do not reach the adhesion layer underneath, which is deposited to establish a strong bond between the matrix and the substrate.

In contrast, the damaged region illustrated in Figure 7.17b shows that the grits have been pushed further down, surpassing the original interface, now altered, between the matrix and the adhesion layer, and become completely buried into the matrix. The matrix/adhesion layer interface, initially straight and horizontal, is now pressed down due to grit penetration, resulting in an upward flow in regions where there is an absence of grits. However, the interface of the blade substrate remains intact.

Sectioning the blades and discovering that the grit anchoring is not solely on account of the matrix failure brings a new layer of complexity to the equation. When the blade congests and gets overheated as a result of a poor interaction, the high temperature reduces the strength of both the matrix and the adhesion layer, to the point they can no longer hold the grits in place. These grits are pushed down by the normal component of the contact forces, penetrate both layers and produce plastic deformation in both. The grits get completely embedded and the cutting capability is completely gone. Then, the bare matrix rubs against the abradable with the contact force/temperature increasing and weakening the matrix, until they are completely removed (Figure 7.2d). This push-in failure mechanism likely took place to a degree on the LSR testing at room temperature, but, raising the blade overall temperature made it far noticeable in the HTR testing.

To bring matters to a close, the different discussion topics brought in this section can be simplified to three main points. The first point is how the test condition affect the performance of the blade. Increasing both incursion rate and input heating compromises the abrasive coating integrity as it becomes softer as a result of the high temperatures. The second point is the effect of the thermal load as a consequence of the contact conditions, where the electroplated blades have demonstrate in this research to produce a more efficient interaction than the DED blades because of their morphology. The third and final point is understanding how these blade variations, TBT429 for the case of electroplated blades and DELTA for the DED blades, break and fail once they locally get saturated. TBT429, which has been evidenced as a better solution than any of the proposed DED alternatives, struggle to manage the heavy material pick-up as a result of the high temperatures arising on the blade. This material pick-up leads in turn to even higher temperatures on the blade and subsequent matrix/adhesion layer damage. Although the blade failure is inevitable as its cutting capability is limited, further optimization work is required around the electroplated blade design to delay their grit depletion and minimise the impact of local failures.

7.5 Conclusion

In conclusion, the performance of the TBT429 and DELTA blade variants has been assessed at room temperature and hot condition. For the hot condition, an induction coil around the disc circumference has provided an external source of heating that increased the temperature of the blade prior and during the test. Introducing temperature in the tribological system as it occurs in gas turbines makes an impact on the general performance of the blades.

Although there is heat released during the cutting mechanism as a result of friction, the external heat provided by the induction coil has a critical role in triggering the wear mechanisms that lead the blade to fail. That said, it has been demonstrated that blade failure is not purely and directly motivated by temperature. The wear mechanisms arising from the contact, which in turn develop more rapidly at increasing temperature, are the root for failure initiation. Material pick-up congestion and local matrix abrasion are the main mechanisms that lead the TBT429 and DELTA blades respectively to a local and subsequent total failure.

For those incursion rates where neither the TBT429 nor DELTA blades failed at either cold or hot tests, TBT429 provided more efficient cut resulted in a low thermal load, which maintained the blade healthy for longer. As consequence, TBT429 blades requires of higher incursion rates to develop the same degree of damage than that found on DELTA blades.

Chapter 8

Conclusions

Abradable seal systems are a key passive feature for ensuring the efficient functioning of both compressor and turbine stages in gas turbines. These abradable seal systems consist of a blade (bare or abrasive tipped) and a sacrificial abradable lining. The interaction between both parts during the engine break-in defines the blade tip clearance of each stage. Ensuring tight tip clearances is essential for an efficient engine operation. Wide clearances not only increases the fuel consumption to maintain the same power/thrust delivery but also reduce the lifetime of the components in the turbine stages as the TET increases with the added fuel to overcome the loss in efficiency. Due to such extreme temperatures in the first stages of the HPT, the material choice for the abradable seal system becomes challenging as they also need to guarantee their integrity in the case of contacts during the engine service life.

Ceramic materials, which are stable at high temperature, are employed as the sacrificial lining material in the HPT. Because of the hardness of ceramic materials, abrasive tipped blades are required to cut these. Whereas the material of the abradable lining shows a thermally stable behaviour at the range of temperature the HPT operates at, the current abrasive solutions employed on the blades on Rolls-Royce's most advanced civil gas turbines has been reported to have some durability limitations in service (45). Hence, several research projects for understanding and optimising the current solutions as well as developing new abrasive solutions have been launched in the last few years to analyse and address these challenges.

The principal abradable seal system currently employed by Rolls-Royce in HPT civil gas turbines consists of an atmospheric plasma sprayed MAS abradable lining and electroplated c-BN tipped blades, commercially available under the name of TBT429. This solution uses a NiCoCrAlYs superalloy as an anchoring matrix for the c-BN grits. As a result of the limitations and challenges found on the TBT429 coatings from in-service engines, Rolls-Royce has been investigating two superalloys, Inconel 792 and

NiAlTa, to replace NiCoCrAlY as the grit anchoring matrix. None of these two blade variants have been effectively evaluated in a test rig so far.

8.1 Test Method development

This research has set the foundations for testing and evaluating at high temperature the performance of abrasive tipped blades employed in abradable seal systems. Firstly, by developing a rig capable of replicating the HPT blade/casing interaction and triggering the wear mechanisms as reported from in-service gas turbines (45), and secondly, by further developing new or already existing methodologies with the aim to assess these complex systems in a representative but cost-effective manner.

An incursion test rig has been developed in the University of Sheffield to assess the blade performance of abradable seal systems at high temperature. This high-temperature incursion rig addresses a crucial gap inherent in existing incursion rigs, as it successfully overcomes limitations observed in fully attaining representative engine conditions on the blade. The wear mechanisms observed on the blade tips from in-service engines have been replicate in Chapter 7 at a lower initial blade temperature but at representative incursion conditions.

Throughout this work, a clear understanding of the failure mechanisms has been achieved. Local temperature on the blade tip is the root of blade failure, however the forces from the contact are what physically removes the grits and damages the matrix. As the metal matrices becomes softer at increasing temperature, lower forces are required to trigger these mechanisms. The main test parameter that determines the forces from the contact for a given blade architecture is the incursion rate. For abrasive tipped blades, forces and grit damage increase at increasing incursion rates as the blade has to remove more material per pass. In turn, contact temperature increases by friction as it has been reported from the room temperature tests studied in Chapter 5 and 6. If the incursion rate is too aggressive and the incursion deep enough, the blade experiences high temperatures by friction which also increases throughout the test as a result of grit damage. This causes a poor performance and manages to trigger a blade failure with no external source of heat.

This mechanism is exemplified by Chapter 7, where the initial aim was to maintain a minimum constant temperature on the blade of 800 °C during testing with the HTR. Although the blades were pre-heated around that temperature, this temperature could not be maintained when the disc started spinning and it dropped to around 400 °C. Nevertheless, the heat put into the blade was enough to make a meaningful

impact when compared to blades tested at the room temperature condition. Failure wear mechanisms were obtained at the high temperature condition and increasing incursion rates in contrast to the clean cut obtained for the equivalent tests at the same rates but at room temperature. These findings again support the requirement of achieving the right incursion and heating conditions at the same time to replicate the failure mechanisms observed on engines (45). For a given incursion rate, the more aggressive the incursion rate is, the lower the external heat addition is required on the blade to trigger failure mechanisms, or vice versa. However, there is a maximum blade temperature prior incursion that will make the blade fail no matter what the incursion rate is due to matrix material failure. This limit has not been investigated due to the challenge of maintaining a high temperature on the blade at the start of the incursion.

As shown, abrasive coatings experience a failure if the blade reaches temperatures, either by friction or by an external source, that exceed the matrix softening temperature. However, exceeding this temperature to prior contact is not strictly necessary to trigger the blade failure, which can occur without any heating if the incursion rate and depth are high enough as analysed in Chapter 5 and 6. In addition, every incursion rig uses an intermittent contact approach where the blade cuts the abradable lining for a tiny interval of the disc period. Considering that the failure is heavily influenced by the contact, having a continuos or, at least, a longer lining segment as occurs in gas turbines would cause the blade to achieve the critical matrix temperature and subsequent failure sooner. In other words, blade performance is always undervalued in intermittent contact rigs as the blade temperature takes longer to develop.

In essence, although the current HTR rig is not able to provide enough heating power to maintain a constant temperature on the blade while it is spinning, this research has established the foundations to both assess the shared influence of both incursion rate and temperature on the blade performance as well as to establish a solid methodology to evaluate it.

8.2 Performance of abrasive tipped blades

Apart from developing a solid methodology for assessing abrasive tipped blades against ceramic linings at both cold and hot conditions, the other main objective of this thesis has been the study of DED tipped blades with the aim to replace the current electroplated tipped blade baseline that shows limited cutting durability (45). Both variants have been firstly independently analysed in the LSR at low temperature

to assess the impact of the incursion rate on the blade performance and characterise the wear mechanisms of each blade type. The LSR has been used for the cold tests as it can accommodate a larger number of instrumentation devices that provide a good understanding of the blade/lining interaction. Subsequently, both types were tested and compared at hot conditions against the same batch of MAS abradable lining samples to establish a direct comparison.

Electroplated tipped blades are characterised by an even layer of matrix material where the grits are partially embedded and protrude from it. The protruding grits lead the cut and experience wear as the contact progresses, as occurs with electroplated grinding wheels (193). Ideally, the blade provides effective material removal as long as grits remain attached and uniformly protrude over the anchoring matrix. However, a couple of local mechanisms take places and accelerate the electroplated blade failure when the right conditions are met. The first of these mechanisms is caused by the local lack of grits as a result of either poor manufacturing or being removed during the contact. This leads to the bare matrix rubbing against the abradable. As the bare matrix does not posses the abradability the sharp grits have, an inefficient contact interaction arises which exponentially increases the contact force and temperature. As a consequence, the surrounded areas also undergo a temperature increase, causing matrix weakening where the grits get either removed or totally embedded. This mechanism keeps propagating until the blade completely fails. The second local mechanism, especially aggressive at the hot condition, is blade congestion as a result of the abradable material getting trapped between the grits. The trapped material buries the grits, reducing their protrusion and, therefore, their cutting capability. Again, the temperature increases due to a poor interaction until the matrix locally fails as a result, and this failure propagates to the surrounding areas. Both mechanisms become more pronounced at increasing incursion rates. Whereas the congestion mechanisms is heavily influenced by temperature as discussed in Chapter 7, the failure by lack of grits only takes places if the blade temperature is maintained low and the material is evacuated properly during the test until the blade cutting capability is depleted.

On the other hand, the two DED abrasive coating variants are Rolls-Royce internal IP which have been developed to replace the current TBT429 baseline with more thermally stable matrix materials (44). The variants are named as DELTA and IP75, and use a Inconel 792 and NiAlTa matrix respectively. In DED abrasive coatings, both the grits and the matrix form a conglomerate where they are deposited onto the blade. Hence, when the contacts starts both the grits and the matrix are simultaneously in contact with the abradable. As the cut progresses, the conglomerate fractures

and releases fresh grits that continue with the cut. However, the contact points from the matrix produce an inefficient local interaction which generates hot spots on the abradable and cause abrasion on the matrix. Although this temperature increase is well managed at cold runs, it becomes a problem when an external source of heat is added to the blade, which then becomes critical at increasing incursion rate. The DED abrasive coating is designed to undergo a brittle fracture to expose fresh grits. However, the high temperature turns this desired mechanisms into local abrasion which increases even further the temperature and keeps propagating to the rest the blade until this completely fails as seen in the abradable thermal maps. These findings are in accordance with the performance of the DELTA variants as the IP75 catastrophically failed at every conditions. As there was not any coating left to analysed for the IP75 blades, it is assumed that the interface incompatibility between matrix and grits was the cause of its rapid failure.

When comparing TBT429 against DELTA back to back against the same batch of MAS abradable linings on the HTR, a superior performance was obtained from the electroplated abrasive coating. Although DELTA uses a more thermally stable matrix material (Inconel 792), the nature of the coating where both the grits and the matrix are simultaneously in contact with the abradable causes a poorer interaction than that of the electroplated abrasive coatings where only the grits lead the cut. This poor interaction from the DED blades overshadows the enhancement on the matrix strength gained by replacing the NiCoCrAlY with a more promising Inconel 792 superalloy, whose yield strength at temperatures above 650 °C is higher.

8.3 Impact on industry

This research has been funded by Rolls-Royce as part of the development programmes run for the improvement and optimization of their civil gas turbines. As previously mentioned, the TBT429 electroplated tipped blades and MAS abradable seal system are currently employed in the HPT of the the Trent XWB and Pearl engine families. As a result of the limited durability of the abrasive coating on the blade, new abrasive coating architecture have been investigated with the aim to replace the current solution (45).

The first of these novel architectures is the DELTA DED abrasive coating. The programme to develop this variant was launched in Rolls-Royce Indianapolis with the aim of replacing the current TBT429 abrasive coating on the HPT stage of the Trent XWB. Although the first iterations for their manufacturing optimisation were done

in-house, it was then externalised to RPM innovations for their further optimisation. The programme was brought to a close as a result of the outcomes obtained from this research.

Conversely, the second of these architectures is the IP75 DED abrasive coating. Rolls-Royce Deutschland launched this programme to study the feasibility of this architecture as part of a LuFo funded programme with the aim to replace the current TBT429 solution on the two HPT stages of their Pearl engine family. The manufacturing process was externalised to Fraunhofer IWS in Dresden.

On account of the DED blades underperformance, the next lines of investigation on abrasive coating have been narrowed to optimise the NiCoCrAlY superalloy to withstand higher temperatures and to reduce the thickness of the adhesion layer that is deposited between the abrasive coating matrix and the blade substrate to avoid the total grit embedment when they are pushed in due to a weakened matrix. In addition, abradable research is currently looking at improving the MAS material fracture by adding a second polymeric phase phase as it was previously done for YSZ (233).

Furthermore, the testing methodologies and techniques developed in this piece of work are not solely restricted to turbine applications. Although the impact cannot be directly measured, these methodologies are also of interest to the ongoing Rolls-Royce lines of investigations in the compressor abradable seal systems, especially when temperature is required.

In conclusion, this research has not only addressed a gap in knowledge and contributed to the further understanding of abrasive tipped blades in abradable seal system, but also has had a direct impact on their use in industry.

Chapter 9

Gap in knowledge and future work

The limitations faced by this work can be divided into two main areas: those related to the various methodologies employed for evaluating tipped blades in abradable seals, and the second, which pertains to the performance of the abradable seal system itself.

The HTR was initially designed to maintain constant temperatures above 800 °C on the blade while rotating at linear speeds close to 400 m/s. However, the rig is currently limited by both linear speed and temperature. The current disc design and spindle restrict the blade speed to a maximum of 220 m/s. Due to the strengthening ribs and the four non-aerodynamic blade slots on the disc, significant windage is generated, pushing the driving spindle to its maximum operating condition. Therefore, to run at higher rotating speeds, a optimisation of the disc design to minimise windage is needed. A spindle with a higher maximum torque may also be required if the higher speeds cannot be achieved with a more aerodynamic design of the disc. It is also worth noting that the rationale behind reaching 400 m/s is because of the typical blade tip speeds in gas turbines HTP. While the Mach number for that speed at HPT temperatures ranges from 0.45 to 0.55, the Mach number will exceed 1 if the same blade speed is required at HTR temperatures, given that the ambient temperature is still 15-25 °C. This would introduce shockwave mechanisms that are not representative of HPT scenarios and might alter the abradable seal performance. However, achieving higher speeds but away from the transonic region, <0.8 Mn, would still be useful to understand and confirm the influence of blade speed on the cutting performance at high temperature, which has been reported negligible by other authors when testing abradable seals but at ambient condition (229; 236; 237), although this should still be confirmed in this context.

On the heating side, the existing design of the induction coil and power supply systems faces challenges in achieving temperatures exceeding 800 °C on the rotating

blade. As illustrated in Figure 9.1a, the current design generates magnetic field anti-nodes and nodes in the circumferential direction, maximizing and minimizing heating on the blade, respectively. Although 800 °C can be reached by statically heating the blade at one of the anti-nodes (Figure 9.1b), this temperature diminishes as the blade begins to rotate. This reduction occurs not only due to the windage effect cooling the blade, but also because of the succession of anti-nodes and nodes encountered while spinning. To address the cooling effect, the blade speed in the HTR has been limited to 100 m/s.

Reaching higher blade temperatures with the current coil design also faces challenges as the magnetic field also affects the disc rim, which sits within the induction coil magnetic field and gets heated as observed in Figure 9.1b and 9.1c. The heat soaked into the rim flows down throughout the disc and compromises its integrity in high-stress regions during rotation (45). A comprehensive solution demands an optimisation of the induction coil to maintain an uniform circumferential magnetic field as well as a disc design to stay away from the magnetic field anti-nodes, ultimately enabling higher temperatures exclusively on the blade. It is essential to note that elevated blade speeds would mandate increased induction coil power to counterbalance the heat removal through forced convection. The attainment of higher and consistent temperatures on the blade will facilitate a thorough exploration and determination of their impact on incursion rate at given incursion depths.

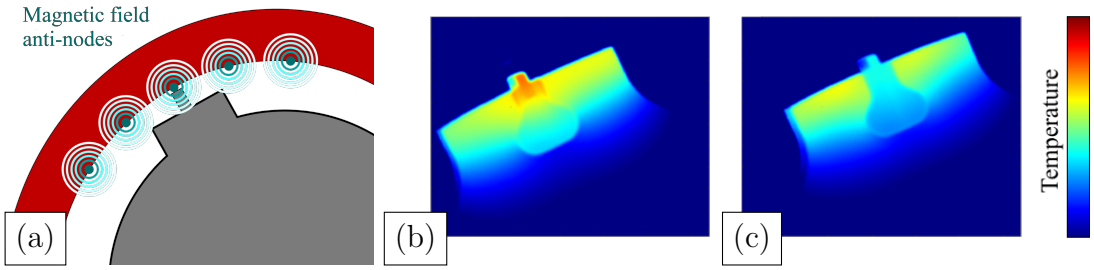

Figure 9.1: Schematics of the magnetic field (a) anti-nodes in the circumferential direction as well as of the resulting heating at (a) an anti-node and (c) a node captured by the thermal camera.

Another parameter not addressed in this study, yet impacting the absolute values of the incursion condition where blades exhibit failure mechanisms, is the hardness of the MAS abradable lining samples. The MAS samples utilized in this research were produced in distinct batches, featuring a nominal hardness ranging from 55 to 66 on the Rockwell hardness scale, using the R15 test method. While samples from the

same batch consistently displayed similar hardness, this uniformity was not observed when comparing samples across different batches. Despite utilizing the same spraying parameters for their manufacturing, the sprayed powder originated from diverse lots. As detailed in Section 5.5, tests on MAS samples from different batches under identical conditions revealed increased forces for the harder samples. Given the established linear relationship between incursion rate, forces, and temperature, it is hypothesized that harder samples may necessitate lower incursion rates and environment temperature to induce failure. Further experimentation under a singular condition with varying MAS sample hardness is imperative to understand the underlying nature of this trend

Examining sample hardness as a controllable parameter in the manufacturing process prompts a reevaluation of the limitations inherent in abradable seals as a system. The definition and constraints of incursion rates, intricately tied to engine performance, suggests a potential avenue for optimisation by assuming a linear relationship between hardness and contact forces. This optimization could involve minimizing the workload on the abrasive coating by strategically reducing the hardness of the abradable lining, essentially enhancing the lining's abradability.

However, the multifunctional role of abradable linings introduces complexities. Besides their role as a sacrificial material in abradable seals, they act as a Thermal Barrier Coating (TBC) to shield the underlying casing from high temperatures and corrosion. They must also exhibit excellent erosion resistance; a requirement that clashes with the pursuit of heightened abradability. Strategies to introduce this desired abradability property without compromising other functionalities include intentionally forming in-built cracks during the spraying process, incorporating microporosity, or introducing a second phase (156; 23; 129; 37; 38). A recent exploration involved adding polyester as second phase to a YSZ ceramic lining for its application for the sealing turbine rotor drum (233). This investigation has laid the groundwork for a statistical analysis of abradable performance in relation to the abradable composition.

Returning the core focus of this thesis, it becomes evident that the cutting performance of electroplated tipped blades surpasses that of DED tipped blades. As a result, the logical trajectory for advancing abrasive coating technology lies in mirroring the architecture seen in electroplated blades, where grits extend beyond a flat anchoring matrix. However, it's noteworthy that the electroplated tipped blades utilized in this thesis, as well as those in operational gas turbines, exhibit durability constraints at elevated temperatures due to material softening. This underscores the immediate

importance of material research to optimize the composition of the MCrAlY superalloy, enhancing its strength specifically at high temperatures. Simultaneously, looking towards the long term, there is a compelling need for exploration into innovative high-temperature high-strength matrix materials that can be manufactured through electroplating techniques.

Ultimately, the adhesion layer, whose role is securing the abrasive coating matrix to the blade substrate, also manifested plastic deformation when the abrasive coating collapsed. As a result of the matrix and adhesion layer softening during the blade failure, grits get pushed in and became entirely embedded due to the the combined thickness between both layers. Total grit embedding renders any remaining cutting capability redundant. As a consequence, an additional avenue for enhancing blade design arises at reducing the thickness of the adhesion layer. This modification aims to mitigate the degree of grit embedding when failures occur. The blade substrate, whose integrity has been reported to be intact after the abrasive coating failure, underneath will prevent the grits from further embedding. This modification is assumed to boost the blade cutting capability prior to its failure.

Appendix A

Convergence and sensitivity studies of the analytical tool

A.1 Grid refinement

Preliminary study performed to analyse the convergence of the grid when exporting the surface of the blade abrasive coating from the Alicona IF-MeasureSuite software in the analytical tool for assessing blade damage. Four repetitions were conducted per grid refinement.

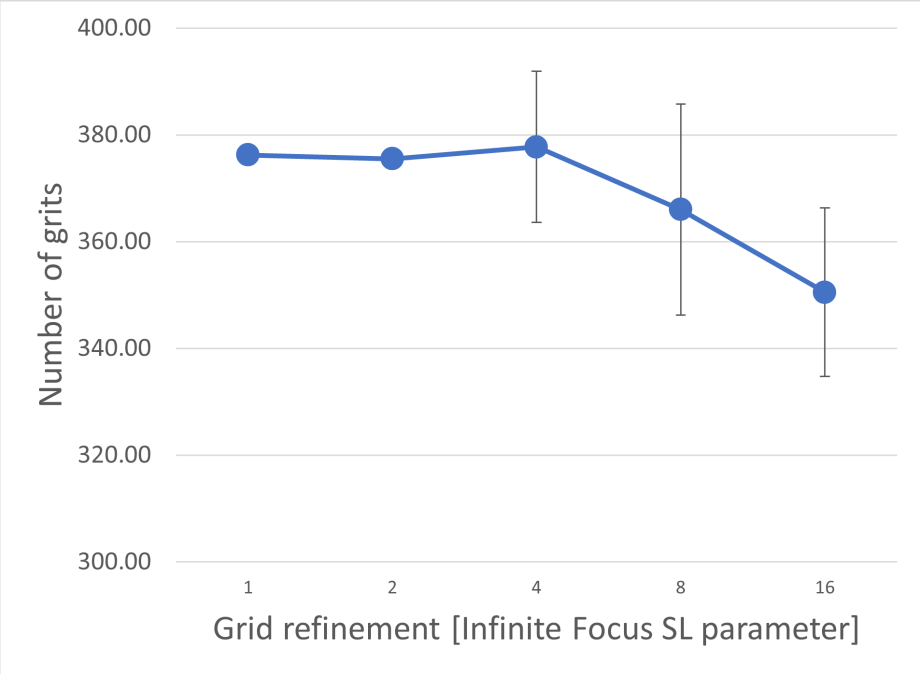

Figure A.1: Convergence study of the grid refinement parameter (1-Finest and 16-Roughest) set on the Alicona IF-MeasureSuite software regarding the analysis output number of grits.

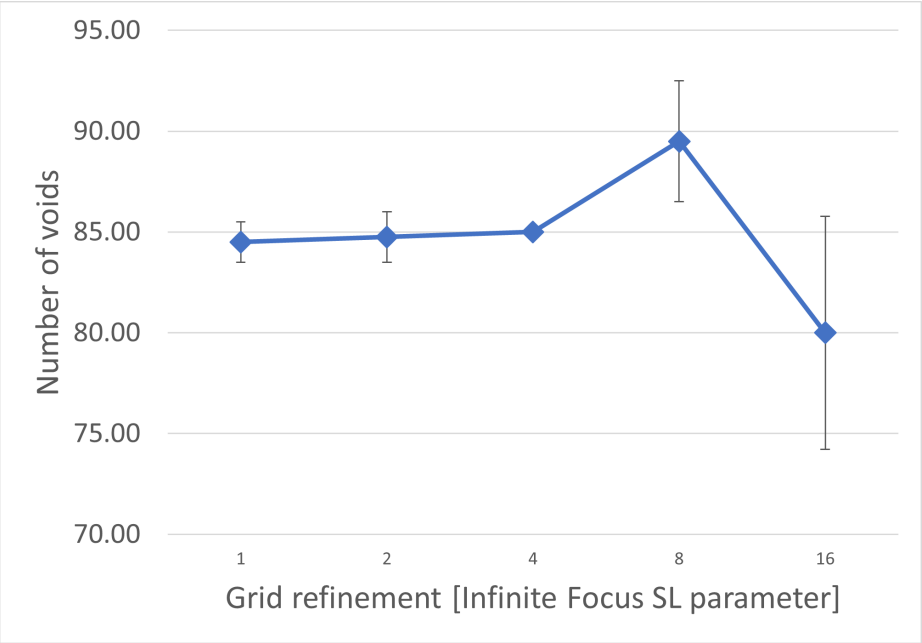

Figure A.2: Convergence study of the grid refinement parameter (1-Finest and 16-Roughest) set on the Alicona IF-MeasureSuite software regarding the analysis output number of voids.

A.2 Number of picked areas for establishing the matrix plane

Preliminary study performed to analyse the convergence of the surface roughness parameters regarding the number of selected areas for establishing the matrix plane in the analytical tool for assessing blade damage. Four repetitions were conducted per grid refinement.

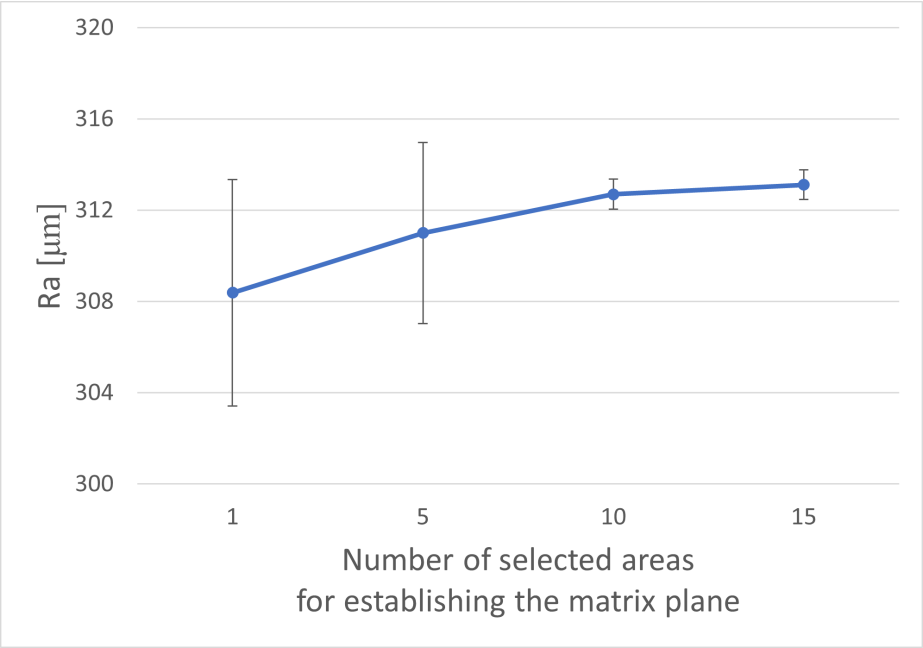

Figure A.3: Convergence study of the Ra surface roughness parameter regarding the selected areas for establishing the matrix plane.

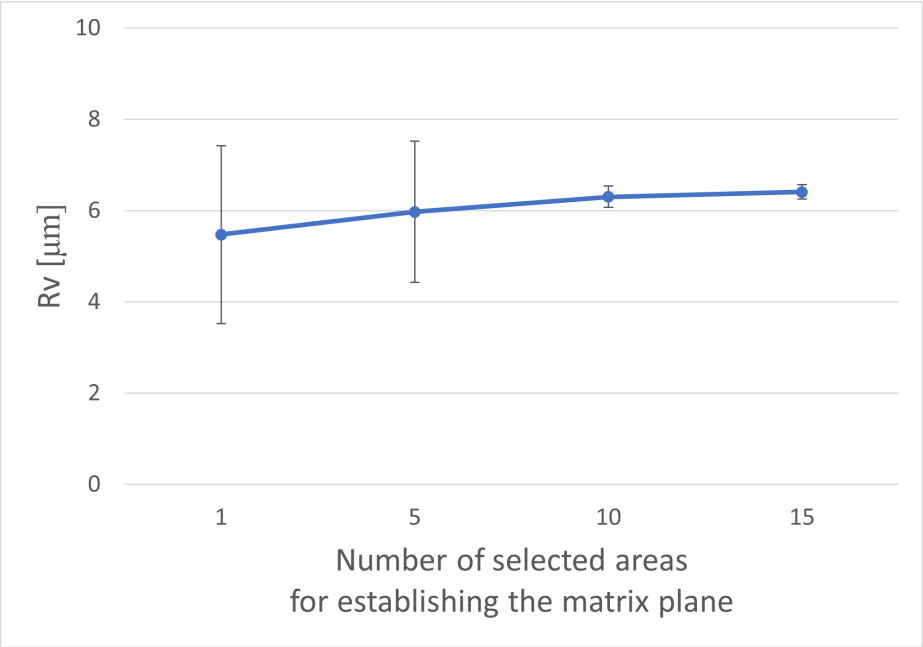

Figure A.4: Convergence study of the Rv surface roughness parameter regarding the selected areas for establishing the matrix plane.

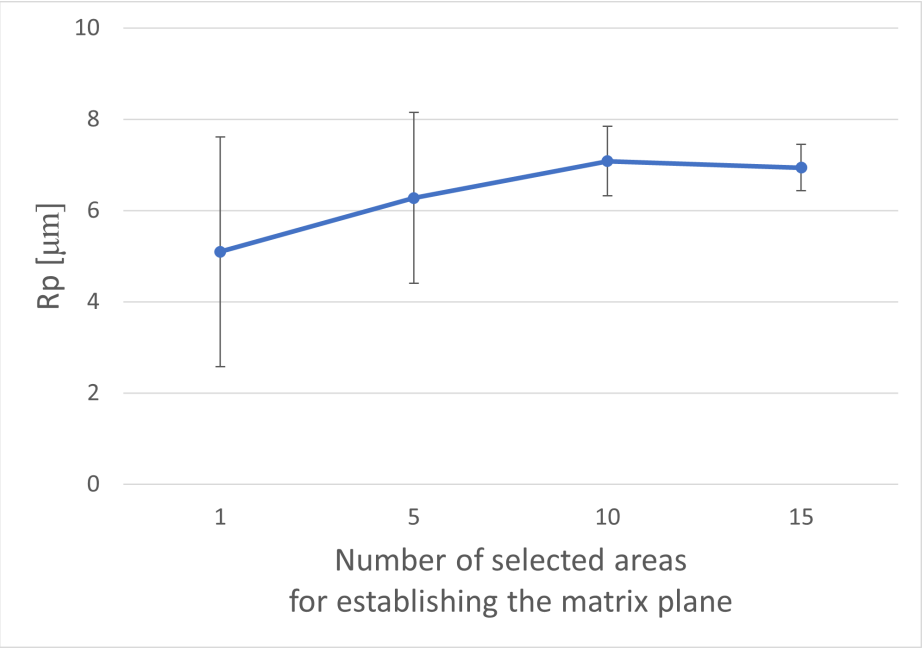

Figure A.5: Convergence study of the Rp surface roughness parameter regarding the selected areas for establishing the matrix plane.

A.3 Material pick-up

Preliminary study performed to analyse the sensitivity of the material pick-up measured for a tested blade regarding the greyscale threshold employed when considering the blade image.

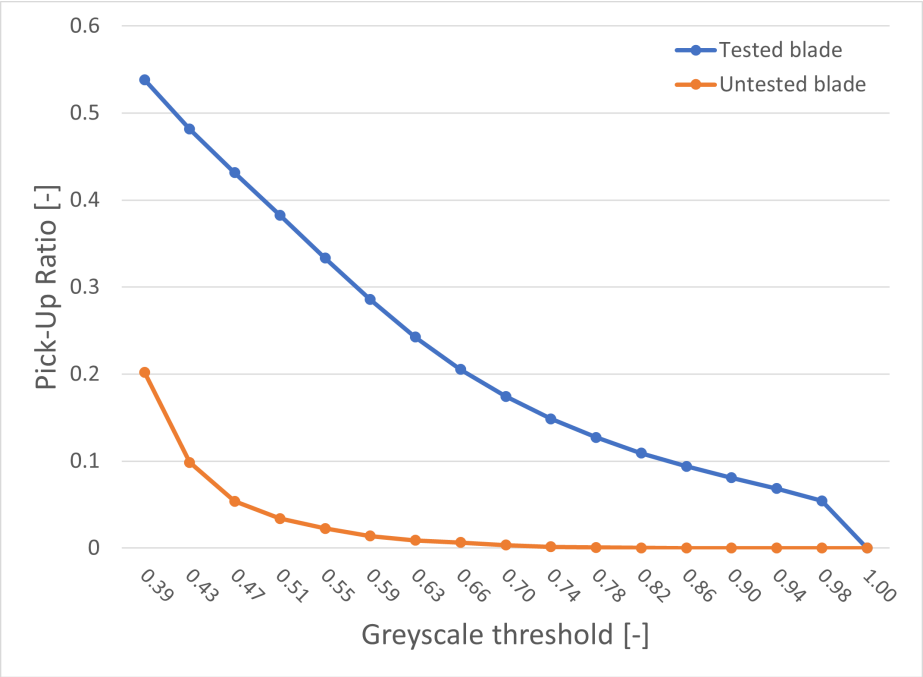

Figure A.6: Sensitivity study of the material pick-up ratio regarding the greyscale threshold.

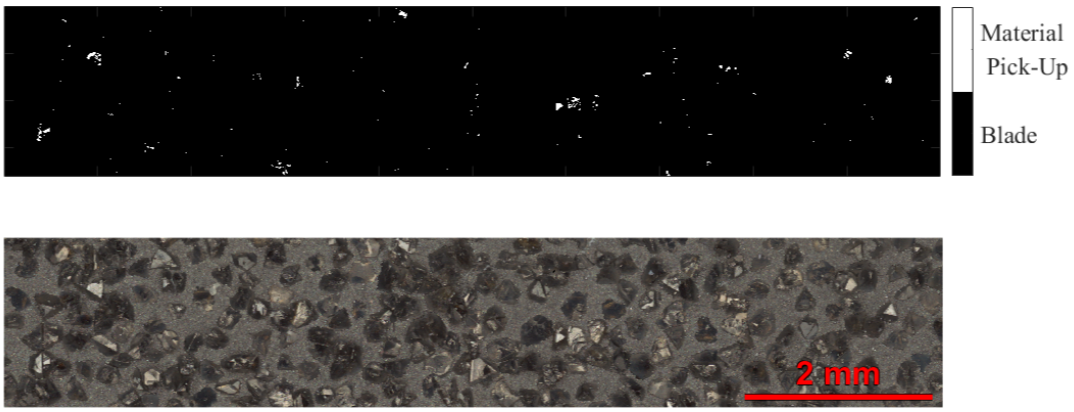

Figure A.7: Example of the material pick-up detected by the analytical tool for an untested blade with a 0.64 greyscale threshold.

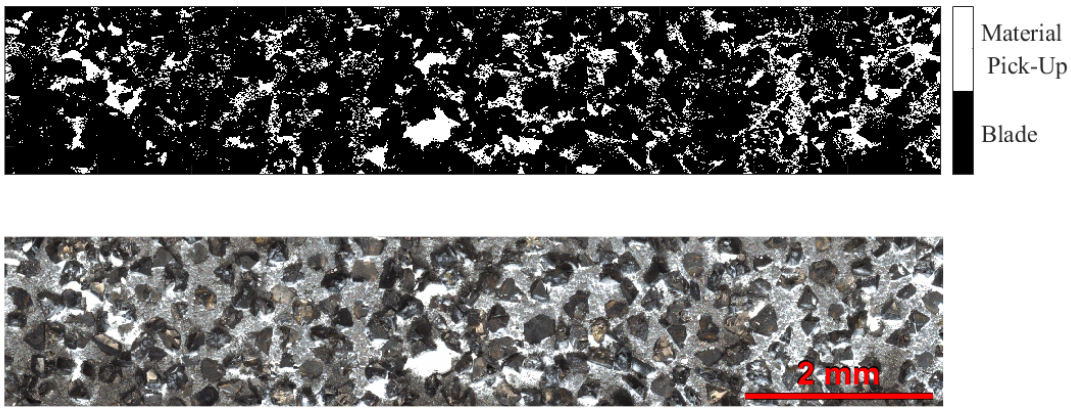

Figure A.8: Example of the material pick-up detected by the analytical tool for an tested blade with a 0.64 greyscale threshold.

Bibliography

[1] Meherwan Boyce. Gas Turbine Engineering Handbook. *Journal of Turbomachinery*, 134(1):1–10, 1990.

[2] Ronald D Flack. *Fundamentals of Jet Propulsion with Applications*. Cambridge University Press, Cambridge, 2005.

[3] Federal Aviation Administration. *Airplane Flying Handbook*, volume FAA-8083-3. U.S. Departmentof Transportation, Federal Aviation Administration, Oklahoma Ci, 2004.

[4] U. Desideri. *Fundamentals of gas turbine cycles: Thermodynamics, efficiency and specific power*. 2013.

[5] Bernard L. Koff. Gas turbine technology evolution: A designer's perspective. *Journal of Propulsion and Power*, 20(4):577–595, 2004.

[6] Li Xu, Sun Bo, You Hongde, and Wang Lei. Evolution of Rolls-royce Air-cooled Turbine Blades and Feature Analysis. *Procedia Engineering*, 99:1482–1491, 2015.

[7] Morumpalle Sai Sahith, G. Giridhara, and R. Suresh Kumar. Development and analysis of thermal barrier coatings on gas turbine blades – A Review. *Materials Today: Proceedings*, 5(1):2746–2751, jan 2018.

[8] M. Konter and H. P. Bossmann. *Materials and coatings developments for gas turbine systems and components*. 2013.

[9] B. Salehnasab, E. Poursaeidi, S.A. Mortazavi, and G.H. Farokhian. Hot corrosion failure in the first stage nozzle of a gas turbine engine. *Engineering Failure Analysis*, 60:316–325, feb 2016.

[10] A.M. Kolagar, N. Tabrizi, M. Cheraghzadeh, and M.S. Shahriari. Failure analysis of gas turbine first stage blade made of nickel-based superalloy. *Case Studies in Engineering Failure Analysis*, 8:61–68, apr 2017.

[11] Sushila Rani, Atul K. Agrawal, and Vikas Rastogi. Failure investigations of a first stage Ni based super alloy gas turbine blade. *Materials Today: Proceedings*, 5(1):477–486, jan 2018.

[12] Tim J Carter. Common failures in gas turbine blades. *Engineering Failure Analysis*, 12(2):237–247, apr 2005.

[13] G W Meetham. Coating requirements in gas turbine engines. *Journal of Vacuum Science & Technology A*, 3(6):2509–2515, nov 1985.

[14] Susanne Gebhard, Dan Roth-fagaraseanu, Tanja Wobst, and Matthew Hancock. Advanced coating systems for future shroudless turbines. (2):1–7, 2013.

[15] William V. Banks, Ali A. Ameri, Jeffrey P. Bons, and Robert J. Boyle. Numerical investigation of effects of tip clearance in shrouded turbine rotor blade performance. *2018 Joint Propulsion Conference*, 2018.

[16] Scott B. Lattime and Bruce M. Steinetz. Turbine engine clearance control systems: Current practices and future directions. *38th AIAA/ASME/SAE/ASEE Joint Propulsion Conference and Exhibit*, (July), 2002.

[17] Scott B Lattime, Bruce M Steinetz, and Malcolm G Robbie. Test Rig for Evaluating Active Turbine Blade Tip Clearance Control Concepts. 21(3), 2005.

[18] Raymond E. Chupp, Robert C. Hendricks, Scott B. Lattime, and Bruce M. Steinetz. Sealing in turbomachinery. *Journal of Propulsion and Power*, 22(2):313–349, 2006.

[19] E.E. Halila, D.T. Lenahan, and T.T. Thomas. High Pressure Turbine Test Hardware Detailed Design Report. Technical report, National Aeronautics and Space Administration, Lewis Research Center., Cleveland, Ohio, 1982.

[20] Sam Beale. Precision engineering for future propulsion and power systems: a perspective from Rolls-Royce. *Philosophical Transactions of the Royal Society A: Mathematical, Physical and Engineering Sciences*, 370(1973):4130–4153, aug 2012.

[21] Jeanine T. DeMasiMarcin and Dinesh K. Gupta. Protective coatings in the gas turbine engine. *Surface and Coatings Technology*, 68-69(C):1–9, 1994.

[22] M. Watson, N. Fois, and M.B. Marshall. Effects of blade surface treatments in tip–shroud abradable contacts. *Wear*, 338-339:268–281, sep 2015.

[23] Dieter Sporer, Scott Wilson, and Mitchell Dorfman. Ceramics for Abradable Shroud Seal Applications. pages 39–54. jan 2009.

[24] Sulzer Metco. Improve Efficiency and Reduce Emissions with Abradable Coatings for Steam Turbines. (October):1–8, 2014.

[25] Scott B Lattime and Bruce M Steinetz. High-Pressure-Turbine Clearance Control Systems: Current Practices and Future Directions. *Journal of Propulsion and Power*, 20(2):302–311, mar 2004.

[26] Agnes Muszynska, Donald Bently, Wesley Franklin, Robert Hayashida, Lori Kingsley, and Arthur Curry. Influence of Rubbing on Rotor Dynamics. Technical report, National Aeronautics and Space Administration, Minden, Nevada, 1989.

[27] Weihai Xue, Siyang Gao, Deli Duan, Jiaping Zhang, Yang Liu, and Shu Li. Effects of blade material characteristics on the high-speed rubbing behavior between Al-hBN abradable seal coatings and blades. *Wear*, 410-411(March):25–33, 2018.

[28] Michael Watson and Matthew Marshall. Wear mechanisms at the blade tip seal interface. *Wear*, 404-405(March):176–193, 2018.

[29] J. Stringer and M. B. Marshall. High speed wear testing of an abradable coating. *Wear*, 294-295:257–263, 2012.

[30] Haijun Xuan, Na Zhang, Bin Lu, Lijun Cheng, and Weirong Hong. Investigation of high-speed abrasion behavior of an abradable seal rubber in aero-engine fan application. *Chinese Journal of Aeronautics*, 30(4):1615–1623, 2017.

[31] Scott Wilson. Thermally sprayed abradable coating technology for sealing in gas turbines. *Future of gas turbine technology, 6th International Conference*, pages 1–9, 2012.

[32] Cleverson Bringhenti and Joao Barbosa. *Effects of Turbine Tip Clearance on Gas Turbine Performance*. jan 2008.

[33] John K Whalen, Eduardo Ed Alvarez, and Lester P Palliser. Thermoplastic labyrinth seals for centrifugal compressors. (Figure 1), 2004.

[34] Iacopo Giovannetti, Manuele Bigi, Massimo Giannozzi, Dieter Sporer, Filippo Cappuccini, and Marco Romanelli. *Clearance Reduction and Performance Gain Using Abradable Material in Gas Turbines*, volume 7. jan 2008.

[35] Farshad Ghasripoor, Richard Schmid, and Mitchell Dorfman. Abradables improve gas turbine efficiency. *Materials world*, 5(6):328–330, 1997.

[36] Boxiu Zhang and Matthew Marshall. Investigating material removal mechanism of Al-Si base abradable coating in labyrinth seal system. *Wear*, 426-427(January):239–249, 2019.

[37] H. I. Faraoun, T. Grosdidier, J. L. Seichepine, D. Goran, H. Aourag, C. Coddet, J. Zwick, and N. Hopkins. Improvement of thermally sprayed abradable coating by microstructure control. *Surface and Coatings Technology*, 201(6):2303–2312, 2006.

[38] R. Rajendran. Gas turbine coatings - An overview. *Engineering Failure Analysis*, 26:355–369, 2012.

[39] Scott Wilson. Overview of Sulzer Metco Compressor and Turbine Abradable Technology. *8th International Charles Parsons Turbine Conference*, pages 1–40, 2011.

[40] Surajit Purkayastha. *Mechanical behaviour of c-BN tipped turbine blades*. PhD thesis, 2016.

[41] Ioan D. Marinescu, W. Brian Rowe, Boris Dimitrov, and Ichiro Inasaki. Abrasives and Abrasive Tools. *Tribology of Abrasive Machining Processes*, pages 369–455, jan 2004.

[42] Richard Karl Schmid. *New high temperature abradables for gas turbines*. PhD thesis, 1997.

[43] J. R. Davenport, L. Mendez-Garcia, S. Purkayastha, M. E. Hancock, R. J. Stearn, and W. J. Clegg. Material needs for turbine sealing at high temperature. *Materials Science and Technology (United Kingdom)*, 30(15):1877–1883, 2014.

[44] Matthew Hancock. Shroudless Turbine Sealing, 2019.

[45] Rolls-Royce. Rolls-Royce internal communications, 2022.

[46] N. Fois, J. Stringer, and M. B. Marshall. Adhesive transfer in aero-engine abradable linings contact. *Wear*, 304(1-2):202–210, 2013.

[47] Romain Mandard, Jean François Witz, Xavier Boidin, Jacky Fabis, Yannick Desplanques, and Jean Meriaux. Interacting force estimation during blade/seal rubs. *Tribology International*, 82(PB):504–513, 2015.

[48] C. Delebarre, V. Wagner, J. Y. Paris, G. Dessein, J. Denape, and J. Gurt-Santanach. The wear mechanisms occurring in a labyrinth seal/abradable contact depending on the incursion depth parameter. *Mechanics and Industry*, 17(6), 2016.

[49] C. Delebarre, V. Wagner, J. Y. Paris, G. Dessein, J. Denape, and J. Gurt-Santanach. Tribological characterization of a labyrinth-abradable interaction in a turbo engine application. *Wear*, 370-371:29–38, 2017.

[50] Xiaozhi Kong, Gaowen Liu, Yuxin Liu, and Longxi Zheng. Experimental testing for the influences of rotation and tip clearance on the labyrinth seal in a compressor stator well. *Aerospace Science and Technology*, 71:556–567, 2017.

[51] Azzedine Dadouche, Martin Conlon, Waldemar Dmochowski, Brian Liko, Azzedine Dadouche, Martin Conlon, Waldemar Dmochowski, Brian Liko, and Jean-pierre Bédard Exper. Experimental Evaluation of Abradable Seal Performance at High Temperature. 2008.

[52] L.T. Shiembob. Continued development of abradable gas path seals. Technical report, NASA Lewis Research Center, Cleveland, Ohio, 1975.

[53] Lawrence T. Shiembob. Development of a plasma sprayed ceramic gas path seal for high pressure turbine applications. Technical Report 1, NASA Lewis Research Center, Cleveland, Ohio, 1977.

[54] Lawrence T. Shiembob. Development of improved high pressure turbine outer gas path seal components. Technical report, NASA Lewis Research Center, Cleveland, Ohio, 1980.

[55] Robert C. Bill. Development of sprayed ceramic seal system for turbine gas path sealing. Technical report, NASA Lewis Research Center, Cleveland, Ohio, 1978.

[56] Robert C. Bill. Plasma-sprayed xirconia gas path seal technology a state-of-the-art review. Technical report, NASA Lewis Research Center, Cleveland, Ohio, 1979.

[57] Dieter R. Sporer, Mitchell R. Dorfman, Massimo Giannozzi, Ulrike Taeck, Andrew R. Nicoll, and Iacopo Giovannetti. Novel ceramic abradable coatings with enhanced performance. *Proceedings of the ASME Turbo Expo*, 4:1017–1023, 2006.

[58] Dieter Sporer, Scott Wilson, Project Leader, and Massimo Giannozzi. On the potential of metal and ceramic based abradables in turbine seal applications. *Proceedings of the thirty-sixth turbomachinery symposium*, pages 79–86, 2007.

[59] Ronald S. Bunker. Axial turbine blade tips: Function, design, and durability. *Journal of Propulsion and Power*, 22(2):271–285, 2006.

[60] Sungho Yoon, Eric Curtis, John Denton, and John Longley. The effect of clearance on shrouded and unshrouded turbines at two levels of reaction. *Journal of Turbomachinery*, 136(2):1–9, 2013.

[61] I Salam, A Tauqir, and A.Q Khan. Creep-fatigue failure of an aero engine turbine blades. *Engineering Failure Analysis*, 9(3):335–347, jun 2002.

[62] Jie Gao and Qun Zheng. Comparative investigation of unsteady flow interactions in endwall regions of shrouded and unshrouded turbines. *Computers and Fluids*, 105:204–217, dec 2014.

[63] N. W. Harvey, D. A. Newman, F. Haselbach, and L. Willer. An investigation into a novel turbine rotor winglet. Part 1: Design and model rig test results. *Proceedings of the ASME Turbo Expo*, 6 PART A(January 2016):585–596, 2006.

[64] Ayman Abou-Salem. *Turbine blade tip leakage loss investigation*. PhD thesis, École de Technologie Supérieure Université du Québec, 2016.

[65] Takuzo Iwatsubo and Yasuhisa Iwasaki. Experimental and Theoretical Study on Swirl Braked Labyrrinth Seal. *Journal of System Design and Dynamics*, 2:451–462, jan 2008.

[66] William Scott Zemitis, Massimillano Mariotti, and Cody Jermaine Ford. "Turbine blade tip shroud", U.S. Patent 7762779, 2006.

[67] Patrick Mohr, Daniel Nowak, Emilio Fernandez, Michael Arnett, David Williams, and Carlos Collado. "Systems for preventing wear on turbine blade tip shrouds", U.S. Patent 2008 / 0317836A1, 2008.

[68] John D Coull, Nick R Atkins, and Howard P Hodson. Winglets for Improved Aerothermal Performance of High Pressure Turbines. 136(September):1–11, 2014.

[69] Sergio Lavagnoli. Experimental and Numerical Investigation of Optimized Blade Tip Shapes — Part I : Turbine Rainbow Rotor Testing and Numerical Methods. 141(January):1–13, 2019.

[70] Ronald S. Bunker. "Turbine blade tip with offset squealer", European Patent 1057972 A2, 2000.

[71] George Liang. "Turbine blade with trailing edge tip corner cooling", U.S. Patent 8011889 B1, 2011.

[72] George Liang. "Turbine blade with curved tip cooling holes", U.S. Patent 8043058 B1, 2011.

[73] Chao Zhou, Howard Hodson, Ian Tibbott, and Mark Stokes. The aerothermal performance of a cooled winglet tip in a high pressure turbine cascade. *Journal of Turbomachinery*, 135(3), mar 2013.

[74] Kevin S Klasing, Ching-Pang Lee, Paul H Vitt, and Brian D Keith. "Flared tip turbine blade", U.S. Patent 8632311 B2, 2014.

[75] L. J. Vandeperre, J. Wang, and W. J. Clegg. Effects of porosity on the measured fracture energy of brittle materials. *Philosophical Magazine*, 84(34):3689–3704, 2004.

[76] Karel Hajmrle and Hougong Wang. "Thermally sprayable powder materials having an alloyed metal phase and a solid libricant ceramic phase and abradable seal assembles manufactured thereform", U.S. Patent 5976695, 1999.

[77] P Fiala, K Hajmrle, A P Chilkowich, and L Shiembob. New High Temperature Titanium Compatible Abradable Seals. Technical report, 2003.

[78] Robert Middleton and William E. Smith. "Method of affixing an abradable metallic fiber material to a metal substrate", U.S. Patent 3936656, 1976.

[79] Robert C. Bill and Lawrence T. Shiembob. Friction and wear of sintered fiber-metal abradable seal materials. *1977 International Conference on Wear of Materials*, (4):1–5, 1977.

[80] D. J. Potter, Y. W. Chai, and G. J. Tatlock. Improvements in honeycomb abradable seals. *Materials at High Temperatures*, 26(2):127–135, 2009.

[81] Oerlikon Metco. Material Product Data Sheet Aluminum Silicon Hexagonal Boron Nitride Abradable, 2014.

[82] Oerlikon Metco. Material Product Data Sheet Nickel Graphite Abradable Powders, 2018.

[83] Oerlikon Metco. Material Product Data Sheet Aluminum Silicon Polymer Thermal Spray Powders, 2012.

[84] Oerlikon Metco. Material Product Data Sheet Aluminum Silicon Graphite Abradable Powders, 2015.

[85] Oerlikon Metco. Material Product Data Sheet Aluminum Bronze / Polyester Abradable Powders, 2014.

[86] Oerlikon Metco. Material Product Data Sheet CoNiCrAlY-BN CoNiCrAlY-BN / Polyester Abradable Thermal Spray Powders, 2018.

[87] Dieter Sporer, Jim Girgulis, Chris Dambra, Mitch Dorfman, and Oerlikon Metco. Segmented 8 % YSZ thermal barrier coating solutions using cascaded arc gun technology. pages 1–5, 2018.

[88] Oerlikon Metco. Material Product Data Sheet Nickel Chromium Tungsten Molybdenum Superalloy Powders, 2019.

[89] Oerlikon Metco. Improve efficiency and reduce emissions with high pressure turbine coatings for industrial gas turbines, 2014.

[90] Oerlikon Metco. Material Product Data Sheet Ytterbium Disilicate Powder for Thermal Spray. pages 1–3, 2017.

[91] Robert T Paine and Chaitanya K Narula. Synthetic routes to boron nitride. *Chemical Reviews*, 90(1):73–91, jan 1990.

[92] Nitin P. Padture, Maurice Gell, and Eric H. Jordan. Thermal barrier coatings for gas-turbine engine applications. *Science*, 296(5566):280–284, 2002.

[93] Robert Vaßen and Detlev Stöver. New Thermal Barrier Coatings Based on Pyrochlore/YSZ Double Layer Systems. pages 2–10. mar 2008.

[94] Svenja Ebert, Robert Mücke, Daniel Mack, Robert Vaßen, Detlev Stöver, Tanja Wobst, and Susanne Gebhard. Failure mechanisms of magnesia alumina spinel abradable coatings under thermal cyclic loading. *Journal of the European Ceramic Society*, 33(15-16):3335–3343, dec 2013.

[95] D L Anton, D M Shah, D N Duhl, and A F Giamei. Selecting high-temperature structural intermetallic compounds: The engineering approach. *JOM*, 41(9):12–17, 1989.

[96] Li Xu, Sun Bo, You Hongde, and Wang Lei. Evolution of Rolls-royce Air-cooled Turbine Blades and Feature Analysis. *Procedia Engineering*, 99:1482–1491, jan 2015.

[97] E. Basuki, A. Crosky, and B. Gleeson. Interdiffusion behaviour in aluminide-coated René 80H at 1150°C. *Materials Science and Engineering: A*, 224(1-2):27–32, mar 1997.

[98] J R Nicholls. Designing Oxidation-Resistant Coatings. *JOM*, 52(January), 2000.

[99] F.H. Stott and G.C. Wood. Growth and adhesion of oxide scales on Al2O3-forming alloys and coatings. *Materials Science and Engineering*, 87:267–274, mar 1987.

[100] K. P.R. Reedy and A. R. Cooper. Oxygen Diffusion in Magnesium Aluminate Spinel. *Journal of the American Ceramic Society*, 64(6):368–371, jun 1981.

[101] A C Fox and Bill Clyne. Oxygen transport through the zirconia top coat in thermal barrier coating systems. *Proceedings of the International Thermal Spray Conference*, 2:1589–1594, jan 1998.

[102] Lucjan Swadzba, Moskal Grzegorz, Boguslaw Mendala, and Gancarczyk T. Characterisation of APS TBC system during isothermal oxidation at 1100°C. *Archives of Materials Science and Engineering*, 28, dec 2007.

[103] Y. D. Liu, J. Sun, Z. L. Pei, W. Li, J. H. Liu, J. Gong, and C. Sun. Oxidation and hot corrosion behavior of NiCrAlYSi+NiAl/cBN abrasive coating. *Corrosion Science*, 167(January), 2020.

[104] B. A. Pint, J. R. Martin, and L. W. Hobbs. The oxidation mechanism of θ-Al2O3 scales. *Solid State Ionics*, 78(1-2):99–107, may 1995.

[105] A. S. Khanna, C. Wasserfuhr, W. J. Quadakkers, and H. Nickel. Addition of yttrium, cerium and hafnium to combat the deleterious effect of sulphur impurity during oxidation of an NiCrAl alloy. *Materials Science and Engineering A*, 1989.

[106] Dae Won Yun, S. M. Seo, H. W. Jeong, and Y. S. Yoo. The cyclic oxidation behaviour of Ni-based superalloy GTD-111 with sulphur impurities at 1100°C. *Corrosion Science*, 2015.

[107] J G Smeggil, A W Funkenbusch, and N S Bornstein. A relationship between indigenous impurity elements and protective oxide scale adherence characteristics. *Metallurgical Transactions A*, 17(6):923–932, 1986.

[108] J. G. Smeggil. Some comments on the role of yttrium in protective oxide scale adherence. *Materials Science and Engineering*, 1987.

[109] J. L. Smialek, D. T. Jayne, J. C. Schaeffer, and W. H. Murphy. Effects of hydrogen annealing, sulfur segregation and diffusion on the cyclic oxidation resistance of superalloys: a review. *Thin Solid Films*, 1994.

[110] B A Pint. Experimental observations in support of the dynamic-segregation theory to explain the reactive-element effect. *Oxidation of Metals*, 45(1):1–37, 1996.

[111] Ramkumar Janakiraman, G. H. Meier, and F. S. Pettit. The effect of water vapor on the oxidation of alloys that develop alumina scales for protection. *Metallurgical and Materials Transactions A: Physical Metallurgy and Materials Science*, 30(11):2905–2913, 1999.

[112] J. Toscano, R. Vaßen, A. Gil, M. Subanovic, D. Naumenko, L. Singheiser, and W. J. Quadakkers. Parameters affecting TGO growth and adherence on MCrAlY-bond coats for TBC's. *Surface and Coatings Technology*, 2006.

[113] Krishan L. Luthra and John H. Wood. High chromium cobalt-base coatings for low temperature hot corrosion. *Thin Solid Films*, 1984.

[114] C Leyens, I G Wright, and Bruce Pint. Hot Corrosion of Nickel-Base Alloys by Alkali-Containing Sulfate Deposits. *Materials Science Forum*, 369-372:571–578, jan 2001.

[115] Michael J. Pomeroy. Coatings for gas turbine materials and long term stability issues. *Materials and Design*, 2005.

[116] S. M. Jiang, X. Peng, Z. B. Bao, S. C. Liu, Q. M. Wang, J. Gong, and C. Sun. Preparation and hot corrosion behaviour of a MCrAlY + AlSiY composite coating. *Corrosion Science*, 2008.

[117] E. Airiskallio, E. Nurmi, M. H. Heinonen, I. J. Väyrynen, K. Kokko, M. Ropo, M. P.J. Punkkinen, H. Pitkänen, M. Alatalo, J. Kollár, B. Johansson, and L. Vitos. High temperature oxidation of Fe-Al and Fe-Cr-Al alloys: The role of Cr as a chemically active element. *Corrosion Science*, 2010.

[118] K. Zhang, M. M. Liu, S. L. Liu, C. Sun, and F. H. Wang. Hot corrosion behaviour of a cobalt-base super-alloy K40S with and without NiCrAlYSi coating. *Corrosion Science*, 2011.

[119] W. Beele, N. Czech, W. J. Quadakkers, and W. Stamm. Long-term oxidation tests on a Re-containing MCrAlY coating. *Surface and Coatings Technology*, 94-95(97):41–45, 1997.

[120] Q. M. Wang, Y. N. Wu, P. L. Ke, H. T. Cao, J. Gong, C. Sun, and L. S. Wen. Hot corrosion behavior of AIP NiCoCrAlY(SiB) coatings on nickel base superalloys. *Surface and Coatings Technology*, 2004.

[121] Y Wu, Q M Wang, Pei-ling Ke, Cangan Sun, Jie Gong, Fiona Wang, and L Wen. Evaluation of arc ion plated NiCoCrAlYSiB coatings after oxidation at 900–1100 °C. *Surface & Coatings Technology - SURF COAT TECH*, 200:2857–2863, feb 2006.

[122] I. Gurrappa. Identification of hot corrosion resistant MCrAlY based bond coatings for gas turbine engine applications. *Surface and Coatings Technology*, 2001.

[123] Delphine Aussavy, Rodolphe Bolot, Ghislain Montavon, François Peyraut, Gregory Szyndelman, Julien Gurt-Santanach, and Serge Selezneff. YSZ-Polyester Abradable Coatings Manufactured by APS. *Journal of Thermal Spray Technology*, 25(1-2):252–263, 2016.

[124] Oerlikon Metco. An Introduction to Thermal Spray. (6), 2016.

[125] ASTM. ASTM C633-13(2017), Standard Test Method for Adhesion or Cohesion Strength of Thermal Spray Coatings, 2017.

[126] Andreas Wank. Basics of thermal spray technology. *GTV Verschleiss-Schutz GmbH*, pages 1–20, 2006.

[127] Once Ab. Atmospheric plasma spray process and associated spraying jet. 77:35–42, jan 2015.

[128] Gerald Odhiambo, WenGe Li, Yuantao Zhao, and ChengLong Li. Porosity and Its Significance in Plasma-Sprayed Coatings. *Coatings*, 9:460, jul 2019.

[129] Tanja Steinke, Georg Mauer, Robert Vaßen, Detlev Stöver, Dan Roth-Fagaraseanu, and Matthew Hancock. Process Design and Monitoring for Plasma Sprayed Abradable Coatings. *Journal of Thermal Spray Technology*, 19:756–764, jun 2010.

[130] Rogerio Lima, B R Marple, Azzedine Dadouche, Waldemar Dmochowski, and Brian Liko. Nanostructured Abradable Coatings for High Temperature Applications. jan 2006.

[131] A.G. Evans, D.R. Mumm, J.W. Hutchinson, G.H. Meier, and F.S. Pettit. Mechanisms controlling the durability of thermal barrier coatings. *Progress in Materials Science*, 46(5):505–553, jan 2001.

[132] A. G. Evans, J. W. Hutchinson, and M. Y. He. Micromechanics model for the detachment of residually compressed brittle films and coatings. *Acta Materialia*, 1999.

[133] W R Chen, R Archer, X Huang, and B R Marple. TGO Growth and Crack Propagation in a Thermal Barrier Coating. *Journal of Thermal Spray Technology*, 17(5):858, 2008.

[134] X. Chen, J. W. Hutchinson, M. Y. He, and A. G. Evans. On the propagation and coalescence of delamination cracks in compressed coatings: With application to thermal barrier systems. *Acta Materialia*, 2003.

[135] E Schumann, C Sarioglu, J R Blachere, F S Pettit, and G H Meier. High-Temperature Stress Measurements During the Oxidation of NiAl. *Oxidation of Metals*, 53(3):259–272, 2000.

[136] M. Y. He, A. G. Evans, and J. W. Hutchinson. Ratcheting of compressed thermally grown thin films on ductile substrates. *Acta Materialia*, 2000.

[137] Abreeza Manap, Dowon Seo, and Kazuhiro Ogawa. Characterization of Thermally Grown Oxide on Cold Sprayed CoNiCrAlY Bond Coat in Thermal Barrier Coating. *Materials Science Forum*, 696:324–329, sep 2011.

[138] R.M. Cannon and P.Y. Hou. Diffusion induced stress generation during oxidation, 1998.

[139] Luochuan Su, Weixu Zhang, Yongle Sun, and T. J. Wang. Effect of TGO creep on top-coat cracking induced by cyclic displacement instability in a thermal barrier coating system. *Surface and Coatings Technology*, 2014.

[140] Gary Lee, Alan Atkinson, and Ahmet Selçuk. Development of residual stress and damage in thermal barrier coatings. *Surface and Coatings Technology*, 2006.

[141] Manuela Martena, D. Botto, P. Fino, S. Sabbadini, M. M. Gola, and C. Badini. Modelling of TBC system failure: Stress distribution as a function of TGO thickness and thermal expansion mismatch. *Engineering Failure Analysis*, 2006.

[142] J A Haynes, B A Pint, W D Porter, and I G Wright. Comparison of thermal expansion and oxidation behavior of various high-temperature coating materials and superalloys. *Materials at High Temperatures*, 21(2):87–94, jan 2004.

[143] T.A. Taylor and P.N. Walsh. Thermal expansion of MCrAlY alloys. *Surface and Coatings Technology*, 177-178:24–31, jan 2004.

[144] Robert Vaßen, Stephan Giesen, and Detlev Stöver. Lifetime of plasma-sprayed thermal barrier coatings: Comparison of numerical and experimental results. *Journal of Thermal Spray Technology*, 18(5-6):835–845, dec 2009.

[145] Chun-Hway Hsueh, Paul Becher, Edwin Fuller, Stephen Langer, and W Carter. Surface-Roughness Induced Residual Stresses in Thermal Barrier Coatings: Computer Simulations. *Materials Science Forum - MATER SCI FORUM*, 308-311:442–449, jan 1999.

[146] D. Liu, M. Seraffon, P. E.J. Flewitt, N. J. Simms, J. R. Nicholls, and D. S. Rickerby. Effect of substrate curvature on residual stresses and failure modes of an air plasma sprayed thermal barrier coating system. *Journal of the European Ceramic Society*, 2013.

[147] Q. M. Yu and Q. He. Effect of material properties on residual stress distribution in thermal barrier coatings. *Ceramics International*, 2018.

[148] L. Cen, W. Y. Qin, and Q. M. Yu. On the role of TGO growth in the interface undulation in MCrAlY coating system upon thermal cycling. *Ceramics International*, 2019.

[149] J A Goebel, F S Pettit, and G W Goward. Mechanisms for the hot corrosion of nickel-base alloys. *Metallurgical Transactions*, 4(1):261–278, 1973.

[150] M K Hossain and S R J Saunders. A microstructural study of the influence of NaCl vapor on the oxidation of a Ni-Cr-Al alloy at 850°C. *Oxidation of Metals*, 12(1):1–22, 1978.

[151] D. Deb, S. Ramakrishna Iyer, and V. M. Radhakrishnan. A comparative study of oxidation and hot corrosion of a cast nickel base superalloy in different corrosive environments. *Materials Letters*, 1996.

[152] Charng Cheng Tsaur, James C. Rock, and Yo Yu Chang. The effect of NaCl deposit and thermal cycle on an aluminide layer coated on 310 stainless steel. *Materials Chemistry and Physics*, 2005.

[153] S. M. Jiang, H. Q. Li, J. Ma, C. Z. Xu, J. Gong, and C. Sun. High temperature corrosion behaviour of a gradient NiCoCrAlYSi coating II: Oxidation and hot corrosion. *Corrosion Science*, 2010.

[154] S. M. Jiang, C. Z. Xu, H. Q. Li, J. Ma, J. Gong, and C. Sun. High temperature corrosion behaviour of a gradient NiCoCrAlYSi coating I: Microstructure evolution. *Corrosion Science*, 2010.

[155] E. A.G. Shillington and D. R. Clarke. Spalling failure of a thermal barrier coating associated with aluminum depletion in the bond-coat. *Acta Materialia*, 1999.

[156] BR Marple, MM Hyland, Y-c Lau, C-j Li, RS Lima, G Montavon, D Sporer, M Dorfman, L Xie Sulzer Metco, A Refke, I Giovannetti, and M Giannozzi. Thermal Spray 2007: Global Coating Solutions Processing and Properties of Advanced Ceramic Abradable Coatings. Technical report, 2007.

[157] E. Irissou, A. Dadouche, and R. S. Lima. Tribological characterization of plasma sprayed CoNiCrAlY-BN abradable coatings. *Proceedings of the International Thermal Spray Conference*, 23(January):602–607, 2013.

[158] Boxiu Zhang and Matthew Marshall. Investigating the application of a honeycomb abradable lining in the turbine stage of an aero-engine. *Tribology International*, 125(October 2017):66–74, 2018.

[159] Gwidon W. Stachowiak and Andrew W. Batchelor. *Engineering Tribology: Fourth Edition*. Elsevier Inc., 2013.

[160] Eric H Jordan, Chen Jiang, Jeffrey Roth, and Maurice Gell. Low Thermal Conductivity Yttria-Stabilized Zirconia Thermal Barrier Coatings Using the Solution Precursor Plasma Spray Process. *Journal of Thermal Spray Technology*, 23(5):849–859, 2014.

[161] Robert Vaßen, Alexandra Stuke, and Detlev Stöver. Recent developments in the field of thermal barrier coatings. *Journal of Thermal Spray Technology*, 18(2):181–186, 2009.

[162] Robert Miller, James Smialek, and Ralph Garlick. Phase Stability in Plasma-Sprayed Partially Stabilized Zirconia Yttria. *Advances in Ceramics*, 3, feb 1981.

[163] Olivia A Graeve. Zirconia BT - Ceramic and Glass Materials: Structure, Properties and Processing. pages 169–197. Springer US, Boston, MA, 2008.

[164] Dai Huang, K. R. Venkatachari, and Gregory C. Stangle. Influence of yttria content on the preparation of nanocrystalline yttria-doped zirconia. *Journal of Materials Research*, 10(3):762–773, 1995.

[165] Gregoire Witz, Valery Shklover, Walter Steurer, Sharath Bachegowda, and Hans-Peter Bossmann. Phase Evolution in Yttria-Stabilized Zirconia Thermal Barrier Coatings Studied by Rietveld Refinement of X-Ray Powder Diffraction Patterns. *Journal of the American Ceramic Society*, 90:2935–2940, sep 2007.

[166] Dan Roth-Fagaraseanu and Thomas Wunderlich. Shroud segment for a turbomachine, jul 2005.

[167] Ganesh Ibram. A Review on Magnesium Aluminate (MgAl2O4) Spinel: Synthesis, Processing and Applications. *International Materials Reviews*, 58:63–112, feb 2013.

[168] J Göring, S Hackemann, and B Kanka. WHIPOX®: Ein faserverstärkter oxidkeramischer Werkstoff für Hochtemperatur– Langzeitanwendungen. *Materialwissenschaft und Werkstofftechnik*, 38(9):766–772, sep 2007.

[169] Mikell P. Groover. *Fundamentals of Modern Manufacturing*. 2010.

[170] John Richard Davenport. *Anchor phases for high temperature abrasive systems*. PhD thesis, 2014.

[171] Stephen Malkin and Changsheng Guo. *Grinding Technology Theory and Application of Machining with Abrasives*, volume 2. 2008.

[172] Mark J. Jackson and Paulo Davim. *Machining with Abrasives*. Number 9. 2008.

[173] Dennis V. De Pellegrin, Normand D. Corbin, Gary Baldoni, and Andrew A. Torrance. Diamond particle shape: Its measurement and influence in abrasive wear. *Tribology International*, 42(1):160–168, 2009.

[174] Dennis V. De Pellegrin and Gwidon W. Stachowiak. Assessing the role of particle shape and scale in abrasion using 'sharpness analysis' part I. Technique development. *Wear*, 253(9-10):1016–1025, 2002.

[175] Valentin L Popov. *Contact Mechanics and Friction - Physical Principles and Aplications*. 2010.

[176] D. V. De Pellegrin and G. W. Stachowiak. Sharpness of abrasive particles and surfaces. *Wear*, 256(6):614–622, 2004.

[177] E. Rabinowicz and A. Mutis. Effect of abrasive particle size on wear. *Wear*, 8:381–390, 1965.

[178] J.J. Coronado. Effect of abrasive particle size on wear. In *Abrasion Resistance of Materials*, pages 167–184. Colombia, 2012.

[179] J. J. Coronado and A. Sinatora. Effect of abrasive size on wear of metallic materials and its relationship with microchips morphology and wear micromechanisms: Part 1. *Wear*, 271(9-10):1794–1803, 2011.

[180] J. J. Coronado and A. Sinatora. Effect of abrasive size on wear of metallic materials and its relationship with microchips morphology and wear micromechanisms: Part 2. *Wear*, 271(9-10):1804–1812, 2011.

[181] Jianbo Dai, Honghua Su, Hao Hu, Tengfei Yu, Wenbo Zhou, Wenfeng Ding, Shijun Ji, and Yihao Zheng. The influence of grain geometry and wear conditions on the material removal mechanism in silicon carbide grinding with single grain. *Ceramics International*, 43(15):11973–11980, oct 2017.

[182] Siyu Huang, Wen Hao Kan, Hongjian Wang, and Li Chang. The effect of abrasive particle size on the wear behavior of SS 440 Siyu. *Proceedings of The 11th International Conference on Structural Integrity and Failure*, (December), 2018.

[183] Zhenghai Yang, Yuexin Ge, Xu Zhang, Bao Shangguan, Yongzhen Zhang, and Yao Wang. Effect of particle size on current-carrying friction and wear properties of copper graphite composites. *Materials*, 2019.

[184] G. W. Stachowiak. Particle angularity and its relationship to abrasive and erosive wear. *Wear*, 241(2):214–219, 2000.

[185] M. J. Jackson. Fracture dominated wear of sharp abrasive grains and grinding wheels. *Proceedings of the Institution of Mechanical Engineers, Part J: Journal of Engineering Tribology*, 218(3):225–235, 2004.

[186] Sebastian Buhl, Christian Leinenbach, Ralph Spolenak, and Konrad Wegener. Failure mechanisms and cutting characteristics of brazed single diamond grains. *International Journal of Advanced Manufacturing Technology*, 66(5-8):775–786, 2013.

[187] Kai Ding, Yucan Fu, Honghua Su, Xiaobei Gong, and Keqin Wu. Wear of diamond grinding wheel in ultrasonic vibration-assisted grinding of silicon carbide. *International Journal of Advanced Manufacturing Technology*, 71(9-12):1929–1938, 2014.

[188] Zhengcai Zhao, Yucan Fu, Jiuhua Xu, and Zhiwei Zhang. Behavior and quantitative characterization of CBN wheel wear in high-speed grinding of nickel-based superalloy. *International Journal of Advanced Manufacturing Technology*, 87(9-12):3545–3555, 2016.

[189] Wenfeng Ding, Barbara Linke, Yejun Zhu, Zheng Li, Yucan Fu, Honghua Su, and Jiuhua Xu. Review on monolayer CBN superabrasive wheels for grinding metallic materials, 2017.

[190] Jingwei Wang, Tianyu Yu, Wenfeng Ding, Yucan Fu, and Ashraf F. Bastawros. Wear evolution and stress distribution of single CBN superabrasive grain in high-speed grinding. *Precision Engineering*, 54(March):70–80, 2018.

[191] W. Brian Rowe. *Principles of modern grinding technology*. 2013.

[192] Q. Jane Wang and Yip-Wah Chung, editors. *Encyclopedia of Tribology*. Springer US, 2013.

[193] Z. Shi and S. Malkin. Wear of electroplated CBN grinding wheels. *Journal of Manufacturing Science and Engineering, Transactions of the ASME*, 128(1):110–118, 2006.

[194] S. Y. Luo and Y. S. Liao. Study of the behaviour of diamond saw-blades in stone processing. *Journal of Materials Processing Tech.*, 51(1-4):296–308, 1995.

[195] M. Fujimoto and Y. Ichida. Micro fracture behavior of cutting edges in grinding using single crystal cBN grains. *Diamond and Related Materials*, 17(7-10):1759–1763, 2008.

[196] Yoshio Ichida, Ryunosuke Sato, Masakazu Fujimoto, and Hiromichi Tanaka. Fractal analysis of cutting edge wear in superabrasive grinding. *LEM 2007 - 4th International Conference on Leading Edge Manufacturing in 21st Century, Proceedings*, 2(4):640–650, 2007.

[197] Wenfeng Ding, Barbara Linke, Yejun Zhu, Zheng Li, Yucan Fu, Honghua Su, and Jiuhua Xu. Review on monolayer CBN superabrasive wheels for grinding metallic materials. *Chinese Journal of Aeronautics*, 30(1):109–134, 2016.

[198] I. Özkan, E. Dokumaci, and A. B. Önay. Cyclic oxidation behavior of c-BN and h-BN at elevated temperatures. *Acta Physica Polonica A*, 134(1):61–63, 2018.

[199] Keith J. Laidler. The development of the Arrhenius equation. *Journal of Chemical Education*, 61(6):494–498, 1984.

[200] Ihsan Barin. Thermochemical data of pure substances. page 1885, 1995.

[201] Ke Chen, Bai Song, Navaneetha K Ravichandran, Qiye Zheng, Xi Chen, Hwijong Lee, Haoran Sun, Sheng Li, Geethal Amila Gamage Udalamatta Gamage, Fei Tian, Zhiwei Ding, Qichen Song, Akash Rai, Hanlin Wu, Pawan Koirala, Aaron J Schmidt, Kenji Watanabe, Bing Lv, Zhifeng Ren, Li Shi, David G Cahill, Takashi Taniguchi, David Broido, and Gang Chen. Ultrahigh thermal conductivity in isotope-enriched cubic boron nitride. *Science*, 367(6477):555 LP – 559, jan 2020.

[202] W. G. Sloof and T. J. Nijdam. On the high-temperature oxidation of MCrAlY coatings. *International Journal of Materials Research*, 100(10):1318–1330, 2009.

[203] Peiling Ke, Qimin Wang, Weigang Hua, Jun Gong, Chao Sun, and Yanchun Zhou. Stresses and microstructural development of thermal barrier coatings using AIP/D-gun two-step processing. *Journal of the American Ceramic Society*, 90(3):936–941, 2007.

[204] R. D. Liu, S. M. Jiang, C. Q. Guo, J. Gong, and C. Sun. The alumina scale growth and interdiffusion behaviour of Pt modified AlSiY coating during cyclic oxidation. *Corrosion Science*, 120:121–129, 2017.

[205] Yoshitada Isono, Hirokazu Kishimoto, and Takeshi Tanaka. Evaluation of mechanical and thermal properties of cubic boron nitride by AB-initio calculation. *Materials Science Research International*, 4(1):39–44, 1998.

[206] Thomas A. Taylor and David F. Bettridge. Development of alloyed and dispersion-strengthened MCrAlY coatings. *Surface and Coatings Technology*, 86-87(PART 1):9–14, 1996.

[207] Y Tamarin. *Protective Coatings for Turbine Blades*. 2002.

[208] M. G. Hebsur and R. V. Miner. Stress rupture and creep behavior of a low pressure plasma-sprayed NiCoCrAlY coating alloy in air and vacuum. *Thin Solid Films*, 147(2):143–152, 1987.

[209] W. J. Brindley and J. D. Whittenberger. Stress relaxation of low pressure plasma-sprayed NiCrAlY alloys. *Materials Science and Engineering A*, 163(1):33–41, 1993.

[210] Praxair Surface Technologies. Tribomet Abrasive Coatings. page 10372, 2010.

[211] Megan McGregor. *Ni-Al-Ta alloys for high temperature abrasive coatings*. PhD thesis, 2019.

[212] J Hakl, T Vlasák, and J Lapin. Creep behaviour and microstructural stability of cast nickel based superalloy IN 792 5A. *Kovove Materialy*, 45:177–188, 2007.

[213] Karel Obrtlík, Martin Petrenec, Jiří Man, Jaroslav Polák, and Karel Hrbáček. Isothermal fatigue behavior of cast superalloy Inconel 792-5A at 23 and 900 °C. *Journal of Materials Science 2009 44:12*, 44(12):3305–3314, jun 2009.

[214] Jan-Erik Kanesund. Influence of deformation and environmental degradation of Inconel 792. *Linköpings Studies in Science*, 2017.

[215] M. S.A. Karunaratne, S. Kyaw, A. Jones, R. Morrell, and R. C. Thomson. Modelling the coefficient of thermal expansion in Ni-based superalloys and bond coatings. *Journal of Materials Science*, 51(9):4213–4226, may 2016.

[216] P. N. Quested, R. F. Brooks, L. Chapman, R. Morrell, Y. Youssef, and K. C. Mills. Measurement and estimation of thermophysical properties of nickel based superalloys. *https://doi.org/10.1179/174328408X361454*, 25(2):154–162, feb 2013.

[217] S. L. Sing, C. F. Tey, J. H.K. Tan, S. Huang, and Wai Yee Yeong. 3D printing of metals in rapid prototyping of biomaterials: Techniques in additive manufacturing. *Rapid Prototyping of Biomaterials: Techniques in Additive Manufacturing*, pages 17–40, jan 2019.

[218] Ester M. Palmero and Alberto Bollero. 3D and 4D Printing of Functional and Smart Composite Materials. *Encyclopedia of Materials: Composites*, pages 402–419, 2021.

[219] Torsten Petrat, C Brunner-Schwer, Benjamin Graf, and Michael Rethmeier. Microstructure of Inconel 718 parts with constant mass energy input manufactured with direct energy deposition. *Procedia Manufacturing*, 36:256–266, 2019.

[220] M. Palm, J. Preuhs, and G. Sauthoff. Production-scale processing of a new intermetallic NiAl–Ta–Cr alloy for high-temperature application: Part I. Production of master alloy remelt ingots and investment casting of combustor liner model panels. *Journal of Materials Processing Technology*, 136(1-3):105–113, may 2003.

[221] Du Xinghao, Guo Jianting, and Wu Baolin. Compressive properties of high-pressure die cast IP 75 alloy with strengthening Laves phase. *Materials Letters*, 61(1):288–291, jan 2007.

[222] B. Zeumer and G. Sauthoff. Intermetallic NiAlTa alloys with strengthening Laves phase for high-temperature applications. I. Basic properties. *Intermetallics*, 5(7):563–577, jan 1997.

[223] B. Zeumer and G. Sauthoff. Deformation behaviour of intermetallic NiAlTa alloys with strengthening Laves phase for high-temperature applications. II. Effects of alloying with Nb and other elements. *Intermetallics*, 5(8):641–649, jan 1997.

[224] B. Zeumer and G. Sauthoff. Deformation behaviour of intermetallic NiAlTa alloys with strengthening Laves phase for high-temperature applications III. Effects of alloying with Cr. *Intermetallics*, 6(5):451–460, jan 1998.

[225] B. Zeumer, W. Sanders, and G. Sauthoff. Deformation behaviour of intermetallic NiAl–Ta alloys with strengthening Laves phase for high-temperature applications IV. Effects of processing. *Intermetallics*, 7(8):889–899, aug 1999.

[226] Gwidon Stachowiak, Andrew Batchelor, and Grazyna Stachowiak. Tribometers. In *Tribology Series*, volume 44, pages 25–78. Elsevier, jan 2004.

[227] Tao Zhang, Feng Jiang, Lan Yan, Zhengyi Jiang, and Xipeng Xu. A novel ultrahigh-speed ball-on-disc tribometer. *Tribology International*, 157:106901, may 2021.

[228] E. Novinski, J. Harrington, and J. Klein. Modified zirconia abradable seal coating for high temperature gas turbine applications. *Thin Solid Films*, 95(3):255–263, sep 1982.

[229] Mike Watson. *Modifications of blade tips in abradable contacts*. PhD thesis, The University of Sheffield, 2019.

[230] J. W. Vogan, N. G. Solomon, and A.R. Stetson. Advanced ceramic material for high temperature turbine tip seals. Technical report, NASA Lewis Research Center, Cleveland, Ohio, 1979.

[231] Lin Tian, Yucan Fu, Jiuhua Xu, Haiyan Li, and Wenfeng Ding. The influence of speed on material removal mechanism in high speed grinding with single grit. *International Journal of Machine Tools and Manufacture*, 89:192–201, feb 2015.

[232] M. Schnieder and T. Sommer. *Turbines for industrial gas turbine systems*. 2013.

[233] Julian Alberto Garcia Panizo. *Investigating the Tribological Behaviours of a Jet Engine ' s Abrasive Rotor and Stator Vane Contact*. PhD thesis, 2022.

[234] Eldar Rahimov, Michael Watson, Andreas Hadjisoteriou, and Matthew Marshall. Investigation of wear mechanisms in AlSi-polyester abradable - Ti(6Al4V) blade contacts using stroboscopic imaging. *Wear*, 494-495, apr 2021.

[235] Allan Liu, Matthew Marshall, Eldar Rahimov, and Julian Panizo. Investigation of wear mechanics and behaviour of NiCr metallic foam abradables. *Proceedings of the Institution of Mechanical Engineers, Part C: Journal of Mechanical Engineering Science*, 236(9):4962–4972, may 2022.

[236] Andreas Hadjisoteriou. *Investigation of material removal mechanism and thermal response of compressor abradable materials The University of She eld*. PhD thesis, 2021.

[237] Eldar Rahimov. *Investigation of Wear Mechanisms in Abradable-Blade Contacts*. PhD thesis, 2022.

[238] Leticia Méndez García. *Oxides as High Temperature Abrasives*. PhD thesis, 2016.

[239] LabIR. HERP-HT-MWIR-BK-11 Thermographic paint data sheet. page 832, 2019.

[240] Various Authors. *Advanced Ceramic Coatings and Interfaces IV*. 2009.

[241] Alvaro Parody. Blade comparisons, Rolls-Royce internal reports. Technical report, 2021.

[242] N Fois, M Watson, J Stringer, and M B Marshall. An investigation of the relationship between wear and contact force for abradable materials. *Proceedings of the Institution of Mechanical Engineers, Part J: Journal of Engineering Tribology*, 229(2):136–150, 2015.

[243] Danilo De Jesus Oliveira, Luiz Gustavo Guermandi, Eduardo Carlos Bianchi, Anselmo Eduardo Diniz, Paulo Roberto De Aguiar, and Rubens Chinali Canarim. Improving minimum quantity lubrication in CBN grinding using compressed air wheel cleaning. *Journal of Materials Processing Technology*, 212(12):2559–2568, dec 2012.

[244] Kai Chen, Yang Song, Pengfu Ding, Zhiwu Ke, and Zhenxing Zhao. The MD simulation of friction heat dissipation and generation in high-speed dry sliding system. *Energy Reports*, 9:101–112, jun 2023.

[245] J. B. Johnson, J. R. Nicholls, R. C. Hurst, and P. Hancock. The mechanical properties of surface scales on nickel-base superalloys—II. Contaminant corrosion. *Corrosion Science*, 18(6):543–553, jan 1978.

[246] Damian Migas, Grzegorz Moskal, and Dawid Niemiec. Surface Condition of New Co-Al-Mo-Nb and Co-Al-W Cobalt-Based Superalloys After Oxidation at 800 °C. *Journal of Materials Engineering and Performance*, 27(2):447–456, feb 2018.

[247] Shang Gao, Li Hong Yang, Yi Gan, and Qiang Chen. The Influence of Sliding Speed on the Friction Behavior of Silica Surface. *ACS Omega*, 6(4):3384, feb 2021.

[248] B. Denkena, A. Krödel, and M. Wilckens. High performance peel grinding of steel shafts using coarse electroplated CBN grinding wheels. *Production Engineering*, 15(5):717–724, oct 2021.